Uninhabited Aircraft Design Optimised for Close Formation Air-Refuelling Flight

by

Sma Nilsuwan

Department of Aeronautics

Imperial College London

A thesis submitted for the degree of

Doctor of Philosophy

2010

Declaration

The work presented in this thesis is based on the research carried out at Imperial College London. No part of the thesis has been submitted elsewhere for any other degrees or qualifications. And all the work is my own unless referenced to the contrary in the text.

Abstract

Uninhabited combat aerial vehicles (UCAVs) are intended for carrying out high-risk combat missions with a high degree of precision, effectiveness and efficiency and without endangering pilots' lives. An air refuelling system for UCAVs could bring out their full potential in wartime action, by extending their range capability and increasing their airborne time. Hence, the main aim of this PhD research programme was to develop a design and optimisation methodology for an innovative concept consisting of a large uninhabited tanker and a number of UCAVs flying in a close formation, with an optimised and fully autonomous air refuelling capability. The close formation flight of this tanker and UCAVs combination provides aerodynamic benefits which together with an optimised air-to-air refuelling sequence will result in a significantly extended combat radius and capability without unnecessarily compromising the UCAVs' physical size. With a stealth design approach, the proposed combination could fly directly to a faraway destination without any intermediate stops, hence minimizing any risk of detection, with significant fuel and time savings. To fully exploit the potential advantages the above combination, both the autonomous tanker and the UCAV concepts have been designed through specially developed and separate synthesis methodologies and each aircraft was subsequently optimised for its respective operational role. An investigation into formation flight aerodynamics has also been conducted. A method for evaluating the associated aerodynamic benefits has been developed using a modified vortex-lattice approach, to automatically locate an optimal formation position for each aircraft in flight. A further method has also been developed to optimise the air refuelling sequence of the UCAVs by utilising the design synthesis and formation flight results aiming to maximise a range objective function. The above design synthesis and optimisation methodologies have all been integrated into an automated program written in Visual Basic.NET, featuring Graphical User Interfaces for simpler, faster and repetitive implementation.

Acknowledgements

First of all, I would like to thank my supervisor Dr. Varnavas Serghides who has tirelessly provided me with invaluable guidance, support and knowledge both in terms of science and philosophy over the years of studies. The completion of this research project would have been impossible without him.

Special thanks to Richard Mcsherry, Mark Frederick and Matthew Laffan who I shared the office with. They assisted me in various ways and made the environment in the office educational and enjoyable at the same time.

Beyond work, the most important people that I am indebted to are my parents. They receive my deepest gratitude and love for their dedication and support throughout twenty five years of my life.

Contents

Nomenclature

A_{inlet}	- Inlet area
A_p	- Tire contact area
AR	- Wing aspect ratio
AR_{in}	- Inlet aspect ratio
AR_{ex}	- Exhaust-pipe aspect ratio
b	- Semi-span
b_W	- Total wing span
BFL	- Balanced field length
BPR	- Engine bypass ratio
c	- Chord
c'	- Flapped mean aerodynamic chord
C_{D0}	- Zero-lift drag coefficient
C_{Di}	- Induced drag coefficient
C_{Dw}	- Wave drag coefficient
c_f / c	- Flap-to-chord ratio
$C_{l\alpha}$	- Aerofoil lift-curve slope
C_L	- Lift coefficient
$C_{L\text{dsn}}$	- Design lift coefficient
$C_{l\max}$	- Aerofoil maximum lift coefficient
$C_{L\max}$	- Maximum lift coefficient
$C_{L\alpha}$	- Wing lift-curve slope
$C_{m\alpha}$	- Total pitching-moment derivative
$C_{m\alpha F}$	- Fuselage pitching moment

c_R	- Reference root chord
d	- Diameter
e	- Oswald efficiency
E_{WD}	- Empirical wave-drag efficiency parameter
ESWL	- Equivalent single wheel load
f_{CL}	- Increment of UCAV C_L in formation flight
f_{STR}	- Structural thickness factor
ff	- Fuselage factor
g	- Gravitational constant
h	- Height
h_g	- Minimum height clearance
i_w	- Wing incidence relative to the fuselage
inc	- Internal clearance
K	- Induced-drag factor
l	- Length
L/D	- Lift-to-drag ratio
L_{rs}	- Radius of relative stiffness
LCN	- Load classification number
LP	- Static load proportion
M	- Mach number
M_{dd}	- Drag-divergence Mach number
mac	- Mean-aerodynamic chord
n	- Load factor
N_{RF}	- Number of refuelling
N_{ucav}	- Number of UCAVs assigned per tanker
N_z	- Maximum load factor
q	- Dynamic pressure
P_{inf}	- Inflation pressure
P_S	- Specific excess power
psf	- Pilot-support weight fraction

R_{IC}	- Area ratio between the inlet and the engine
R_{IE}	- Area ratio between the exhaust and the inlet planes
r_{LE}	- Leading-edge radius of aerofoil
R_{LIC}	- Ratio between the lengths of the intake diffuser and the engine
R_{LEC}	- Ratio between the lengths of the exhaust pipe and the engine
R_r	- Rolling radius factor
R_{yRF}	- Relative spanwise position of HDU on the outboard-wing partition
Rw_F	- Ratio of the fairing span relative to the fuselage width
RF	- Reserve fuel fraction
S	- Range
S_{flapped}	- Flapped wing area
S_G	- Ground-roll distance
S_W	- Reference wing area
sfc	- Specific fuel consumption
SM	- Static margin
spr_{F}	- Front spar location relative to the chord
spr_{R}	- Rear spar location relative to the chord
tc	- Maximum thickness of aerofoil
T_{en}	- Uninstalled thrust
$T_{\max}$	- Maximum thrust
T/W	- Thrust-to-weight ratio
V	- Air speed
$V_{\max}$	- Maximum speed
V_{stall}	- Stall speed
V_V	- Touch-down sink speed
w	- Width
W	- Weight
W_0	- Maximum takeoff weight
w_{fw}	- Engine firewall thickness
W/S	- Wing loading

W_e / W_0	- Empty-weight fraction
W_f / W_0	- Fuel-weight fraction
x	- Horizontal distance
x_{com}	- Strut compression factor
x_{Q4}	- Position of root quarter chord relative to total fuselage length
x_{stg}	- Stagger distance relative to the engine length
xc	- Relative position on the wing chord
y	- Lateral distance
$\bar{y}$	- mac spanwise location
z	- Vertical distance
α	- Angle of attack
α_d	- Wing dihedral
α_0	- Zero-lift angle
$\alpha_{CL\max}$	- Stall angle
β	- Aerofoil efficiency
γ_{CL}	- Climb angle
∂f	- Flap deflection angle
$\Delta C_{D0\ \mathrm{flap}}$	- Zero-lift drag coefficient due to flap deflection
Δx_{acw}	- Aerodynamic centre measured from the wing leading edge
Δx_{fcp}	- Centre of pressure of the flap lift increment
ε	- Wing twist
θ_{noz}	- Nozzle taper angle
θ_{RF}	- Fairing pod alignment angle
θ_{sd}	- Maximum deflection angle of the duct
θ_{stg}	- Longitudinal stagger angle
θ_{tp}	- Inlet/exhaust trapezium angle
θ_{zt}	- Top-fuselage curvature angle
λ	- Taper ratio
λ_{noz}	- Nozzle taper ratio

Λ_{Q4}	- Quarter-chord sweep angle
Λ_{HL}	- Hinge-line sweep angle
Λ_{LE}	- Wing leading-edge sweep
Λ_{TE}	- Wing trailing-edge sweep
$\Lambda_{T\max}$	- Wing sweep at the maximum thickness-to-chord position
μ	- Ground rolling resistance
ρ	- Air density

Chapter 1

Introduction

1.1 Introduction to UAVs

Uninhabited aerial vehicles (UAVs) have been extensively employed in various military operations for the past decade mainly for intelligence, surveillance and reconnaissance purposes. Recently, UAVs have begun to emerge as major aerospace systems not only in military applications but also in civilian roles, due to advances in state-of-the-art technologies, control systems reliability levels, payload sophistication and more importantly due to their effectiveness and affordability in comparison to their manned counterparts [1]. On the other hand, manned aircraft still maintain their advantages in terms of flexibility and adaptability in the operations.

It is stated that UAVs are designed for serving the missions, which are long, tiring and high-risk for pilots [2]. UAVs offer distinct advantages over the manned aircraft particularly in terms of performance and operating cost. The huge training cost of an experienced operational pilot and the sensitive security issues associated with a loss or capture of pilots in action is a major concern for Armed Forces. UAVs could eliminate any intense political situations which may arise when the pilots are captured or shot down in hostile territory. In the current demanding environment, a cockpit and pilot support systems account for a considerable amount of the total aircraft design time and cost, while the operational, flight training, and maintenance costs can be even much higher. Therefore, removing the pilot from the system allows a significant reduction in both the development and operational costs [3].

The development of UAV technologies has made the use of such systems as offensive platforms possible. The concept of uninhabited combat aerial vehicles (UCAVs) has been created to perform high-risk missions in which may prove difficult for manned aircraft to survive; e.g. attacking chemical/biological warfare facilities, suppression of enemy air defences (SEAD) and other deep strike missions. Brian [34] stated that the UCAV missions could be characterised by three “D’s”: *dull*, *dirty* and *dangerous*. *Dull* means long endurance missions which may last for days exceeding pilot’s physical endurance. *Dirty* missions refer to those where chemical/biological contamination is a major concern. *Dangerous* missions in which there is a great risk involved most likely due to heavy enemy air defences. SEAD is considered as one of the most dangerous missions for manned aircraft and it has therefore become a primary focus in current UCAV development.

From an aircraft design perspective, since the shape and functionality of UCAVs are no longer constrained by the need for a cockpit and pilot support systems, they provide a higher degree of design freedom, thus allowing cleaner aerodynamics, lower radar cross-section and greater flexibility for packaging internal components. The low observability features of a UCAV design, generally provides the capability to release weapons at closer distance from the target. Also UCAV manoeuvrability levels are no longer constrained by human physiological limitations, but only by the maximum load that the airframe structure can sustain.

As mentioned above, training a pilot costs a large sum of money and to maintain the pilot skills, expensive combat training needs to continue regularly even during peacetime. UCAVs do not require routine training, only periodic inspections to maintain systems in storage are sufficient. Also every flight cycle causes structural fatigue to an airframe and deteriorates aircraft systems; therefore, operating aircraft only when they are needed, can extend their service life and reduce maintenance costs considerably. As far as the system competition is concerned, UCAVs would not fully replace manned aircraft but they could complement them by performing the aforementioned dangerous missions where there is a high probability that manned aircraft may not survive such missions [33].

1.2 UCAV Considerations

As in the case of conventional fighter aircraft, the majority of offensive operations require UCAVs to be operated in groups to increase combat effectiveness and thus the chances of success during a campaign. By employing multiple UCAVs flying in formation, the overall aircraft performance may be enhanced without the need for additional modifications to the individual vehicles. Apart from improving the overall combat efficiency through a concentration of firepower, formation flight also provides increased aerodynamic efficiency, reduced fuel consumption and hence an extended combat radius.

The above aerodynamic formation flight benefits occur as a result of the trailing aircraft flying in the upwash region produced by the wingtip vortices of the leading aircraft. Nonetheless, flying in such a turbulent environment requires more attention from the pilot to keep the trailing aircraft steady in the formation position. Due to the continuous flying precision demanded from the pilot, formation flying proves to be difficult especially in a long-haul flight. However, this extra workload would be no longer needed in the case of UCAVs, since with the aid of a specially configured autonomous flight control system the UCAVs would be easily capable of maintaining a precise close formation throughout the flight.

Without cockpit and pilot support systems, the size of a UCAV can be much smaller than that of an equivalent manned fighter aircraft, resulting in lower fuel consumption and reduced manufacturing, operating and maintenance costs. Although these UCAV advantages are economically appealing, the major drawback of operating such systems is that the combat radius, endurance, and weapon payloads are not great due to their reduced size, and hence limited fuel capacity. The combat radius may be extended by employing formation flight techniques, as mentioned earlier; however, the performance gains obtained from such techniques are not, by all means, significantly sufficient to meet the demanding range capability, not to mention other performance requirements which still might remain unsatisfied. As far as the weapon payload is concerned, no matter how advance the weapon technologies are, a small amount of armaments would not be able to cause sufficient damage to the enemy. The sizes of the weapons have been optimised over the years to enable combat aircraft to carry more and to perform an operation more effectively.

In order to rectify various operational drawbacks, the overall size of a UCAV needs to be increased, as mentioned in the terminated J-UCAS programme, in order to be able to carry more weapons and more fuel. Jumper [8] also said that a UCAV would be fairly big for long endurance and would be able to pursue the mission persistently by simply air refuelling. As he noted, the purpose of integrating an in-flight refuelling capability into UCAVs is to bring out their full performance in wartime. Figures 1.1 and 1.2 together show a comparison between the first and the second versions of a UCAV developed by Northrop Grumman for operating from U.S. Navy's aircraft carriers. It is clear that the size of the latter X-47 has increased significantly from its predecessor in order to meet mission requirements for greater payload, longer range, higher endurance; and also improving stability and durability in the harsh environment of carrier operations.

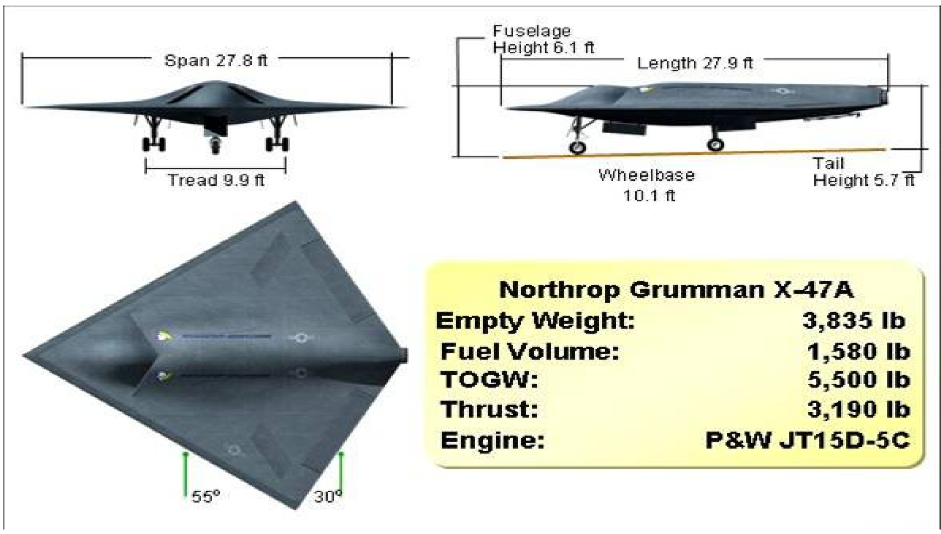

Figure 1.1: Northrop Grumman X-47A general specifications [7]

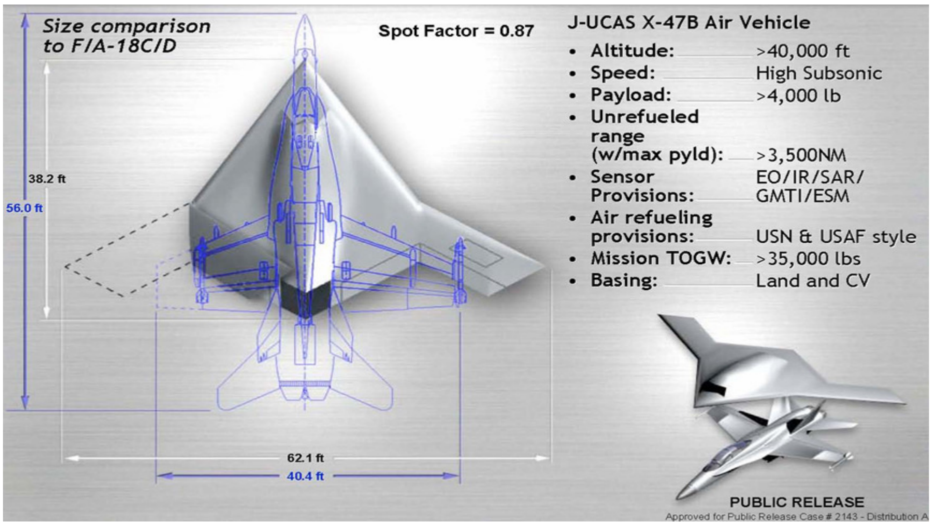

Figure 1.2: Northrop Grumman X-47B general specifications compared to F/A-18C/D [11]

In-flight refuelling (a.k.a. air refuelling) is an airborne fuel-transferring operation from a tanker to a receiver aircraft, which enhances the range, endurance and payload carrying capabilities of the latter. A tanker is an aircraft developed primarily to perform this fuel dispensing role. By incorporating the air refuelling capability to unmanned combat systems, their operating time would be limited only by the need for re-arming or by critical system failures. Figure 1.3 compares the UCAV's combat persistency with other piloted aircraft deploying from an aircraft carrier and two different main operation bases (MOB). Undoubtedly, the continuous operating time of the UCAV can be greater than the majority of piloted aircraft, especially due to the elimination of any aircrew fatigue constraints. Though in the figure below the time parameter indicated for a dedicated bomber is exceptionally high due to its design role characteristics, overall size and support systems available on-board.

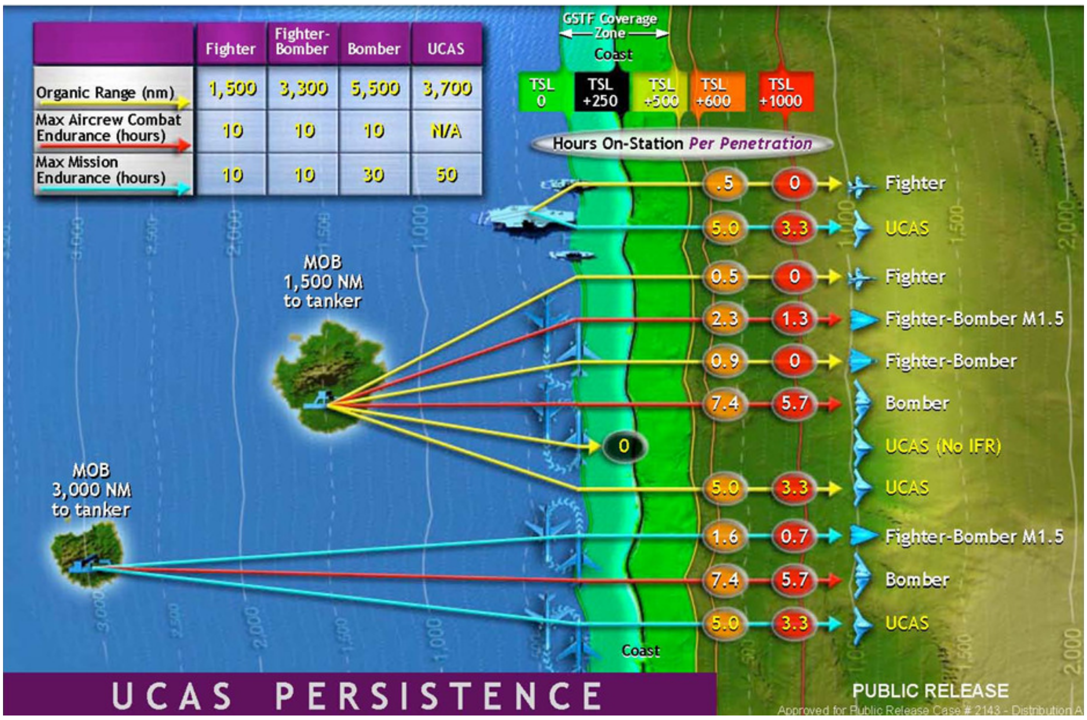

Figure 1.3: UCAS persistence comparison [11]

During the development of various UCAVs, a research into automated air-to-air refuelling (AAR) systems was conducted by NASA Dryden Flight Research Centre and the U.S. Air Force Research Lab to assist piloted aircraft in such an operation and also to explore the possibility of performing AAR on UCAVs. Jacob [12] who investigated an AAR model for UCAVs, stated that future combat derivatives would require in-flight refuelling to reach their full potential. According to an official X-47B report [11], the AAR system will be integrated and will be compatible with both U.S. Air Force's boom-receptacle and U.S. Navy's probe-drogue standard refuelling types. The development of that AAR system strengthens the need for a complete autonomous combination system consisting of an uninhabited tanker and UCAVs.

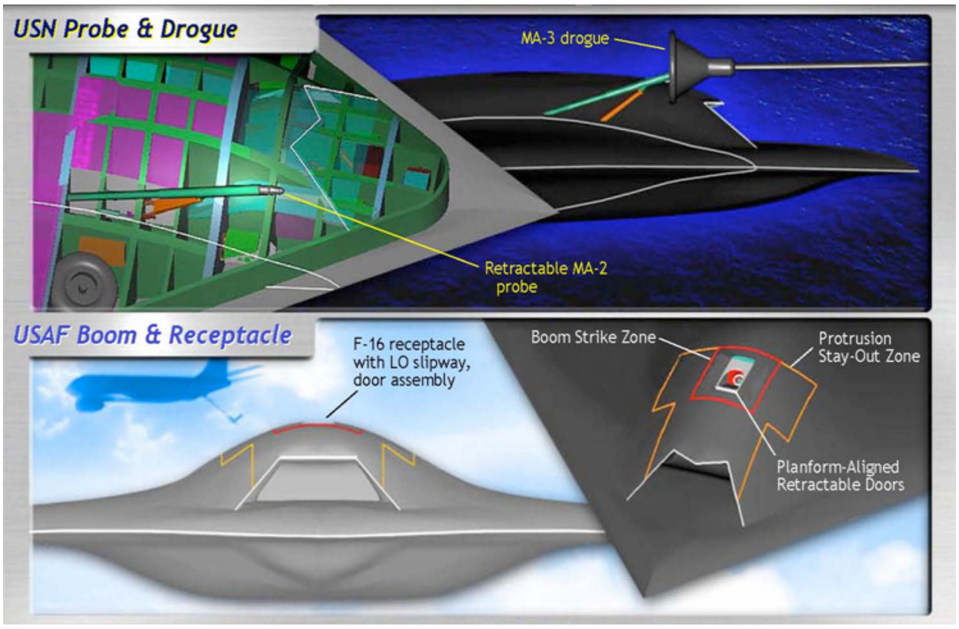

Figure 1.4: X-47B In-flight Refuelling Provisions [11]

1.3 Uninhabited Tanker Considerations

Although an air refuelling technique enables various strategic advantages, the operation itself is difficult and hazardous for both the tankers and the receiver. A further major problem is fleet crewing [10]. It is very difficult to train well-qualified tanker crews and requires a considerable amount of resources. The receiver's pilot also needs a lot of experience in order to perform the refuelling operation precisely avoiding hose/boom collisions with the aircraft especially when encountering various challenging circumstances such as turbulence, obscured visibility, darkness and fatigue [37]. For these reasons, an uninhabited tanker concept proposed in this PhD research programme, would provide a highly desirable solution while serving this essential role, not only for UCAVs, but for all other types of receiver aircraft. With the fully autonomous tanker and UCAVs combination proposed in this research programme, a very high reliability in the air refuelling operation can be achieved since such a system would be able to perform the operation with higher precision and react to any external disturbances much more quickly than the pilots. In addition, any human fatigue-related issues would be eliminated.

Existing tankers are specially modified commercial aircraft which are normally intended to perform dual roles such as transporting cargo/passengers together with air refuelling. The performance requirements for the tanker role are generally more demanding than those for troop and freight transportation. Hence, those requirements define the availability of commercial aircraft choices that can be converted to this role [38] and the resulting aircraft is usually a compromising solution. The main tanker modifications include the installation of additional fuel tanks in the cargo compartment and the integration of the specialised air refuelling systems; while the passenger cabin is left free for the cargo/passenger role. For these reasons, designing a fully dedicated tanker would offer distinct benefits especially in terms of cost effectiveness and operational performance, assuming the required number of such aircraft will be relatively high.

As for the UCAV, the flexibility of uninhabited aircraft design, allows stealthy features to be easily applied on the configuration of the tanker, to significantly reduce its radar signature. The shape of the offload fuel tanks can be designed around the available internal space, hence, optimising the internal arrangement and therefore maximising the fuel payload capacity, without any unnecessary excess airframe volume. Currently, the existing tankers do not possess any radar warning systems or defensive countermeasures; therefore, these aircraft entirely rely on the defence provided by fighters and other support aircraft. On the other hand, the uninhabited tanker can be designed to carry electronic/infrared countermeasures or even internally-carried defensive weapons, for self-protection.

1.4 The Uninhabited Tanker/UCAV Combination

In general, tankers are only requested when refuelling support is needed in an operation. The tanker would orbit at a designated rendezvous point waiting for the receiver's arrival, perform air refuelling, and then either wait for the next group of receivers or abort the operation and return to the air base. Nonetheless, the tankers also serve deployment support operations in which they escort and refuel combat aircraft to extend their range during inter-theatre deployments allowing non-stop flight and swift response to a regional crisis. This deployment support role of the tanker together with the introduced formation flight approach, justify the development of more advanced techniques to operate an unmanned aircraft system comprising an uninhabited tanker and UCAVs.

This research programme aims to provide a long-range capability and enhance the combat effectiveness of a group of UCAVs, by operating them in a close formation with a much larger uninhabited tanker during cruise which will be providing air refuelling to the group, at various intervals, as required. The UCAV group will be flying in an inverted ‘V’ formation behind the tanker, thus enhancing their aerodynamic efficiency and extending their range much further than could be achieved by air refuelling alone.

The above concept has been adopted as the basis for this research programme after considering various other alternative long-range UCAV deployment scenarios which are briefly described below.

I: UCAVs make a refuelling stop at allied airbases along the route.

This actually resembles the way piloted aircraft are usually operated in long-range missions. Another approach is to send the tankers up periodically for refuelling from the alliance bases situated along the mission route. Although the total fuel consumed throughout the entire mission could be less than using the proposed tanker system, the following downsides are significant.

- Allied airbases may not always be available along the route or they may be even located beyond the maximum range of the UCAVs.
- For cost effectiveness tankers need to operate within reasonable range from allied airbases.
- Every landing and take-off consumes considerable amount of both time and fuel, hence any operational requirements for rapid response may no longer be effective.

- Crew and operating costs from remote airbases may well exceed the costs of using an uninhabited tanker.

II: UCAVs transported close to the combat zone by heavy military transport aircraft.

Transport aircraft are normally used in military logistic operations to carry all kind of vehicles from helicopters to armoured vehicles. If the long-range requirement is rigidly applied to the transport aircraft itself, i.e. no refuelling stops and assuming that a reasonable number of UCAVs will be carried, then such a concept would lead to an ultra-heavy transport that would not be feasible or economical to operate. Furthermore, the nearest airbase available for UCAV deployment could practically be at a distance from the combat zone, which is beyond the reach of the UCAV‘s combat radius. Also over a decade ago, a similar concept had been envisaged by the U.S. Air Force [25] to carry small UCAVs onboard and deploy them from a ‘mother ship’. However, for a reasonable number and size of UCAVs the mother ship’s size could be so large that would be again impractical and costly to operate. Furthermore, reliable airborne UCAV deployment and retrieval could turn out to be a major challenge.

Upon considering the above alternative deployment scenarios, it becomes clear that the proposed tanker/UCAV combination system does not only provide a practical solution, but also offers both cost and operational advantages over other available means of operating the UCAVs in long-range, rapid response missions.

The potential gains provided by an uninhabited tanker and UCAV combination are not simply resulting from the individual sub-systems, but from the combined system as a whole. The tanker is an airpower enabler and multiplier, which improves the overall operational effectiveness of combat, support and air mobility aircraft [9]. On the other hand, the uninhabited tanker would be regarded as a ‘fleet master’ that would accompany a group of UCAVs, supporting and enhancing their operational effectiveness throughout the mission. Thus, the tanker could be more threatening to an enemy than the UCAVs themselves.

With an optimally designed uninhabited tanker, the aircraft combination would be able to fly fast, long-range missions, non-stop without having to deal with any crew limitations, ground maintenance/refuelling delays and other operational constraints. Also the UCAV fleet may need to engage in combat within a very large hostile area and far from allied airbases, where it is not possible for the fleet to land. The tanker would be able to approach very close to remote enemy zones supplying fuel to the UCAVs for completing their mission and also for assisting those to safely return back home.

During deployment operations with existing conventional tankers, it is not possible to escort combat aircraft close to the enemy zone. This is primarily due to lack of stealthiness and self-defence systems. Therefore, the accompanied combat aircraft are required to split from the tanker a long distance away from the enemy zone to avoid early detection. And this indirectly forces the combat aircraft to carry a larger amount of fuel and less weapon payload in order to reach the intended target. For these reasons, stealth design is essential for an uninhabited tanker to be able to loiter and refuel UCAVs close to the target's territory. This close-proximity deployment allows the UCAVs to perform combat operations consistently with lower fuel and greater weapon loads and hence it enhances the chances of success during a campaign. Additionally, arming the uninhabited tanker with a limited number of weapons for self-defence would greatly increase its survivability.

The capability of the aircraft combination to remain airborne throughout the entire mission also provides a higher level of security regarding the mission. The probability of information leaks increases when more command contacts and more airbases are involved in the operation. This information security in conjunction with stealth design provide another major combat advantage, which allows the UCAVs to perform a 'surprise attack' while enemy's forces are not fully aware of the intended operation.

In practice, a formation flight involving dissimilar aircraft, such as a large tanker and typical combat aircraft, is much more dangerous compared to flying in formation with the aircraft featuring similar characteristics, as in the example of the mid-air accident occurred in 1966 during the close formation of XB-70 Valkyrie and other four different supersonic fighter/trainer aircraft resulting a collision between XB-70 and F-104 [57]. Although the actual cause of the collision is still debated since the pilots involved were all experienced; one of the speculations was that the F-104 was hit by strong vortices generated by the wing tip of the significantly larger XB-70 which led to control loss and the F-104 was pulled into the collision. In addition, the F-104 pilot had not previously flown in formation with the XB-70 and thus might be unfamiliar with the specific properties and vortex strength of the new XB-70 configuration.

Also in a recent accident of a BAE Nimrod XV230, which exploded over Afghanistan [53], after the investigation had been thoroughly conducted, it was concluded that the accident occurred as a result of fuel leakage following an air refuelling operation. Fuel leaking through a gap created by the heavily loaded airframe reached a hot air pipe ignited causing a catastrophic explosion. The above accidents show that both air refuelling and formation flight are potentially some of the most dangerous non-combat operations and they help support the argument that using uninhabited aircraft in such operations could eliminate human error and at the same time prevent aircrew losses.

Since the proposed tanker/UCAV system consists of several complex aircraft operating together performing difficult tasks like formation flying and air refuelling, the risk mission failure due to a system failure is undoubtedly important. Even more important could be the loss of the tanker due to a critical failure of one of its own systems or due to any other external factor. That could subsequently cause the loss of the UCAVs that would eventually run out of fuel. However, within the context of this research, a reasonable assumption is made that by the time that these aircraft become operational all their systems would have proven an extremely high-level of reliability, safety and survivability which could be even above the level expected from their currently operational military counterparts. When it comes to an engine failure, the tanker is multi-engine by design so that it can safely continue the refuelling operation until they all reach a suitable diversion airfield. On the other hand, assuming good planning, if one of the UCAVs was to suffer an engine failure, that would not necessitate an aborting of the mission.

1.5 The Proposed Design Synthesis and Optimisation

An uninhabited tanker is a novel aircraft concept which has not been designed or built before; therefore, as implied in the concept introduction (see section 1.3), such an aircraft needs to be developed using a special design synthesis which is optimised for air refuelling operations. On the other hand, several UCAV concepts and prototypes have been released to date; however, for the proposed tanker/UCAV combination to be fully optimised, it is important to also design from the outset a special UCAV that will provide an excellent match with the new tanker. Therefore a separate design methodology is needed that will size and configure the UCAV specifically for the proposed combined operation.

The aerodynamic performance benefits obtained from close formation flying depend on various factors e.g. flight conditions, aircraft configurations and relative position between the leading and the trailing aircraft. Study of previous formation flight research shows that, there is no universal method available for reliably predicting the above performance benefits neither for determining the optimal formation arrangement. Since this research study considers a formation flight involving a large tanker and several smaller UCAVs, a new formation flight methodology needs to be developed in order to analyse the aerodynamic effects in a multi-row formation arrangement consisting of dissimilar aircraft and to determine an optimal solution with sufficient accuracy.

Although the designs of both the tanker and UCAV may share similar configurational characteristics, each aircraft would be optimised for its individual operational role. The UCAV design would be optimised for combat performance and agility, while the uninhabited tanker will be optimised for the overall mission fuel payload-range capability. Once both aircraft have been designed and individually optimised, they will be used to optimise further the overall air refuelling sequence and operating conditions of the full aircraft combination in close formation flight, in order to extend its range to its maximum reach. In addition to range, time and fuel consumption will be accounted in the above optimisation problem to determine a solution which will also be operationally effective.

1.6 Research Programme and Objectives

This research programme aims to develop a design and optimisation methodology for an innovative autonomous air refuelling system combination consisting of a tanker and a number of UCAVs flying in close formation. Many benefits could be obtained from such a combination, resulting from both the formation flight and the aerial refuelling operation. Also with the adoption of stealth design features, the system would be able fly directly and quickly to a faraway destination without being detected, which is a highly desirable capability especially for time-critical and highly classified missions.

The concept of this research has been justified by addressing problems of piloted aircraft in a long-haul combat operation and by considering the possible advantages which could be obtained by replacing them with autonomous systems in such an operation. After justifying the research concept, the baseline configuration would be developed according to operational considerations and requirements. Subsequently, the design mission profile of the aircraft combination would be determined and the design processes would be conducted in the following order: initial sizing, internal component sizing, system packaging, geometry modelling, aerodynamic analysis, propulsion analysis, weight and balance, aircraft stability, and performance assessments. Also as described earlier, the aircraft combination would fly in close formation increasing aerodynamic efficiency; therefore, such effects in formation flying would be investigated. Finally, the refuelling sequence of the aircraft combination would also be optimised for long-range operations.

Due to the uniqueness of the aircraft system proposed in this research programme, new design methodologies will need to be developed. The design synthesis codes, implemented from the above design methodologies would be integrated with an optimisation module and compiled into a computer program. The program would provide sufficient flexibility to identify a design configuration solution for a given set of target specifications and mission requirements. Furthermore, current system and payload technologies would be investigated and integrated as necessary to make the tanker system more effective than the existing conventional ones.

Chapter 2

Literature Review

2.1 UCAVs

Uninhabited Combat Aerial Vehicles (UCAVs) are a variant of UAVs which have been developed primarily for combat employment purposes. Although it may seem that the UCAV concept has become rather well-known recently due to the establishment of several UCAV programs in many countries; actually, a possibility of using unmanned aircraft in offensive roles had been studied and had its history set as long as other types of UAVs such as for target drone and reconnaissance purposes. Nonetheless, in the past decades due to the lack of advanced technologies and relatively high developing costs, the majority of UAV projects particularly offensive ones, delivered rather unsuccessful results and hence were brought to an end not long afterward.

2.1.1 UAV Background

UAVs have existed in aviation history for a long period of time; however, their early applications were limited to military uses of aerial target drones and remotely pilot vehicles (RPVs). Although the first unmanned aircraft developed during World War I, Curtiss/Sperry Flying Bomb, was intended for using as cruise missiles, the system had never been employed in actual operations and the entire program was terminated shortly after the wars ended [28]. A decade later, this pilotless concept led to the development of radio-controlled target drones. In 1939, a radio-controlled model plane RP-4 built by Reginald Denny, was assigned to the U.S. Army and subsequently developed into a large-scale production of aerial target drones used by the U.S. arm services during World War II [29].

An interest of developing a reconnaissance variant of RPVs emerged in 1961, when BQM-34A Firebee, one of the most successful target drone series, was recommended to be converted to reconnaissance configuration. In the early 1970s, Firebee was also modified to for using in offensive roles carrying air-to-surface missiles. Although the tests were considered to be successful, the project was discontinued. This was partially due to the cause of some Air Force officials seeing RPVs as a competition to conventional piloted aircraft [32]. In the 1980s, Israel and the U.S. began the development of tactical battlefield UAVs, namely RQ-2 Pioneer and Amber which was a predecessor of the well-known RQ-1 Predator [31]. Their missions were mainly for reconnaissance purposes particularly in the area determined to be hazardous for piloted reconnaissance aircraft. At the time, the U.S. Air Force also investigated the possibility of expanding UAV's role beyond reconnaissance, specifically in suppression of air defence and deep strike missions, but they were never operationally fielded [24].

Early generations of the UAVs flew pre-programmed flight path due to limited navigation capabilities, sensor performance, and command and control linked to the UAV operator, which resulted a limitation of the systems to respond to any real-time changes on the battlefield. Until recently, the current technologies have surpassed some significant constraints to the flexibility of previous UAVs while such technologies involved have also become cost effectiveness. This was completely opposite in past when several UAV (RPV) programs were suffered from high costs with minimal returns [33]. Also another important reason for the rise of UAV interests is due to their cost and operational benefits in comparison to piloted aircraft. Nonetheless, the piloted aircraft still maintain the most significant advantage which is the ability of human pilot to sense events within and outside the aircraft, also known in the military jargon as 'situation awareness' [26]. For example, on a battlefield where friendly, enemy, and neutral combatants are scattered throughout, human pilots would have a greater ability to understand and response to the current combat situation than a complete autonomous system or an operator controlling the aircraft from a faraway distance.

From reconnaissance operations' point of view, UAVs' abilities fill the gap between manned airborne and satellite reconnaissance platforms. Due to the principle of orbital mechanics, a satellite reconnaissance can collect information virtually from any places on the Earth without risking human life. However, the coverage time and frequency over a conflict area tend to be limited depending on the target's global position. Although continuous coverage of the conflict area is possible, it would require a large satellite GPS constellation costing an extraordinary amount of money. Also satellite orbits are constant which allow an enemy to predict the observation time, and hence conceal their activities and forces beforehand. UAVs, on the other hand, are capable of conducting an operation regardless the period of time and with various types of information gathering e.g. reconnaissance, surveillance and target acquisition (RSTA), battle damage assessment (BDA), and battlefield management in high-treat or heavily defended areas [24].

According to the U.S. Office of the Secretary of Defence [27], the success of UAVs is highly dependent on their reliability because it fundamentally determines their affordability, mission availability and acceptance into the civil airspace. Improving the reliability also reduces the maintenance man-hour per flight hour (MMH/FH) and procurement of aircraft's spare parts, thus potentially saving overall maintenance costs. The reliability of the UAVs can be normally enhanced by reducing complexity and improving quality of components within appropriate financials. Simpler and smaller designs, however, tend to exhibit poorer reliability performance due to several factors including environmental issues such as weather tolerances.

2.1.2 Recent UAVs and UCAV Developments

Currently, although in civilian applications, UAVs are not used as extensively as in the military, there are certain tasks for which they are well suited such as crop spraying and fertilising, TV broadcasting, telecommunications, aerial surveillance, photography, traffic monitoring and atmospheric sensing [4]. The military employs UAVs in many types of operations particularly for intelligence, surveillance and reconnaissance (ISR). The previous concept of using UAVs for offensive roles has also become feasible due to the advanced technologies; therefore, UCAVs which are highly interested by the Armed Forces, are currently being developed in many places e.g. U.S. Navy, French Dassault Aviation and BAE Systems. Notable UAVs currently employed in military operations are Global Hawk and Predator.

Global Hawk is a high-altitude long-endurance (HALE) UAV providing high-resolution ISR imagery. By cruising at extremely high altitudes, it can survey large geographic areas with precise accuracy, to provide the latest information about enemy location, resources and activities. The aircraft also possesses a high degree of survivability from its very high operating altitude and self-defence measures. After a long series of deployment exercises, it has proved military worthy by providing critical ISR capabilities to the war fighting community [5].

Predator is a medium-altitude long-endurance (MALE) aircraft system used for surveillance and reconnaissance missions. The original Predator's designated name was 'RQ-1' which has been changed to 'MQ-1' in 2002 due to the addition of armed reconnaissance role. The MQ-1 version carries multi-spectral targeting system (MTS) and AGM-114 Hellfire missiles providing combat abilities for armed reconnaissance and critical target interdiction purposes [6]. The MQ-1 Predator has demonstrated that UAV capabilities are not limited to ISR missions; they can also be armed and used for combat support.

Figure 2.1: Global Hawk (left) [5] *and MQ-1 Predator (right)* [6]

A primary objective of UCAVs, as stated by the majority of the system development programs, is for high-risk offensive operations in particular suppression of enemy air defences (SEAD). The SEAD mission is normally performed during initial phases of a military campaign when the enemy's forces are heavily armed with anti-aircraft warfare and thus must be suppressed in order to carry out further operations. A study of the possibility for the UCAV being used in an air superiority role after the retirement of F-22 Raptor has also been conducted. Nonetheless, due to the classified information concerning current UCAV technologies and its future developments, concrete answers were not available [30].

Before the development of existing UCAVs nowadays, the idea of modifying retired F-16A Falcon into unmanned combat aircraft was considered. However, Jim Shane of the UAV Battle Lab [35] stated that UCAVs needed to be designed from scratch in order to take advantages of design freedom and better performance, and the Defence Advanced Research Projects Agency (DARPA) concurred with the proposed concept. UCAVs had been under development by two major aerospace companies, Boeing and Northrop Grumman, as part of the J-UCAS programme before being terminated and subsequently revitalised as the name UCAS-D.

The Joint Unmanned Combat Air Systems (J-UCAS) programme was established by DARPA, U.S. Air Force and U.S. Navy to exploit the technical feasibility, military applicability and operational value of a high performance UCAV system [7]. The UCAVs demonstrated by this programme were the X-45A and X-47A. The X-45A was built by Boeing to meet U.S. Air Force requirements for SEAD and deep strike missions, whereas the X-47A was developed by Northrop Grumman for the U.S. Navy carrier operations [8]. New versions of the X-45C and X-47B were redesigned and integrated with more sensors and weapon options to enhance their mission capabilities. The wing platform of both versions changed drastically from their previous ones; the overall size also increased, improving payload capacity, range and persistence. During the same time, European Aerospace companies led by French Dassault Aviation have been also developing a UCAV called 'nEUROn' which was envisioned as a competitor to X-45C and X-47B.

Figure 2.2: The J-UCAS programme, X-45C (left) [68] *and X-47B (right)* [69]

Figure 2.3: nEUROn developed by Dassault Aviation [70]

January 2006, the J-UCAS programme was terminated; however, the programme was rebuilt into a sole U.S. Navy programme called UCAS-D featuring a further development of Northrop Grumman X-47 Pegasus. After the cease of the J-UCAS programme, although Boeing proposed a carrier-based version of X-45, designated X-45N, to the U.S. Navy, the contract was eventually awarded to the original naval X-47 thus leading to the end of the X-45 project. In the late 2006, under the contract of UK Ministry of Defence, Taranis project led by BAE Systems was announced. The project aims to deliver an experimental UCAV with fully integrated autonomous systems and low observable features, and also to demonstrate how the current state-of-the-art technologies can provide battle capabilities for the UK armed forces [36]. A Russian UCAV named 'Skat' is currently being developed by MiG under a competition with Sukhoi's UCAV programme for proposing to the Russian Defence Ministry [52].

A sudden rise of UCAV developments in the past decade implied that the present technologies have sufficiently matured to produce such an advance system. Although the system would eventually be able to meet its primary objective of eliminating pilot-related issues, in this advancing environment, the performance requirements of the next UCAV would become even more demanding once the previous ones are met.

Aircraft modification is a common solution to achieve an improvement of certain performances; however, there is always a trade-off due to the modification whether in terms of cost or size while the performances increased are relatively small. Therefore, this research aims to investigate and provide the methods for enhancing the performances of the unmanned aircraft several folds without undergoing extensive modifications and demanding technologies. The proposed uninhabited tanker/UCAV combination will take advantages of the unmanned system and apply external methods for enhancing the performances of the aircraft. The air refuelling and the formation flight are common techniques which have been used in the aviation for a long period of time; nonetheless, with the piloted aircraft, the benefits obtained from such techniques are limited to a certain extent due to human constraints. On the other hand, these constraints are not imposed to the unmanned systems, and thus such benefits can be exploited up to the maximum potentials.

2.2 Air Refuelling

Air refuelling refers to an airborne fuel-transferring operation from one aircraft to others which enhances the flexibility and various capabilities of the receiver aircraft. The operation increases combat effectiveness by enabling the receivers to carry larger payloads over a longer time, further distance, thus increasing the capability of delivering greater impact on the enemy. The improved endurance produces ‘force economy’ by allowing combat aircraft to strike greater number of targets in a single sortie with longer persistency and let the remaining aircraft available to perform other missions. The extended combat radius due to the air refuelling also helps to situate air bases beyond an effective range of enemy weapons. This increases air base's security and frees up air power assets to concentrate more on offensive operations. The flexibility and versatility of the combat aircraft are also enhanced by allowing them to reach distant targets with sufficient payload to produce an impact on adversary's forces.

Figure 2.4: KC-135E performs an air refueling operation on F-22A [14]

From the U.S. Air Force strategic perspective [9], air refuelling contributes rapid global mobility by supporting deployed aircraft so that they may fly non-stop to the destination which significantly reduces reliance on en-route staging bases including their availability. As mentioned above, the range, payload, endurance and flexibility of both combat and non-combat air power assets can be enhanced by air refuelling operation. The operation enables the global attack competency which most combat aircraft do not possess due to their limited original range to carry sufficient payload to another theatre, perform combat, and then return back to the base. In fact, multiple air refuelling operations are required for the combat aircraft to conduct global attack missions. Air superiority over the territory can be enhanced and maintained by the air refuelling, and in turn, the air superiority provides protection to air refuelling operations since current tankers do not possess any threat detections or defensive capabilities. The aircraft can be based further away from the enemy and still perform their assigned missions. The distanced bases require less security afford; therefore, more aircraft can be devoted to the offensive tasks than the defensive ones.

2.2.1 Tankers

Generally, tankers are modified from commercial aircraft with high payload capacity and long-range capability. Conversion of such aircraft involves extensive structural changes e.g. installations of air refuelling equipment and additional fuel-line system; the extra fuel payload is usually stored in the cargo hold inside containers called Additional Centre Tanks (ACTs), which take the place of normal cargo containers; and the integration of onboard refuelling control systems. Selecting an aircraft type to be modified is a major issue. As mentioned in the previous chapter, due to several mission requirements of strategic tankers, choices of suitable commercial aircraft are limited. Also the tanker variants are not modified from the current generation of commercial fleets but the previous one to reduce the cost of purchase. Therefore, an airframe fatigue must be taken into consideration in the selection process to subsequently avoid excessive long-term maintenance costs [14].

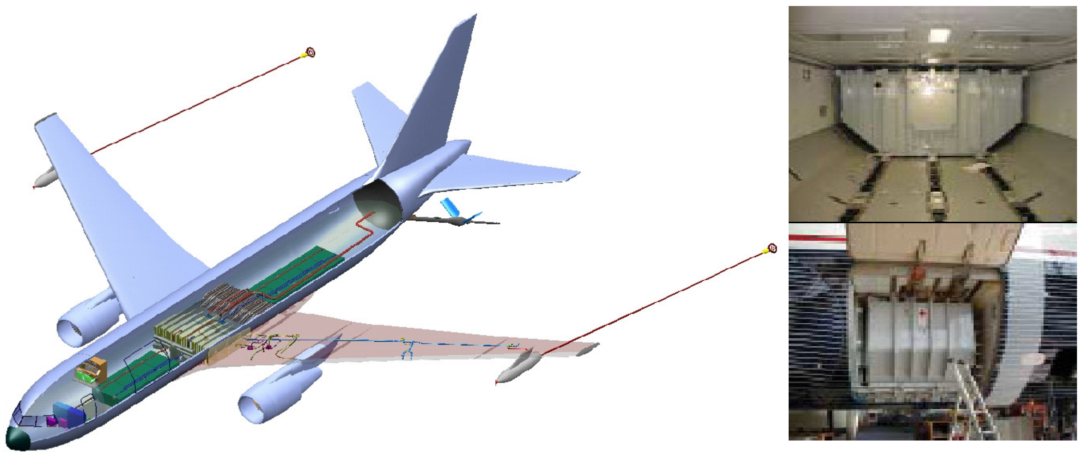

Figure 2.5: Boeing 767 Tanker layout (left) [14] *and Additional Centre Tanks (right)* [71]

In the U.S. Air Force, the main tanker fleets are KC-135s and the larger KC-10s which have approximately twice the refuelling capacity of the KC-135s. These tankers are also capable of performing secondary missions including cargo/ passenger transport as well as aeromedical evacuation. The KC-135s have been in service for more than 40 years and become the oldest tanker fleet in the forces. And the Air Force needed to replace a KC-135 portion due to airframe corrosion and material degradation [13]. The Boeing 767-200 a.k.a. KC-767 was chosen in late

2001 as a replacement for the KC-135s; however, the programme was terminated two years later due to corruption allegations. In February 2008, Northrop Grumman/ EAD proposed K-45, a tanker variant of Airbus A330-200, which was selected for the KC-X programme containing the same objectives as the previously ceased tanker scheme. Five months later, a rebid of the KC-X programme was re-opened after Boeing flied a protest of the award of the contract. Subsequently, it has been announced that the request for proposal of current KC-X solicitation was cancelled [66].

2.2.2 AAR Equipment

Common tankers contain two types of air-to-air refuelling (AAR) equipment; one is a centreline mounted flyable telescopic boom for receptacle compatible aircraft. The boom can be modified to refuel probe-equipped aircraft by installing a boom drogue adapter (BDA) which can only be fitted and removed on the ground. The other AAR equipment type is wing pods with hose and drogue systems which are generally mounted close to wing tips. The hose drogue system may also be installed into the fuselage or other appropriate locations if the installation is permitted.

Boom: Solid fuel-transferring tubes which can be extended or retracted by a boom operator. The boom system offers fast fuel-transfer rate up to 8000 lb/min while wing-pod hose systems offer flow rates between 2800 lb/min and 3200 lb/min [15]. The boom is also equipped with a Boom Interphone System which allows direct communication with receivers. The receiver is required to fly in a steady formation position while the boom operator manoeuvres and extends the boom to make a contact with the receiver's receptacle. Once the contact is secured, the receiver pilot will then maintain the aircraft within the boom operation envelope. If the receiver moves beyond the envelope limits, depending on the mechanical limitations of the boom, a disconnection will automatically occur to prevent boom damage.

Wing Pods: The unit contains a driving mechanism and the hose drum with a conical shaped drogue attached at the end. A ram turbine is located in front of the wing pod providing power for transferring fuel from local tanks. To trail the hose, the hose drum brake is released and the air drag acting on the drogue pulls the hose into the airstream. When the hose is at full trail, a winding-in torque (response system) is applied to the drum which counters the air drag of the drogue, balancing the hose, and absorbs the impact of the receiver making contact. It also damps any tendency for the hose to whip as contact is made, provided that the receiver does not approach with excessive speed. Once the probe-drogue contact is made and secured, the receiver continues to move forward pushing the hose back onto the drum. When sufficient hose is rewound, the AAR equipment fuel valve will open and the fuel can be transferred to the receiver. After the operation is completed, the receiver slowly pulls back to the pre-contact position and then the fuel valve will close when the hose almost reaches its full trail. The boom drogue adapter, on the other hand, does not have this hose response system; therefore, caution is required during approach to contact.

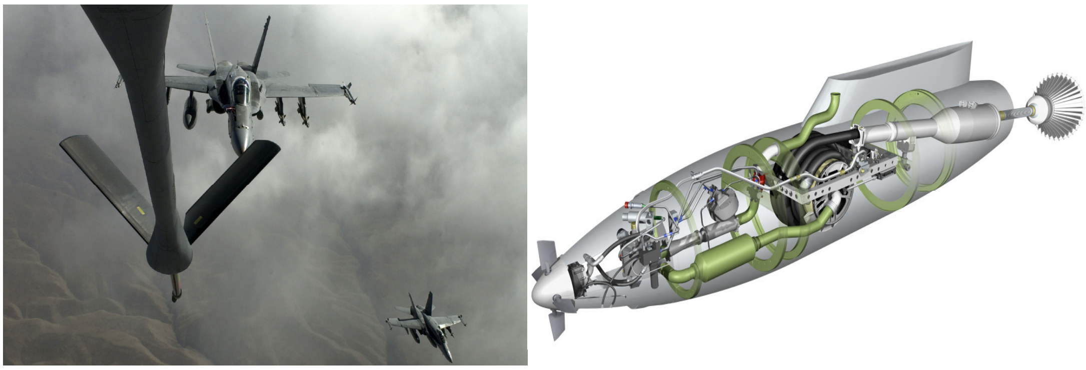

Figure 2.6: Telescopic boom (left) [14] *and wing pod layout (right)* [75]

Every tanker AAR installation is associated with a set of rearward facing signal lights, containing the colours red, amber and green; however, there may be some slight variations depending on the equipments and the nations. Nonetheless, the standard light signals defined by NATO are: red light means do not make contact or breakaway, amber means ready for contact and green signifies that fuel is currently transferred. Most refuelling hoses are marked with a series of colour bands indicating an optimal receiver refuelling position which is achieved when the hose is pushed in so that the markings enter the hose tunnel. Also all AAR equipment are either illuminated or installed with floodlights to assist the air refuelling operations during night time.

2.2.3 Operations and Procedures

Air refuelling operations are normally conducted in one of two ways, in an anchor area or along an air refuelling track. Anchor areas refer to a racetrack pattern by which a tanker orbits within the defined airspace waiting for receiver aircraft to arrive. After joining with the receiver, the tanker then expands the racetrack flying pattern while refuelling the receiver. The anchor air refuelling technique suits for small and highly manoeuvrable aircraft, and is normally used for intra-theatre operations in which the airspace is confined. On the other hand, the air refuelling track method is preferable for inter-theatre operations. The tanker rendezvous can be accomplished by either the tanker orbits at a designated point along the track waiting for the receiver's arrival, or both tanker and receiver arrive simultaneously at the designated point. In any cases, both refuelling methods can also be combined on a certain mission especially when multiple combat aircraft refuel with multiple tanker formations. For joint and multination operations, different countries may have their own refuelling procedure and terminology which could cause a potential danger due to misunderstandings and confusion. Therefore, a standard universal set of tactics, terminology and procedures are required for such operations. The tankers primarily function in the following support missions.

Single Integrated Operation Planned (SIOP), Global Attack and Special Operation Supports, where SIOP refers to the combat employment of suppressing inter-theatre nuclear-equipped forces. In these missions, air refuelling support allows strategic bombers and other combat platforms to reach most distant targets directly from their original base rather than relying on inter-theatre alliance bases to ensure the security of deployment avoiding espionages as well as providing a quick response to the mission.

Air Bridge Support; air bridge is an airborne line communication connecting between theatres consisting of an uninterrupted air travelling route for rapid deployment and sustainment of forces. With air refuelling, the air bridge operations are accelerated due to a reduction or elimination of ground refuelling stops and any possibility of aircraft delay due to base-related issues. This also enables airlifters to maximise the payload without sacrificing range, thus significantly increases the efficiency of deployment.

Theatre Support; during an intra-theatre combat operation, supporting both combat and combat support aircraft executing the campaign is the main priority of tankers, especially when these aircraft fly from faraway bases and may demand refuelling support to extend the range further or to engage the targets. Combat support platforms, e.g. Airborne Warning and Control System (AWACS), Airborne Battlefield Command and Control Centre (ABCC), and various reconnaissance typed aircraft, require air refuelling to increase their airborne endurance, thus extending the period between sorties.

Deployment Support; means escorting and air refuelling combat aircraft to extend their range during inter-theatre deployments allowing non-stop flight and more rapid response to a regional crisis. If a number of tankers available in the operation are limited, the deployment support is provided by the means of ‘force extension’ which refers to a refuelling of one tanker by another tanker. Apart from the primary support missions mentioned so far, the tankers are also used in several other circumstances, e.g. emergency air refuelling, airlift, combat rescue and aeromedical evacuation.

Although it is stated that current strategic tankers are modified to serve various different operations featuring unique characteristics and requirements as described above; these operations can actually be categorised as air refuelling and airlifting roles. Clearly, all primary operations of the tankers focus on air refuelling support for various types of aircraft executing their campaign from Special Operations Forces (SOF) to Command, Control, Intelligence, Surveillance, and Reconnaissance (C2ISR); while their secondary operations are generally to provide cargo/passenger airlift which may be requested during the deployment phase when the airlift fleet is highly demanded.

Several planning and support issues must be thoroughly addressed before including tankers as part of the operation in order to maximise their utilisation and minimise the number of unsupported requests. After the tanker employment has been granted and apportioned through its correspondent chain commands, the number and the type of air refuelling aircraft required in the operation are considered. If the receivers' refuelling compatibilities are amalgamated between probe-drogue and boom-receptacle types, the tanker which is capable of refuelling both types will be allocated. The number of tankers assigned in the operation is primarily justified by the total fuel offloaded against rapid refuelling performances. For the heavy receiver aircraft, in which the total amount of offload fuel is prioritised, a small number of tankers with high fuel payload capacity should be deployed. On the other hand, if the operation emphasises rapid refuelling on multiple receivers, using several tankers is more effective due to the greater number of refuelling points available, and hence reducing the total time to complete the operation. Utilisation rate (UTE) and duration of activity also affect the number of tankers allocated and number of crews per aircraft. The tankers are allowed to support high UTE rates only for a short period of time. To extend the period of high UTE rates, the numbers of tankers and crews must be increased. In addition, high UTE rates drive the need of greater number of crews recruited in order to allow the crews for recuperation periods according to operational regulations.

2.2.4 Uninhabited Tanker Justifications

One of the most important considerations driving the development of UCAVs is to eliminate the risk of endangering pilot's life in combat operations especially those which concerns with suppression of enemy air defences. Although the pilot risk issues are not likely to accelerate the need for an unmanned version of the tankers due to the low possibility of encountering any hostile treats in the operation or becoming their main target; the current tankers face two other major problems regarding fleet crewing and operational effectiveness. Such issues can be overcome with the use of an uninhabited tanker proposed in this research programme.

Tanker crewing is an important issue directly related to the fleet size. In order to fully utilise combat forces, a certain ratio of tankers and combat aircraft must be satisfied. Hence, the larger the combat forces, the greater the number of tanker crews would be needed. According to Air Force Doctrine Document 2-6.2 [9], current tanker fleets have 1.17-1.36 crews per aircraft. Due to this low crew-to-aircraft ratio, if the tanker usage becomes highly demanded, e.g. in a prolonged combat operation that requires continual refuelling supports, the crew members could reach their limit of maximum monthly flying hours. This will haul their availability for further services and may subsequently affect the entire operation. On the other hand, with an unmanned system, the crew availability would be no longer concerned whether due to the lack in numbers, pilot specialisations, or recuperation provisions. This also substantially reduces the need of training qualified tanker operators which is a difficult task and resource consuming.

The choices of aircraft for tanker conversion are generally within a commercial fleet area. Common military transport aircraft, such as C-130 Hercules, may also be modified for air refuelling operations; however, the majority of them were developed solely for airlifting roles without secondary capability of providing air refuelling. With the requirements of a strategic tanker to be able to perform both air refuelling and airlifting roles under various conditions, the available choices of aircraft would be limited to begin with; and the final selection would come down to a compromise of specification rather than meeting all of the original requirement. Although the modified tanker would be able to perform dual-role function, the overall operational effectiveness would not be great, not to mention that of the individual role. This is primarily because the commercial aircraft selected was originally optimised for civil transportation not for the air refuelling or the dual-role function.

Upon considering the above tanker recruitment processes, from selecting retiring commercial aircraft to standard installation modifications, they clearly emphasise the minimisation of overall purchase costs. However, air refuelling requirement is long-term and, due to the airframe fatigue and material degradation of the commercial aircraft accumulated before being converted into the tanker, maintenance costs may become excessive later on and thus indirectly force for a new unit replacement. For a dedicated designed tanker, the service life would last longer with less maintenance costs since current material technologies would be taken into consideration for a manufactured airframe. This would also result a reduction in airframe weight and thus improve overall aircraft performances. With an integration of autonomous flight control system, the benefits of flight training reduction would further decrease operational and maintenance costs substantially. Therefore, the proposed concept of the uninhabited tanker would eventually provide better long-term cost effectiveness compared to the modified tanker.

As far as the primary missions of the tankers are concerned, operational performances and effectiveness of unmanned system would highly exceed those of the piloted tankers mainly due to the elimination of crew recuperation needed after a long period of operating time. This significantly reduces a number of tanker sorties, and allows the aircraft to provide continuous refuelling support. Furthermore, fewer tankers would be required to perform a mission containing high UTE rate and long period of activity. Unless a critical system failure occurs, with a capability of the aircraft to be also in-flight refuelable (i.e. force extension), the uninhabited tanker can remain airborne indefinitely and carry on its assigned missions until they are completed or being called off. Although a dedicated designed tanker would not be capable of performing airlifting roles in the same manner as strategic tankers, the need for the tankers to be used in the air transport and miscellaneous missions are much lower than the requirements for air refuelling which also take the highest priority over others. Albeit the strategic tankers are requested for an airlift operation, their performance would be inferior compared to other military transport aircraft generally due to cargo/troops accessibility, payload weight capability, and internal space available.

Although the proposed uninhabited tanker would outperform the existing strategic tankers in various aspects whether in terms of cost or performance, the development of the uninhabited tanker does not aim to replace the strategic tankers. Its primary objective, however, is to assist the designed UCAVs in long-range combat operations. Nonetheless, the aircraft can be considered as part of air refuelling assets to enhance the forces' capabilities by performing any long-endurance high-precision missions, supplying for aircrew shortfalls, as well as reducing numbers of crews and tankers recruited.

2.3 Formation Flight

An uninhabited tanker/UCAV combination concept does not acquire a long-range capability by only performing air refuelling operations, but also enhancing the aerodynamic efficiency of the UCAVs when flying in close formation with a much larger aircraft in comparison such as the tanker. Nonetheless, from military perspectives in the past, formation flying was primarily concerned for operational effectiveness and strategic advantages rather than improving aircraft aerodynamic performance.

The primary objectives of formation flight stated by the Royal Air Force [40] are to obtain a concentration of power whether for offensive or defensive action in any form of air operations. A well-organised formation of aircraft would be able to eliminate blind spot, enable fire to be concentrated on any direction, and hence increase mutual survivability. The moral effect upon enemies of the organised formation is significantly greater than that produced by a number of isolated aircraft operating independently, also the squadron pilots' consciousness of being closely supported by others increases their morale. In addition, flying in close formation enhances the ability of the trailing aircraft to maintain visual contact of the leading one, which is especially useful for penetrating obscuring weather conditions. Recently, the rise in fuel costs and the demanding aircraft performances have driven a revision of formation flight techniques to be used as an alternate solution for externally improving aircraft aerodynamic performance.

Figure 2.7: Two Dryden F/A-18 fly an Autonomous Formation Flight (left) [72]
B-52 with other 16 aircraft fly in formation (right) [73]

2.3.1 Background

The fundamental theory behind the aircraft performance improvement in formation flight is that the leading aircraft generates tip vortices which produce upwash regions outside its span as illustrated in Figure 2.8. The trailing aircraft flying in one of the upwash regions essentially gains additional lift allowing it to fly at a lower angle of attack to maintain the current altitude. As a result of the decrease angle of attack, the induced drag is also reduced and hence the thrust required for continuing the same speed of aircraft is lower, leading to the lower fuel consumption. Though in practice, a pilot needs to adjust the aircraft pitch altitude and throttle setting when flying in formation to maintain all forces acting on the aircraft in balance. As far as common formation arrangements are concerned, the additional lift gained tends to be asymmetric across the aircraft's span due to greater upwash strength toward the inboard of the aircraft. Thus, in order to prevent the aircraft from rolling away from the formation, control surfaces must be applied to counteract the rolling moment generated.

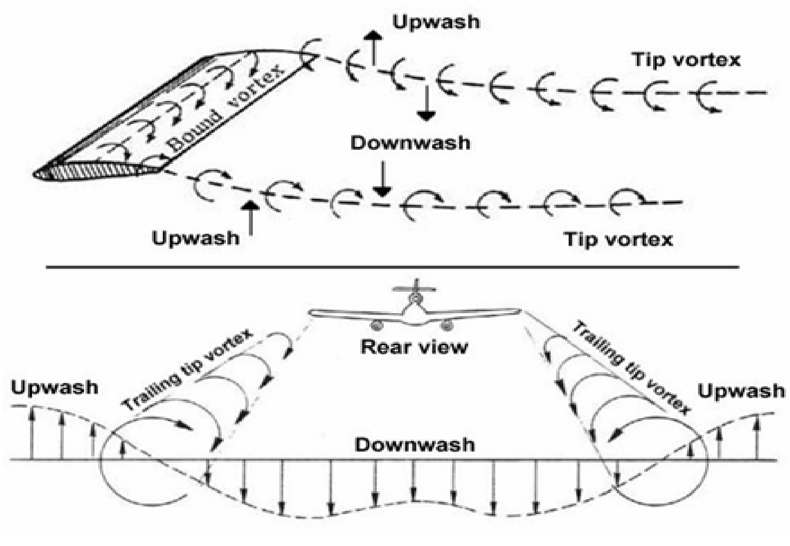

Figure 2.8: Vortices and downwash regions from leading aircraft [74]

Although the benefits of formation flight can be described in various forms such as lift increment, drag reduction and fuel savings; as mentioned above, these beneficial effects are in fact related to each other. Within the contexts of this research programme, however, an investigation of the formation flight benefits will be focused on the range capability of the trailing aircraft improved as a result of enhanced aerodynamic performance, i.e. the lift-to-drag ratio term according to the Breguet range equation.

2.3.2 Research Development

The concept of flying aircraft in formation to improve aerodynamic performance was initiated from an observation of migratory birds' behaviour particularly the natural tendency of the birds to fly in regular V-shaped formations (where the apex of the V being the direction of flight). The rationale behind this flying behaviour is to reduce their energy expenditure by exploiting an aerodynamic advantage due to the effect of vortex wake generating by leading birds; and also to improve communication within the flock by flying together in close proximity [41]. The researches in the formation flight area have been conducted for many years; the most fundamental aerodynamic method adopted, the horse-shoe vortex, proposed by Hummel [16] assumed a simple horseshoe shaped vortex with a span width of approximately 78.5% of the original wing value.

Although the above method has been frequently used for a simulation of bird migratory behaviour, it did not provide accurate results on the aircraft formation case especially when aerodynamic interference was taken into account. Also control surface deflections applied to counteract the rolling moment generated due to asymmetric lift distribution, which are major contributions to accurately determine the drag reduction and thus fuel savings, were neglected in the investigated model. Furthermore, the horse-shoe vortex method proved to be very difficult to apply for any shapes other than a rectangular wing. For these reasons, many subsequent formation flight researches focused on using other methods of vortex-lattice codes, flight tests and wind-tunnel tests to investigate the aerodynamic effects of the formation flight as well as validating the results.

To improve the accuracy of fundamental horse-shoe vortex model prediction, NASA developed a vortex-lattice code called HASC95 (High Angle of Attack Stability and Control) which has been widely used not only in formation flight, but various aircraft aerodynamic researches. In essence, the vortex-lattice method divides the model surface into several horse-shoe vortex elements and computes overall aerodynamic performance. With a large number of small surface elements, a more realistic model configuration of the aircraft can be constructed and hence providing higher fidelity of the prediction results than the horse-shoe vortex model method.

A formation flight research comparing the performances between the horse-shoe vortex and vortex-lattice (HASC95) methods was conducted by Blake and Multhopp [17]. Although both methods were applied on the same basic rectangular shaped wing, the results from the vortex lattice method gives better drag-reduction prediction due to the use of multiple quadrilateral vortices. Wagner [43] also developed HASC95 models of T-38 Talon formation to validate the performance of the vortex-lattice method by comparing the predicted results with actual flight test data. Both results showed some difference in fuel savings; however, the flight test data obtained were rather inconclusive due to the lack of automated station-keeping systems on T-38s to maintain the aircraft position precisely as performed in the computational vortex-lattice experiment.

NASA Dryden Flight Research Centre [18, 19] conducted the Automated Formation Flight (AFF) project using two F/A-18 Hornets to measure drag and fuel-consumption reductions of the trailing F/A-18 with the aid of station-keeping autopilot to position the aircraft at precise locations. Apart from investigating the effects of formation flying, another main objective of this project was to experiment an autonomous system capability to maintain formation position while flying in the dynamic flow field of vortices. Afterward this autonomous system would be further developed and subsequently apply for military formations, UCAVs and air refuelling operations. As far as the flight test results are concerned, the station-keeping system proved to be successful; also the optimal drag reduction region and the amount of fuel reduction appeared to be varied with Mach number and altitude. A follow-up analysis of rolling moment effects on the same F/A-18 formation flying test [41] was also performed to acquire database of other formation flight information which would be used for further AFF control system development.

Aerodynamic effects of dissimilar formation flight have been experimented by Gingras [45] using wind-tunnel testing of scale aircraft models. Subsequently, Morgan [20] performed a similar research using vortex lattice models of F-16 and KC-135 to compare with flight testing data. Two experiments were conducted for a sole F-16s formation and dissimilar formation of KC-135 and F-16. Undoubtedly, the results showed different levels of fuel reduction and different optimal positions for each aircraft combination. However, the data obtained from flight testing were inconclusive due to unstable engine performance measurement and pilot's issues regarding visual reference estimation of the aircraft position. Thus, a direct comparison between the flight test and the vortex-lattice prediction results could not be performed.

From all of the above formation flight researches conducted using the flight testing method, the only successful experiment was performed by NASA with the use of autonomous flight-control systems. Clearly without such a computational assistance, it is difficult for a pilot to achieve and preserve the aircraft in a certain formation position precisely. This also implies that the concept of long-haul formation flight to improve the range performance by maintaining the optimal formation position of the aircraft throughout is much more feasible for uninhabited aircraft.

As far as the previous formation flight investigations are concerned, no universal methodology has been developed for concretely predicting the drag reduction or any other terms which describe the same performance benefit. This is because an optimal formation solution primarily depends on the airframe configurations and also varies between different combinations of aircraft. Although a few numerical methodologies have been developed for the aforementioned purpose, they were fundamentally derived from experimental data of rectangular shaped wings and the horse-shoe vortex theory [16, 44]. Therefore, the prediction results acquired from such methodologies would not provide accuracy when the wing shapes other than the rectangular one are applied. Also some input parameters required can only be obtained from experimental tests and thus prove to be rather inconvenient for any applications.

In order to acquire sufficiently accurate formation flight data of a certain aircraft combination, an individual analysis must be carried out using any of the methods described earlier. However, since both tanker and UCAV, featuring novel unconventional design configurations, will be developed in a form of design synthesis methodology, two of the above analysis methods, i.e. flight testing and wind-tunnel testing, were considered to be inappropriate particularly in terms of investigation feasibility and flexibility. Thus, it was decided that the vortex lattice method would be used for analysing aerodynamic performance changes due to formation flight, since such a method provides better accuracy compared to the horse-shoe vortex approach and is well reasonable for the scope of the formation flight investigation and analysis. Due to an unavailability of HASC95 for public release, a vortex lattice program recommended by ESDU, MATLAB Tornado [76], was selected for investigating the effects of close-formation flight and the associated aerodynamic benefits.

2.4 Design Methodology

One of the primary objectives of this research programme is to develop an aircraft design methodology, which implies that the results obtained at the end of the research will not be limited only to one specific aircraft, but will be applicable to a range of aircraft with similar operational roles and design configurations. Therefore, the methodologies behind the modelling and the design synthesis must possess sufficient flexibility in order to accommodate certain variations of airframe and component specifications resulting from different sets of design requirements. The design methodology developed by Serghides [46] applied mathematical equations in an innovative manner to automatically generate canard-delta combat aircraft configurations that would satisfy a flexible set of design requirements. The above design methodology as well as the follow-on design optimisation methodology by

Serghides [67] had been since widely adopted as the basis for several aircraft design research programmes at Cranfield University and Imperial College London.

One of the most relevant works to this research project was performed by Whittle [50] involving the development of a design methodology for combat aircraft with enhanced supportability features. Several new methods for predicting the physical properties of aircraft components as well as new performance analysis modules have been developed. The final result was an optimised low-support flying-wing aircraft configuration with certain design considerations that may be used for the baseline configuration of the UCAV developed in this project. Hall [54] created an interactive program for the preliminary design of combat aircraft with a wide variety of geometric configurations, offering high flexibility and accuracy. Extensive investigations of pattern search methods for multi-dimensional optimisation and regression analyses were carried out by Tirovolis [55]. These tools are necessary for producing the design synthesis and optimisation methods in a computational design environment.

As far as academic textbooks are concerned, Fielding [56] provides an introduction to aircraft design methods as well as essential design considerations for various types of aircraft. Raymer [47] describes a comprehensive set of simplified methods which are sufficiently accurate for conceptual aircraft design; nonetheless, a number of performance evaluation methods provided in the reference were also taken from more detailed analysis methodologies which are widely used in the aircraft design field. In addition, references [51, 44, and 21] include several useful conceptual and preliminary design methods which will be examined and appropriately applied to corresponding modules in the design synthesis methodology developed in this research project.

There have been a number of optimisation methods available up to date; however, the majority of them were developed specifically for application to a particular set of of problems, and hence they may not be fully compatible with other applications. Therefore, it was considered to be more appropriate to investigate some basic optimisation methods. An optimisation textbook written by Shoup and Mistree [22] was recommended particularly due to its content of fundamental optimisation methods as well as example codes which can be used as a guideline for developing a computational optimisation algorithm module.

Chapter 3

Baseline Configuration and Initial Sizing Development

3.1 Baseline Configuration

The baseline configuration is generally created from a drawing sketch that represents the overall airframe aerodynamic concept as well as the locations of major internal components e.g. undercarriages, payload compartments, propulsion systems and any other unique components. The drawings of general airframe appearance and internal component layout would help the designer to choose and/or develop appropriate methodologies for applying to a certain part in the design synthesis. The baseline sketch mostly represents the product of qualitative ideas and considerations rather than numerical calculations, and may feature a completely new design or portray from existing aircraft.

3.1.1 Initial Baseline Justifications

The baseline configurations of the uninhabited tanker and the UCAV were initially intended to be broadly similar to B-2 Spirit and X-45C respectively since these existing flying-wing aircraft were developed to satisfy stealth requirements while maintaining the simplicity and aerodynamic efficiency of the airframe shape. Three-view drawings of the initial baseline aircraft illustrated in Figure 3.1 were sketched using a computer-aided design program, AutoCAD, to provide crude presentation of the two targeted concepts and their basic internal component layout. The baseline drawings share airframe similarities with the original B-2 and X-45C; nonetheless, their internal component layouts were based on available information from the original aircraft and unmanned design considerations. At this stage, the figure of internal components does not reflect their actual shape and size, only the overall arrangement and locations are the primary concerns. Each component was drawn on different layers for being identifiable from each other when multiple model lines are overlapped. The line colours represent the following components,

Blue	Airframe structure
Red	Undercarriage spaces
Orange	Avionic bays
Green	Engine and air ducts
Turquoise	Fuel payload tanks (tanker)
Purple	Refuelling units (tanker) and weapon bays (UCAV)

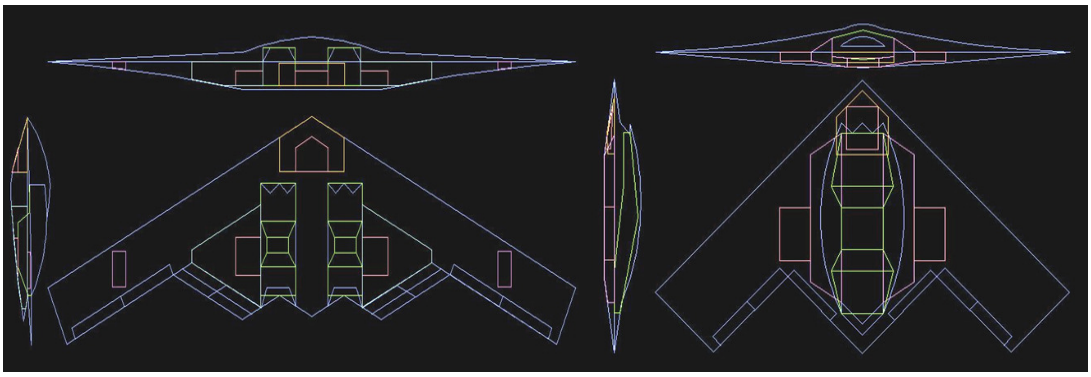

Figure 3.1: Initial design layout of the tanker (left) and a UCAV (right)

In order to exploit the design freedom gained from unmanned aircraft characteristics, with an absence of the cockpit, intake diffusers could be allocated along the centre line at the top surface of the aircraft closer to the nose area. This particular configuration which has been used in the majority of existing UCAV designs, leads to the reduced total length of the airframe, and is favourable to the design for stealth characteristic emphasising a reduction of radar detectability. By eliminating gaps or edges perpendicular to the flat side of the aircraft, e.g. inlet and exhaust cavities, corner reflectors and airframe discontinuities, in the directions that the radar signature is likely to come from, the overall radar cross section (RCS) of the aircraft can be reduced, and thus significantly lower a concentration of the radar returning to its source. The saw-tooth sheath plates are integrated to suppress the inlet and exhaust cavities from being clearly exposed in particular directions. Also in order to decrease the radar spike to the ground, all weapon payloads are designed to be carried in internal storage bays. The fuel payload tanks of the tanker are initially placed adjacent to the sides of the engine-allocated space similar to the UCAV's weapon bays.

Flight control surface design is a subject of major concern for flying-wing aircraft. The lack of horizontal and vertical tail surfaces in both the tanker and UCAV designs leads to a reduction of overall aircraft weight. Also the profile drag of the aircraft decreases substantially while any interference between tails and fuselage, another contribution to the drag, is eliminated. Furthermore, the stealth capability of the aircraft improves due to the absence of corner reflectors. However, the above benefits of the flying-wing design do not come without costs. The primary role of tail surfaces on a conventional aircraft is to maintain stability and control in flight, without them, the aircraft needs to resort to the use of control surfaces located on the wing trailing edge, while any need for yaw control can be performed by differential/split ailerons.

Due to the above reason, ideally tailless flying-wing aircraft should be designed in such a way that the overall centre of gravity is located in front of the aerodynamic centre in order to trim the aircraft effectively using limited control surfaces available. The counter-balance force produced from the main wing itself is potentially less than that from the tail wings due to a relatively small moment-arm distance between the aerodynamic centre and the control surfaces. Thus, the overall airframe design requires more attentions especially the sweep angles and the position of the wing relative to the fuselage. These need to be appropriately adjusted so that the main wing can provide sufficient counter-balancing forces while maintaining control surfaces deflection in a certain limit to provide enough room for the devices to be used for aircraft manoeuvring.

The longitudinal trim of the aircraft can be minimised by fuel management which is performed by transferring fuel longitudinally so that the c.g. of the aircraft always maintains an optimal position in terms of the static margin and the weapons c.g. location. Although in most missions the carried weapons will be released sequentially, prior to a drop, the fuel management system will adjust the overall aircraft c.g. to coincide with the weapon bay c.g. in order to eliminate any need for excessive trim or any possibility of control loss due to a sudden c.g. shift, even after a simultaneous release of all the weapons.

A tricycle undercarriage arrangement, which is widely used in military aircraft, is applied to both tanker and UCAV, while the numbers of wheels associated with the strut will be varied according to their approximated takeoff weight. Without a pilot controlling onboard the aircraft, UAV avionic modules are not required to be located in a single area. It is possible to have the modules distributed over the aircraft locating close to where their functions are; this would increase system survivability if the common location of avionic bays had been damaged. Despite the survivability advantage, it was decided to contain all general avionic modules in the nose area similar to normal aircraft. This would provide better benefits in terms of aircraft weight distribution as well as maintenance accessibility. Also the majority of avionic components are required to be stored in an air-conditioning bay which would unnecessarily increase the complexity of internal structures if the components were distributed to various places in the aircraft.

In the case of the uninhabited tanker, two hose drum units are installed on each side of the wings toward the outboard. A central refuelling unit had also been considered, however, the idea was dropped since the three-point refuelling operation is prohibited due to the spanwise hose clearance [61]. Thus, the operation cannot be performed any faster on several UCAVs despite the additional refuelling point. Also unlike modified conventional tankers, high-temperature engines and exhaust pipes of the uninhabited tanker are located in a confined space near the centreline. Therefore, an installation of refuelling unit in such an area should be avoided.

As far as current UCAV developments are concerned, their operating conditions are primarily at high-subsonic speed, and also for the same size of airframe, unmanned aircraft tend to possess less weight than the manned counterpart. For these reasons, a single low-bypass turbofan engine is deemed to provide sufficient amount of thrust to cover typical UCAV performance requirements. On the other hand, a dedicated design of flying-wing tanker has not been created, not to mention an uninhabited one; therefore, a twin-engine configuration is assumed at this stage. Also for design flexibility, fuel tanks of both aircraft are not concretely depicted.

3.1.2 Development of the Baseline Configuration

Although several design considerations have been accounted in the initial baseline configurations of the aircraft, a number of issues were subsequently found during the developments of design synthesis and aircraft model especially in terms of operational feasibility, design flexibility and limited performance. These were primarily due to a rather constrained configuration of the previous airframe design. For these reasons, the baseline configurations of both tanker and UCAV have been substantially modified in order to become operationally feasible, providing flexibility to answer the objective of developing design methodology, and being optimised for the tanker/UCAV combination mission requirement.

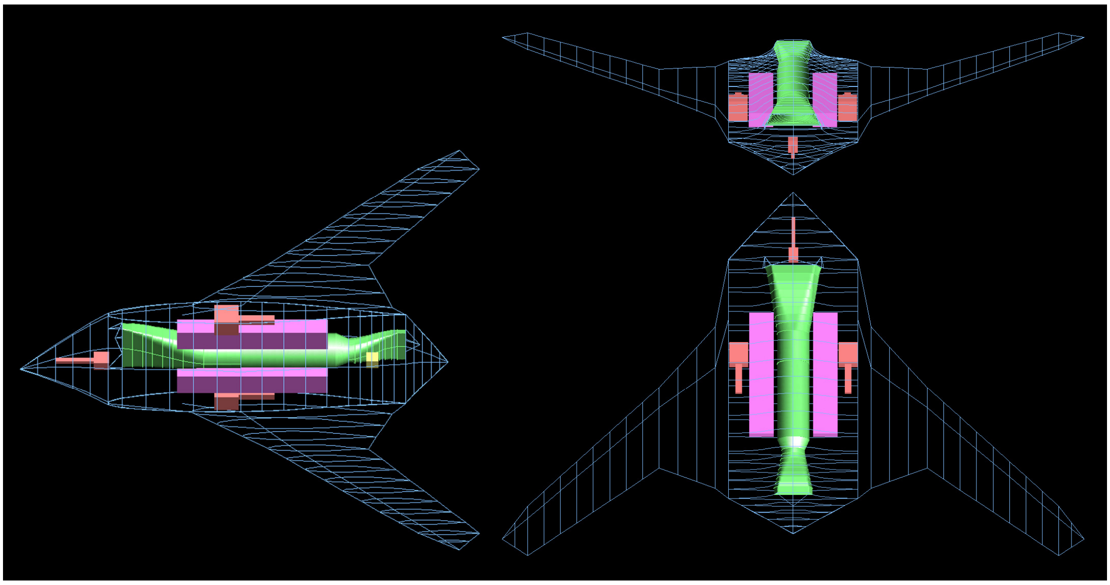

Figure 3.2.1: Baseline configuration of UCAV

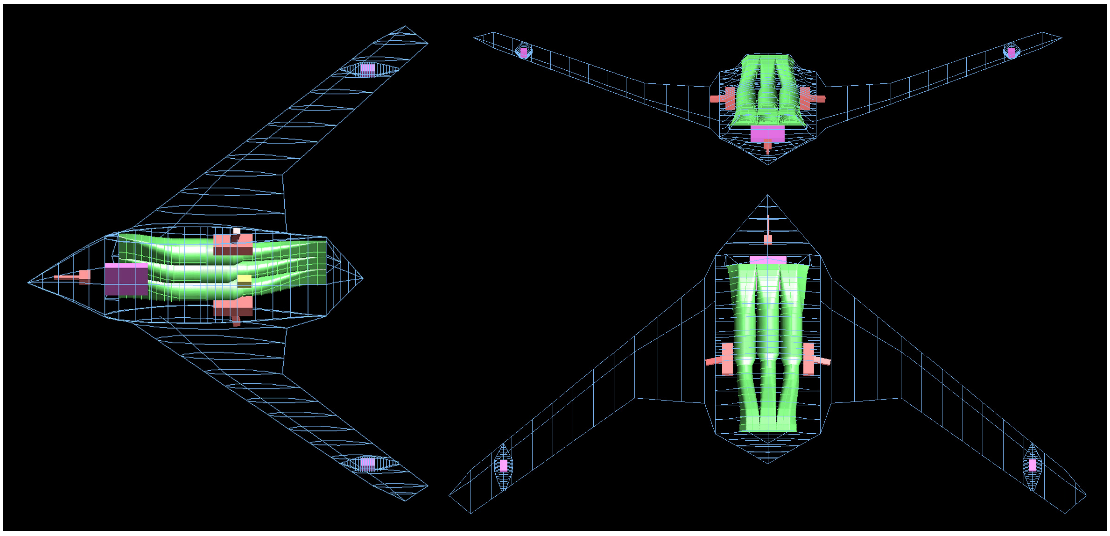

Figure 3.2.2: Baseline configuration of uninhabited tanker

Figures 3.2.1 and 3.2.2 depict the finalised baseline configuration models of the UCAV and the uninhabited tanker respectively. For both aircraft, the most significant change from their initial baseline configuration is clearly the wing design. As mentioned the previous section, the lack of tail wings highly increases the difficulty of designing the aircraft to achieve sufficient stability. Therefore, it was considered to be more appropriate for the aircraft to be able to freely adjust the position of the main wing on the fuselage rather than constraining the wing location and the chord length to match those of the fuselage junction. Also the original wing configuration leads to excessive reference wing area while its actual effective wing area is relatively much smaller resulting poor lifting performance and other consequences in the design synthesis evaluations.

Since the stability of the designed aircraft entirely relies on the use of the control surfaces affixed on the main wing, a multi-partition wing configuration is essential for increasing the effectiveness and operational feasibility of these devices. Thus, the original wing configuration was broken down into four partitions; the fairing, inboard wing, outboard wing and pointed tip, joining to the centre part of the fuselage to achieve a blended wing-fuselage airframe. This cranked-wing configuration would impose fewer constraints and offer more flexibility to the design of aircraft allowing better aerodynamic and stability performances. Nonetheless, due to the flexibility obtained from the current cranked-wing configuration, the previous wing design can also be achieved.

The internal component layout of the UCAV is maintained from the initial design while this is not the case for the tanker. In general for both aircraft, avionic bays are now assumed to be distributed in the nose area of the fuselage instead of being specified as a fixed-shape component, which significantly increases the flexibilities of nose undercarriage's location and surrounding airframe shape. An additional model of auxiliary power unit (APU), depicted as yellow colour, is included under the exhaust pipe since the weight, and hence, the force balance of such a component need to be estimated individually.

All propulsion ducts feature variable cross-section and vertical S-shaped deflection designs. The purposes of the duct deflection are to fit such components optimally in the aircraft and more importantly to prevent the engine from being exposed to incoming radar energy. Without this duct obscuration, an operating engine would emit a large amount of RCS as a result of rotating turbine blades causing several reflections of the radar energy within the duct's cavity before returning to the source. Also a high temperature produced at the engine nozzle would result the aircraft being prone to heat detection. At the inlet and the exhaust planes, the cross-sectional area of the duct must be aligned in such a way for stealth design contribution, while the other end of the component is required to fit with a circular-facet engine; therefore, trapezium-to-circle area transformation is applied.

Both aircraft share the same nose undercarriage deployment of forward retraction which has been considered on the account of larger space for wheel storage toward the fuselage's centre. As far as the UCAV is concerned, a backward retraction is configured for the main undercarriage deployment in order to provide sufficient wheel-base distance for ground stability and also the fact that greater fuselage's thickness is available for accommodating the wheels. On the other hand, the significant estimated takeoff weight of the tanker leads to the demand of bogey-wheel configuration for the main undercarriage which requires reasonably large storage space. Therefore, a side-retraction configuration is considered for main undercarriage deployment allowing the components to be laterally positioned further away from the centreline once they are released, hence providing adequate overturn angle for taxiing precisely around the sharp corner. Also for ground stability purposes, storage angles of the strut are applied to increase the flexibility of deployment positions.

During the development of the UCAV baseline configuration, it was decided that the airframe configuration of the uninhabited tanker would be similar to the UCAV primarily due to the design simplicity and the need of minimising modelling modifications between two aircraft. Undoubtedly, various changes have been made to the tanker from its initial B-2-resembled design. Since the tanker design emphasises cruise performance rather than manoeuvrability, the thrust requirement for the aircraft is on a low side relative to its weight. Nonetheless, the significant design weight of the tanker itself gives rise to the demand of high amount of thrust in total, and thus increases the size and/or the number of the engines required. As far as an internal installation of the engine is concerned, increasing the size of the engines to satisfy the thrust requirement is not an ideal solution; however, it would be more appropriate to increase the number of the engines used instead. This would reduce the diameter of individual engine and hence the overall fuselage's thickness needed, while comfortably meeting the thrust requirement. Also with the side-by-side engine arrangement, the shape of the airframe can be laterally maintained for wing-fuselage blending. For these reasons, the propulsion system of the tanker features an installation of three engines instead the previous twin-engine configuration in the initial design.

In additional to the vertical duct deflection and variable cross-section features, the side propulsion ducts are deflected in the lateral direction in order to provide sufficient room for accommodating the engines and firewall installation with the side-by-side engine arrangement. At the inlet and the exhaust planes of the tanker, the cross-sectional area of three ducts together forms a single trapezium shape instead of three individual objects. This is to maintain the majority of UCAV airframe model configuration and minimise the modelling modifications. The longitudinal position of side engines is also staggered to increases the survivability of the propulsion system in case of collateral damages caused by nearby engine failure.

Generally installing external wing pods is an effective solution for modifying a certain aircraft to perform air refuelling operations. Nonetheless, due to the shape and the installation of these storage components, typical wing pods would generate substantial aerodynamic interference and also would considerably reduce stealth capability of an uninhabited tanker. Therefore, hose-reel refuelling units are installed directly into the wing from underneath between the front and the rear spars. Although the thickness of the wing toward the outboard cannot fully cover the entire unit, with a semi-submerged configuration, any remaining portion of the unit can be accommodated by a blended fairing pod under the wing. This would minimise RCS contribution from refuelling equipment while maintaining operational effectiveness of the tanker.

As addressed in the first chapter, current tankers lack of defensive capability and rely on the protection from other combat aircraft in the vicinity. Such an issue may become critical once the tanker is targeted by an enemy especially for the proposed tanker/UCAV combination, since all of the UCAVs in the fleet would be deployed for combat operation while the uninhabited tanker would loiter outside the hostile area unprotected by any aircraft. In order to increase the survivability of the tanker, an additional space for weapon storage, depicted by the same purple colour as in the UCAV diagram, has been allocated under the intake diffusers allowing the tanker to carry any desired weapon payloads for self-protection purpose.

It is possible to design the tanker with an integrated fuel system for both refuelling operations and its own use, providing higher flexibility for typical air-refuelling operations in which require a large amount of offload fuel while the range from the deployed air base to the rendezvous point is relatively close. However, such a concept results operational limitations if the receivers require different types of fuel from the tanker, thus the design of separated fuel systems is considered. The offload fuel tanks are distributed in the wing box while the fuel storage of the tanker itself is the potential remaining space in the centre part of the fuselage. In additional to modelling flexibility, the purpose of this fuel tank scheme is to reduce the complexity of the fuel systems by allocating the tanks close to their utilisations.

3.2 Initial Sizing

At the beginning of the design synthesis, an approximated takeoff weight of the aircraft must be identified using initial sizing methods. The initial sizing process is an empirical methodology for estimating the fuel consumed and hence the total weight of an aircraft for a given mission profile, from a combination of statistical aerodynamic, propulsion and weight data. The total fuel weight calculated in the above sizing evaluations is generally specified in a form of weight fraction which is determined according to corresponding operation segments in the mission profile of the aircraft. Thus, prior to develop the methods for sizing the tanker/UCAV combination, the design mission profiles of each aircraft must be established first.

3.2.1 Design Mission Profiles

The concept of operating an uninhabited tanker and a group of UCAVs in combination developed in this research project is based on the deployment support mission of tankers in which such aircraft are required to accompany and air refuel combat platforms to extend their combat radius. However, with appropriate design configurations, the proposed unmanned aircraft system would bring the combat aircraft deployment operation to the next level described as follows,

- The aircraft system would be operated directly from its assigned air base, in which the uninhabited tanker would fly in close formation with the UCAVs escorting them directly to a faraway target while conducting air refuelling operations as required.

- Once the above system reaches the designated deployment point near a hostile territory where the target is located, the UCAVs would break away from the tanker formation and continue to fly the target, whereas the tanker, would loiter at the deployment point waiting for the UCAVs' return after performing combat employment.

- From the deployment point, the UCAVs' operations are assumed with a simple 'hi-lo-hi' profile which refers to descending directly from a high altitude to strike the target at low level then dashing climb back.

- The UCAVs would fly back to rendezvous with the tanker loitering at the deployment point, and afterward the tanker-UCAV formation cruise would resume until they arrive at the original departed air base.

The overall mission profile of the tanker/UCAV combination which represents the above operation concept is illustrated in Figure 3.3.

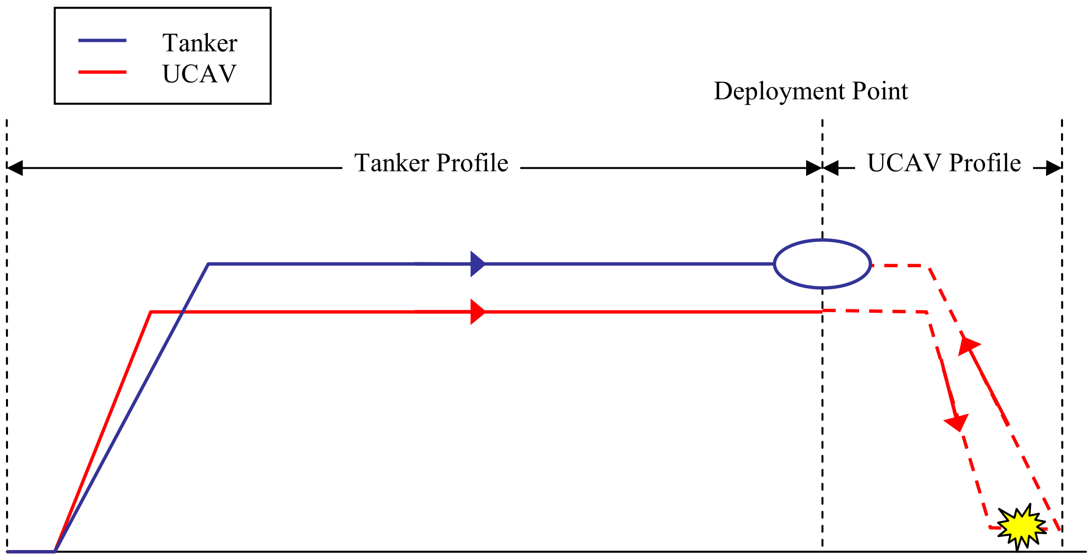

Figure 3.3: Tanker/UCAV combination mission profile

From the above figure, the red line indicates the entire mission profile of the UCAV and the blue one refers to the tanker case. The tanker would takeoff first and then continues to climb whereas the sortie of UCAVs would follow afterward. The UCAVs which possess greater thrust performance would be capable of accelerating with steeper climb angle and arrive at the cruise altitude to initiate close formation flight with the tanker. Once the UCAVs rejoin with the tanker at the deployment point after the combat employment, both aircraft would continue the same cruise path as the previous outbound leg back to the air base. The above mission profile was established in accordant with the entire operation of the aircraft in combination;

however, in order to estimate the weights of the tanker and the UCAV appropriately, the mission profile accounted for designing each aircraft must be individually considered.

3.2.1.1 UCAV

Design mission profiles are an essential part of the initial sizing process for estimating the total fuel consumption of the aircraft to ensure such a unit can complete its design operation without running out of fuel beforehand. However, with an incorporation of uninhabited tanker, the majority of the entire UCAV mission profile is overruled by periodically performing air refuelling operations during the long-haul cruise segments. For this reason, an appropriate UCAV mission profile considered for the fuel weight estimation should start from the point where the UCAV operations become independent from the tanker and end where the formation of the tanker and the UCAVs is resumed. Thus, the design mission profile of the UCAVs, illustrated in Figure 3.4, begins from their departure at the deployment point until they rendezvous with the tanker after the hi-lo-hi combat profile.

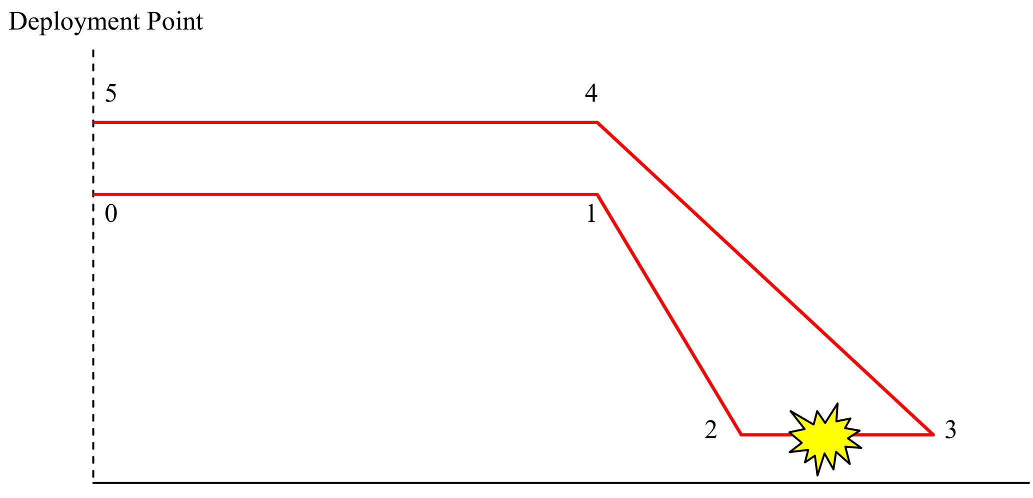

Figure 3.4: Design mission profile of UCAV

Segment	**Description**
0-1	Continue to fly from the deployment point
1-2	Descend to the target

2-3	Employ weapons
3-4	Dashing climb to the cruise altitude
4-5	Fly back to join with the tanker at the same point

3.2.1.2 Uninhabited Tanker

In contrast to the design mission profile of the UCAVs, the tanker is required to complete its entire operation without additional fuel supplied. Thus, its design mission profile, depicted in Figure 3.5, would be considered as normal from the takeoff until the landing at the air base. Nonetheless, the formation cruise segments denoted by 2-3 and 4-5 contain sub-mission profiles of air refuelling sequence which will be subsequently accounted in the second initial sizing process of the tanker. In order to develop a flexible design synthesis methodology, these sub-mission profiles cannot be simply specified as a fixed refeulling sequence procedure for all design cases. However, they will be determined according to certain operational criteria after accurate weight and performance parameters of the UCAV are acquired. The method developed for this air refuelling sequence evaluation will be described later on in the initial sizing section.

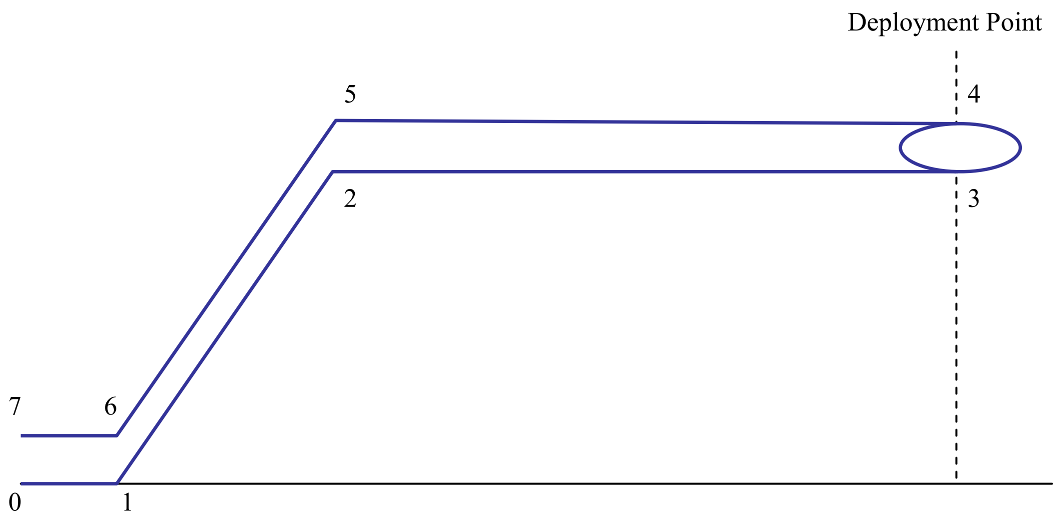

Figure 3.5: Overall design mission profile of tanker

Segment	Description
0-1	Takeoff
1-2	Climb to the cruise altitude
2-3	Formation cruise
3-4	Loiter at the deployment point
4-5	Formation cruise
5-6	Descend to land
6-7	Landing

3.2.2 Initial Sizing Development

In general, initial sizing methods feature an iterative evaluation approach to converge to a result. Within the contexts of this research project, however, two such procedures are needed since there are two types of aircraft in the system and the amount of fuel payload carried in the tanker is directly proportional to the UCAV's fuel capacity. An additional sizing procedure is also required for the tanker case to account for significant fuel payload reduction after every air refuelling operation. This causes the tanker to demand less fuel than the initial assumption of normal cruise with constant payload weight carried. Since it is desirable to size the aircraft with sufficient accuracy while the input requirements are not excessive, the initial sizing method suggested by Raymer [47] is applied to the UCAV and the first sizing procedure of the tanker in correspondent to their design mission profiles established above.

The design takeoff weight of unmanned aircraft W_0 primarily consists of payload weight, fuel weight and empty weight. This can be formulated as shown in Eq. (3.1), and rearranged to Eq. (3.2) to be used for evaluating the takeoff weight once the values of W_e / W_0 and W_f / W_0 are determined.

$$W_0 = W_{\text{payload}} + W_{\text{fuel}} + W_{\text{empty}} \tag{3.1}$$

$$W_0 = \frac{W_{\text{payload}}}{\left(1 - \frac{W_f}{W_0} - \frac{W_e}{W_0}\right)} \tag{3.2}$$

when, $$\frac{W_e}{W_0} = A \cdot {W_0}^C \cdot K_{vs} \cdot (1 - \text{psf}) \tag{3.3}$$

$$\frac{W_f}{W_0} = \left[1 - \left(\frac{W_1}{W_0}\right) \cdot \left(\frac{W_2}{W_1}\right) \cdot \left(\frac{W_3}{W_2}\right) \cdot \ldots \cdot \left(\frac{W_n}{W_{n-1}}\right)\right] \cdot (1 + \text{RF}) \tag{3.4}$$

While the payload weight is given as a design requirement, the empty weight and the fuel weight must be initially estimated as a function of the total weight at takeoff. The empty-weight fraction W_e / W_0 can be evaluated using an empirical equation presented in Eq. (3.3), where A, C and K_{vs} are statistical developed constants which vary depending on the types of aircraft. Suggested values for these constants can be found in reference [47].

The above method also requires W_0 which is, in fact, the objective parameter that needs be evaluated; therefore, an iterative procedure must be incorporated as shown in Figure 3.6. Since the Eq. (3.3) is originally formulated for sizing piloted aircraft, the cockpit and pilot support equipments, which are normally accounted for 10-15% of the total aircraft empty weight, should be excluded from the weight estimation of unmanned aircraft. Thus, the above equation has been modified with an additional term of the pilot-support weight fraction ' psf ' included.

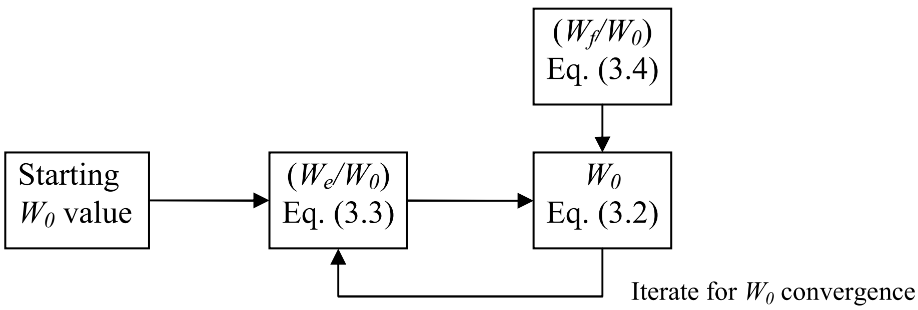

Figure 3.6: Initial sizing procedure

The fuel fraction W_f / W_0, on the other hand, is evaluated from an accumulated weight fraction of all mission segments in the design mission profile established previously. From Eq. (3.4), W_n / W_{n-1} represents a ratio of the final weight to the initial weight at the nth segment of the mission profile and also the reserve fuel fraction RF is included. A typical 6% of reserve fuel may be assumed for the tanker; however, for the UCAV, such a provision must be sufficient to cover an air refuelling period at the end of its design mission profile. And the reserve fuel value of 15%, determined from preliminary testings of the design synthesis, was found to be appropriate.

Although the weight fractions of the following mission segments; takeoff, climb, descent and landing, can be commonly specified based on the statistical values suggested in the Aerospace Vehicle Design course [65]. There are certain types of mission segment which must be evaluated in order to determine the value of the weight fraction accurately. These are the level-flight, combat and loiter conditions. The following methods are applied to both tanker and UCAV for estimating the values of the weight fractions which fall into the aforementioned mission segment categories.

The Breguet range equation presented in Eq. (3.4) can be rearranged to Eq. (3.5) for evaluating the weight fraction of any level-flight segment. The lift-to-drag ratio L / D value at such a condition, recommended by Raymer [47], can be approximated as $0.866 \cdot (L / D)_{\max}$.

$$S = \frac{V}{\mathrm{sfc}} \cdot \frac{L}{D} \cdot \ln\left(\frac{W_{n-1}}{W_n}\right) \tag{3.4}$$

$$\frac{W_n}{W_{n-1}} = \exp\left(-\frac{S \cdot \mathrm{sfc}}{V \cdot L / D}\right) \tag{3.5}$$

where,

S	- Range	sfc	- Specific fuel consumption
V	- Air speed	W_n / W_{n-1}	- Weight fraction

The combat segment weight fraction can be found from Eq. (3.6) which is formulated as a function of specific fuel consumption, time and thrust-to-weight ratio at the combat condition.

$$\frac{W_n}{W_{n-1}} = 1 - \mathrm{sfc}_{co} \cdot d \cdot \left(\frac{T}{W}\right)_{co} \tag{3.6}$$

when, $$d = \frac{2\pi \cdot V_{co} \cdot x}{g \cdot \sqrt{(n_{co}{}^2 - 1)}} \tag{3.7}$$

where,

d	- Combat duration (sec.)	g	- Gravitational constant
n	- Load factor	x	- Number of turns

subscript:

co - Combat condition

The endurance equation shown in Eq. (3.8) can be derived in a similar way to the Eq. (3.5) for estimating the loiter weight fraction. $(L/D)_{\max}$ is used as initial input parameter which implies the most efficient loiter performance of an aircraft. Since the loiter segment of the tanker coincides with the period in which the UCAVs depart for combat operation, the loiter time E can be acquired directly from the total time taken for the UCAV to complete its design mission profile.

$$E = \frac{1}{\mathrm{sfc}_{lo}} \cdot \left(\frac{L}{D}\right)_{\max} \cdot \ln\left(\frac{W_{n-1}}{W_n}\right) \tag{3.8}$$

$$\frac{W_n}{W_{n-1}} = \exp\left(\frac{-E \cdot \mathrm{sfc}_{lo}}{(L/D)_{\max}}\right) \tag{3.9}$$

subscript:

lo - Loiter condition

Once W_e / W_0 and W_f / W_0 have been evaluated according to the methods described above and the convergence of W_0 from Eq. (3.2) has been achieved, the empty weight and the fuel weight can be found simply from a multiplication of the resulted W_0 and the above corresponding weight fraction values. Thus, the initial sizing of the UCAV is now completed, while for the tanker, this procedure serves primarily to provide appropriate starting weights condition for using in the subsequent sizing process.

The second initial sizing of the tanker features a different iterative approach in which the sizing procedure will be formulated according to the breakdown refuelling sequence in the formation cruise segments specified earlier in the design mission profile of the tanker. Since the evaluations of the refuelling sequence require several UCAV performance parameters, the design synthesis of the UCAV must be carried out prior to the initial sizing and hence the remaining design calculations of the tanker. This is to acquire accurate value of the total additional fuel UCAVs required to complete the entire operation. This total fuel payload would become part of the input specifications for designing the tanker which would remain unchanged throughout its design synthesis computations, thus it is important to determine such a value as precisely as possible.

3.2.2.1 Preliminary Refuelling Sequence

As far as the mission profile of the tanker/UCAV combination is concerned, apart from the number of UCAVs assigned per tanker, the amount of fuel payload carried by the tanker primarily depends on the following factors; the frequency of air refuelling operations, distance travelled by the UCAVs before being refuelled, total range to the destination, and fuel capacity of the UCAVs. Although one of the research objectives is to optimise this aircraft combination's refuelling sequence; at this stage of the design synthesis, it is not possible to determine an optimal solution due to the unknown specifications and performances of the tanker. However, the refuelling sequence is also necessary for establishing the detailed mission profile and hence appropriately sizing the tanker at the beginning. For this purpose, a preliminary refuelling sequence has been developed by considering the following criteria,

- According to an operational envelope of hose drum unit [49], refuelling operations require the aircraft combination to slow down from high subsonic speed at normal cruise condition to the maximum air speed of 350 knots (approximately Mach 0.6 at high cruise altitude). The speed reduction implies that the more frequent the UCAVs perform the refuelling operation, the longer time they take to reach the destination and thus complete the campaign. This is not desirable especially when time becomes a critical requirement in the mission; therefore, ideally the air refuelling operation should be performed as fewer times as possible.

- An improvement of UCAV aerodynamic performance (i.e. lift-to-drag ratio) as a result of close-formation flying with the tanker is accounted throughout the formation cruise segments. However, since the refuelling operation requires the UCAVs to break out from their optimal formation for a short period of time, it is reasonable to assume that there is no formation flight effect accounted in the UCAVs' performance during any refuelling segments.

- As far as the Breguet range equation is concerned, the range performance of an aircraft is proportional to the ratio of its initial weight to its final weight, which means that any unused fuel at the end of each cruise segment is considered as a 'dead weight' reducing the potential range of the aircraft. Therefore, the air refuelling operation should start at a certain fuel level which is just sufficient to cover the queuing time before the UCAV actually being refuelled by the tanker.

- Since the size of the UCAV is estimated on a basis of the mission segments after departing from the tanker until both aircraft rendezvous at the same point, the amount of fuel transferred to the UCAV in the last refuelling segment before arriving at the deployment point must be at full capacity.

After considering the above criteria, it is concluded that the number of refuelling as well as the remaining fuel in the UCAV should be minimised, and also the fuel must be offloaded to the maximum level before the deployment. For a given mission range requirement, an optimised refuelling sequence for tanker's initial sizing can be constructed as follows.

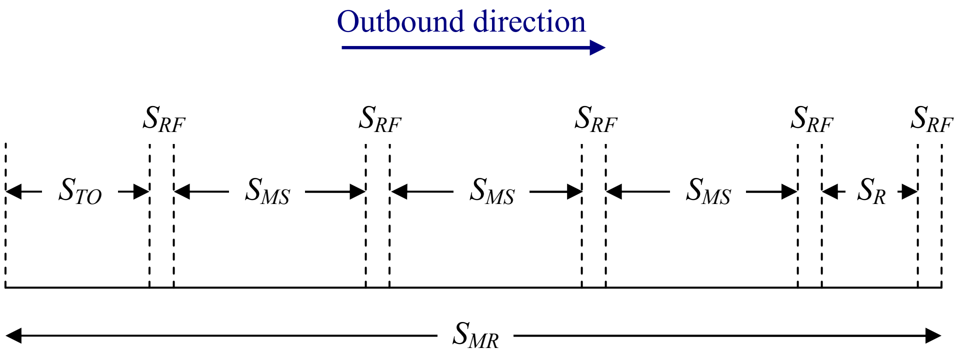

Figure 3.7: Initial outbound refuelling sequence

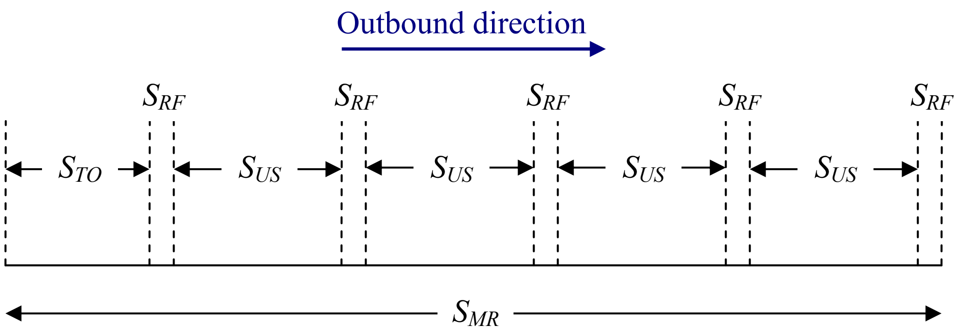

Figure 3.8: Optimal outbound refuelling sequence

$$N_{RF} = \left(\frac{S_{MR} - S_{TO} - S_{RF}}{S_{MS} + S_{RF}} \right) + 1 \tag{3.10}$$

$$S_{US} = \left(\frac{S_{MR} - S_{TO} - S_{RF}}{N_{RF}} \right) - S_{RF} \tag{3.11}$$

where,

S_{MR}	- Mission range	S_{MS}	- Maximum segment range
S_{TO}	- Takeoff segment range	S_{US}	- Uniform segment range
S_{RF}	- Refuelling segment range	S_{R}	- Remaining range
N_{RF}	- Number of refuelling		

As far as the outbound mission leg is concerned, the original fuel which the UCAV carried from an air base should be depleted until reaching the refuelling level to maximise the first cruise segment after takeoff denoted by S_{TO}. Afterward the aircraft would slow down to perform an air refuelling operation, if the total time and the speed of the aircraft during the operation are assumed to be constant then so does the refuelling range S_{RF} in all associated segments. After the takeoff cruise and the first refuelling segments, minimising the refuelling numbers N_{RF} is one of the main considerations, and this lowest possible value of N_{RF} can be determined from Eq. (3.10) when the result is an integer. The equation was formulated based on the N_{RF} required to complete the remaining course if the UCAV is to carry full fuel capacity, and hence being capable of producing the maximum cruise segment range S_{MS}.

Figure 3.7 shows an example of the refuelling sequence established by the above S_{MS}. Clearly, the last cruise segment S_R has a tendency to be shorter than the S_{MS}. This results unused fuel remaining in the UCAV toward the end of the segment if the aircraft started with the full fuel capacity as any previous S_{MS} segments, which is undesirable according to the operational criteria considered at the beginning. Also in the worst scenario, S_R could be extremely short or even negative causing the last two S_{RF} segments to be overlapped. For these reasons, the initial refuelling sequence has been re-constructed uniformly as illustrated in Figure 3.8 to optimise the operation based on the same minimum N_{RF} value obtained previously, while the uniform cruise segment S_{US} can be found from Eq. (3.11).

Once the uniform refuelling sequence has been specified, in order to reduce any unused fuel carried by the UCAV, the fuel level at the beginning of each S_{US} segment should be about sufficient to cover the S_{US} and the next S_{RF} segments. Since the total fuel required for these range segments must be evaluated based on the minimum fuel carried assumption, not a typical case of the fuel consumption from a given total amount, thus the starting weight of the UCAV are not known. However, if the reserve fuel fraction (RF) of the UCAV from the previous initial sizing is used as a fuel-level signal to initiate the refuelling operation, then the fuel weight and thus the total aircraft weight at the end of every S_{US} segment can be determined, and so do the starting weight parameters at the beginning of every S_{RF} segment. The Breguet range equation introduced previously can be rearranged to the equation forms shown below for evaluating the required fuel weight under two different input aircraft weight conditions.

$$W_{\text{fuel}} = (1 - \text{frc}) \cdot W_{\text{initial}} \tag{3.12}$$

$$W_{\text{fuel}} = \left(\frac{1 - \text{frc}}{\text{frc}} \right) \cdot W_{\text{final}} \tag{3.13}$$

when, $\quad \text{frc} = \exp\left(- \dfrac{S \cdot \text{sfc}}{V \cdot L / D} \right)$

where,

W_{initial} - Total aircraft weight at the beginning of the segment.

W_{final} - Total aircraft weight at the end of the segment.

As far as the design synthesis computations are concerned, the above equations are evaluated in multiple sub-segments to improve accuracy, and also the performance parameters involved are calculated based on associated performance analyses which will be described in subsequent chapters. The total fuel offloaded from the tanker to all UCAVs in the outbound leg can be found in accordant with the equations shown below, when Eq. (3.15) refers to the last refuelling segment before UCAV deployment. Since the first cruise segment of S_{TO} consumes original UCAV fuel carried from the air base, such a contribution is excluded from Eq. (3.16).

$$W_{FUS} = (f_1(S_{RF}) + f_2(S_{US})) \cdot N_{\text{ucav}} \tag{3.14}$$

$$W_{FMS} = (W_{FM} - W_{FR} + f_1(S_{RF})) \cdot N_{\text{ucav}} \tag{3.15}$$

$$W_{FO} = N_{RF} \cdot W_{FUS} + W_{FMS} \tag{3.16}$$

where,

$f_1(S)$ - Fuel weight evaluated using Eq. (3.12) for a given range S

$f_2(S)$ - Fuel weight evaluated using Eq. (3.13) for a given range S

N_{ucav} - Number of UCAVs assigned per tanker

W_{FO} - Total fuel offloaded in the outbound leg

W_{FUS} - Offloaded fuel weight for the uniform range segment

W_{FMS} - Offloaded fuel weight for the full capacity

W_{FM} - Maximum fuel weight of UCAV

W_{FR} - Reserve fuel weight of UCAV

The uniform refuelling sequence of the inbound mission leg is also established using the same approach as the outbound case. By considering the minimum N_{RF} requirement, it is suggested that the UCAV should proceed in the last cruise segment before landing S_{LD} with the maximum fuel capacity, hence maximising this range segment value similar to S_{TO} in the outbound sequence. The previous Eq. (3.10) and Eq. (3.11) can be applied to formulate the inbound refuelling sequence with a parameter changes from S_{TO} to S_{LD}. Due to the weapon payload released in the combat section, the UCAV weight would become lighter in the inbound leg. Therefore, the range segment values and hence the associated offload fuel weights would be different from the outbound case.

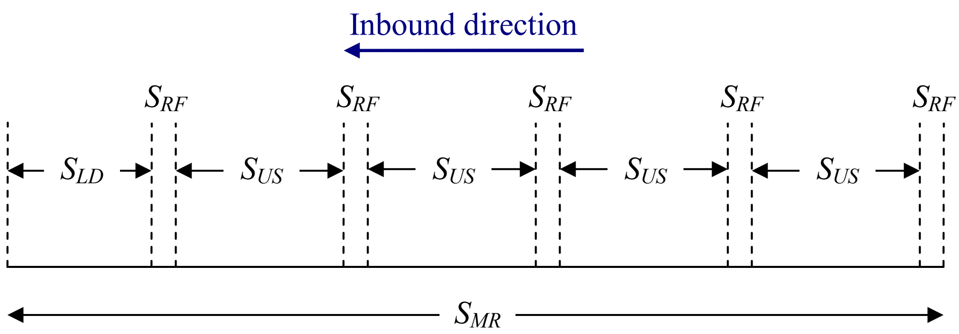

Figure 3.9: Optimal inbound refuelling sequence

where,

S_{LD} - Landing segment range

Since the amount of offload fuel required for the S_{LD} would be at the maximum capacity similar to the combat section, the Eq. (3.12) to Eq. (3.16) can be applied for evaluating the total fuel offloaded for the corresponding inbound range segments, and finally the total fuel payload of the tanker can be found simply from the accumulation equation below.

$$W_{FP} = W_{FO} + W_{FI} \tag{3.17}$$

where,

W_{FI} - Total fuel offloaded in the inbound leg

W_{FP} - Tanker fuel payload

Although the above preliminary refuelling sequence method developed based on logical operational criteria may not yield an absolute optimal answer, it provides an effective solution for establishing a decently optimised design mission profile for sizing the tanker. Also the method can be applied to any design requirements, not only limited to a single case. Regardless, an optimisation of the air refuelling sequence for maximising the range performance will be conducted once both tanker and UCAV designs have been synthesised.

3.2.2.2 Second Initial Sizing of the Uninhabited Tanker

The first initial sizing of the tanker requires only the total fuel payload W_{FP} obtained from the above preliminary refuelling sequence to crudely estimate the tanker weights according to its overall design mission profile, in which the tanker is assumed to carry constant payloads throughout the entire cruise leg. In the second initial sizing, however, periodical fuel releases and hence the reduced tanker's fuel consumption will be accounted to predict more accurate weights of the tanker. The information obtained from the above refuelling sequence analysis, such as numbers of refuelling, all range segments and their associated offload fuel weights, is required for establishing sub-mission segments in the outbound and the inbound cruise segments of the design mission profile of the tanker as shown in the diagram below.

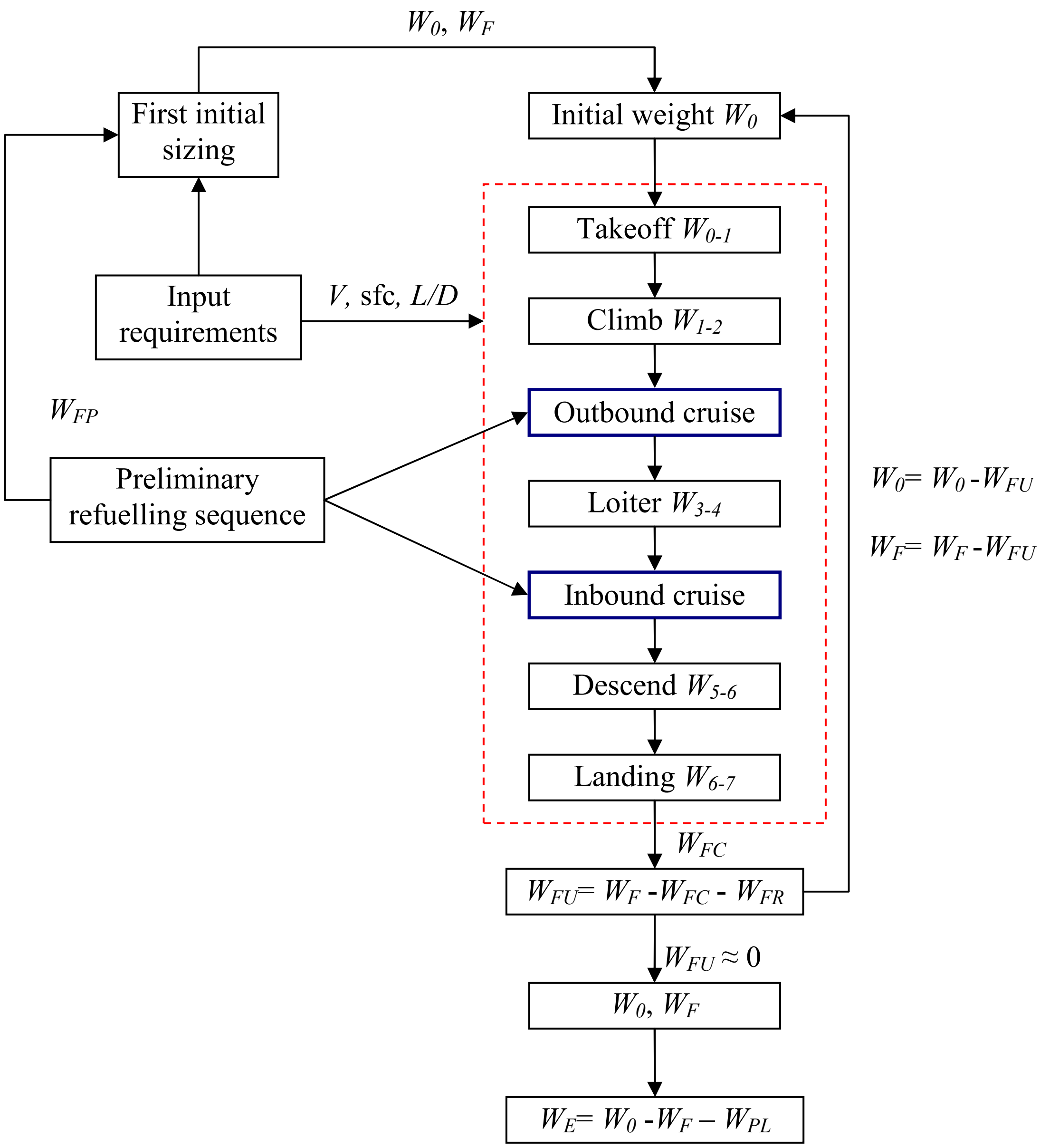

Figure 3.9: Operation of tanker's initial sizing processes

where,

W_E	- Empty weight
W_{PL}	- Total payload weight (fuel and weapon)
W_{FC}	- Total fuel consumed in the operation
W_{FU}	- Unused fuel in the operation
W_{FR}	- Reserve fuel

Figure 3.9 illustrates the main operation of the second initial sizing process of the tanker and how it is connected to other related modules. Since initial values of the takeoff weight W_0 and the fuel weight W_F have been found from the first initial sizing, the actual fuel consumption of the tanker (i.e. no longer in a form of W_f / W_0) for the entire operation can be calculated directly according to the associated operation segments in the design mission profile circled by the red box in the above figure. With an exception of the outbound and the inbound cruise segments, the rest of the mission profile segments carried on the same weight fraction values as in the previous initial sizing to evaluate the decreased tanker weight, and thus the reduced fuel consumption after each mission segment. On the other hand, for the cruise segments, the aforementioned refuelling sequence parameters are used for to constructing sub-mission segments in the original formation cruise segments as shown in the figure below.

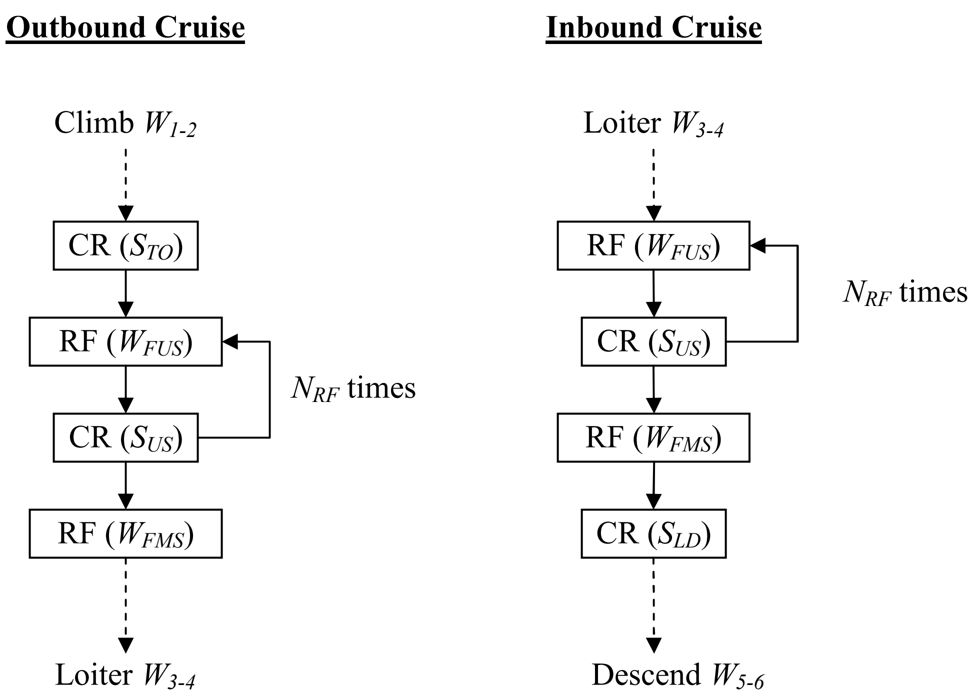

Figure 3.10: Refuelling sequence sub-operation segments

where,

CR(S_X) - Cruise segment for a given range S_X

RF(W_{FX}) - Refuelling segment with offloaded fuel weight W_{FX}

In contrast to the minimum fuel weight evaluation of Eq. (3.13) in the preliminary refuelling sequence analysis, the starting weight condition of the tanker for every operation segment is known in this case; therefore, Eq. (3.12) can be used for calculating the fuel consumption throughout the entire cruise segments. For each CR and RF blocks displayed in Figure 3.10, the fuel consumption and hence the reduced tanker weight are evaluated in succession according to the following calculation procedures.

Cruise segment, $\mathrm{CR}(S_X)$

$$W_i = W_x \tag{L1}$$

$$W_{FS} = f(S_X, \mathrm{sfc}, V, L/D, W_i) \tag{L2}$$

$$W_f = W_i - W_{FS} \tag{L3}$$

Refuelling segment, $\mathrm{RF}(W_{FX})$

$$W_i = W_x - \frac{W_{FX}}{2} \tag{L4}$$

$$W_{FS} = f(S_{RF}, \mathrm{sfc}, V_{RF}, L/D, W_i) \tag{L5}$$

$$W_f = W_i - W_{FS} - \frac{W_{FX}}{2} \tag{L6}$$

where,

f	- Evaluation of Eq. (3.12) for given input parameters
W_i	- Initial tanker weight of the current segment
W_f	- Final tanker weight of the current segment
W_x	- Final tanker weight of the previous segment
W_{FS}	- Fuel consumption of the current segment

The calculation procedures (L1-L3) and (L4-L6) are constructed in accordant with the order of the CR and RF blocks given by the refuelling sequence diagrams shown in the Figure 3.10. This will provide an estimation of the reduced tanker weight after every operation segment in the sequence including the fuel payload dropped at the refuelling periods in the mission. The air speeds V and V_{RF} are separately applied to the cruise and the refuelling segments; however, sfc and L/D are initially assumed with the same cruise condition for both. Nonetheless, the variations of these parameters will be appropriately accounted in subsequent iterations of the design synthesis evaluations. In order to improve the accuracy of the above calculation procedures, W_{FS} evaluation in (L5) is carried out under the assumption of the tanker weight in the middle of the refuelling operation; therefore, half of W_{FX} is included in the fuel consumption calculation.

At the end of the mission profile, the total amount of fuel consumed by the tanker through the entire operation can be determined, and any remaining unused fuel W_{FU} will be calculated and subtracted from the initial values of W_0 and W_F for the next iteration as shown in the main operation figure. After a certain number of iterations passed, the value of W_{FU} will be converged to zero, then new estimated weights of W_0, W_F and W_E will be obtained.

3.2.3 Thrust-to-Weight Ratio and Wing Loading

In additional to an estimated takeoff weight obtained from the initial sizing porcess, another two important parameters which highly affect designed aircraft's configuration and performances are thrust-to-weight ratio T/W and wing loading W/S. At the beginning of the design synthesis, these parameters are used in conjunction with the sized takeoff weight to determine the engine thrust and the wing area needed to satisfy performance requirements. For example, low W/S implies a large wing area which generally results higher lift force generated and hence reduces the takeoff distance; however, additional drag and weight penalised due to the larger wing would also incur accordingly throughout the operational course. On the other hand, the reduction of the takeoff distance may also be achieved with higher T/W; nonetheless, this solution usually gives rise to the demand for greater engine size. Therefore, a compromise between T/W and W/S is desirable.

Due to the significance of these T/W and W/S values on the design configuration of the aircraft and also the fact that a number of performance criteria are related to these parameters, it is not appropriate to select these parameter values based on historical data. Instead the performance criteria of takeoff distance, landing distance, stall speed, maximum speed, climb rate, sustained turn and instantaneous turn, are normally used for justifying an optimal combination of such parameters. For this purpose, the equations representing the aforementioned performance criteria are developed to a form of either T/W as a function of W/S, or sole W/S requirement. Since only common design parameters are available at this stage, an Oswald efficiency evaluation based on swept-wing aircraft [48] shown in Eq. (3.18) will be applied to any induced drag analysis required in the following performance criterion equations.

$$e = 4.61 \cdot (1 - 0.045 \cdot AR^{0.68}) \cdot \cos^{0.15} \Lambda_{C/4} - 3.1 \qquad (3.18)$$

where,

e	- Oswald efficiency	AR	- Aspect ratio
$\Lambda_{C/4}$	- Quarter-chord sweep angle (rad)		

Although the statistical estimations of T/W and W/S relative to the takeoff and landing performances suggested by Raymer [47] can be applied to airliners with reasonable accuracy; it is not the case for military aircraft, not to mention unconventional design ones. Also since the ground-roll specification is commonly used in military aircraft category, the performance calculation shown in Eq. (3.19) from the above reference can be developed to Eq. (3.20) and Eq (3.21) for analysing takeoff and landing performance criteria respectively.

$$S_G = \frac{1}{2 \cdot g \cdot K_a} \cdot \ln\left(\frac{K_T + K_A \cdot V_f^{\,2}}{K_T + K_A \cdot V_i^{\,2}}\right) \qquad (3.19)$$

when, $K_T = \left(\frac{T}{W}\right) - \mu$

$$K_A = \frac{\rho}{2 \cdot (W/S)} \cdot \left(\mu \cdot C_L - C_{D0} - \frac{C_L^{\,2}}{\pi \cdot AR \cdot e}\right)$$

$$\left(\frac{T}{W}\right)_{takeoff} = \frac{K_A \cdot V_f^{\;2}}{\exp(2 \cdot g \cdot K_a \cdot S_G) - 1} + \mu \tag{3.20}$$

$$\left(\frac{T}{W}\right)_{\text{landing}} = \frac{K_A \cdot V_i^{\;2} \cdot \exp(2 \cdot g \cdot K_a \cdot S_G)}{1 - \exp(2 \cdot g \cdot K_a \cdot S_G)} + \mu \tag{3.21}$$

where,

ρ	- Air density	S_G	- Ground-roll distance
C_{D0}	- Zero-lift drag coefficient	V_i	- Initial velocity
C_L	- Lift coefficient	V_f	- Final velocity
μ	- Ground rolling resistance		

The specific excess power formula shown in Eq. (3.22) can be rearranged to Eq. (3.23) for representing the relationship between T/W and W/S in the sustained turning and climb performance criteria. The sustained turn refers to the level turning flight in which an aircraft is capable of maintaining the same altitude; therefore, P_S is zero whereas the T/W in this criterion is governed by the load factor requirement. On the other hand, the climb rate requirement directly represents the P_S value itself, and providing that the aircraft is in steady state during the climb, the load factor $n = 1$. Also the air density ρ at sea-level is assumed for climb condition.

$$P_S = V \cdot \left[\frac{T}{W} - \frac{\rho \cdot V^2 \cdot C_{D0}}{2 \cdot (W/S)} - n^2 \cdot \frac{2 \cdot K}{\rho \cdot V^2} \cdot \left(\frac{W}{S}\right)\right] \tag{3.22}$$

$$\left(\frac{T}{W}\right)_{\text{SEP}} = \frac{P_S}{V} + \frac{\rho \cdot C_{D0} \cdot V^2}{2 \cdot (W/S)} + n^2 \cdot \frac{2 \cdot K \cdot}{\rho \cdot V^2} \cdot \left(\frac{W}{S}\right) \tag{3.23}$$

where,

P_S	- Specific excess power	n	- Load factor

The maximum speed criterion which the aircraft can produce at the design cruise altitude is shown in Eq. (3.27). The equation is derived from fundamental aerodynamic lift and drag formulae under steady flight conditions where all forces acting on the aircraft are balanced i.e. $L = W$ and $T = D$.

$$W = \frac{1}{2} \cdot \rho \cdot V_{\max}^2 \cdot S \cdot C_L \qquad (3.24)$$

$$C_L = \frac{2}{\rho \cdot V_{\max}^2} \cdot \left(\frac{W}{S}\right) \qquad (3.25)$$

$$T = \frac{1}{2} \cdot \rho \cdot V_{\max}^2 \cdot S \cdot (C_{D0} + K \cdot C_L{}^2) \qquad (3.26)$$

Substitute Eq. (3.25) into Eq. (3.26) and rearrange,

$$\left(\frac{T}{W}\right)_{\mathrm{V\,max}} = \frac{\rho \cdot C_{D0} \cdot V_{\max}^2}{2 \cdot (W/S)} + \frac{2 \cdot K}{\rho \cdot V_{\max}^2} \cdot \left(\frac{W}{S}\right) \qquad (3.27)$$

where,

$V_{\max}$ - Maximum speed

In additional to the aforementioned T/W-W/S criteria, there are two other performance criteria which are solely a function of W/S namely the stall speed and the instantaneous turn. Eq. (3.28) and Eq. (3.29) developed for these respective criteria serve as boundary constraints for the minimum W/S requirement. Assuming a structural safety factor of 1.5, the maximum load factor N_z required in the Eq. (3.29) can be approximated as 1.5 times the design value of the sustained-turn load factor n. This maximum load factor is used to define the structural limit value during an instantaneous turn.

$$\left(\frac{W}{S}\right)_{\mathrm{V\,stall}} = \frac{1}{2} \cdot \rho \cdot C_{L\max} \cdot V_{stall}^2 \qquad (3.28)$$

$$\left(\frac{W}{S}\right)_{\mathrm{ITR}} = \frac{1}{2 \cdot N_z} \cdot \rho \cdot C_{L\max} \cdot V^2 \qquad (3.29)$$

where,

N_z - Maximum load factor $\qquad$ V_{stall} - Stall speed

Since the total weight and the throttle setting of the aircraft in each performance criterion condition are generally varied, in order to evaluate and compare all T/W and W/S values based on the same standard, weight and thrust corrections are applied to their associated parameters in the performance criterion equations described above. These performance corrections are developed by referencing the current aircraft weight and the throttle setting values to those at the takeoff condition which signifies the initial aircraft weight as well as maximum throttle input. A combination of the T/W and W/S values which is compromised for all performance criteria is determined as follows.

For the takeoff, landing, sustained turning, climb and maximum speed performance criteria, the T/W equations formulated earlier will be evaluated for a given range of W/S values, and then the T/W-W/S data will be plotted on the same graph as depicted in Figure 3.11, whereas the W/S results provided by the stall speed and instantaneous turning performance evaluations will be imposed as constraint boundaries on the above graphical figure.

The T/W-W/S combination which meets given performance requirements can be selected from any points in the upper region bounded by the T/W function plots, and also satisfy the stall speed and instantaneous turning W/S constraints. Clearly, feasible T/W-W/S solutions to the problem can be easily determined; however, the majority of such solutions are, by all means, not optimal for the performance requirements and could result inappropriate wing configuration, excessive weight and other undesirable consequences. Thus, an optimal T/W-W/S combination is essential for designing an aircraft correctly.

In general, the optimal combination of the T/W and W/S values can be found at the point in the feasible region of the graph where the majority of the performance criterion plots crossing through. This creates a bottom-left corner of the feasible region which usually represents the minimum T/W and W/S values needed in order to accommodate the performance requirements. From the example figure shown below, an optimal solution is clearly presented, in which the required T/W

value is primarily driven by the sustained turning and climb performances while the stall speed governs the minimum W/S value of the stall speed.

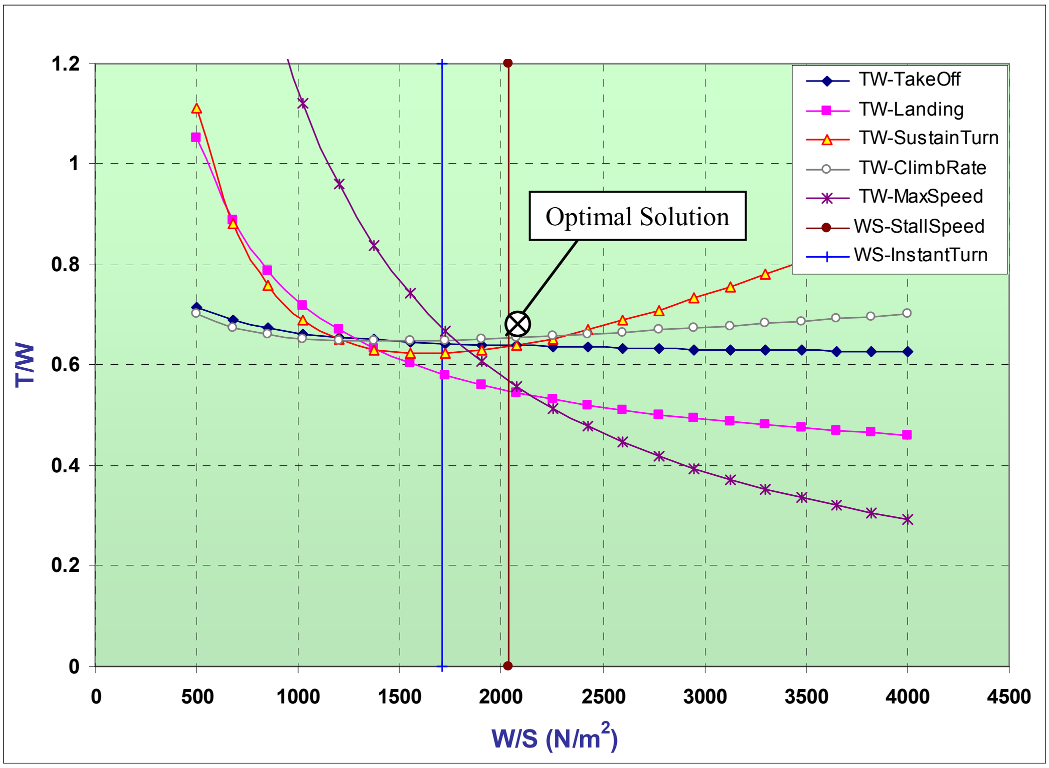

Figure 3.11: Thrust-to-weight ratio and wing loading plot

Due to the need of manual verification for this optimal solution, the evaluations of the T/W and W/S parameters are carried out prior to the main design synthesis operation using a separated program. Nonetheless, any performance parameters used in this T/W-W/S analysis may also be required in the following design synthesis evaluations. Therefore, the values of corresponding input parameters together with the T/W and W/S results should be recorded for further uses. Since the T/W-W/S analysis mainly relies on knowledge-based assumptions of the parameter values, the results obtained at this stage do not, by any chances, reflect the precise values and the user does not need to accurately follow. This analysis is, however, intended to provide approximate values of these important design parameters for synthesising the aircraft optimally for its mission and performance characteristics.

Chapter 4

System Packaging

Once the weight properties and major performance parameters of the aircraft have been estimated from the initial sizing and the T/W-W/S analysis, the aircraft model can be generated in accordant with design geometry and configuration inputs. However, in order to build such a model correctly corresponding to the baseline configuration created previously, and also to provide flexibility for aircraft's components to be freely allocated within certain limits, the packaging of aircraft system and its associated constraints must be developed. This chapter will focus on how the packaging of the aircraft model are generated from the design parameter inputs as well as the modelling of internal components, whereas the methods used for creating mathematical models of the airframe surface and variable-shaped components will be described in the next chapter.

4.1 UCAV

The modelling of UCAV's airframe and the packaging of the system are developed primarily based on the dimensions of its internal components and their allocation within the aircraft according to the baseline configuration. This is to provide the flexibility of model generation as well as to reduce the number of individual design parameter uses preventing incoherent input values and hence reducing the chance of the internal components to violate the airframe and local constraints. For these reasons, it would be more appropriate to describe how the dimensional specifications of the aircraft's internal components together with the modelling of their allocated spaces in the airframe before proceeding to the packaging of the UCAV.

For design simplicity, the spaces allocated for weapon bays and APU are represented by rectangular box models as depicted in Figure 4.1, while their physical properties are considered as part of the design requirements and thus are specified as input parameters.

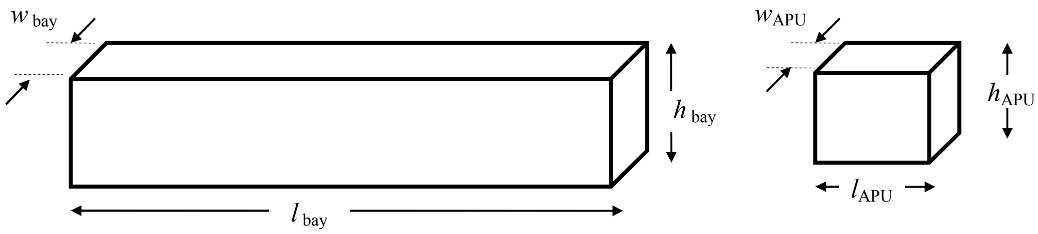

Figure 4.1: Modelling of the weapon bay (left) and APU (right)

The dimensions of the engine and the undercarriage are primarily determined by an estimated design weight of the aircraft and its product of the thrust requirement obtained from the initial sizing and T/W - W/S analysis. Therefore, the following evaluation methods are applied to correctly compute and optimise these components'dimensions and hence ensuring operational feasibilities of the aircraft. Note that for any equations described below, the design variables mentioned in the formulae are specified as input parameter unless they are carried out from previous evaluations or exceptionally stated.

4.1.1 Engine

In order to size the engine's dimensions or to select a suitable manufactured engine for designing a certain aircraft, an uninstalled thrust parameter is needed. This uninstalled thrust can be found from the maximum thrust requirement including thrust losses due to engine installation. These losses occur as a result of the following factors, inlet pressure recovery, engine bleed, power extraction and nozzle performance. Since the fraction values of these losses are approximately constant for a certain type of engine installation, a simplified equation suggested in the Aerospace Vehicle Design course [65] shown below is deemed to be adequate for correcting the maximum thrust requirement to the uninstalled value.

$$T_{\text{en}} = T_{\max} \cdot (1 + c_{\text{ram}} \cdot \left[\left(\frac{P_1}{P_0} \right)_{\text{ref}} - \left(\frac{P_1}{P_0} \right)_{\text{actual}} \right] + c_{\text{bleed}} \cdot mf_{\text{bleed}} + f_{\text{pow}} + f_{\text{noz}}) \qquad (4.1)$$

where,

T_{en} - Uninstalled thrust

$T_{\max}$ - Maximum thrust

c_{ram} - Ram recovery correction factor ≈ 1.2 -1.5

c_{bleed} - Bleed correction factor ≈ 2.0

mf_{bleed} - Bleed mass flow ≈ 1-5 %

f_{pow} - Thrust loss due to power extraction ≈ 1-3 %

f_{noz} - Thrust loss due to nozzle performance ≈ 1-3 %

P_1 / P_0 is the pressure recovery ratio in which its uninstalled reference value may be ideally assumed as 1. And due to the long S-shaped configuration of the intake diffuser, the actual value of P_1 / P_0 suggested by Mattingly [21] is 0.94.

Since it is desirable to obtain the engine's dimensions which optimally reflect given values of the uninstalled thrust and other specification requirements, selecting the data from existing off-the-shelf engines is not a suitable approach. This is due to the difficulty of finding an engine which precisely fits the requirements, and hence results the one with greater specifications being used instead. For this reason, it was decided that the engine would be developed specifically according to the UCAV's requirements. Thus, the engine size's prediction method developed by Whittle [50] for low-bypass ratio engine configurations is applied to the UCAV case as follows.

$$d_{en} = \sqrt{\frac{\dot{m}}{132}} \tag{4.2}$$

$$l_{en} = 3.77 \cdot d_{en}^{\;0.7911} \cdot (1 + BPR)^{-0.4729} \tag{4.3}$$

$$W_{en} = 472.5 \cdot l_{en}^{\;0.8278} \cdot d_{en}^{\;0.5754} \cdot (1 + BPR)^{-0.095} \tag{4.4}$$

where,

$\dot{m}$	- Engine mass flow rate at maximum sea-level Mach number (kg/s)
d_{en}	- Engine diameter (m)
l_{en}	- Engine length (m)
W_{en}	- Engine weight (kg)

The mass flow rate $\dot{m}$ required in Eq. (4.2) can be obtained from an evaluation of engine performance analysis at sea-level operating conditions, while such methods applied are described in section 8.1. The above engine dimension parameters can be used for accurately modelling the component as a cylinder with tapered nozzle as depicted below.

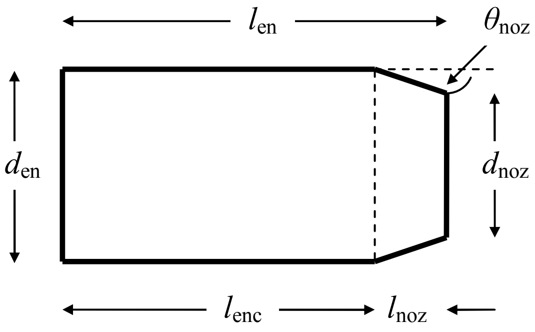

$$d_{noz} = \lambda_{noz} \cdot d_{en} \tag{4.5}$$

$$l_{noz} = \frac{d_{noz}}{2} \tag{4.6}$$

$$\theta_{noz} = \tan^{-1}\left(\frac{d_{en} - d_{noz}}{2 \cdot l_{noz}}\right) \tag{4.7}$$

Figure 4.2: Mathematical model of the engine

where,

λ_{noz}	- Nozzle taper ratio	θ_{noz}	- Nozzle taper angle

For a certain iteration of the design synthesis evaluations, the engine's physical properties would remain unchanged throughout the process; however, once more-refined takeoff weight value is used in subsequent iterations, the maximum thrust required and hence the predicted engine dimensions will be altered accordingly. Due to the above continuous input changes, this engine sizing approach is more suitable for this design synthesis compared to the off-the-shelf engine selection method.

4.1.2 Undercarriage

The sizes of the undercarriages are governed by their wheel-assembly configuration and the associated tire dimensions. Nonetheless these two factors are also interconnected, e.g. for a certain amount of load bearing, single-wheel undercarriages generally require a large tire size resulting the demand of fuselage's thickness for internal storage. On the other hand, two smaller tires may be used in a dual-wheel configuration to reduce this thickness needed while increasing the total width requirement instead. A numerical method for sizing the undercarriage dimensions has been developed based on the evaluation approach suggested in the Aerospace Vehicle Design course [65]. In order to estimate or select appropriate tire specifications for each undercarriage, the static load per wheel must be determined first using the equation below.

$$W_W = \frac{1.07 \cdot W_0 \cdot LP}{N_{\mathrm{st}} \cdot N_{\mathrm{wh}}} \tag{4.8}$$

where,

W_W	- Static load per wheel (lb)	W_0	- Maximum takeoff weight (lb)
N_{st}	- Number of associated struts	N_{wh}	- Number of wheels per strut
LP	- Static load proportion		

Eq. (4.8) is applied to the nose and the main undercarriages separately according to their corresponding wheel configuration. From the baseline design considerations of the UCAV, it was decided that a tri-cycle undercarriage arrangement with two-wheel support per strut was deemed to be sufficient for sustaining the aircraft weight; therefore, N_{wh} and N_{st} are applied to the above equation accordingly. The 1.07 factor applied to the above equation is the tire safety factor suggested by Raymer

[47]. The static load proportion LP may be initially assumed with an optimal ratio of 0.08 and 0.92 for the nose and the main undercarriages respectively. However, the undercarriage positions allocated to achieve such an optimal proportion may not be feasible due to the airframe constraints or the stability issues. Therefore, the LP values will be also calculated as the output from the design synthesis. For the nose undercarriage, the static load result must be compared for the maximum with the dynamic braking load evaluated using Eq. (4.9).

$$W_{W\,d} = \frac{10 \cdot z_{\mathrm{CG}} \cdot W_0}{g \cdot B_{\mathrm{wh}} \cdot N_{\mathrm{wh}}} \tag{4.9}$$

where,

$W_{W\,d}$	- Dynamic breaking load (lb)	B_{wh}	- Wheel base
z_{CG}	- Aircraft c.g. height	g	- gravitational constant

Once W_W values for each undercarriage have been found, the statistical equations suggested by Raymer [47] are used for predicting the tire dimensions. Since the constant values in Eq. (4.10) and Eq. (4.11) vary for different categories of the aircraft, the values of jet fighter/trainer category are considered to be reasonably appropriate for the UCAV case on account of their close weight and physical properties. The ground contact area produced by the tire dimensions, evaluated using Eq. (4.12), is necessary for the subsequent estimation of wheel spacing.

$$d_{\mathrm{ty}} = 1.59 \cdot {W_W}^{0.302} \tag{4.10}$$

$$w_{\mathrm{ty}} = 0.098 \cdot {W_W}^{0.467} \tag{4.11}$$

$$A_p = 2.3 \cdot \sqrt{w_{\mathrm{ty}} \cdot d_{\mathrm{ty}}} \cdot \left(\frac{d_{\mathrm{ty}}}{2} - R_r \right) \tag{4.12}$$

where,

d_{ty}	- Tire diameter (in)	w_{ty}	- Tire width (in)
A_p	- Tire contact area (in^2)	R_r	- Rolling radius factor

Another important parameter which is necessary for evaluating the minimum wheel space requirement for multi-wheel undercarriage configuration is an equivalent single wheel load (ESWL). This can be determined using the graphical data of load classification number (*LCN*) for various combinations of tire pressure and wheel load provided by International Civil Aviation Organisation [58]. Although the ESWL result can be found easily by analysing the charts manually, due to the necessity of the design synthesis methodology to accommodate computational implementation, any manual intervention during the computation is not desirable. Also in order to minimise the complexity of the codes involved in the graphical analysis process, the above chart data have been converted into numerical equations shown below via the use of a regression analysis program called 'Datafit'.

$$L_1 = 0.1456 \cdot P_{\inf} + 0.798 \tag{4.11}$$

$$L_2 = 0.8323 \cdot P_{\inf} + 3.422 \tag{4.12}$$

$$\mathrm{ESWL} = 15 \cdot LCN^{1.2} P_{\inf}^{-0.77} \qquad , \; L_1 \leq \mathrm{ESWL} \leq L_2 \tag{4.13}$$

where,

$P_{\inf}$ - Inflation pressure (lb/ in^2) LCN - Load classification number

ESWL - Equivalent single wheel load (lb)

The minimum lateral wheel space required for a dual-wheel undercarriage can be determined using the ESWL assessment curves also provided by the previous reference [58]. Eq. (4.12) has been developed from these graphical plots using the same program as above. Since the original ESWL assessment curves were created based on rigid runway pavement, the radius relative stiffness L_{rs} value applied in the wheel spacing equations shown below is 34.4 inches.

$$\begin{aligned} \frac{S_t}{L_{rs}} &= 5.156 + 0.427\ln(x_1) + 0.125\ln(x_1)^2 + 0.031\ln(x_1)^3 + 0.004\ln(x_1)^4 \\ &\quad -15.707x_2 + 19.465{x_2}^2 - 10.218{x_2}^3 + 2.089{x_2}^4 \end{aligned} \tag{4.12}$$

when, $$x_1 = \frac{N_{\mathrm{wh}} \cdot A_p}{{L_{rs}}^2} \tag{4.13}$$

$$x_2 = \frac{N_{\text{wh}} \cdot W_W}{\text{ESWL} \times 1000} \tag{4.14}$$

where,

S_t	- Lateral wheel space (in.)	L_{rs}	- Radius of relative stiffness (in)

With the tire dimensions and the minimum lateral wheel space acquired, the size of the undercarriage's wheel-assembly model can now be approximated. For the strut model, oleo shock absorber's dimensional specifications are used for considering the minimum size of the component. The oleo dimensions can be calculated using the following equations.

$$stk = \frac{6 \cdot {V_V}^2}{g \cdot \eta \cdot N_g} - \frac{\eta_t}{\eta} \cdot \left(\frac{d_{\text{ty}}}{2} \cdot (1 - R_r) \right) + 1 \tag{4.15}$$

$$sd_{\text{ol}} = \frac{2}{3} \cdot stk \tag{4.16}$$

$$l_{\text{ol}} = 2.5 \cdot stk \tag{4.17}$$

$$d_{\text{ol}} = 0.04 \cdot f_{STR} \cdot \sqrt{N_{\text{wh}} \cdot W_W} \tag{4.18}$$

where,

stk	- Stroke (in)	sd_{ol}	- Oleo static deflection (in)
l_{ol}	- Oleo length (in)	d_{ol}	- Oleo diameter (in)
f_{STR}	- Structural thickness factor	V_V	- Touch-down sink speed (ft/s)

According to JAR-25, the maximum sink speed for landing is 10 ft/s which can be applied to the V_V value. The f_{STR} parameter is included in Eq. (4.18) to account for an external oleo structure into the diameter result and the approximated value of 1.2 is recommended. Also the values of other associated parameters in Eq. (4.15) may be specified as follows.

η	- Shock absorber efficiency ≈ 0.65 - 0.90
η_t	- Tire efficiency = 0.47
N_g	- Gear load factor ≈ 2.7 - 3.0

Although the above d_{ol} value can be directly used for representing the diameter of the actual strut, this is not the case for l_{ol}. The l_{ol} value itself only provides the minimum length requirement of the strut model which must be considered with other criteria. As far as the design synthesis operation is concerned, the strut length evaluation contains two phases concerning the geometry and the operational requirements of the undercarriage. In the first phase, which is focused in this modelling section, the total length of the strut is determined according to various geometry attributes such as the aircraft's height clearance from the ground, the internal height to the pivot point, and the static oleo deflection. For the purpose of modelling the storage bays for the undercarriages, the strut length is calculated based on the space allocation within the fuselage rather the individual component's dimension. The space allocated for the entire undercarriage is modelled as a combination of rectangular boxes consisting of the strut and the wheel-assembly parts as illustrated in Figure 4.3.

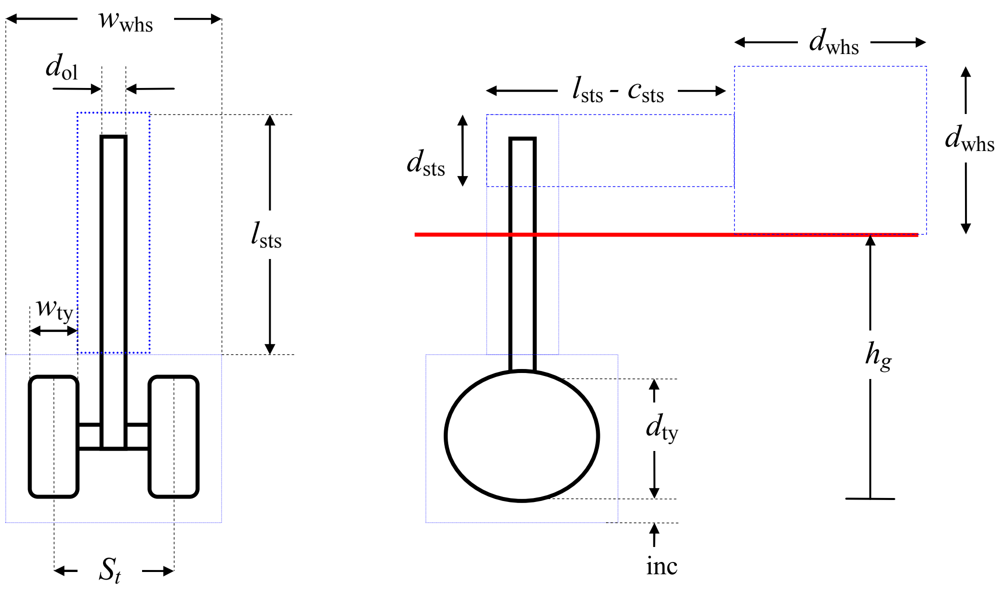

Figure 4.3: Modelling of UCAV's undercarriage storage bay

Wheel section

$$d_{\text{whs}} = d_{\text{ty}} + 2 \cdot \text{inc} \tag{4.19}$$

$$w_{\text{whs}} = d_{\text{ol}} + 2 \cdot \left(w_{\text{ty}} + 2 \cdot \text{inc}\right) \quad , \text{if } d_{\text{ol}} > S_t - w_{\text{ty}} \tag{4.20}$$

$$w_{\mathrm{whs}} = S_t + 2 \cdot \left(\frac{w_{\mathrm{ty}}}{2} + 2 \cdot \mathrm{inc} \right) \quad \text{, otherwise} \qquad (4.21)$$

Strut section

$$d_{\mathrm{sts}} = d_{\mathrm{ol}} + 2 \cdot \mathrm{inc} \qquad (4.22)$$

$$c_{\mathrm{sts}} = x_{\mathrm{com}} \cdot sd_{\mathrm{ol}} \qquad (4.23)$$

Nose undercarriage:

$$l_{\mathrm{sts}} = h_g - d_{\mathrm{whs}} + sd_{\mathrm{ol}} + \frac{d_{\mathrm{sts}}}{2} \quad \text{, if } h_g > l_{\mathrm{ol}} - sd_{\mathrm{ol}} - \left(\frac{d_{\mathrm{sts}} - d_{\mathrm{whs}}}{2} \right) \qquad (4.24)$$

$$l_{\mathrm{sts}} = l_{\mathrm{ol}} - \frac{d_{\mathrm{whs}}}{2} \quad \text{, otherwise} \qquad (4.25)$$

Main undercarriage:

$$l_{\mathrm{sts}} = h_g + sd_{\mathrm{ol}} - \frac{d_{\mathrm{whs}}}{2} \quad \text{, if } h_g > l_{\mathrm{ol}} - sd_{\mathrm{ol}} \qquad (4.26)$$

$$l_{\mathrm{sts}} = l_{\mathrm{ol}} - \frac{d_{\mathrm{whs}}}{2} \quad \text{, otherwise} \qquad (4.27)$$

where,

inc	- Internal clearance	h_g	- Minimum height clearance
c_{sts}	- Compressed length	x_{com}	- Strut compression factor

subscript:

whs	- Wheel model	sts	- Strut model

As far as the wheel model is concerned, the evaluation of its total width is separated into two different conditions as depicted by Eq. (4.20) and Eq. (4.21). This is to verify whether a normal close assembly of given wheel and strut dimensions already provides sufficient lateral wheel space that satisfies the load distribution requirement. If that is not the case then the evaluated wheel space value would be appropriately accounted in the calculation. A similar verification regarding the undercarriage height criteria, shown from Eq. (4.24) to Eq. (4.27), is also applied to the length of the strut model. This is to measure whether the wheel-assembled oleo length can sufficiently accommodate the minimum height clearance including the internal space measured from the aircraft's bottom surface to the actual pivot point of the strut. Due to the variation of local fuselage depths, different assumptions of the internal strut length for the nose and the main undercarriages are used, thus resulting separated sets of equations. Also it is desirable to increase the flexibility of the undercarriage locations within the limited fuselage space; therefore, a strut compression is applied during the storage to slightly decrease the overall length of the undercarriage model.

The second phase of the above strut length evaluations focuses on various field operational requirements of the undercarriages, e.g. rake angle, taildown angle and track limitations, which will be verified and increase the length of the strut model if necessary. Furthermore, the strut length of the nose undercarriage will be adjusted to match the overall main undercarriage's height measured from the ground for static aircraft balance. Since these operational criteria require geometry specification data which can only be obtained from a complete model of the aircraft, these verification and amendment processes of the undercarriages are included in subsequent iterations of the design synthesis evaluation. This is in order to acquire the above necessary data computed in the previous design synthesis iteration and use them as an input for the current one.

4.1.3 Propulsion Ducts

As far as the design configuration of the UCAV is concerned, the dimensions of the propulsion ducts (i.e. intake diffuser and exhaust pipe) greatly influence the overall size of the fuselage as well as playing an important role in defining the locations of fuselage stations. In general, the configurations of these duct components are an S-shaped vertical deflection and cross-sectional area transformation. In contrast to the previous dimensional sizing of the engine and the undercarriages, there is no absolute performance requirement which would directly influence the size of the propulsion ducts. Neither their geometry specifications can be independently input in a similar manner to the weapon bay and the APU due to their association with the size of the engine. For these reasons, the majority of the parameters used for generating the duct models are specified as a function of the engine's dimensional properties.

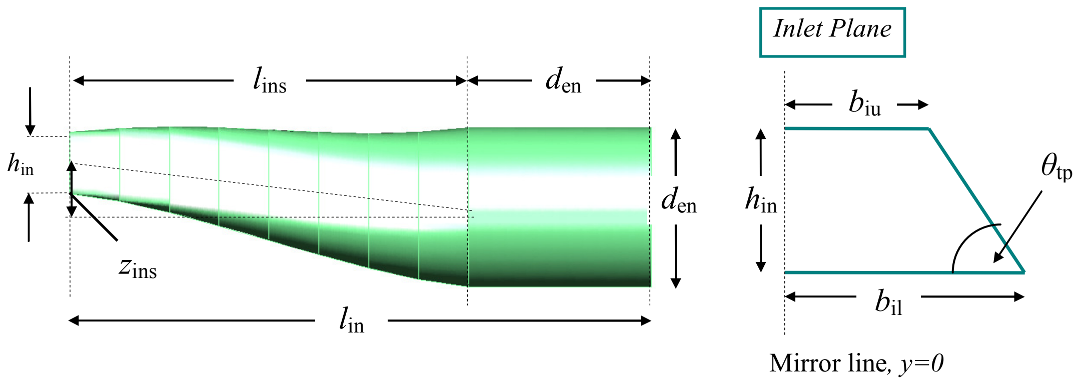

Figure 4.4: Geometry of the intake diffuser model

From the above figure (left), the side-view geometry of the intake diffuser contains two sections, the variable shaped and the straight uniform sections. The uniform duct section toward the engine compressor is required to prevent inlet-flow distortion which can stall the engine while the minimum length of the section is equal to the engine diameter d_{en}. The length of the transformation section l_{ins} is determined as a function of the engine length l_{en} as shown in Eq. (4.32). The height difference between the centres of the inlet and the engine z_{ins} depends on the maximum deflection angle allowed at any points along the diffuser's length.

$$l_{\text{ins}} = R_{LIC} \cdot l_{\text{en}} \tag{4.32}$$

$$l_{\text{in}} = l_{\text{ins}} + d_{\text{en}} \tag{4.33}$$

$$z_{\text{ins}} = l_{\text{ins}} \cdot \frac{2}{\pi} \cdot \tan(\theta_{\text{sd}}) \tag{4.34}$$

where,

R_{LIC} - Ratio between the lengths of the intake diffuser and the engine

θ_{sd} - Maximum deflection angle of the duct

The cross-sectional area of the intake diffuser at the inlet plane, illustrated on Figure 4.4 (right), features symmetrical trapezium geometry which would gradually change into a circular shape with the diameter of the engine toward the end of the intake diffuser's transformation section. This trapezium edge alignment of the duct at the inlet plane is developed for stealth design purposes. The geometry specifications of the above inlet cross-section are evaluated based on the engine's frontal area and non-dimensional geometry parameters of the trapezium as shown below.

$$b_{\text{il}} = \sqrt{\frac{AR_{\text{in}} \cdot R_{IC} \cdot \pi \cdot \left(\frac{d_{\text{en}}}{2}\right)^2}{(1+R_{\text{ib}})^2}} \tag{4.28}$$

$$b_{\text{iu}} = b_{\text{il}} \cdot R_{\text{ib}} \tag{4.29}$$

$$h_{\text{in}} = (b_{\text{il}} + b_{\text{iu}}) \cdot AR_{\text{in}} \tag{4.30}$$

when, $$R_{\text{ib}} = \frac{1 - 0.5 \cdot AR_{\text{in}} \cdot \tan(\theta_{\text{tp}})}{1 + 0.5 \cdot AR_{\text{in}} \cdot \tan(\theta_{\text{tp}})} \tag{4.31}$$

where,

R_{IC} - Area ratio between the inlet and the engine

AR_{in} - Inlet aspect ratio

θ_{tp} - Trapezium angle

The geometry specifications of the exhaust pipe model are developed using the same approach as the intake diffuser with the primary difference of the cross-sectional area transformation being reverse to circle-to-trapezium. Also the uniform duct region is set toward the exhaust plane where the section length is assumed to have the same value as the exhaust cross-section height. A list of equations applied for evaluating the exhaust pipe model's specifications can be found in Appendix A.1.

4.1.4 Fuselage

The packaging of internal component models within the fuselage airframe are carried out according to the longitudinal fuselage stations, in which from the modelling point of view, these are specified primarily for the purpose of transitioning different sets of mathematical modelling equations applied to generate variations of the fuselage's cross-sections. In general, the locations of the fuselage stations are determined by the positions of large-scale internal components such as the intake diffuser, engine and exhaust pipe, because they induce drastic changes in the shape of the overall fuselage's cross-section and thus the modelling equations needed, in order to accommodate such items. On the other hand, the remaining internal components such as undercarriages, payload compartments and APU, also use the fuselage stations as boundary constraints or reference positions for component allocation purposes.

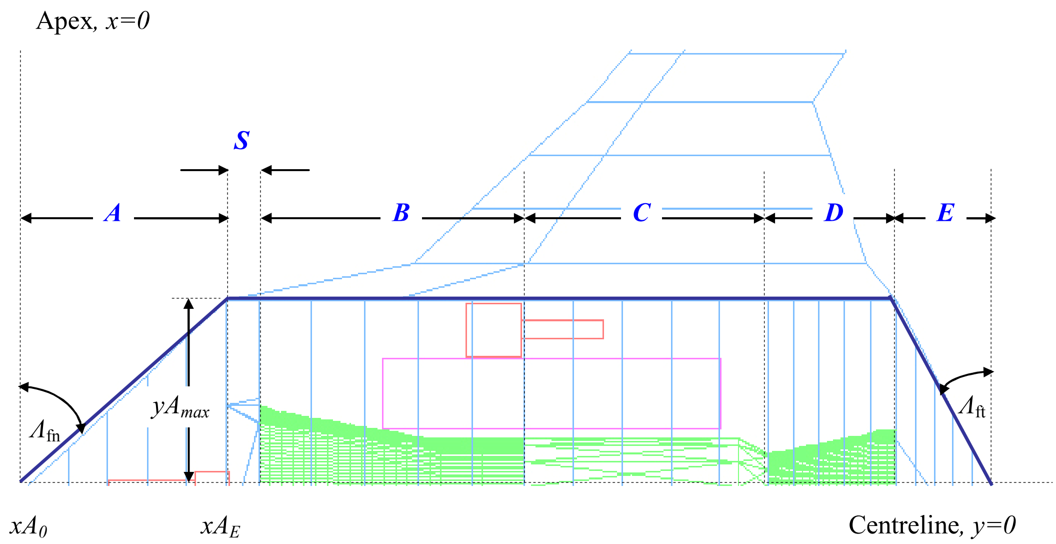

Figure 4.5: Fuselage station diagram of UCAV

Figure 4.5 depicts the longitudinal fuselage stations of the UCAV model in the planform view. Stations *B*, *C* and *D* together are considered as the fuselage's centre body, in which the distances between stations are directly determined by the lengths of the intake diffuser, engine and exhaust pipe respectively. Stations *A* and *E* represent the nose and the tail sections of the fuselage where the station lengths are specified as a function of the maximum width of the fuselage and their corresponding sweep angles of Λ_{fn} and Λ_{ft}. The maximum fuselage width at station *A*, denoted as $yA_{\max}$, can be calculated from the lateral dimensions of the packaging internal components and their arrangement according to the baseline configuration as shown in Eq. (4.32). Also as far as the planform geometry of fuselage is concerned, it is clear that the above maximum fuselage width value remains constant from the end of the station *A* to station *D*, thus

$$yA_{\max} = \frac{d_{\mathrm{en}}}{2} + w_{\mathrm{fw}} + w_{\mathrm{bay}} + w_{\mathrm{mgw}} + 3 \cdot \mathrm{inc} \tag{4.32}$$

$$xA_E = yA_{\max} \cdot \tan(\Lambda_{\text{fn}}) + xA_0 \tag{4.33}$$

where,

w_{fw} - Engine firewall thickness

w_{bay} - The width of weapon bay

w_{mgw} - The width of main-undercarriage wheel model

The xE_E station coordinate, which basically represents the overall length of the fuselage itself, can be calculated using a similar equation form to Eq. (4.33) once its starting station coordinate of xE_0 is found from an accumulated length of all prior fuselage stations. The remaining station *S* is included for the purpose of bridging the gap between the stations *A* and *B* since the intake diffuser (i.e. station *B*) cannot be allocated immediately after the xA_E due to the stagger distance required for inlet sheath plate integration. This stagger length is formulated as a function of the inlet cross-section height as shown below.

$$l_{\text{stg}} = \frac{h_{\text{in}}}{\tan(\theta_{\text{stg}})} \tag{4.34}$$

where,

l_{stg} - Stagger length of the intake diffuser

θ_{stg} - Longitudinal stagger angle

The fuselage-wing fairing area covers from the end of the station *A* to station *D* as illustrated in Figure 4.6. Due to the difference between the fuselage and the wing modelling structures, some model discontinuities may occur at the bridge point. For this reason, the thickness of the side fuselage has been developed in such a way that it would be evaluated from an interpolation of selected aerofoil’s coordinate in accordant with the total chord length of the fairing area shown in Eq. (4.35). Due to this aerofoil-interpolated side fuselage, it is reasonable to assume that any slight discontinuities remain at the bridge point are negligible, and so does the associated aerodynamic interference.

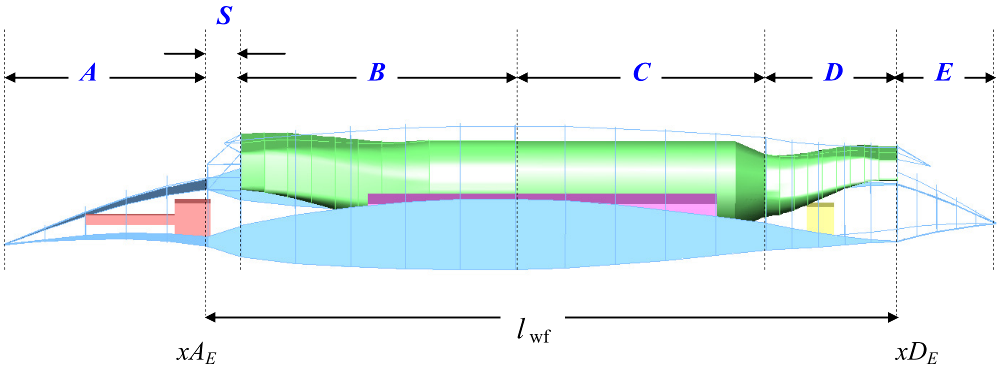

Figure 4.6: Side-view of UCAV's fuselage model

$$l_{\rm wf} = l_{\rm stg} + l_{\rm in} + l_{\rm en} + l_{\rm ex} \tag{4.35}$$

Theoretically, the aerofoil interpolation of the side fuselage at xA_E, i.e. the first aerofoil coordinate, would yield zero magnitude of thickness; however, it is desired for the station *A* to gain sufficient internal space for accommodating the nose undercarriage, and also for smooth interpolation transition of an aerofoil shape, the above thickness parameter is approximated as presented in Eq. (4.36).

$$zA_s = 2 \cdot r_{LE} \cdot l_{\rm wf} \tag{4.36}$$

where,

zA_s - The thickness of the side fuselage at the end of station *A*

r_{LE} - Leading-edge radius of a selected aerofoil.

As far as the location constraints of other internal components are concerned, the position of the nose undercarriage is limited within stations *A* and *S*. The main undercarriage and the weapon bay are allowed to be allocated in both stations *B* and *C*, while the APU is allocated in station *D* under the exhaust pipe. The components are free to move longitudinally within these fuselage station constraints as long as the internal space is permitted and the local airframe surfaces are not violated. The allocation of these internal components is performed based on aircraft's c.g. balance considerations with an assistance of automated algorithm which will be described in the next chapter.

In general, the geometry specifications of fuselage cross-sections are initiated from the station A where the parameters are calculated from the dimensions of the intake diffuser and various criteria of other internal components.

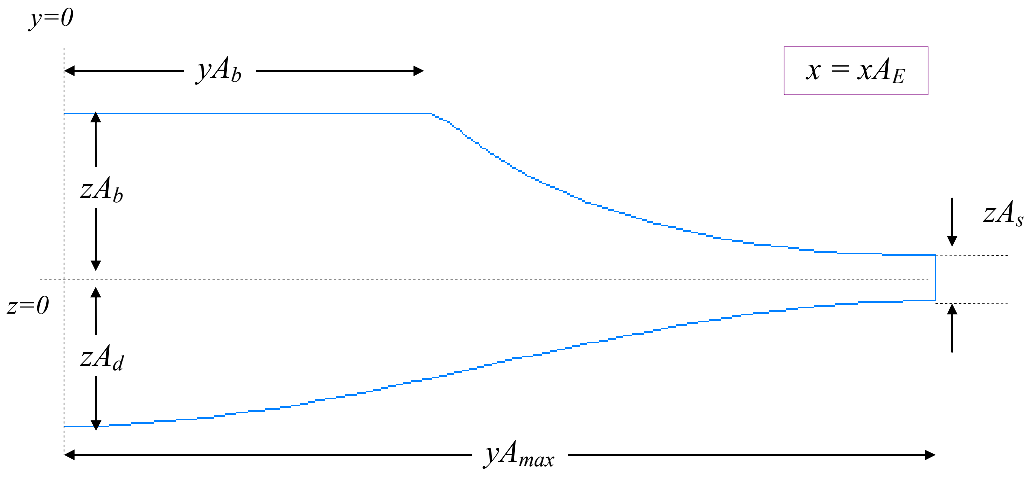

Figure 4.7: fuselage cross-section model at the end of station A

From Figure 4.7, the evaluations of zA_s and $yA_{\max}$ have been described earlier. The fuselage base on the upper surface, denoted as yA_b, is developed to support the inlet geometry of the diffuser (see Figure 4.4) in the subsequent station, thus $yA_b = b_{\text{il}}$. The height of this fuselage base measured from the centreline zA_b depends on the vertical location of the engine z_{en} which is initially set at $z = 0$. Hence, from the same Figure 4.4 (right), $zA_b = z_{\text{ins}}$. However, in order to maintain appropriate shape of the cross-sections along the fuselage length, the fuselage's thickness at the centre should not be less the side. For this reason, the maximum thickness of the side fuselage is accounted in the zA_b evaluation and adjusts the value of z_{en} if necessary.

$$zA_b = z_{\text{tm}},\; z_{\text{en}} = z_{\text{tm}} - z_{\text{ins}} \qquad \text{, if } z_{\text{tm}} > z_{\text{ins}} \qquad (4.37)$$

$$zA_b = z_{\text{ins}},\; z_{\text{en}} = 0 \qquad \text{, otherwise} \qquad (4.38)$$

when, $$z_{\text{tm}} = \frac{1}{2} \cdot tc \cdot l_{\text{wf}} \qquad (4.39)$$

where,

tc - Maximum thickness of aerofoil

The bottom depth of the fuselage zA_d takes multiple constraints of the internal components into consideration and compares for the maximum zA_d value required in order to entirely accommodate all of the items.

$$zA_d = \max\left[(z_{\mathrm{tm}}),\left(\frac{h_{\mathrm{mgw}}}{2}\right),\left(\frac{d_{\mathrm{en}}}{2}+w_{\mathrm{fw}}-z_{\mathrm{en}}\right),\left(\frac{3}{2}\cdot d_{\mathrm{ngw}}-zA_b\right)\right]+\mathrm{inc} \tag{4.40}$$

where,

h_{mgw} - The height of main-undercarriage wheel model

d_{ngw} - The diameter of nose-undercarriage wheel model

The rest of the fuselage stations utilise the above cross-section geometry parameters specified for the station A to generate their own variations. Generally, the same type of the parameters, e.g. zB_b, zC_b and zD_b, are determined according to their prior station values or any definite constraints in other nearby fuselage stations. Nonetheless, additional parameters are also included in certain fuselage stations to accommodate different internal component constraints, providing smooth transition between stations as well as increasing the modelling flexibility. The equations and their evaluation sequences used for determining the cross-section geometry parameters of the remaining fuselage stations can be found in Appendix A.2.

4.1.5 Wing

As described previously in the baseline configuration, the UCAV wing consists of four following partitions; the fairing, inboard-wing, outboard-wing and pointed tip as illustrated in Figure 4.8. Similarly to the maximum thrust evaluation, the estimated design weight and the wing loading parameters together provide the result of the wing reference area required for the UCAV design. And for a given value of wing aspect ratio AR, the total wing span of the aircraft can be found from Eq. (4.41) below.

$$b_W = \sqrt{S_W \cdot AR} \tag{4.41}$$

where,

b_W - Wing span S_W - Reference wing area

Although structural wise, the UCAV wing configuration contains four partitions in total, the pointed tip exists primarily for the purpose of stealth airframe alignment. Due to its taper ratio λ_3 of zero, the aerodynamic performance produced by the partition itself would be undoubtedly poor if typical aerodynamic calculations were applied. And this would result incorrect equivalent geometry of the entire wing if such a partition were taken into performance calculations. For this reason, it was decided that the effective wing span of the UCAV would be measured from the fuselage centreline to the end of the outboard-wing partition only. The fairing partition, on the other hand, has been developed for the purposes of smoothly bridging and adjusting the aerofoil-shaped fuselage's side to the inboard-wing partition. Therefore, as long as the span of the fairing partition is relatively small, its aerodynamic contribution can be excluded from the effective wing area, and thus the reference geometry of the inboard-wing partition can be established directly to the centreline of the UCAV as shown in the Figure 4.8.

Regardless of the finalised wing configuration, the overall wing geometry should reflect approximately the same reference area as that evaluated using Eq. (4.41) satisfying the wing loading requirement. Therefore, in order to avoid the wing geometry being over constrained while maintaining the flexibility of configuration generations at the same time; the design input parameters used for developing such component are considered based on their influence and necessity in determining the entire wing configuration. Thus, the leading-edge sweep Λ_{LE} for every wing partition as well as the non-dimensional geometry parameters of the fairing and the inboard-wing partitions, such as taper and span ratios, are selected for this purpose.

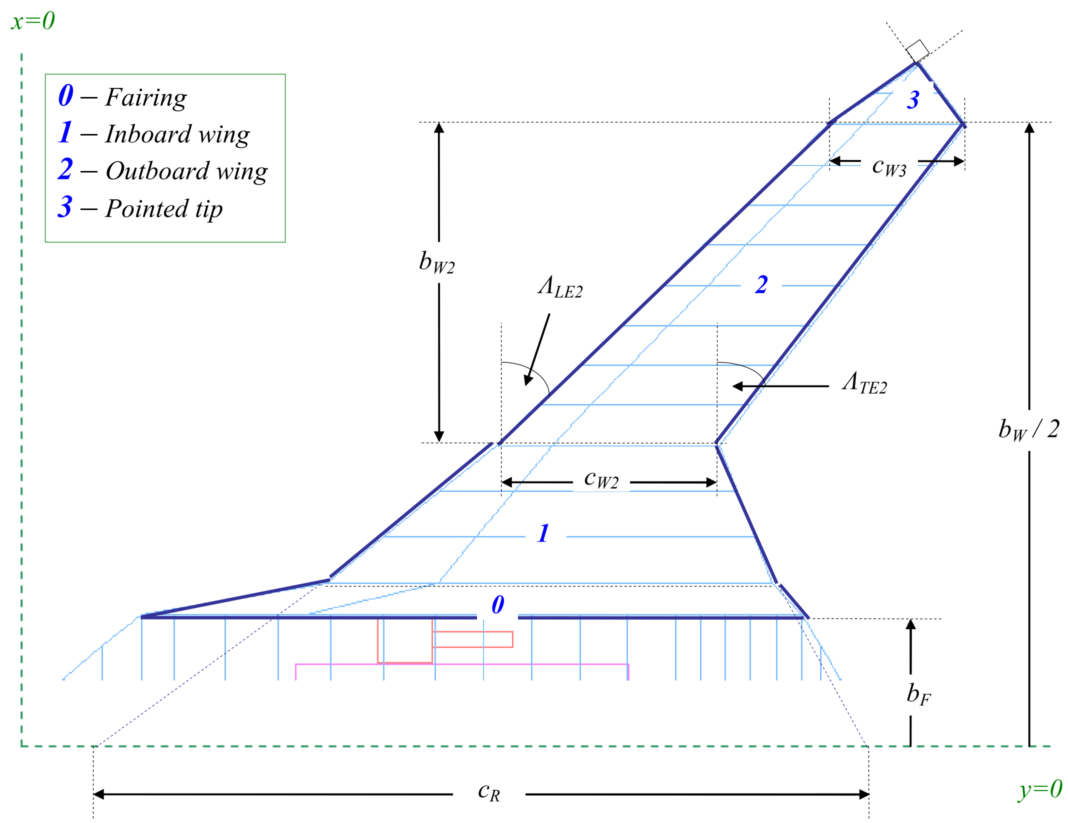

Figure 4.8: UCAV wing-geometry model

The evaluations of planform wing geometry parameters, e.g. main chord, span ratios and taper ratios, are conducted from the fairing toward the outboard. The main chord of the fairing partition is equal to length of the side fuselage i.e. $c_{W0} = l_{\mathrm{wf}}$, while other wing geometry parameters of the same partition are determined as follows,

$$b_{W0} = Rw_F \cdot b_F \tag{4.42}$$

where,

Rw_F - Ratio of the fairing span relative to the fuselage width

$$\Lambda_{TE0} = \tan^{-1}\left(\frac{c_{W0} \cdot (\lambda_0 - 1) + b_{W0} \cdot \tan(\Lambda_{LE0})}{b_{W0}}\right) \tag{4.43}$$

The fuselage width b_F required in Eq. (4.42) is correspondent to the $yA_{\max}$ value calculated previously in the fuselage section. Eq. (4.43) is also applied to the trailing-edge sweep evaluation in other wing partitions using their associated parameters unless specified. Similarly, Eq. (4.44) is adopted for calculating any current-partition tip chord, hence the main chord of the following partition toward the outboard.

$$c_{W1} = \lambda_0 \cdot c_{W0} \tag{4.44}$$

The values of b_F and its associated fairing span b_{W0} have been defined, thus the remaining span for the inboard-wing and the outboard-wing partitions can be divided according to the span-ratio parameter Rw_{IR} as shown below.

$$b_{W1} = \left(\frac{b_W}{2} - b_F - b_{W0} \right) \cdot Rw_{IR} \tag{4.45}$$

$$b_{W2} = \left(\frac{b_W}{2} - b_F - b_{W0} \right) \cdot (Rw_{IR} - 1) \tag{4.46}$$

where,

Rw_{IR} - Ratio of the inboard-wing span to the total remaining span

Once Λ_{TE1} has been calculated from the applied Eq. (4.43), the reference root chord of the inboard-wing partition c_R, depicted in the Figure 4.8, can be evaluated using Eq. (4.47) below.

$$c_R = c_{W1} + (b_F + b_{W0}) \cdot [\tan(\Lambda_{LE1}) - \tan(\Lambda_{TE1})] \tag{4.47}$$

Since the total wing reference area S_W calculated at the beginning is the design requirement for developing the wing configuration, such a parameter is applied for evaluating the value of the outboard-wing taper ratio λ_2.

$$\lambda_2 = \left(\frac{S_W - S_I}{b_{W2} \cdot c_{W2}} \right) - 1 \tag{4.48}$$

when, $$S_I = (c_R + c_{W2}) \cdot (b_F + b_{W0} + b_{W1}) \tag{4.49}$$

Despite a major constraint of the wing reference area, the geometry evaluation method described above is still capable of producing various wing configuration results. Some of them, however, prove to be inappropriate such as small tapered or over size partition. This is primarily because the input values of the non-dimensional wing parameters i.e. λ_0, λ_1 and Rw_{IE} are not reasonable for a given reference wing area. Therefore, in order to ensure that the wing configuration produced is practically feasible, the above non-dimensional parameters need to be verified and adjusted within appropriate taper-ratio constraints as shown in the diagram below.

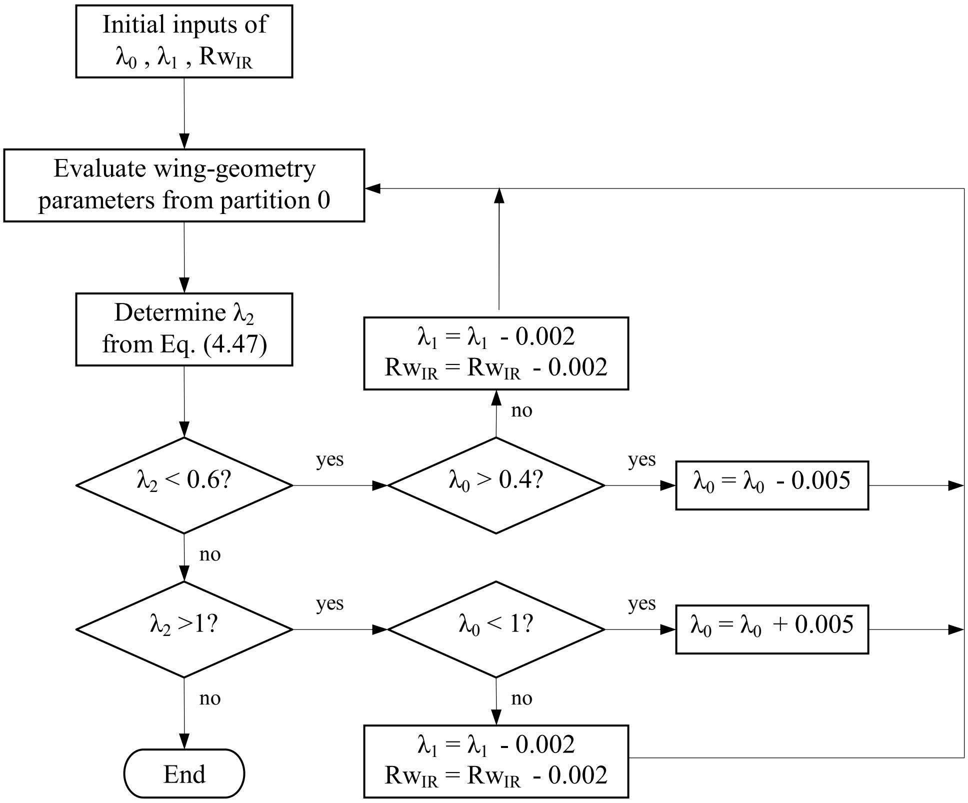

Figure 4.9: Wing configuration verification algorithm

Once the above wing partitions' configurations have been evaluated and verified, the remaining pointed-tip partition is then determined based on an assumption of perpendicular planform geometry, thus

$$b_{W3} = \frac{c_{W3}}{\tan(\Lambda_{LE3}) - \tan(\Lambda_{TE3})} \tag{4.50}$$

when, $$\Lambda_{TE3} = \Lambda_{LE3} - 90° \tag{4.51}$$

The flap control surfaces are located only on the inboard-wing and the outboard-wing partitions where their overall geometry configurations can be specified from spanwise flap positions and flap-to-chord ratio.

In the subsequent analyses of the designed aircraft in terms of both performance and physical property, the derived wing geometry parameters such as the mean aerodynamic chord mac and its spanwise location $\bar{y}$ are normally required in the evaluations. Also the partition area and the sweep angle at a certain position on the wing chord (denoted as S_{WS} and Λ_X respectively) will be required at some points. For a given wing-partition configuration, these parameters can be calculated using the equations provided below.

$$mac = \frac{2}{3} \cdot c_{WS} \cdot \left(\frac{1+\lambda+\lambda^2}{1+\lambda} \right) \tag{4.52}$$

$$\bar{y} = \frac{b_{WS}}{3} \cdot \left(\frac{1+2\cdot\lambda}{1+\lambda} \right) \tag{4.53}$$

$$S_{WS} = \frac{1}{2} \cdot c_{WS} \cdot (1+\lambda) \cdot b_{WS} \tag{4.54}$$

$$\Lambda_X = \tan^{-1}\left(\frac{b_{WS} \cdot \tan(\Lambda_{LE}) + (\lambda-1)\cdot c_{WS} \cdot xc}{b_{WS}} \right) \tag{4.55}$$

where,

xc - Relative position on the wing chord

subscript:

WS - Wing partition

Since certain performance analyses in particular the aerodynamic lift and stability require the use of single-partition wing configuration, equivalent geometry of the UCAV's wing must be applied in such cases. This equivalent wing can be developed by firstly evaluating mac of the reference inboard-wing and the outboard-wing partitions using Eq. (4.52) and then joining them together to create a new trapezium wing. The mac value of this trapezium wing will reflect that of the equivalent wing geometry. Afterward the same trapezium-wing generation is repeated using this mac

and the original outboard tip chord and then finally extend the developed trapezium sweeps to the fuselage's centreline to obtain the entire geometry of the equivalent reference wing. Although there may be slight differences between the geometry parameter values obtained from the equivalent and the actual wing configurations, it is commonly acceptable to neglect these minor changes due to the conversion.

4.2 Uninhabited Tanker

In general, the airframe packaging and the modelling of UCAV's internal components are directly adopted for using with the tanker. Despite their similar airframe designs, the majority of internal component configurations and the associated packaging within the fuselage are somehow different. Therefore, the methods applied previously for estimating various dimensional specifications of the UCAV's components are appropriately modified to meet the design requirements and the baseline configuration of the tanker.

4.2.1 Engine

The previous uninstalled thrust estimation and cylindrical engine modelling approaches are directly applied to the tanker. However, due to the aircraft requirement of higher bypass ratio engine, providing an advantage of lower specific fuel consumption in comparison to the low-bypass ratio designs, the engine sizing methods must be changed accordingly. The methods developed by Whittle [50] previously selected for the UCAV were calibrated on a basis of low-bypass ratio engines and hence they would not be appropriate for the tanker application. Also the conceptual methods for predicting the engine dimensions suggested by Raymer [47] produce rather inaccurate results compared to existing engine data. For these reasons, the following empirical equations have been created specifically for the tanker using Datafit program and appropriate engine data Jane's Aero-Engines [77].

$$d_{\text{en}} = 1.49\ln(T_{\text{en}}) + 13.74 \cdot BPR - 1.51 \cdot BPR^2 - 45.3 \tag{4.56}$$

$$l_{\text{en}} = (1.54 \times 10^{-9}) \cdot T_{\text{en}}{}^2 - (1.42 \times 10^{-4}) \cdot T_{\text{en}} - \frac{2.62}{BPR} + 6.83 \tag{4.57}$$

$$W_{\text{en}} = \left(0.1\ln(T_{\text{en}}) + 1.03 \cdot BPR - 1.13 \cdot BPR^2 - 3.34\right) \times 10^6 \tag{4.58}$$

The units of the parameters associated with the above equations are the same as the UCAV case with an exception of W_{en} unit being in lb instead of kg. Normally, the higher the bypass ratio, the greater the engine diameter. And due to the internal installation requirement of the tanker's engines, the engine data selected from reference [77] for generating the above equations range in the medium-high bypass ratio values between 4 and 6. Although it is possible to supply greater range of the bypass ratio engine data to develop these equations, the results obtained from such equations produce rather-significant errors in general due to non-linear relationships between the engine performances and their dimensional specifications.

4.2.2 Undercarriage

The methods used for sizing UCAV's undercarriages are adopted for the tanker case; nonetheless, some modifications have been made due to the differences of aircraft's tire sizing category and overall configuration layout of the main undercarriage. The constant values applied to the Eq. (4.10) and Eq. (4.11) for tire dimensions prediction are changed to those for the transport/bomber aircraft category according to the same reference [47] resulting the equations shown below.

$$d_{\text{ty}} = 1.63 \cdot W_W{}^{0.315} \tag{4.59}$$

$$w_{\text{ty}} = 0.1043 \cdot W_W{}^{0.798} \tag{4.60}$$

As far as the baseline configuration of the tanker is concerned, the nose undercarriage features the same dual-wheel layout as in the UCAV, while the tri-dual tandem configuration was selected for the main undercarriage due to the demand of a large weight support with an optimal tire size. Therefore, the minimum longitudinal space between wheel rows must be verified using the dual-tandem undercarriage data provided together with the previous ESWL assessment curves by reference [52]. The dual-tandem graphical data have been developed into a set of numerical equations depicted as follows.

$$\frac{S_b}{L_{rs}} = 3.52 - \frac{1.165}{x_3} - \frac{1.126}{x_4} + \frac{0.421}{x_3^{\,2}} + \frac{0.395}{x_4^{\,2}} - \frac{0.634}{x_3 \cdot x_4} - \frac{0.059}{x_3^{\,3}} - \frac{0.05}{x_4^{\,3}} + \frac{0.064}{x_3 \cdot x_4^{\,2}} + \frac{0.083}{x_3^{\,2} \cdot x_4} \tag{4.61}$$

when, $x_3 = S_t \cdot L_{rs}$ (4.62)

$$x_4 = 3.471 - \frac{2.624}{x_1} - 0.488\ln(2 \cdot x_2) + \frac{0.355}{x_1^{\,2}} + 0.003\ln(2 \cdot x_2)^2 + 0.955 \cdot \frac{\ln(2 \cdot x_2)}{x_1} \tag{4.63}$$

where,

S_b - Longitudinal wheel space (in.)

x_1 and x_2 are the results obtained from associated evaluations of Eq. (4.13) and Eq. (4.14) when $N_{\mathrm{wh}} = 2$. The modelling of tanker's undercarriage spaces is similar to the UCAV; however, due to the aforementioned differences of the main undercarriage configuration, the evaluations of the component's dimensions need to be changed accordingly. Furthermore, an initial estimation of tanker strut model's length is also modified to suit the side-retraction deployment scheme. The new equations developed from the packaging of the tanker's main undercarriage are presented below.

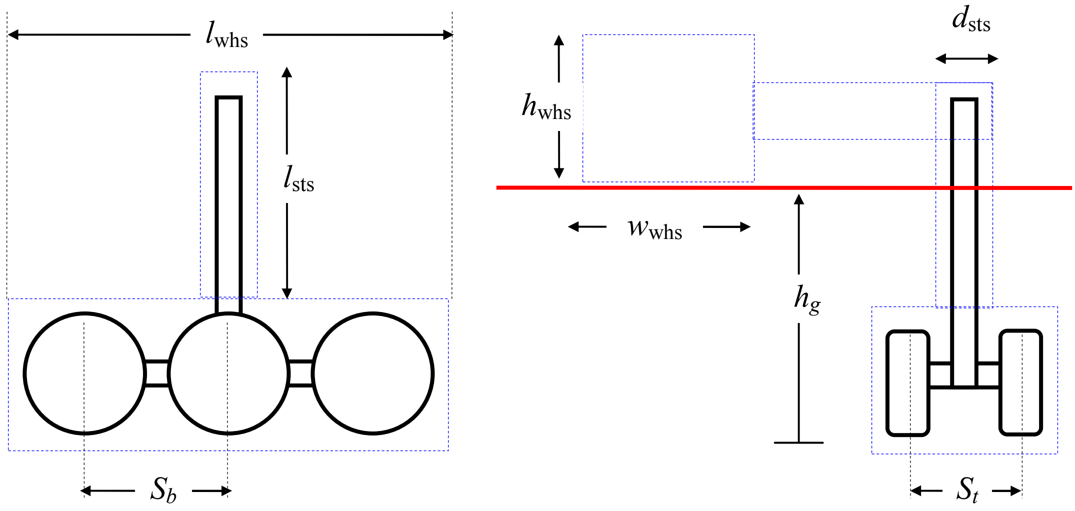

Figure 4.10: Main undercarriage model of the tanker

Wheel section

$$w_{whs} = d_{ty} + 2 \cdot \mathrm{inc} \tag{4.64}$$

$$h_{whs} = d_{ol} + 2 \cdot (w_{ty} + 2 \cdot \mathrm{inc}) \quad \text{, if } d_{ol} > S_t - w_{ty} \tag{4.65}$$

$$h_{whs} = S_t + 2 \cdot \left(\frac{w_{ty}}{2} + 2 \cdot \mathrm{inc} \right) \quad \text{, otherwise} \tag{4.66}$$

$$l_{whs} = 3 \cdot d_{ty} + 2 \cdot \mathrm{inc} \quad \text{, if } d_{ty} > S_b \tag{4.67}$$

$$l_{whs} = 2 \cdot S_w + d_{ty} + 6 \cdot \mathrm{inc} \quad \text{, otherwise} \tag{4.68}$$

Strut section

$$l_{sts} = h_g - w_{whs} + l_{ol} + \frac{h_{whs}}{2} \quad \text{, if } h_g > l_{ol} - \left(\frac{h_{whs} + w_{whs}}{2} \right) \tag{4.69}$$

$$l_{sts} = l_{ol} - \frac{w_{whs}}{2} \quad \text{, otherwise} \tag{4.70}$$

4.2.3 Propulsion Ducts

Due to the requirement of the side-by-side internal installation of three engines, three separated propulsion ducts are employed. Since the fundamental configurations of the tanker's ducts i.e. cross-sectional area transformation and S-shaped deflections are presented, the propulsion duct geometry modelling approach described previously in the UCAV section can be applied and further developed for multi-engine configuration of the tanker. Figure 4.11 illustrates the trapezium cross-sectional area formed by two individual intake diffusers at the inlet plane, in which the geometry specifications of each component are determined using the equations below.

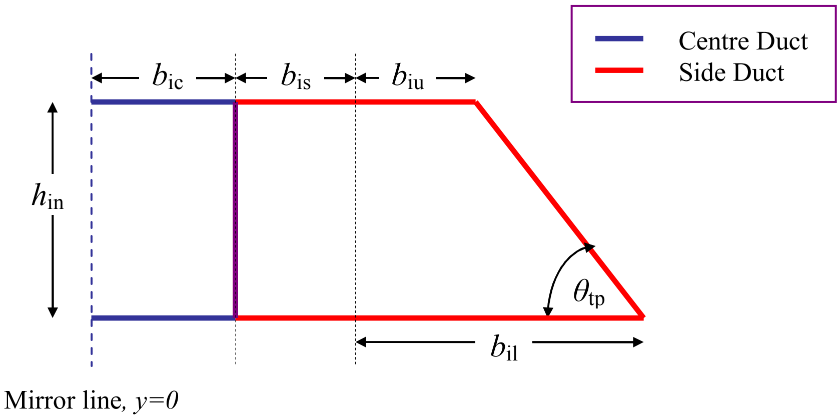

Figure 4.11: Inlet cross-section model of the tanker

Centre duct

$$b_{ic} = \sqrt{\frac{R_{IC} \cdot \pi \cdot \left(\frac{d_{en}}{2}\right)^2}{4 \cdot AR_{in}}} \tag{4.71}$$

$$h_{in} = 2 \cdot b_{ic} \cdot AR_{in} \tag{4.72}$$

Side duct

$$b_{is} = b_{iu} = \frac{2 \cdot b_{ic} \cdot R_{ib}}{R_{ib} + 1} \tag{4.73}$$

$$b_{il} = b_{iu} \cdot \left(\frac{2}{R_{ib}} - 1\right) \tag{4.74}$$

The R_{ib} parameter can be evaluated using the previous Eq. (4.31). As far as the longitudinal geometry of tanker's intake diffusers is concerned, Eq. (4.32) to Eq. (4.34) described in the UCAV section can be directly applied for calculating overall dimensional specifications of the centre duct. The side ducts also feature the same dimension values; however, in order to satisfy lateral spacing between the engines, the lateral deflection is integrated to the side duct configuration. Also an extra longitudinal length is included to the side intake diffuser on account of the stagger position of side engines. These side duct configurations modified from the centre one can be developed into the following equations.

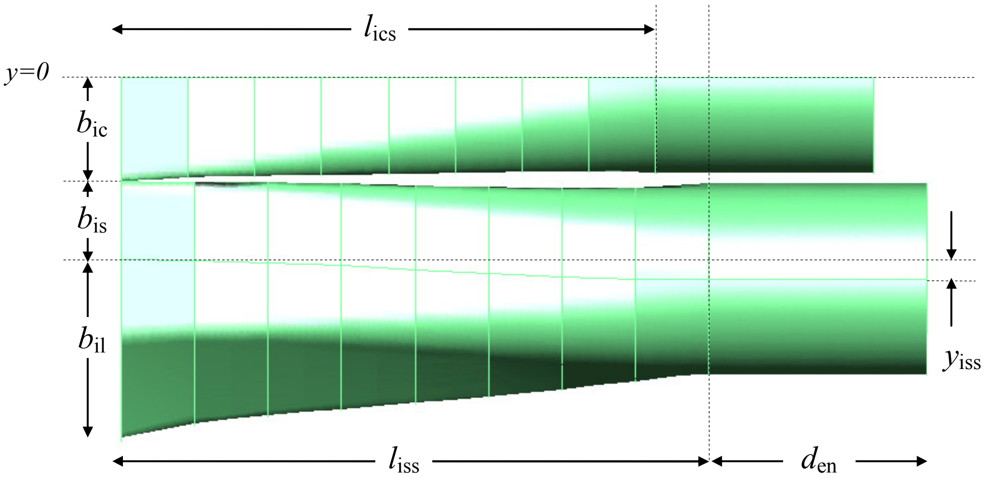

Figure 4.12: Plan-view geometry of tanker's intake diffusers

$$l_{iss} = l_{ics} + x_{stg} \cdot l_{en} \tag{4.75}$$

$$l_{is} = l_{iss} + d_{en} \tag{4.76}$$

$$y_{iss} = (d_{en} + 2 \cdot w_{fw}) - (b_{ic} + b_{is}) \tag{4.77}$$

where,

x_{stg} - Stagger distance relative to the engine length

A clearance has been taken into account for thickness and structure around the ducts and the engines (see Eq, 4.32, variable ' inc '). The exhaust pipe configurations of the tanker are similar to the UCAV with the same design modification approach described above. A list of additional equations used for evaluating the exhaust pipes' specifications of the tanker is provided in Appendix A.3.

4.2.4 Airframe

The wing geometry evaluation approach of the UCAV is directly adopted for the tanker without changes. The packaging of the tanker's fuselage is also conducted using similar structure of longitudinal stations; nonetheless, the evaluations of certain packaging constraints are slightly amended due to the different aircraft's internal components layout as illustrated in Figure 4.13.

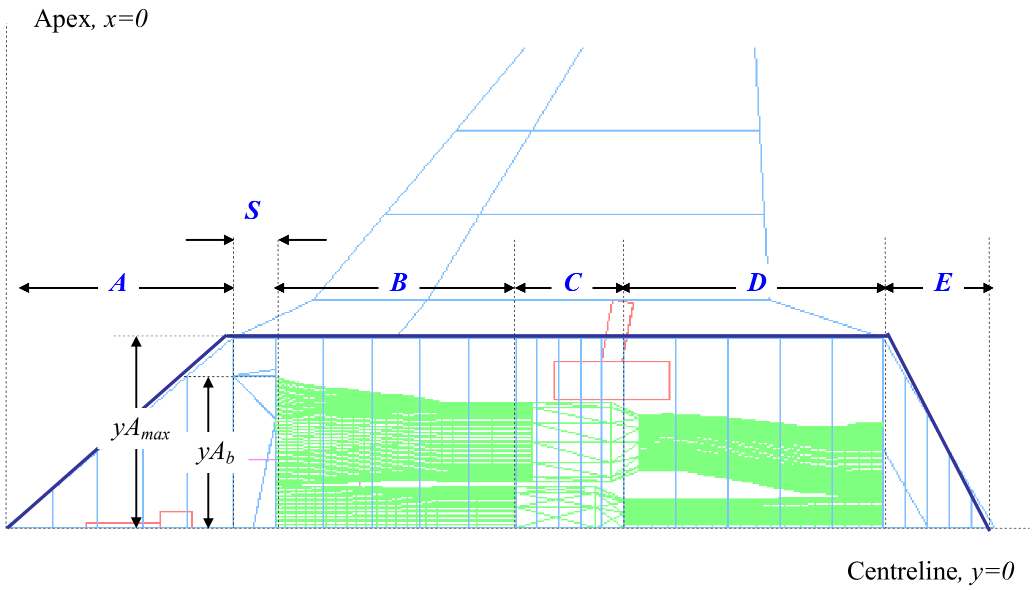

Figure 4.13: Fuselage station diagram of tanker

Due to the tanker's multi-duct configuration, an accumulated width of the intake diffusers at the inlet plane is relative large in comparison to the lateral dimensions of other internal components, and thus governs the requirement of maximum fuselage width. Therefore, $yA_{\max}$ parameter depicted in the Figure 4.13 is calculated from the total inlet base width (see Figure 4.11) including further lateral-space clearances for maintaining appropriate cross-section shape and providing the flexibility of main undercarriage allocation.

$$yA_{\max} = yA_b + w_{\mathrm{mgw}} + 2 \cdot \mathrm{inc} \tag{4.78}$$

when, $$yA_b = b_{\mathrm{ic}} + b_{\mathrm{is}} + b_{\mathrm{il}} \tag{4.79}$$

The remaining fuselage's upper base-width constraints i.e. yA_{bu}, yD_{bu} and yD_b are also determined using the same approach as the above yA_b in accordant with their corresponding inlet/exhaust plane geometry parameters.

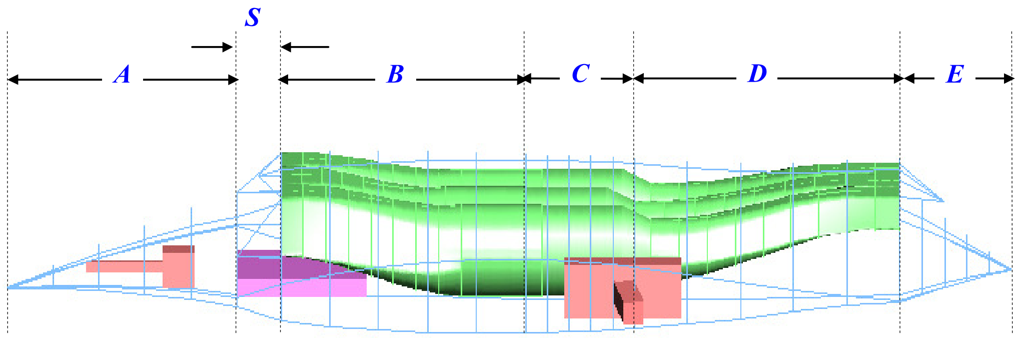

Figure 4.14: Fuselage station diagram of tanker

The majority of the allocation constraints of the tanker's internal components are similar to those of the UCAV. Nonetheless, due to the significantly larger size of the tanker in comparison, the weapon bay could be now fitted under the intake diffusers as displayed in Figure 4.14. Thus, the longitudinal constraints of this component are specified between stations *S* and *B* causing the nose undercarriage's location to be limited within station *A*. The main undercarriages, on the other hand, are allowed to be positioned between stations *C* and *D* measuring at the rear of the wheel model.

4.2.5 Refuelling Equipment

The refuelling component contains two parts; the hose drum unit (HDU) and the fairing pod which is to provide sufficient coverage for the remaining part of the HDU from the semi-submerged unit installation. In general, the designed tanker would be big and the local chord would be very large in comparison to the fixed geometry of the HDU; therefore, most of the HDU assembly would be submerged inside the wing, and the remaining protruding part would require a relatively small fairing. For this reason, with the faceted geometry design of the fairing pod, the radar cross-section contribution due to the pods themselves would be minimal compared the entire tanker. Due to the assumption of simultaneous refuelling of two UCAVs, the lateral location of the HDUs needs to be sufficient to allow a safe refuelling operation.

An HDU model is represented by a rectangular box in which the dimensions are specified by the design inputs similar to the weapon bay and APU models. The spanwise location of the HDU is defined as a function of the outboard-wing partition span as shown in Eq. (4.80). Nonetheless, since the unit needs to be allocated between the wing spars as illustrated in Figure 4.15, the longitudinal wing-box space at such a location must be verified against HDU dimensions and relocate the unit toward inboard for greater spaces if necessary.

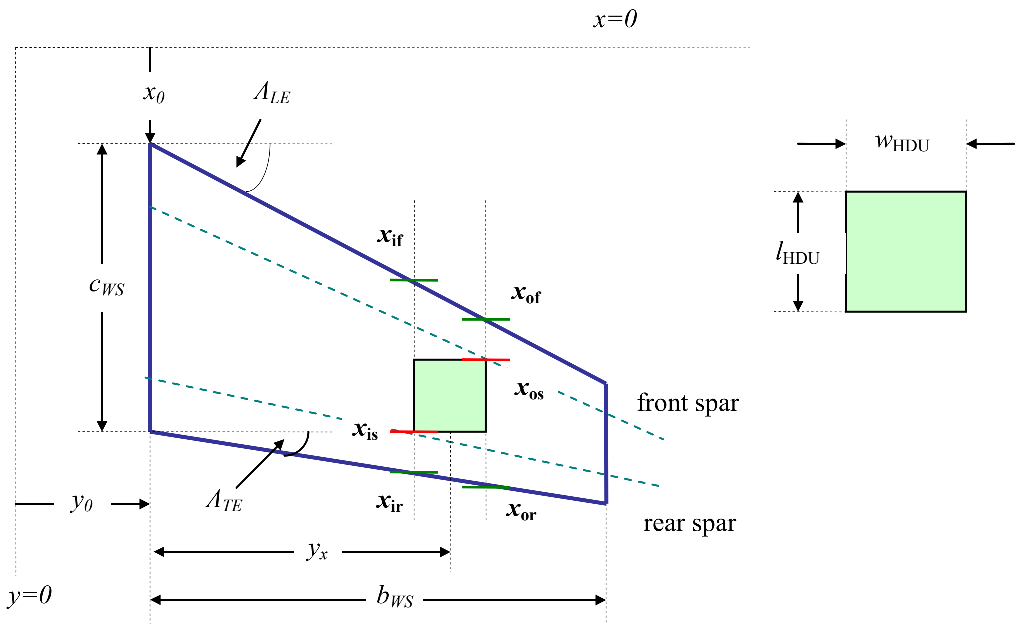

Figure 4.15: Allocation of the hose drum unit between the wing spars

$$y_x = R_{yRF} \cdot b_{WS} \tag{4.80}$$

where,

R_{yRF} - Relative spanwise position of HDU on the outboard-wing partition

The wing-box space verification is executed by identifying the boundary points of x_{if}, x_{ir}, x_{of} and x_{or} shown in the above figure for a given value of y_x, and then the wing spar constraints x_{is} and x_{os} can be evaluated in accordant with the equations shown below.

$$x_{\mathrm{is}} = x_{\mathrm{if}} + \mathrm{spr}_{\mathrm{R}} \cdot (x_{\mathrm{ir}} - x_{\mathrm{if}}) \tag{4.81}$$

$$x_{\mathrm{os}} = x_{\mathrm{of}} + \mathrm{spr}_{\mathrm{F}} \cdot (x_{\mathrm{or}} - x_{\mathrm{of}}) \tag{4.82}$$

where,

$\mathrm{spr}_{\mathrm{F}}$ - Front spar location relative to the chord

$\mathrm{spr}_{\mathrm{R}}$ - Rear spar location relative to the chord

Afterward verifying whether $(x_{\mathrm{is}} - x_{\mathrm{os}}) < (l_{\mathrm{HDU}} + 2 \cdot \mathrm{inc})$, if so then relocating the HDU position toward inboard by decreasing y_x. And go back to the evaluation of the boundary points with the new y_x value. Otherwise, the component can be allocated at the current spanwise location.

Once the spanwise HDU location has been determined, the fairing pod can be created at the same location where the component has been allocated to develop from the leading-edge to the trailing positions, thus covering the entire chord length. This is for the purpose of minimising abrupt transitions of the fairing pod on the tanker's wing and hence maintaining aerodynamic efficiency. The fairing pod model consists of three longitudinal stations as illustrated in Figure 4.16 (left). The starting locations of these fairing stations measured from the nose can be evaluated using Eq. (4.83) to Eq. (4.85) while some parameters in these equations are referenced from the Figure 4.15. As shown in the Eq. (4.84), the HDU is designed to be allocated close to the rear spar regardless of the wing-box space available. The reasons for this are to increase the length of station A for gradual fairing transition and to bring the actual unit closer to the hose exit at the trailing edge. A rectangular slot at the exit plane of the fairing pod, shown in the figure below (right), is created for hose deployment where the associated dimensions of w_{he} and h_{he} are specified as input parameters.

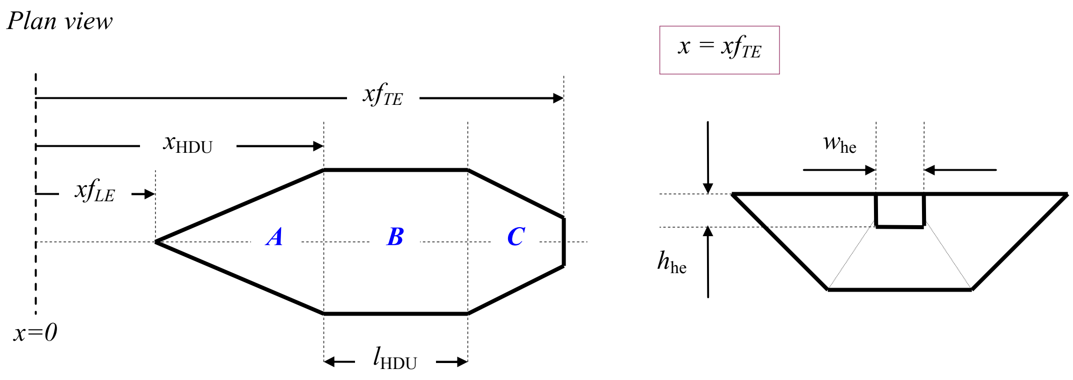

Figure 4.16: Fairing pod design

$$x_{\mathrm{HDU}} = x_{\mathrm{is}} + l_{\mathrm{HDU}} + \mathrm{inc} \tag{4.83}$$

$$xf_{LE} = x_0 + y_x \cdot \tan(\Lambda_{LE}) \tag{4.84}$$

$$xf_{TE} = (x_0 + c_{WS}) + y_x \cdot \tan(\Lambda_{TE}) \tag{4.85}$$

The overall cross-section model of the fairing pod is developed as shown in Figure 4.17. Although the HDU is modelled as a rectangular box, the fairing's cross-section is designed to expand laterally forming a trapezium shape for the purpose of reducing the radar cross-section produced by the refuelling pod. Due to the dihedral wing configuration, the upper base of the fairing cross-section would be positioned accordingly at the relative height of the wing where the HDU is located. And z_{RF} is the distance measured from zero horizontal line to the above fairing base position.

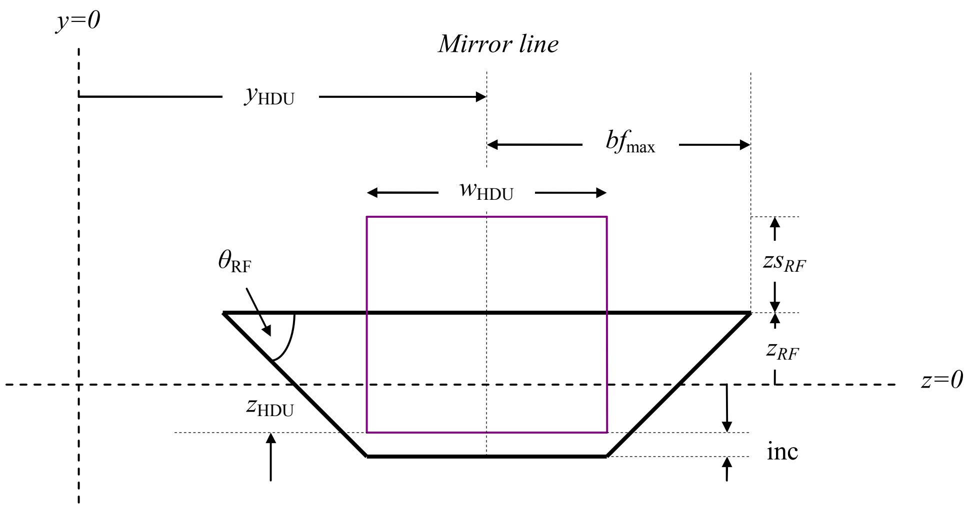

Figure 4.17: Fairing pod's cross-section model

$$y_{\text{HDU}} = y_0 + y_x \tag{4.86}$$

$$z_{\text{HDU}} = z_{RF} + zs_{AF} - h_{\text{HDU}} \tag{4.87}$$

$$bf_{\max} = \frac{w_{\text{HDU}}}{2} + \frac{\left|z_{RF} - z_{\text{HDU}} - \text{inc}\right|}{\tan(\theta_{\text{RF}})} \tag{4.88}$$

where,

θ_{RF} - Fairing pod alignment angle.

As illustrated in the above figure, zs_{AF} is the HDU portion above the upper fairing base which submerges into the wing. It is desirable to embed the component inside the wing as much as possible in order to minimise the extrusion part and hence improving the slenderness of the fairing pod. Therefore, the HDU is designed to submerge all the way up to a certain internal clearance of the local upper wing surface. An interpolation of the upper-surface aerofoil coordinate at the above local position is applied for the evaluation of this submerged height parameter.

Chapter 5

Airframe Geometry

5.1 Mathematical Modelling Approach

Since this research project aims to deliver a design methodology which possesses a certain level of flexibility to generate an aircraft according to given design requirements, the airframe surface modelling, one of the major parts incorporated into the design synthesis, needs to be developed in such a way that it is capable of supporting the above variation. For this reason, the mathematical modelling methods, developed by Serghides [46] which utilise various arithmetical equations to produce desired aircraft configurations have been applied to generate flexible modelling structures of the designed tanker and UCAV's airframes.

Despite the versatility and the flexibility of the above modelling methods; the development of the equations for an entire aircraft model requires comprehensive understanding in terms of both mathematical and modelling relations. Also the level of this comprehension determines the adaptability and the refinement of the model produced at the end. Nonetheless, no matter how flexible the developed mathematical model is, if the desired aircraft configuration is highly diversified from the original one founded in the model then a different set of the equations and modelling structures would be needed. Since developing the mathematical model of the entire aircraft is undoubtedly time-consuming, and in order to prevent substantial waste of efforts if the investigated preliminary model becomes inapplicable to the actual design due to the significant airframe configuration differences; the baseline configurations of both tanker and UCAV together with their associated airframe packaging developed previously are used to provide a guideline and constraints for selecting appropriate equations applied to a certain part of the aircraft model.

5.1.1 Function Implementation

It is necessary for an aircraft to have an airframe which provides high aerodynamic efficiency; therefore, any sharp changes in cross-sectional area transformation are not desirable, especially for a flying-wing design in which wings and fuselage are blended together smoothly. In order to achieve that, a modelling technique called 'lofting' is introduced. Lofting is defined as a process of generating the external geometry of the entire aircraft based on mathematical functions. This technique has a wide range of methods and applications which would be beyond the scope of this thesis; however, its fundamental concept can be summarised as a smooth transformation or change of a geometric element from one shape to another by altering the values of variables within the mathematical models defining them. For example; transforming the cross-sectional area of an intake diffuser from a trapezium to a circular shape gradually and smoothly, avoiding pressure losses and flow separation inside the duct. In order to apply the lofting technique for modelling the entire airframe, the mathematical equations behind every design element need to be derived first.

It is undeniable that there have been countless of mathematical equation forms existing so far. While the majority of them produce different graphical appearances, some equation forms share similar behaviours for a certain region, thus the process of selecting appropriate functions for designing specific element of the airframe may prove to be complicated. Nonetheless, since both tanker and UCAV designs feature a flying-wing configuration which emphasises the blending of most external components together, the airframe model could be considered to be dominated by spline-type equations. Although polynomial functions are well-known for producing flexible spline geometry appearances, their equation forms are rather difficult to control and predict for precise modelling works. Therefore, an alternate type of spline functions introduced by Serghides [46] was applied for developing the airframe models of both aircraft. These functions can be used for creating various geometry shapes from an arc to several spline types, providing high degree of modelling flexibility while maintaining the simplicity of controlling and predicting the resulted geometry appearance. The equation forms which represent the aforementioned mathematical functions and govern the majority of the airframe model are formulated as shown below.

$$f(x) = \left(\frac{x - x_0}{x_e - x_0}\right) \cdot A + I \tag{5.1}$$

$$f(x) = \sin\left(\frac{\pi}{2} \cdot \left(\frac{x - x_0}{x_e - x_0}\right)\right)^N \cdot A + I \tag{5.2}$$

$$f(x) = \cos\left(\frac{\pi}{2} \cdot \left(\frac{x - x_0}{x_e - x_0}\right)\right)^N \cdot A + I \tag{5.3}$$

$$f(x) = \tan\left(\frac{\pi}{4} \cdot \left(\frac{x - x_0}{x_e - x_0}\right)\right)^N \cdot A + I \tag{5.4}$$

where,

N	- Exponent	x_0	- Starting x value
A	- Amplitude	x_e	- Final x value
I	- Independent variables		

It is clear that these four equations share similar structures with the primary differences of the exponent and the dominant trigonometry terms. For the purpose of describing the equations, the *XY*-coordinate will be used as a reference system. The *division* term represents a ratio of the current x value (numerator) relative to the total range of x which the equation applied (denominator). This in conjunction with the applied trigonometry and the exponent terms, a function shape would be generated accordingly within the range defined by the denominator of the *division* term. Afterward the amplitude A would determine how great the function shape varies in the vertical direction, and finally the vertical position of the entire function shape could be externally adjusted by the total value of independent variables I .

The geometry shapes produced by these mathematical functions are highly dependent on the trigonometry and the exponent terms applied. The most basic equation form shown in Eq. (5.1) is equivalent to a well-known straight-line function $f(x) = mx + c$. Both Eq. (5.2) and Eq. (5.3) produce the same S-shaped function mirrored to each other as depicted in Figure 5.1. On the other hand, if $\pi/2$ was applied to Eq. (5.4) in the same manner as the above Eq. (5.2) and Eq. (5.3) then the function result would rise infinitely as the *division* term approaches unity. However, by replacing $\pi/2$ with $\pi/4$, the tangent function would yield the value of 1 instead of the infinity at the unity *division* term, and thus can be applied for generating a semi-convex shape as shown in Figure 5.1 below.

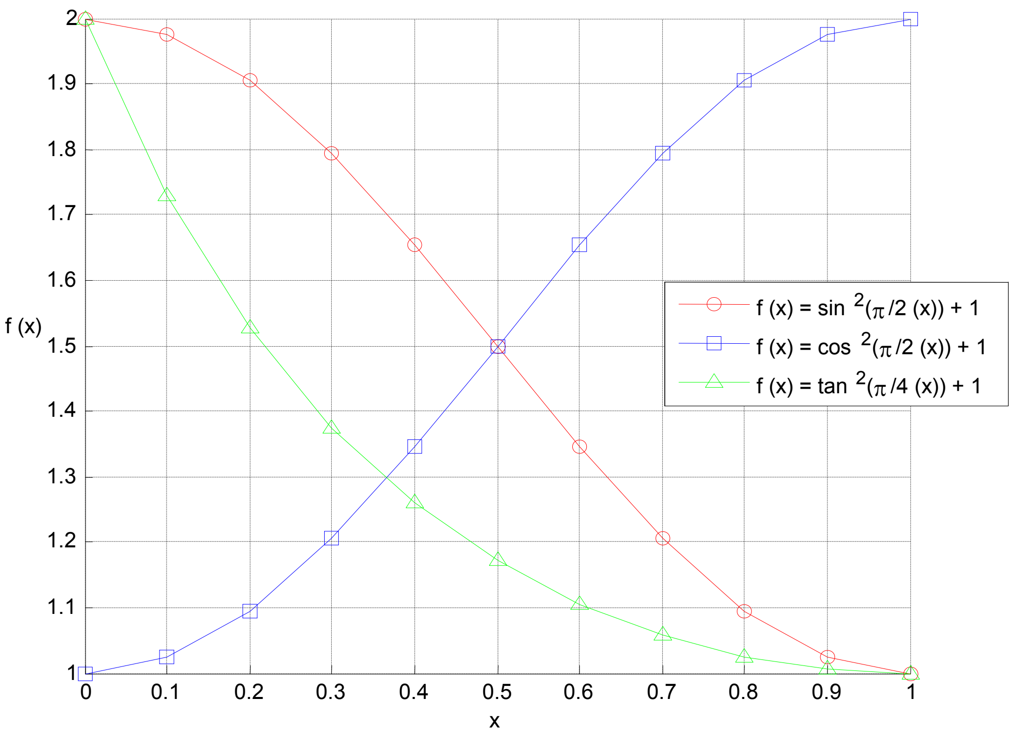

Figure 5.1: A comparison of trigonometry modelling functions

The degree of curvature changes in the above trigonometry modelling functions vary depending on the exponent term as illustrated in Figure 5.2. In general, the greater the exponent value, the more deflection the function shape develops. However, the envelopes in which the function applied remains unchanged regardless of the trigonometry and the exponent terms.

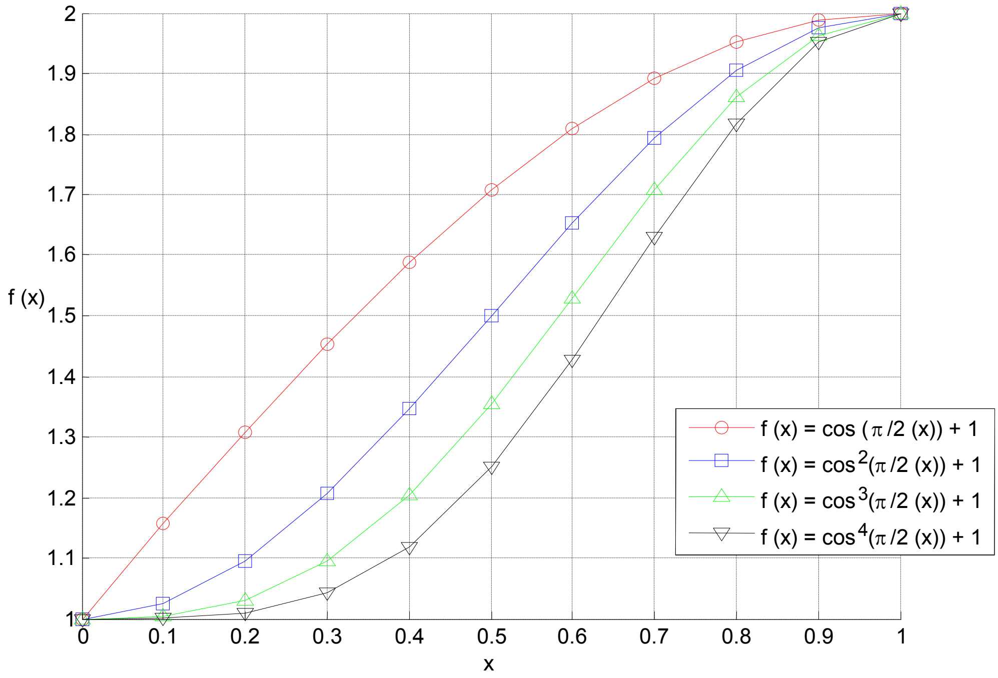

Figure 5.2: The effect of exponent values on the modelling function

5.1.2 Two-Dimensional Modelling

The mathematical modelling functions introduced in the previous section have demonstrated a capability of generating flexible spline shapes. However, since the airframe and propulsion ducts feature rather complicated figure and transformation, it is not likely that a single equation would be able to entirely contain and adapt a particular design part. Therefore, the majority of 2D mathematical models developed for representing specific design aspects of the aircraft components contain a set of equations in which each of them is applied to a certain region in the design picture. For example, the cross-section model of the UCAV's fuselage illustrated in Figure 5.3 consists of the following equations.

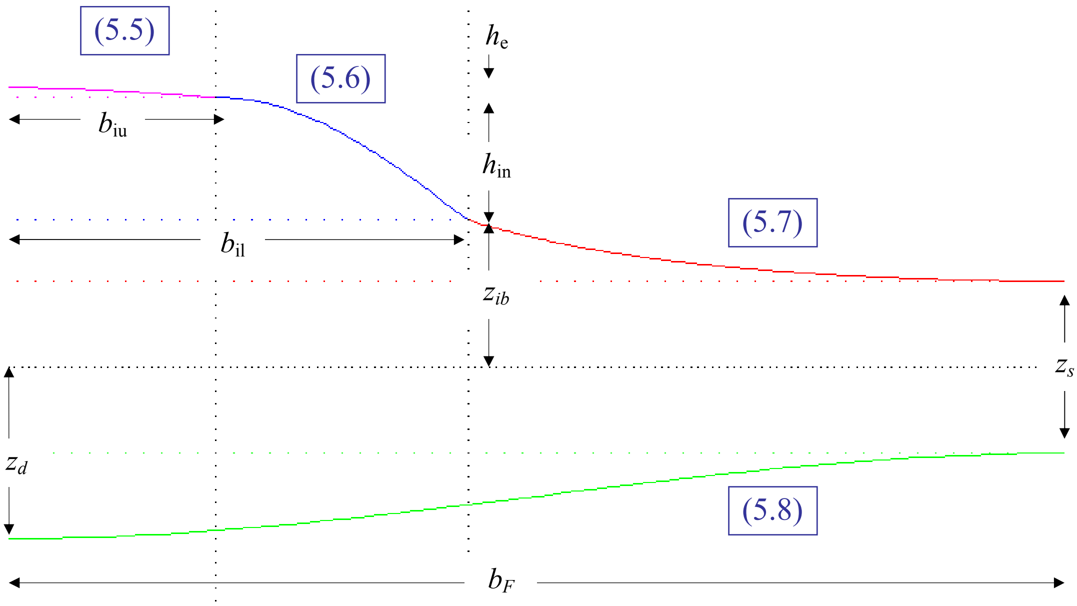

Figure 5.3: Mathematical Model of fuselage cross-section

Upper surface

$$f(x) = \sin\left(\frac{\pi}{2}\cdot\left(\frac{b_{iu}-x}{b_{iu}-0}\right)\right)\cdot h_e + h_{in} + z_{ib} \qquad , 0 \le x < b_{iu} \qquad (5.5)$$

$$f(x) = \sin\left(\frac{\pi}{2}\cdot\left(\frac{b_{il}-x}{b_{il}-b_{iu}}\right)\right)\cdot h_{in} + z_{ib} \qquad , b_{iu} \le x < b_{il} \qquad (5.6)$$

$$f(x) = \tan\left(\frac{\pi}{4}\cdot\left(\frac{b_F-x}{b_F-b_{il}}\right)\right)^2\cdot\left(z_{ib}-\frac{z_s}{2}\right)+\frac{z_s}{2} \qquad , b_{il} \le x \le b_F \qquad (5.7)$$

Lower surface

$$f(x) = -\sin\left(\frac{\pi}{2}\cdot\left(\frac{b_F-x}{b_F-0}\right)\right)^2\cdot\left(z_d-\frac{z_s}{2}\right)-\frac{z_s}{2} \qquad , 0 \le x \le b_F \qquad (5.8)$$

where,

b_{iu}	- Upper inlet width	z_d	- Bottom depth from the centreline
b_{il}	- Lower inlet width	z_{ib}	- Inlet base height from the centreline
b_F	- Fuselage width	h_e	- Additional clearance above the inlet
z_s	- Side fuselage thickness	h_{in}	- Inlet cross-section height

The above modelling equations all together produce a smooth blister at the centre of the cross-section providing adequate space for installing the propulsion system and other internal components, while the cross-sectional area would reduce gradually and become saturated toward the outboard of the fuselage where the wing-fairing is assembled. Due to the requirement of accommodating flexible inlet specifications, the upper surface of the fuselage cross-section is divided into multiple regions which are constrained by the inlet geometry variables as noted on the right of the associated equations. This allows the cross-section model of the fuselage to automatically adjust the overall figure according to the inlet constraints.

The 2D model of aircraft may provide sufficient visualisation of the design concept; however, more-advanced presentation of the model in three dimensions is essential in order to accurately determine model-derived geometry parameters for the subsequent design synthesis calculations, e.g. surface areas, centre of gravities and internal volumes. Although there are existing numerical methods available for approximating such parameters directly from general aircraft specifications, these methods were developed based on statistical data of conventional aircraft, and thus would be less applicable to the flying-wing configuration of the tanker and UCAV developed in this research project.

Apart from providing an all-round aircraft presentation and accurate geometry specifications, the 3D-modelling aircraft also help the designer to justify whether the appearance of the aircraft is appropriate and matches the initial design they had for the baseline configuration before proceeding to the next stages. This would save a considerable amount of time and efforts in further design processes if the aircraft configuration was conceptually correct from the start. Also since the 3D model provides superior visualisation details, the aircraft result can be verified more rapidly and more accurately than the 2D counterpart. The methodology used for developing a 3D model of the aircraft based on the 2D mathematical equations is described in the following section.

5.1.3 Three-Dimensional Modelling

The example in the 2D modelling section (see Figure 5.3) has demonstrated how a certain part of the aircraft could be modelled with mathematical equations from the front view. However, as far as the 2D aircraft geometry is concerned, the modelling view points can be generally categorised into three different directions. These are the front, side and planform views as usually shown in a three-view drawing of the aircraft. Although individual 2D modelling equations can be described with the *XY*-coordinate system regardless of their actual view points in the 3D aspect, due to the need of the *XYZ*-coordinate system used in 3D models, any applied 2D modelling equations must be specified according to their corresponding view point and the direction terminology illustrated in the figure below.

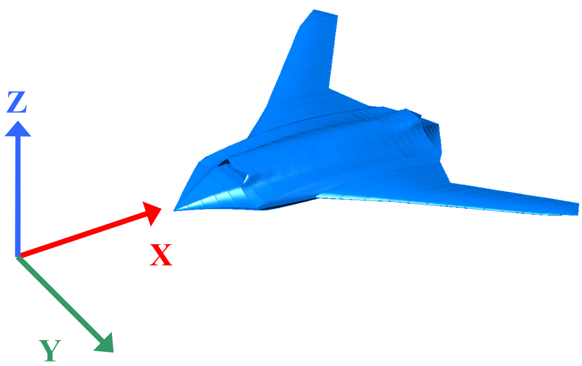

Figure 5.4: 3D mathematical modelling coordinate system

From Figure 5.4, the front view refers as the *YZ* plane while the typical *XY* plane is used for representing the planform view and the remaining side view is specified on the *XZ* plane. With this common definition of the coordinate system, function variables of the 2D modelling equations generated on any view point, can be recognised in an entire 3D model, and hence can be appropriately linked to other relevant 2D modelling equations defined on different view points.

In essence, the 3D mathematical model of a certain aircraft component is created on a basis of 2D cross-section model variations developed on a selected coordinate plane, i.e. the *YZ* plane for the fuselage and the *XZ* for the wing. The mathematical equations used for generating these cross-section models are formulated in correspondent with various geometry variables which define other design aspects of the same component. This would result 3D coordinate data which can be plotted in a wireframe pattern comprising a series of cross-sections and perpendicular directional lines joining in-between. With an assistance of computer aid design (CAD) programs, a mesh surface of a certain component can be formed in accordant with the structure of the wireframe model, hence ultimately provides a realistic 3D model presentation. For the purpose of clarification, an intake diffuser of the UCAV will be used as an example to describe how the 3D mathematical model is developed.

The intake diffuser model consists of two longitudinal stations, the transformation and the uniform duct regions, as previously described in section 4.1.3. Eq. (5.9) represents a relationship between three longitudinal coordinates of the component measured from the apex of the UCAV, hence the reason xin_0 is left uncancelled.

$$xin_S = xin_0 + (xin_E - xin_0) - d_{\mathrm{en}} \tag{5.9}$$

where,

xin_0 - Starting x-coordinate of the intake diffuser

xin_E - Final x-coordinate of the intake diffuser

xin_S - End of the inlet transformation region

From the modelling point of view, the uniform duct section can be created straightforwardly, which will be explained at the end of this example. The variable shaped section, however, requires the inlet cross-section to smoothly transform from a trapezium to a circle shape while the associated area must be gradually increased to meet that of the engine's front face. Furthermore, vertical duct deflection is also applied throughout the section. The modelling equations which are subject to such complex changes are presented as follows.

***XY* Plane:** for $xin_0 \le x_i \le xin_S$

$$biu_i = \left(\frac{xin_S - x_i}{xin_S - xin_0} \right) \cdot b_{\mathrm{iu}} \tag{5.10}$$

$$bil_i = \left(\frac{xin_S - x_i}{xin_S - xin_0} \right) \cdot b_{\text{il}} \tag{5.11}$$

$$ri_i = \left(\frac{x_i - xin_0}{xin_S - xin_0} \right) \cdot \frac{d_{\text{en}}}{2} \tag{5.12}$$

***XZ* Plane:** for $xin_0 \le x_i \le xin_S$

$$zic_i = \left(\frac{x_i - xin_0}{xin_S - xin_0} \right) \cdot \left(\frac{d_{\text{en}} - h_{\text{in}}}{2} \right) + \frac{h_{\text{in}}}{2} \tag{5.13}$$

$$zis_i = \left(\frac{xin_S - x_i}{xin_S - xin_0} \right) \cdot \frac{h_{\text{in}}}{2} \tag{5.14}$$

where,

biu_i	- Inlet upper base	zic_i	- Inlet height at the centre
bil_i	- Inlet lower base	zis_i	- Inlet height at the side
ri_i	- Radius of inlet corner transformation		

subscript:

i	- Corresponding longitudinal sub-station

Eq. (5.10) to Eq. (5.14) are responsible for the changes of various inlet geometry parameters (see Figure 5.5) in both *XY* and *XZ* planes as the model evaluation progresses in the longitudinal direction. For every specified interval of x, a cross-section model on the *YZ* plane will be calculated using Eq. (5.15) to Eq. (5.18) below which are associated with the parameter values determined from the above equations.

***YZ* Plane:**

Upper section, for $0 \le y_u \le yu_{\max}$

$$f(x_i, y_u) = zic_i \qquad ,0 \le y_u < biu_i \tag{5.15}$$

$$f(x_i, y_u) = \frac{\sqrt{(ri_i \cdot (zic_i - zis_i))^2 - ((y_u - biu_i) \cdot (zic_i - zis_i))^2}}{ri_i} + zis_i \qquad ,biu_i \le y_u \le yu_{\max} \tag{5.16}$$

Lower section, for $0 \le y_l \le yl_{\max}$

$$f(x_i, y_l) = -zic_i \qquad ,0 \le y_l < bil_i \tag{5.17}$$

$$f(x_i, y_l) = -\frac{\sqrt{(ri_i \cdot (zic_i - zis_i))^2 - ((y_l - bil_i) \cdot (zic_i - zis_i))^2}}{ri_i} - zis_i$$

$$,bil_X \le y_l \le yl_{\max} \tag{5.18}$$

when, $yu_{\max} = biu_i + ri_i$

$yl_{\max} = bil_i + ri_i$

subscript:

u - Corresponding upper-surface y-coordinate point

l - Corresponding lower surface y-coordinate point

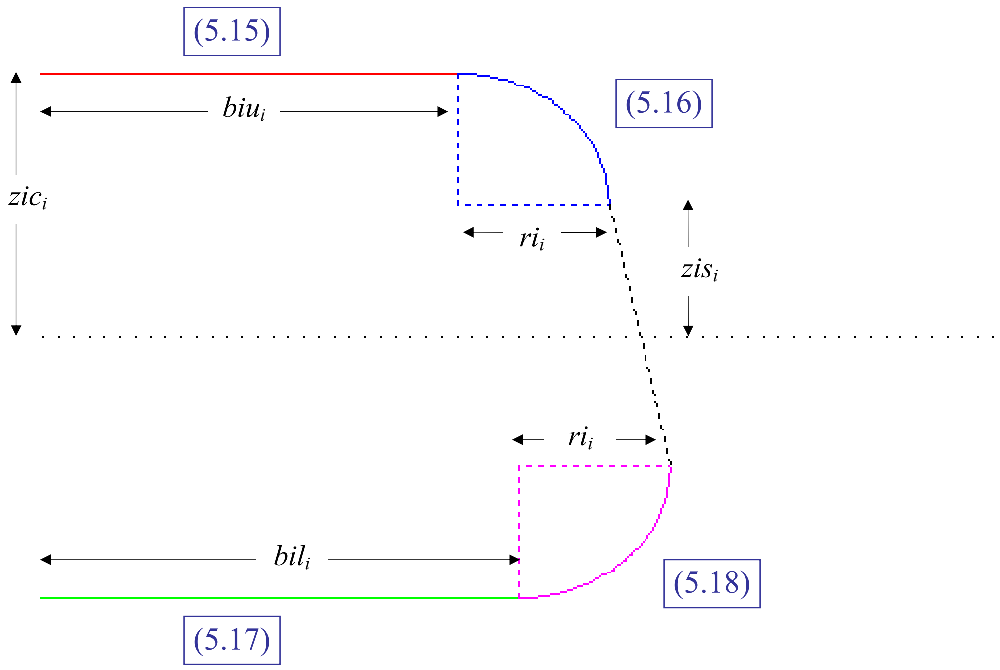

Figure 5.5: Mathematical model of intake diffuser cross-section

Figure 5.5 depicts the modelling equations scheme developed for accommodating the trapezium-to-circle cross-section transformation of the intake diffuser. A trapezium model contains two asymmetrical parallel edges biu_i and bil_i which despite the difference in length, both objects are required to simultaneously arrive at the same quarter-circle figure in the end. For this reason, the trapezium model is divided into the upper and the lower surface regions as shown in the above corresponding *YZ*-plane equations in order to employ different rates of parameter value changes. As far as a fundamental geometry transformation approach is concerned, the corner of the trapezium can be simplified as a rectangle as depicted by the first model (left) of Figure 5.6. The figure displays the transformation process of the rectangle into a quartered circle where the associated line colours represent the same mathematical equations shown in Figure 5.5.

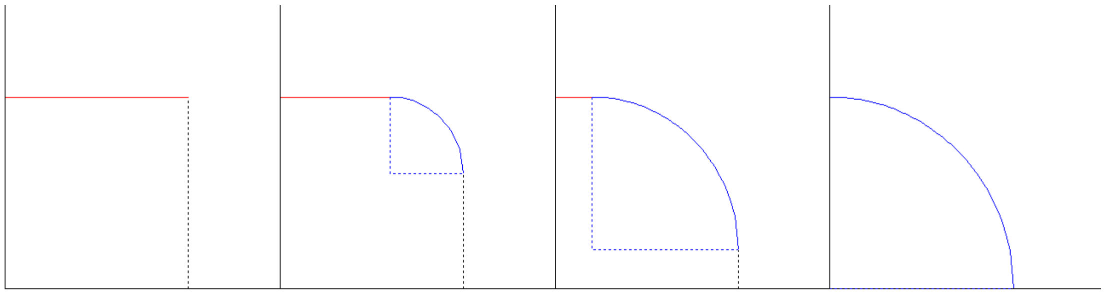

Figure 5.6: Rectangle-to-circle transformation process

The rectangle may be viewed as a vertical line zis_i and a horizontal line biu_i fully extended and joining at the corner where an imaginary arc situates with the radius ri_i of zero. Once the transformation starts, both zis_i and biu_i would gradually decrease while the arc located previously at the corner would move toward the centre of the cross-section as well as increasing the value of ri_i. This would result a round corner being formed instead of the sharp one initially presented when $ri_i = 0$. Also during the transformation, zic_i would slowly increase to the value of the engine radius. Eventually the cross-section arc area would be completely formed as shown in the Figure 5.6 (left), while biu_i and zis_i would become points located on the axes of the arc. The same concept is applied to the lower corner of the trapezium using the corresponding Eq. (5.17) and Eq. (5.18) to generate a mirrored configuration of the transformation process described above.

Once a series of the transforming inlet cross-section models have been evaluated along the downstream direction, the vertical duct deflection can be applied by using the spline-type equation introduced earlier to compute an S-shaped course based on the same x interval defined for the cross-section models. Eq. (5.19) shown below would gradually adjust the vertical position of the cross-section models at the inlet plane to the same level as the engine at the end of the transformation section.

$$f(x_i) = \sin\left(\frac{\pi}{2} \cdot \left(\frac{x_i - xin_0}{xin_S - xin_0}\right)\right)^2 \cdot \left(\frac{h_{\text{in}}}{2} + z_{ib} + z_{\text{en}}\right) + z_{\text{en}} \qquad , xin_0 \le x_i \le xin_S \qquad (5.19)$$

Finally, the z-coordinates of the intake diffuser model as a function x and y can be found from an accumulation of the cross-section model data and the above height variation result.

$$zinu_{\text{i},\text{u}} = f(x_i, y_u) + f(x_i) \qquad (5.20)$$

$$zinl_{\text{i},\text{l}} = f(x_i, y_l) + f(x_i) \qquad (5.21)$$

where,

$zinu$ - z-coordinate of the upper intake diffuser model

$zinl$ - z-coordinate of the lower intake diffuser model

Modelling-wise, the subsequent straight uniform duct section of the intake diffuser can be created in a few ways either by duplicating a completed circular cross-section from the variable section or constructing the same object based on the engine perimeter. A 3D wireframe model of the intake diffuser, generated from the mathematical modelling equations described above, is illustrated in Figure 5.7 (left) while the model on the right depicts the same wireframe object after the mesh surface has been rendered.

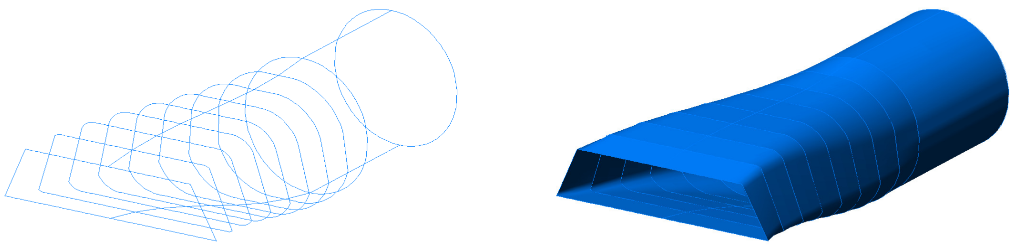

Figure 5.7: 3D wireframe (left) and surface (right) models of the intake diffuser

5.2 Aircraft Modelling Implementation

5.2.1 UCAV

The flying-wing configuration of the UCAV may imply the development of a blended airframe model comprising both fuselage and wings; however, it was considered to be more appropriate to develop these components individually similar to other typical aircraft. In doing so, each component can be modelled in accordant with its appropriate wireframe structure e.g. a normal front-view cross-section is applied to the fuselage while the cross-section models of the wing, on the other hand, can portray an aerofoil shape in the spanwise direction.

5.2.1.1 Fuselage

The equations applied for modelling the fuselage cross-sections in general have been described in the previous example of 2D modelling (see Figure 5.3). Although the modelling approaches of all fuselage station's cross-sections are fundamentally the same, different equations and geometry parameters are employed corresponding to the cross-section design of each fuselage station and their associated packaging constraints developed in the previous chapter. Also cambered fuselage equations have been integrated into the model to improve the streamline figure. This camber integration is performed in a similar manner to the S-shaped deflection in the intake diffuser case. A complete list of the equations used in UCAV fuselage modelling can be found in Appendix B.1.

After the cross-section models have been defined for all fuselage stations, the airframe surface's boundary constraints for any movable internal components can be developed according to their assigned longitudinal packaging constraints (mostly corresponding to the fuselage stations) and the fuselage cross-section equations defined for such stations. Also the automated functions of internal component allocation and packaging constraint verification, which are necessary for an iterative procedure of the design synthesis, have been developed, e.g. for a given location of the nose undercarriage, if any of the undercarriage bay corners exceeds the airframe boundary surfaces then the component will be automatically moved to the nearest point where it can be entirely allocated within the surfaces. A flow-chart diagram described this automated component allocation algorithm is illustrated in Figure 5.8.

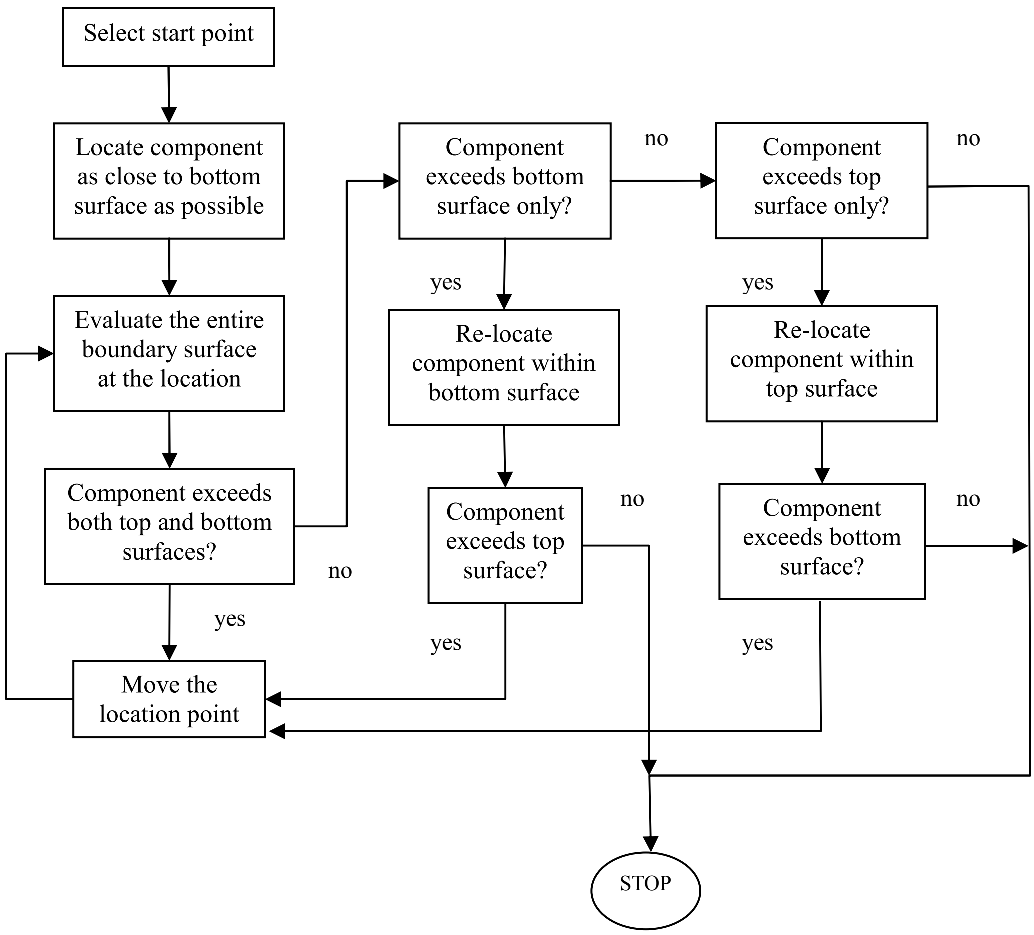

Figure 5.8: Automated internal-component allocation algorithm

The above algorithm is applied to the majority of the internal components in which their allocated spaces in the fuselage are modelled as rectangular box and their positions are flexible within the constraints. Although the models of the undercarriage are specified as a combination of the strut and wheel box models, this algorithm can be applied by including additional surface constraint verification at the location of each box model.

5.2.1.2 Wing

The coordinate data of a selected aerofoil are used for generating cross-sectional geometry of UCAV wing model along the span, referencing to its planform shape developed previously in the system packaging. For the purpose of this research study, it is assumed that the wing aerofoil would be created specifically for the UCAV, thus all associated performance characteristics of the aerofoil required in the subsequent aerodynamic analysis are specified as input parameters. Nonetheless, as far as the modelling of the wing aerofoil's cross-section is concerned, NACA 65-series are selected as the based aerofoil geometry since they provide the most suitable shape for blending with the designed fuselage model. Furthermore, wing twist and dihedral angles are also included into the wing model to enhance overall presentation details. In general, the mathematical modelling approach of the wing component is similar to the fuselage with the primary difference of the cross-section coordinate evaluations being on the *XZ* plane instead of the *YZ* plane. The equations developed for producing a swept-wing model are listed as follows.

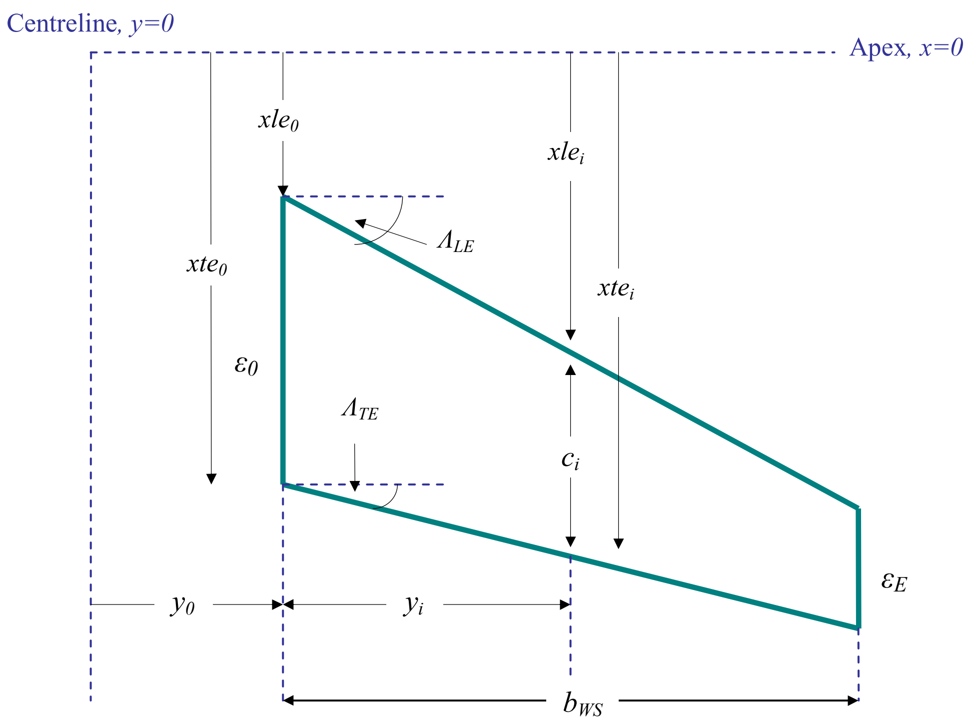

Figure 5.9: Mathematical modelling scheme of wing in the planform direction

***XY* Plane:** for $0 \le y_i \le b_{WS}$

$$xle_i = xle_0 + y_i \cdot \tan(\Lambda_{LE}) \tag{5.22}$$

$$xte_i = xte_0 + y_i \cdot \tan(\Lambda_{TE}) \tag{5.23}$$

$$c_i = xte_i + xle_i \tag{5.24}$$

$$xqc_i = xle_i + \frac{c_i}{4} \tag{5.25}$$

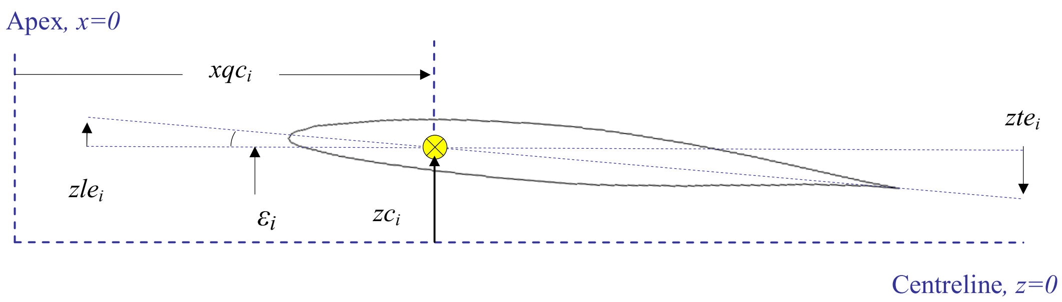

Figure 5.10: Mathematical modelling scheme of wing in the spanwise direction

***YZ* Plane:** for $0 \le y_i \le b_{WS}$

$$\varepsilon_i = \frac{y_i}{b_{WS}} \cdot (\varepsilon_E - \varepsilon_0) \tag{5.26}$$

$$zc_i = zc_0 + \frac{y_i}{b_{WS}} \cdot \tan(\alpha_d) \tag{5.27}$$

$$zle_i = (xqc_i - xle_i) \cdot \tan(\varepsilon_i) + zc_i + c_i \cdot \left(\frac{af_{\mathrm{UZ}}(1)}{100}\right) \tag{5.28}$$

$$zte_i = (xqc_i - xte_i) \cdot \tan(\varepsilon_i) + zc_i + c_i \cdot \left(\frac{af_{\mathrm{UZ}}(n_{AF})}{100}\right) \tag{5.29}$$

where,

ε	- Wing twist	af_{UZ}	- Upper-surface aerofoil z-coordinates
α_d	- Wing dihedral	n_{AF}	- Max aerofoil coordinates number

***XZ* Plane:** for $1 \le j \le n_{AF}$

$$xwu_{\mathrm{i,j}} = xle_i + c_i \cdot \left(\frac{af_{\mathrm{UX}}(j)}{100}\right) \tag{5.30}$$

$$zwu_{i,j} = c_i \cdot \left(\frac{af_{UZ}(j)}{100}\right) + zc_i + (xqc_i - xwu_{i,j}) \cdot \tan(\varepsilon_i) \tag{5.31}$$

$$xwl_{i,j} = xle_i + c_i \cdot \left(\frac{af_{LX}(j)}{100}\right) \tag{5.32}$$

$$zwl_{i,j} = c_i \cdot \left(\frac{af_{LZ}(j)}{100}\right) + zc_i + (xqc_i - xwl_{i,j}) \cdot \tan(\varepsilon_i) \tag{5.33}$$

where,

af_{UX} - Upper-surface aerofoil x-coordinates

af_{LX} - Lower-surface aerofoil x-coordinates

af_{LZ} - Lower-surface aerofoil z-coordinates

subscript:

i - Corresponding spanwise sub-station

j - Corresponding aerofoil coordinate number

The above modelling equations are applied to each wing partition in the UCAV's cranked-wing planform according to their corresponding geometry parameters evaluated previously in the system packaging.

5.2.1.3 Propulsion Ducts

The method and the corresponding equations used for modelling the intake diffuser have been described earlier in section 5.1.3. Due to similar duct configurations, the modelling of the exhaust pipe is conducted using the same equation forms as the intake diffuser with a primary difference of the geometry parameters variations in the non cross-section planes (i.e. *XY* and *XZ*) being transformed in the other way round. This would produce a reverse circle-to-trapezium transformation starting from the engine nozzle to the exhaust plane instead of the trapezium-to-circle change presented in the intake diffuser case. A list of the equations used for generating the exhaust pipe model can be found in Appendix B.2.

5.2.2 Uninhabited Tanker

Since both the tanker and the UCAV fundamentally feature the same airframe configuration, the mathematical models of the fuselage and wing described in the previous UCAV section can be directly applied to the tanker design without changes. Despite the resemblance of their modelling equations, the appearances of both aircraft in general would eventually become distinctive due to the differences of their internal component constraints, design requirements and methods applied in the design synthesis methodology.

5.2.2.1 Propulsion Ducts

The mathematical equations used in the transformation of the tanker's centre duct are very similar to the UCAV's trapezium inlet case with an exception of the upper and the lower horizontal bases changes being now identical. Although the majority of aircraft components can be modelled based on half of the design geometry and then subsequently mirror the model results to create a complete object; due to the asymmetry trapezium shape of the side propulsion ducts, the entire cross-section model and hence the arc transformation of such components must be developed for all four corners as shown in Figure 5.9.

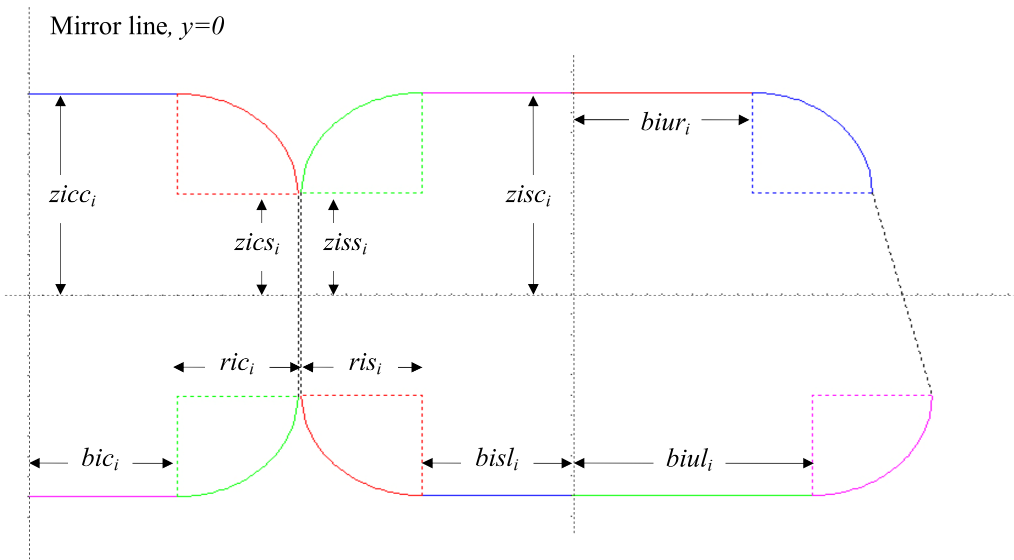

Figure 5.9: Mathematical model scheme of tanker's intake diffusers

A lateral S-shaped deflection is applied to the side propulsion ducts by integrating the spline function results to the y-coordinates of the evaluated cross-section model in a similar manner to the vertical deflection and its corresponding z-coordinates. The mathematical equations used in the modellings of the tanker's intake diffusers and exhaust pipes are provided in Appendix B.3.

5.2.2.2 Refuelling Equipment

Refer to the Figures 4.14 and 4.15, since the fairing pod design is symmetrical about its longitudinal centreline, any associated modelling equations can be developed based on half geometry, and then subsequently mirroring the results to generate a complete model of the component. The cross-section models generated in station *B*, illustrated in the Figure 4.14 (left), remains unchanged from the end of station *A*. Therefore, a duplicate of the last cross-section model of the station *A* can be directly used for the entire station *B* and hence additional modelling equations are not necessary. At the exit plane, the fairing dimensions would be reduced to the rectangular exit area required for refuelling hose deployment. The equations developed for modelling the above variable shaped stations of the fairing pod model (i.e. stations *A* and *C*) are formulated as shown below.

<u>Station A</u>

XY **Plane:** for $xf_{LE} \le x_i \le x_{\mathrm{HDU}}$

$$yfA_i = \frac{w_{\mathrm{HDU}}}{2} \cdot \left(\frac{x_i - xf_{LE}}{x_{\mathrm{HDU}} - xf_{LE}} \right) + y_{\mathrm{HDU}} \tag{5.37}$$

$$yfmA_i = bf_{\max} \cdot \left(\frac{x_i - xf_{LE}}{x_{\mathrm{HDU}} - xf_{LE}} \right) + y_{\mathrm{HDU}} \tag{5.38}$$

XZ **Plane:** for $xf_{LE} \le x_i \le x_{\mathrm{HDU}}$

$$zftA_i = z_{RF} \tag{5.39}$$

$$zfbA_i = \sin\left(\frac{\pi}{2} \cdot \left(\frac{x_i - xf_{LE}}{x_{\mathrm{HDU}} - xf_{LE}} \right) \right)^2 \cdot (z_{\mathrm{HDU}} - \mathrm{inc} - zftA_i) + zftA_i \tag{5.40}$$

***YZ* Plane:** for $y_{\mathrm{HDU}} \le y_j \le yfmA_i$

$$zfA_{\mathrm{i,j}} = zftA_i \qquad , \; y_{\mathrm{HDU}} \le y_j < yfA_i \tag{5.41}$$

$$zfA_{\mathrm{i,j}} = \left(\frac{yfmA_i - y_j}{yfmA_i - yfA_i}\right)\cdot(zfbA_i - zftA_i) + zftA_i$$

$$, \; yfA_i \le y_j \le yfmA_i \tag{5.42}$$

Station C

***XY* Plane:** for $xf_{T0} \le x_i \le xf_{TE}$

$$yfC_i = \frac{w_{\mathrm{HDU}}}{2} - \left(\frac{x_i - xf_{T0}}{xf_{TE} - xf_{T0}}\right)\cdot\left(\frac{w_{\mathrm{HDU}} - w_{\mathrm{he}}}{2}\right) + y_{\mathrm{HDU}} \tag{5.43}$$

$$yfmC_i = bf_{\max} - \left(bf_{\max} - \frac{w_{\mathrm{he}}}{2} - \frac{h_{\mathrm{he}}}{\tan(\theta_{\mathrm{RF}})}\right)\cdot\left(\frac{x_i - xf_{T0}}{xf_{TE} - xf_{T0}}\right) + y_{\mathrm{HDU}} \tag{5.44}$$

***XZ* Plane:** for $xf_{T0} \le x_i \le xf_{TE}$

$$zftC_i = z_{RF} - h_{\mathrm{he}} \tag{5.45}$$

$$zfbC_i = \sin\left(\frac{\pi}{2}\cdot\left(\frac{xf_{TE} - x_i}{xf_{TE} - xf_{T0}}\right)\right)^2 \cdot(z_{\mathrm{HDU}} + \mathrm{inc} - zftC_i) + zftC_i \tag{5.46}$$

***YZ* Plane:** for $y_{\mathrm{HDU}} \le y_j \le yfmC_i$

$$zfC_{\mathrm{i,j}} = zftC_i \qquad , \; y_{\mathrm{HDU}} \le y_j < yfC_i \tag{5.47}$$

$$zfC_{\mathrm{i,j}} = \left(\frac{yfmC_i - y_j}{yfmC_i - yfC_i}\right)\cdot(zfbC_i - zftC_i - h_{\mathrm{he}}) + z_{RF}$$

$$, \; yfC_i \le y_j \le yfmC_i \tag{5.48}$$

when, $\qquad xf_{T0} = x_{\mathrm{HDU}} + l_{\mathrm{HDU}} + \mathrm{inc}$

5.2.3 Model Geometry Specifications

As mentioned earlier in this chapter, one of the primary purposes for developing the 3D-aircraft model is to obtain accurate derived geometry specifications such as surface areas, cross-sectional area variation, and internal volume. Since the airframe and other components modelling data produced by mathematical equations are presented in a form of point coordinates, the above aircraft specifications can be evaluated from such data using fundamental integration theorem.

5.2.3.1 Integration Approach

As far as the principles of the integration are concerned, an integral of lines created by mathematical functions yields an area under the graph and this area can be further integrated in the direction perpendicular to its plane to obtain a volume. There are various integration methods available; however, the majority of them are not suitable for this application mainly due to unavailability of an integral solution or the complexity involved in the implemented methods. Therefore, one of the numerical quadrature methods employing trapezium approximation is selected on account of its methodical simplicity and sufficiently accurate estimation.

A surface area of the airframe can be found from an integration of the cross-section model coordinates between two adjacent model stations in the direction along the facet plane wrapping around the component. A cross-sectional area in each fuselage station can be evaluated similar to the above surface area except the integration is carried out on the cross-section plane instead of the surface plane. The internal volume available in the fuselage can be obtained by integrating the above cross-sectional areas in the aircraft's longitudinal direction, and then subtracting any occupied spaces due to internal components. A structural thickness factor is also included into the calculation to appropriately determine the free-volume result. As far as the wing component is concerned, the internal volume which can be effectively used for fuel storage is the wing-box section bounded by the front and the rear spars not the entire wing model, thus this is computed accordingly.

The above surface area and internal volume are mainly used in the refined empty-weight estimation, balance evaluation and aerodynamic performance analysis. Nonetheless, an application of the cross-sectional area is somehow different from others, which is theoretically used in a form of volume distribution for determining wave drag rise in the transonic flight regime. Generally this drag contribution is minimal when the cross-sectional area distribution of the aircraft resembles a perfect Sears-Haack body (i.e. a bell shape).

5.2.3.2 Cross-sectional Area Distribution Analysis

Although the distribution of aircraft's cross-sectional areas can be obtained from an integral of model geometry data as described above, this integration approach is applicable to the fuselage component where all cross-section models are projected on a plane perpendicular to the flight direction. This, however, is not the case for the wing component. The cross-section plane of the wing is formed in the spanwise direction; therefore, it is difficult to accurately translate the variation of spanwise cross-sections to the same plane as the fuselage, especially for the cranked-wing configuration of both tanker and UCAV. Thus, for the purpose of determining the contribution of the wing components to the total cross-sectional area distribution, a new method has been developed based on experimental wing-aerofoil data in conjunction with the spline modelling functions introduced in section 5.1.1 to predict the wing area distribution according to common wing geometry parameters.

In order to investigate the effects of wing configurations on the cross-sectional area distribution, and to acquire sufficient amounts of data used for developing the aforementioned prediction method, various configurations of the solid wing model were created on a dedicated 3D modelling program, SolidWorks, where their cross-sectional areas were measured uniformly using available tools in the program. These wing models were generated in accordant with the variations of the following geometry parameters; taper ratio λ, quarter-chord sweep Λ_{Q4}, semi-span b_{WS}, main chord c_{WS} and aerofoil thickness tc. As described in section 5.2.1.2, NACA-65 series aerofoils are applied in the modelling of the aircraft's wing due to its optimal figure for the overall fuselage model. Thus, this solid-model investigation was conducted on a basis of such aerofoil series.

Once the cross-sectional area data obtained from the above solid wing models had been plotted and analysed, it was found that the area distribution of trapezium wings always resembled a bell shape similar to the Sears-Haack body with the difference of the maximum area coordinate depending on the values of the aforementioned wing geometry parameters. The Sears-Haack body shape can be approximated as a combination of two S-shaped equations joining at the maximum area coordinate as shown below.

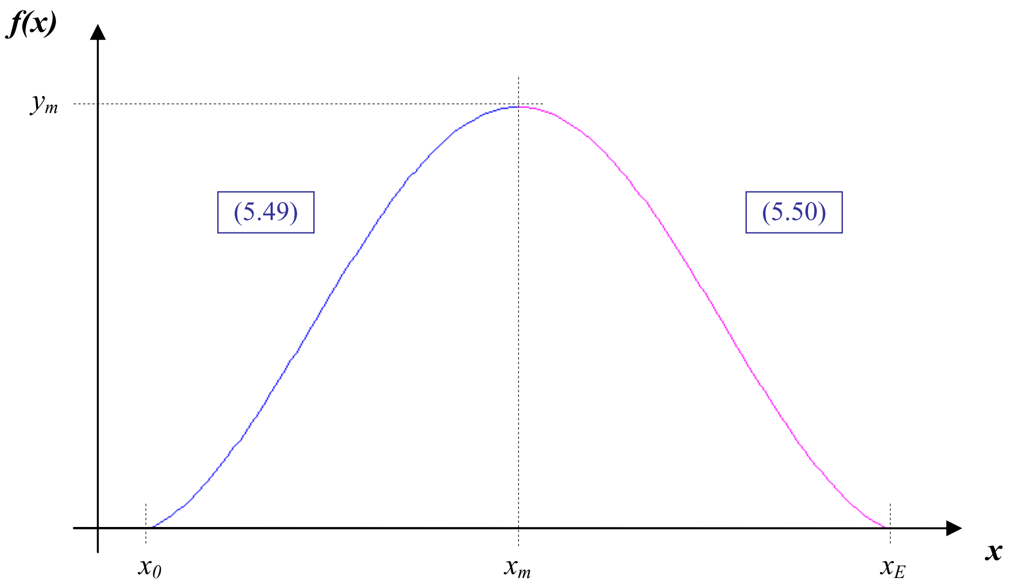

Figure 5.10: Sear-Haack body modelling

$$f(x) = \cos\left(\frac{\pi}{2}\cdot\left(\frac{x_m - x}{x_m - x_0}\right)\right)^{1.9}\cdot y_m \qquad , x_0 \le x \le x_m \qquad (5.49)$$

$$f(x) = \sin\left(\frac{\pi}{2}\cdot\left(\frac{x_E - x}{x_E - x_m}\right)\right)^{1.9}\cdot y_m \qquad , x_m \le x \le x_E \qquad (5.50)$$

Eq. (5.49) and Eq. (5.50) are developed for the exactly figure of the Sears-Haack body; however, for an accurate bell shape of the wing area distribution, both exponent values applied in the above equations should be corrected to 1.5.

The equation forms for the wing area distribution has been established, and the remaining parameters which need to be determined are the locations of x_0, x_E, x_m and y_m. For a given wing model, the x_0 can be simply specified at zero and then the x_E would equal to the total length of the model. On the other hand, the maximum cross-sectional area coordinates of x_m and y_m varies depending on the wing geometry parameters selected earlier. Due to a number of parameters influenced this coordinates variation, the position-shifting method has been developed to solve such a problem by initially specifying the starting x_m and y_m coordinates according to a certain wing configuration and then subsequently evaluating for the coordinates shifted from the original starting point due to the changes of geometry parameter values. And this correction procedure is carried out in orders for all of the geometry parameters involved to identify the final coordinate solution.

Since the equations associated with the above method were developed using specific scaled dimensions of the solid wing models, in order to implement such a method for actual wing geometry, the dimensional wing geometry parameters i.e. the main chord c_{WS} (m) and semi-span b_{WS} (m) must be converted to the following forms before proceeding to the rest of the evaluations.

$$b = \frac{b_{WS}}{\gamma_C} \tag{5.51}$$

when, $$\gamma_C = \frac{c_{WS}}{4} \tag{5.52}$$

For constant wing geometry parameters of $c_{WS} = 4$, $\lambda = 0.2$ and $b = 6$, the x_m coordinate varies with the quarter-chord sweep Λ_{Q4} (deg) as follows,

$$f_x(\Lambda_{Q4}) = 0.028 \cdot \Lambda_{Q4} + 1.76 \tag{5.53}$$

Similarly, the variation of x_m due to the taper ratio λ and the semi-span b values, provided that $c_{WS} = 4$ and $\Lambda_{Q4} = 40°$, can be developed into Eq. (5.54).

$$f_x(\lambda, b) = 0.338 + 0.648 \cdot \lambda + 0.752 \cdot b - 0.093 \cdot \lambda^2 - 0.065 \cdot b^2 + 0.104 \cdot \lambda \cdot b \tag{5.54}$$

The above equation is used for correcting the input taper ratio and semi-span from their original values specified in the conditions of Eq. (5.53). Thus, the x_m position for any given geometry parameters can be evaluated according to the equation shown below.

$$x_m = \gamma_C \cdot f_x(\Lambda_{Q4}) \cdot \frac{f_x(\lambda, b)}{f_x(\lambda_0, b_0)} \quad \text{, when } \lambda_0 = 0.2 \text{ and } b_0 = 6 \tag{5.55}$$

The evaluation of y_m coordinate shift is similar to the above x_m with the difference of the aerofoil thickness tc (%) now also effecting the changes of the y_m position. A list of the equations applied in the evaluation are summarised as follows,

For $\lambda = 0.2$, $b = 6$ and $c_{WS} = 4$,

$$f_y(tc, \Lambda_{Q4}) = 0.234 \cdot tc^{0.985} 0.976^{\Lambda_{Q4}} \tag{6.56}$$

For $\Lambda_{Q4} = 40°$, $c_{WS} = 4$ and $tc = 12\%$,

$$f_y(\lambda, b) = -0.069 - 0.089 \cdot \lambda + 0.373 \cdot b + 0.025 \cdot \lambda^2 - 0.036 \cdot b^2 + 0.135 \cdot \lambda \cdot b \tag{6.57}$$

$$y_m = \gamma_C \cdot f_y(tc, \Lambda_{Q4}) \cdot \frac{f_y(\lambda, b)}{f_y(\lambda_0, b_0)} \quad \text{, when } \lambda_0 = 0.2 \text{ and } b_0 = 6 \tag{6.58}$$

The above numerical method was developed on a basis of trapezium wing configurations; therefore, in order to apply such a method to the cranked-wing design of the tanker and the UCAV, the area distribution of each wing partition must be evaluated independently and then superposing all the results in accordant with their relative starting longitudinal positions as illustrated in Figure 6.4.

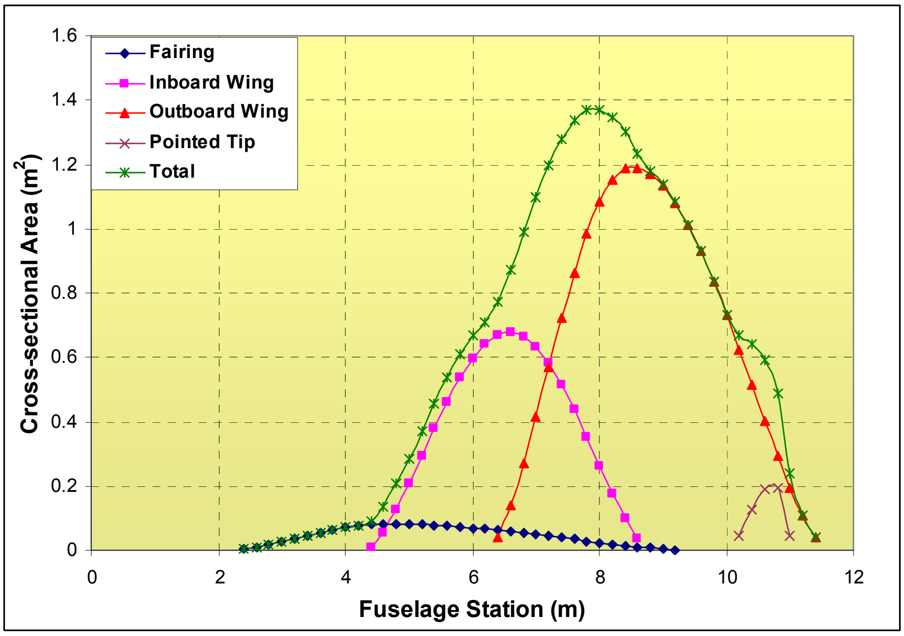

Figure 5.11: A superposition of wing cross-sectional area distributions

Theoretically, the distribution of the cross-sectional area accounted in the Sears-Haack body is that of the entire airframe, excluding the streamtube section. This refers to a region in which the airflow is considered passing through the aircraft, i.e. intake diffusers, engines and exhaust pipes. Thus the cross-sectional area produced by these components must be subtracted from that of the total airframe.

Although it is desirable to develop the design synthesis program which is capable of adjusting the cross-sectional area distribution of the aircraft to closely match the ideal Sears-Haack body; this requires complex computational algorithms assimilated into various geometry modules which would be highly time-consuming to develop. Furthermore, this ideal area distribution can normally be achieved by simultaneously optimising the entire airframe configuration together with the aircraft performances and operational feasibilities, which would be beyond the scope of the research works. For these reasons, a subroutine operation was integrated into the design synthesis to improve the shape of the overall cross-sectional area distribution by adjusting the values of fuselage packaging constraints within appropriate limits. The operations of the design synthesis including this cross-sectional area analysis subroutine are summarised in chapter 11.

Chapter 6

Aerodynamic Analysis

In this chapter, the principles of aerodynamic methods used for predicting lift and drag performances of the aircraft at a certain flight condition will be described. The majority of existing analysis methods, especially the accurate ones, require the uses of numerical formulae in conjunction with graphical plot estimations to achieve the results. Nonetheless, in an intricate flight regime such as the transonic, there is still no numerical method available for concretely predicting the aerodynamic behaviours of the aircraft. Thus the transonic aerodynamic analyses are normally performed by using wind tunnel testing and computational fluid dynamics. From a conceptual design perspective, it is suggested that manual approximations may be used together with a guideline of existing experimental data and numerical evaluation results to generate graphical plots of aerodynamic performance, e.g. lift-curve slope and wave drag rise, related to the Mach number [47]. However, since this research programme aims to deliver an automated design synthesis program, the methods used for numerically generating these graphical plots have been developed. Hence any computational code implementing such methods would be capable of evaluating the aerodynamic performances without manual intervention and thus optimising program's executions.

6.1 Lift

Initially USAF Digital Datcom program had been considered for using in the evaluations of lift and stability performances on account of its overall accurate prediction as well as the provision of non-linear aerodynamic performance results. However, since the designs of both tanker and UCAV are unconventional, the predicted results may not be well-accurate in their case. Also the input parameters Datcom required are not fully compatible with those available from the flying-wing configuration, and thus may result unknown errors easily. Although a computational interface between Datcom, a complex FORTRAN-based program, and Visual Basic.NET has been developed by Tormo [60], only the Missile category was fully validated, while the Aircraft part still remains in questions. After considering the above drawbacks, it was decided that the lift performance analysis methods suggested by Raymer [47], would be applied in conjunction with the numerical approximation of graphical plots mentioned earlier.

Although time was not permitted for a study and implementation of the actual Datcom methodology, the methods selected above are, in fact, a simplified version of those featuring in the Datcom itself. Despite the unavailability of non-linear region performance evaluations, the methods themselves provide accurate prediction for fundamental elements which deem to be sufficient for the context of this aerodynamic performance study. The methods recommended for calculating the lift-curve slope in the subsonic and supersonic regions are presented as follows.

Subsonic region

$$C_{L\alpha} = \frac{2\pi \cdot AR}{2 + \sqrt{4 + \left(\frac{AR \cdot \beta}{\eta}\right)^2 \cdot \left(\frac{1 + \tan^2(\Lambda_{T\max})}{\beta^2}\right)}} \cdot \left(\frac{S_{\text{exp}}}{S_{\text{ref}}}\right) \cdot F \qquad (6.1)$$

when, $$\beta = \sqrt{1 - M^2} \qquad (6.2)$$

$$\eta = \frac{C_{l\alpha}}{(2\pi / \beta)} \qquad (6.3)$$

$$F = 1.07 \cdot \left(1 + \frac{d}{b}\right)^2 \quad (6.4)$$

Supersonic region

$$C_{L\alpha} = \frac{4}{\beta} \quad (6.5)$$

when, $\beta = \sqrt{M^2 - 1}$ (6.6)

where,

$C_{L\alpha}$	- Lift-curve slope (rad^{-1})	$C_{l\alpha}$	- Aerofoil lift-curve slope (rad^{-1})
S_{ref}	- Reference wing area	S_{exp}	- Exposed wing area
$\Lambda_{T\max}$	- Wing sweep at the maximum thickness-to-chord position		

Since Eq. (6.1) requires the reference wing parameters, equivalent geometry of an actual cranked-wing of the aircraft is applied accordingly. A local fuselage diameter d is considered from the longitudinal position on the aircraft where half of the mean aerodynamic chord is located while b refers to the maximum width of the fuselage.

Although both tanker and UCAV are designed to operate at high-subsonic speed, it is desired to develop the aerodynamic analysis method which is capable of predicting the behaviour of the lift-curve slope throughout the entire transonic region i.e. between $0.8 \le M \le 1.2$. In general, the shape of the graphical plot between the lift-curve slope and Mach number in the transonic and the initial supersonic areas can be approximated fairly accurately with a spline-type equation applied between appropriate boundary constraints. Such an equation has been developed in a form shown below.

$$C_{L\alpha}(M_{\mathrm{x}}) = \sin\left(\frac{\pi}{2} \cdot \left(\frac{M_{\mathrm{u}} - M_{\mathrm{x}}}{M_{\mathrm{u}} - M_{\mathrm{l}}}\right)\right)^N \cdot \left(C_{L\alpha}(M_{\mathrm{l}}) - C_{L\alpha}(M_{\mathrm{u}})\right) + C_{L\alpha}(M_{\mathrm{u}}) \quad (6.7)$$

$C_{L\alpha}(M)$ refers to the lift-curve slope value at the Mach number M. Two boundary constraints of M_{l} and M_{u} are located in the subsonic and supersonic regions respectively. As described previously in section 5.1.1, an exponent value in the above equation influences how abrupt the geometry curvature developed. Thus, a rather-high exponent N would be considered for the purpose of fitting the general course of the lift-curve slope behaviour with the Mach number.

Raymer [47] recommended that Eq. (6.1) could be applied up to almost the sonic speed with reasonable accuracy, which implies that the subsonic boundary constraint M_l cannot exceed $M = 1.0$. On the other hand, the Eq. (6.5) representing the supersonic region is directly taken from the 2D theoretical equation which tends to overestimate the lift-curve slope values near $M = 1.0$ before starting to converge and concur with the general course of experimental data at very high Mach number. An extensive investigation has been conducted to identify appropriate parameter values for Eq. (6.7), and it was found that a combination of $N = 6$, $M_1 = 0.99$ and $M_u = 2.5$ produces a smooth fairing curve which reflects the overall behaviour of the lift-curve slope in the transonic and the initial supersonic regimes as depicted in the example figure below.

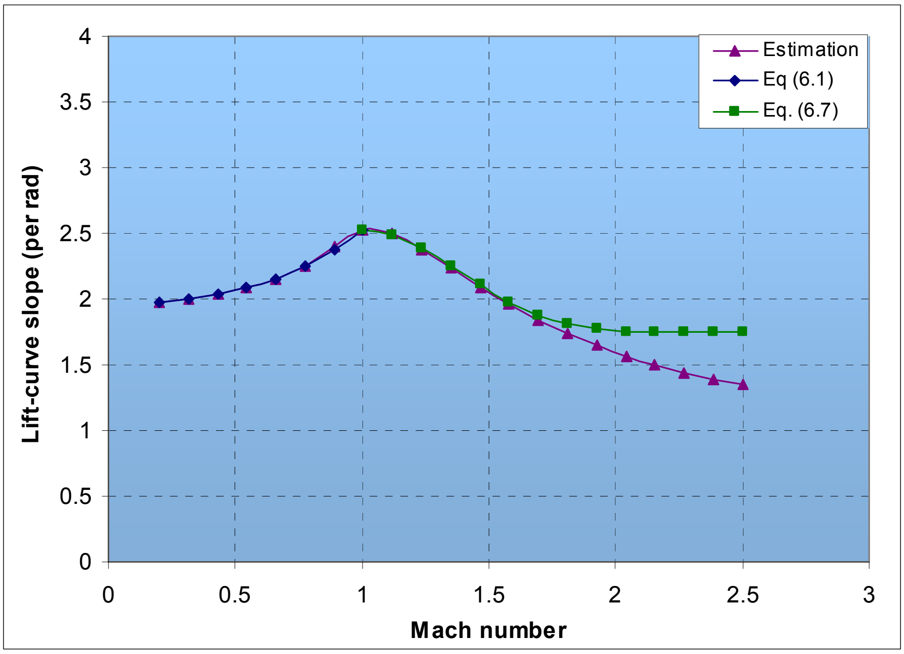

Figure 6.1: Lift-curve slope vs. Mach number

For any given Mach number, Eq. (6.1) will be applied for calculating the lift-curve slope up to $M = 0.99$, while the performance evaluation at greater Mach number can be found from Eq. (6.7) together with the constraint values defined above. Nonetheless, as illustrated in Figure 6.1, the above equation can only produce the results which reflect the initial part of the estimated fairing curve in the supersonic region, and thus it is appropriate to state that the Eq. (6.7) can be applied in the lift-curve slope evaluation up to $M = 1.5$.

Since the wing configurations of both tanker and UCAV are highly swept and possess a rather-low aspect ratio, additional vortices would be generated from the wing's leading edge providing increments of the maximum lift coefficient and stall angle. The methods used for appropriately computing these improved performances due to the vortex induced effects are provided in reference [47]. However, due to a number of graphical plot analyses involved in the evaluations, any associated graphical references used have been developed into numerical equations shown below. The methodology consists of two evaluation methods for different categories of high-aspect ratio and low-aspect ratio wings. For a given wing geometry, the aspect ratio categories are considered based on taper-ratio correction factor C_1 which can be found using Eq. (6.8). Also both C_1 and C_2 will be required in subsequent evaluations if the wing geometry falls into the low-aspect ratio category.

$$C_1 = -4.633 \cdot \lambda^4 + 13.3 \cdot \lambda^3 - 13.188 \cdot \lambda^2 + 4.549 \cdot \lambda - 0.023 \tag{6.8}$$

$$C_2 = \frac{\lambda}{(1.477 + 3.995 \cdot \lambda - 4.245 \cdot \sqrt{\lambda}} \tag{6.9}$$

If $AR > \dfrac{3}{(C_1 + 1) \cdot \cos(\Lambda_{LE})}$ then the following equations representing the high-aspect ratio wing will be applied, otherwise the low-aspect ratio methods from Eq. (6.21) onward will be used instead.

High aspect ratio

If $M > 0.5$ then Eq. (6.10) is needed for determining Mach-number correction factor mcr, otherwise, $mcr = 1$.

$$mcr = 0.185 \cdot M^3 - 0.738 \cdot M^2 + 0.305 \cdot M + 1.008 \tag{6.10}$$

For the high-aspect-ratio wing evaluation, the leading-edge sharpness Δy needed can be found from the maximum aerofoil thickness tc.

$$\Delta y = 19.3 \cdot tc \tag{6.11}$$

Maximum lift coefficient:

$$\begin{aligned}\frac{C_{L\max}}{C_{l\max}} = {} & 0.067 + 0.635 \cdot \Delta y + 0.033 \cdot \Lambda_{LE} - 0.089 \cdot \Delta y^2 + (2.78 \times 10^{-5}) \cdot \Lambda_{LE}{}^2 \\ & - 0.018 \cdot \Delta y \cdot \Lambda_{LE}\end{aligned} \tag{6.12}$$

$$C_{L\max} = mcr \cdot C_{l\max} \cdot \left(\frac{C_{L\max}}{C_{l\max}} \right) \tag{6.13}$$

where,

$C_{L\max}$ - Maximum lift coefficient Λ_{LE} - Leading-edge sweep (deg)

$C_{l\max}$ - Aerofoil maximum lift coefficient

Stall Angle:

$$\Delta\alpha_{CL_{\max}} = 0.048 \cdot \Delta y^{-0.523} \cdot \Lambda_{LE}{}^{1.393} \tag{6.14}$$

$$\alpha_{CL_{\max}} = \frac{C_{L\max}}{C_{L\alpha}} + \alpha_0 + \Delta\alpha_{CL_{\max}} \tag{6.15}$$

where,

$\alpha_{CL\max}$ - Stall angle (degree) α_0 - Zero-lift angle (degree)

Low aspect ratio

As mentioned earlier, the derived parameters of the taper-ratio correction factors C_1 and C_2 are needed for the low-aspect ratio case. Such parameters are represented by the equations below.

$$Ct_1 = (C_1 + 1) \cdot \frac{AR}{\beta} \cdot \cos(\Lambda_{LE}) \tag{6.16}$$

$$Ct_2 = (C_2 + 1) \cdot AR \cdot \tan(\Lambda_{LE}) \tag{6.17}$$

β refers to the aerofoil efficiency which can be calculated using Eq. (6.6) in the lift-curve slope evaluation.

Maximum lift coefficient:

$$C_{L\max} = (C_{L\max})_{\text{base}} + \Delta C_{L\max} \tag{6.18}$$

when,

$$\begin{aligned}(C_{L\max})_{\text{base}} = {} & 0.042 \cdot Ct_1^{\ 5} - 0.423 \cdot Ct_1^{\ 4} + 1.666 \cdot Ct_1^{\ 3} - 3.124 \cdot Ct_1^{\ 2} \\ & + 2.496 \cdot Ct_1 + 0.504\end{aligned} \tag{6.19}$$

$$\begin{aligned}\Delta C_{L\max} = {} & -0.253 - 0.257 \cdot \ln(M) - 0.087 \cdot \ln(M)^2 - 0.004 \cdot Ct_2 + 0.012 \cdot Ct_2^{\ 2} \\ & - (1.46 \times 10^{-3}) \cdot Ct_2^{\ 3} + (1.2 \times 10^{-4}) \cdot Ct_2^{\ 4} + (4.87 \times 10^{-6}) \cdot Ct_2^{\ 5}\end{aligned} \tag{6.20}$$

Stall Angle:

$$\alpha_{CL_{\max}} = (\alpha_{CL_{\max}})_{\text{base}} + \Delta\alpha_{CL_{\max}} \tag{6.21}$$

If $Ct_1 \leq 0.8$ then $(\alpha_{CL_{\max}})_{\text{base}} = 35$, otherwise the parameter is evaluated as follows,

$$(\alpha_{CL_{\max}})_{\text{base}} = 20.747 - 0.224 \cdot Ct_1^{\ 2} \ln(Ct_1) + \frac{14.896}{Ct_1^{\ 1.5}} \tag{6.22}$$

Similarly for $\Delta\alpha_{CL_{\max}}$ evaluation, if $Ct_2 \leq 4$ then Eq. (6.23) below is applied and Eq. (6.25) if that is not the case.

$$\begin{aligned}\Delta\alpha_{CL_{\max}} = {} & 9.919 - 1.683 \cdot x - 4.248 \cdot Ct_2 + 0.036 \cdot x^2 + 0.621 Ct_2^{\ 2} \\ & + 0.135 \cdot x \cdot Ct_2\end{aligned} \tag{6.23}$$

when, $\quad x = AR \cdot \cos(\Lambda_{LE}) \cdot (1 + 4 \cdot \lambda^2) \quad (6.24)$

$$\Delta\alpha_{CL_{\max}} = -5.573 + 20.571 \cdot M + 0.531 \cdot Ct_2 - 17.708 \cdot M^2 + 0.075 \cdot Ct_2 - 1.661 \cdot M \cdot Ct_2 \tag{6.25}$$

6.2 Drag

Under incompressible flow assumptions, the total drag on an aircraft consists of zero-lift and induced drags. The primary contribution of the zero-lift drag comes from skin-friction drag which highly depends on the aircraft's surface area and its overall airframe design, while the induced drag, on the other hand, is directly proportional to the lift force generated by the aircraft. Since both tanker and UCAV are designed to fly at high subsonic speed i.e. in the transonic flow regime, an increase in the total drag would also incur due to the pressure of shocks called 'wave drag.' The general methods used for evaluating the aforementioned three drag categories are provided in reference [47]. However, additional modifications and further developments have also been made in order to be able to implement such methods in the computational design synthesis program.

6.2.1 Zero-lift drag

The component build-up method has been selected for zero-lift drag prediction. Such a method features an accumulation of subsonic skin-friction drags produced by each airframe's component including their mutual interference effects between nearby objects, thus providing sufficient accuracy for this drag evaluation section. Since the equations and the methodology from reference [47] are adopted without changes, they will not be discussed in details. Nonetheless, the above reference does not contain an accurate method for evaluating the skin-fraction drag due to flap deflection which is necessary for identifying the total drag value when the aircraft is trimmed in flight using flap control surfaces. A semi-empirical method used for predicting an increment of the zero-lift drag coefficient due to the flap deflection is also provided by reference [44]. Such a method, however, requires a graphical analysis of the flap drag coefficient at zero-sweep angle and other associated parameters; thus the graphical data have been developed into Eq. (6.26) shown below.

$$\Delta C_{DP_0} = (5.3\times 10^{-3}) + 0.049\cdot\left(\frac{c_f}{c}\right) + (7.29\times 10^{-4})\cdot\partial f + 0.019\cdot\left(\frac{c_f}{c}\right)^2 + (1.17\times 10^{-5})\cdot\partial f^2 + 0.012\cdot\left(\frac{c_f}{c}\right)\cdot\partial f \tag{6.26}$$

Once the above ΔC_{DP_0} has been evaluated, the sweep-angle correction is applied to determine the actual result.

$$\Delta C_{D0\text{ flap}} = \Delta C_{DP_0}\cdot\cos(\Lambda_{Q4})\cdot\left(\frac{S_{\text{f}}}{S_{\text{ref}}}\right) \tag{6.27}$$

where,

Λ_{Q4}	- Quarter-chord sweep angle (deg)	S_{f}	- Flapped area
∂f	- Flap deflection angle (deg)	c_f/c	- Flap-to-chord ratio
$\Delta C_{D0\text{ flap}}$	- Zero-lift drag coefficient due to flap deflection		

During air refuelling operations, the tanker is required to trail refuelling hose-drogues into the freestream which would undoubtedly incur additional drag to the aircraft. According to an investigation regarding this matter conducted by NASA Dryden Flight Research Centre [63], the zero-lift drag coefficient increment due to a single hose-drogue unit trailing was found to be approximately a constant value of 0.0056 for all typical refuelling flight conditions. Thus, the above drag coefficient value is appropriately accounted to the tanker's aerodynamic performance calculations for every refuelling segment.

At the end of the mission when the tanker and the UCAVs decend to land, the weights of both aircraft are light compared to their thrust capabilities. Also due to the lack of tail stabilisers, these flying-wing aircraft possess less zero-lift drag in general. Thus, it proved to be highly difficult for these aircraft to properly descent at near-empty weight condition using idle thrust. In order to rectify such an issue, air brake installations are assumed at the top and the bottom of the fuselage airframe near the aircraft c.g. location where the pitching moment contributions from such devices can be reasonably neglected. For both aircraft, the same air brakes are also deployed in field performance operation to shorten the landing distance. An increase in drag due to the air brakes employment is accounted as a percentage of the total clean zero-lift drag coefficient of respective aircraft.

6.2.2 Wave drag

A conceptual-level method applied for estimating the transonic drag rise suggested by Raymer [47] requires the use of graphical plot which must be created according to certain Mach number stations and their corresponding drag increments due to the shockwaves. These wave drag values are determined using various approaches from simplified assumptions to numerical evaluations depending on the flight regime in which the Mach number stations are located. The majority of these parameter stations, however, are pre-stated with an exception of the drag-divergence Mach number which is governed by the design of the aircraft.

6.2.2.1 Drag-divergence Mach Number

The drag-divergence Mach number M_{dd} refers to the point where the wave drag at any part of the airframe starts to increase. The methods applied for evaluating M_{dd} are separated for two individual airframe components, the fuselage and the wing, by which the final M_{dd} value of the aircraft will be selected from the lowest Mach number result produced by any part of the above components.

Fuselage

Generally, the fuselage M_{dd} value depends on how slender the nose geometry is; however, as far as the designs of the proposed aircraft are concerned, the nose geometry section can be longitudinally extended to the frontal engine location (i.e.

maximum fuselage cross-sectional area). Eq. (6.28) has been developed based on supersonic curve data of M_{dd} and fuselage factor ff provided by reference [59].

$$M_{\mathrm{dd}} = (4.4 \times 10^{-4}) \cdot ff^{3} - (1.17 \times 10^{-3}) \cdot ff^{2} + 0.109 \cdot ff + 0.594 \tag{6.28}$$

when, $$ff = \frac{2 \cdot l_n}{d} \tag{6.29}$$

l_n is the length of the nose geometry section while d is an equivalent diameter of the fuselage at end of the section.

Wing

The quarter-chord sweep Λ_{Q4} and the maximum aerofoil thickness tc of the wing primarily influence the Mach number at which the drag divergence occurs. Since the cranked-wing design of both uninhabited aircraft contains a variation of sweep angles, the M_{dd} of each wing partition would occur at different values. For this reason, the equations presented below must be applied to each partition individually and then compare the Mach number results for the lowest value together with that obtained from the above fuselage evaluation. Also under super-critical-aerofoil performance assumptions, a factor of 0.6 is multiplied to the value of tc (%) in Eq. (6.31) and Eq. (6.32) which have been created from the associated graphical data that need to be analysed in this wing M_{dd} evaluation.

$$M_{\mathrm{dd}} = M_{\mathrm{dd}0} \cdot LF_{\mathrm{dd}} - 0.5 \cdot C_{L\mathrm{dsn}} \tag{6.30}$$

when,

$$\begin{aligned} LF_{\mathrm{dd}} = {} & 0.976 + 0.13 \cdot C_L + (5.81 \times 10^{-3}) \cdot tc - 0.157 \cdot C_L^{\,2} - (2.9 \times 10^{-4}) \cdot tc^2 \\ & - 0.022 \cdot tc \cdot C_L \end{aligned} \tag{6.31}$$

$$\begin{aligned} M_{\mathrm{dd}0} = {} & 0.636 + (1.27 \times 10^{-3}) \cdot \Lambda_{Q4} + \frac{1.836}{tc} + (4 \times 10^{-5}) \cdot \Lambda_{Q4}^{\,2} - \frac{4.197}{tc^2} \\ & - \frac{(7.59 \times 10^{-3}) \cdot \Lambda_{Q4}}{tc} \end{aligned} \tag{6.32}$$

The designed lift coefficient $C_{L\mathrm{dsn}}$ can be estimated based on the lift performance and hence the weight of the aircraft in cruise condition with half of the fuel and the payloads carried.

6.2.2.2 Drag-rise Curve Evaluation

Once the M_{dd} of the aircraft has been determined, the Mach number stations on the transonic drag-rise curve are specified as follows. The first two stations, from the highest value, are located at $M_A = 1.2$ and $M_B = 1.05$ where their corresponding wave drag coefficients C_{D_w} are evaluated using a supersonic wave-drag equation shown below.

$$C_{D_w} = \frac{E_{WD}}{S_{\mathrm{ref}}} \cdot \left(1 - 0.386 \cdot (M - 1.2)^{0.57} \cdot \left(1 - \frac{\pi \cdot \Lambda_{LE-\deg}{}^{0.77}}{100} \right) \right) \cdot \left(\frac{D}{q} \right)_{\mathrm{Sears-Haack}} \tag{6.33}$$

when, $$\left(\frac{D}{q} \right)_{\mathrm{Sears-Haack}} = \frac{9 \cdot \pi}{2} \cdot \left(\frac{A_{\max}}{l_{a/c}} \right) \tag{6.34}$$

where,

E_{WD} - Empirical wave-drag efficiency parameter

$l_{a/c}$ - Total aircraft length

$A_{\max}$ - Maximum cross-sectional area of aircraft

Due to the complexity of the methods involved in a proper evaluation of E_{WD} based on a given cross-sectional area distribution of the aircraft, and as far as the contexts of this drag performance analysis are concerned, it is more appropriate to specified a reasonble value of such a parameter instead. The next station is considered at the sonic speed (i.e. $M_C = 1$) where the corresponding C_{D_w} is linearly approximated from the value at M_B.

$$C_{D_{wC}} = \left(\frac{C_{D_{wB}} - 0.002}{2} \right) + 0.002 \tag{6.35}$$

The last two stations located in the subsonic region are determined by the M_{dd} value, where $M_D = M_{\text{dd}}$ and $M_E = M_{\text{dd}} - 0.08$. The C_{Dw} at the drag-divergence Mach number can be approximated as 0.002. Also M_E is the critical Mach number which indicates the starting point of this drag rise phenominon, thus $C_{DwE} = 0$.

In order to develop a complete transonic drag-rise curve, the above Mach number stations together with their corresponding wave drag coefficients are used as control points for the manual drawing of fairing curves. However, for the purpose of accommodating computational implementation of the methods, the spline equations used in the modelling of airframe have been applied for generating the aforementioned fairing curves between the Mach number stations in a similar fashion to the previous lift-curve slope evaluation in transonic region. The equations applied in the respective regions of the drag rise curve are presented as follows.

$$C_{Dw} = \tan\left(\frac{\pi}{4} \cdot \left(\frac{M - M_E}{M_D - M_E}\right)\right) \cdot \left(C_{DwD} - C_{DwE}\right) + C_{DwE} \qquad , M_E \le M < M_D \qquad (6.36)$$

$$C_{Dw} = \tan\left(\frac{\pi}{4} \cdot \left(\frac{M - M_D}{M_C - M_D}\right)\right)^{1.5} \cdot \left(C_{DwC} - C_{DwD}\right) + C_{DwC} \qquad , M_D \le M < M_C \qquad (6.37)$$

$$C_{Dw} = \left(\frac{M - M_C}{M_B - M_C}\right) \cdot \left(C_{DwB} - C_{DwC}\right) + C_{DwC} \qquad , M_C \le M < M_B \qquad (6.38)$$

$$C_{Dw} = \sin\left(\frac{\pi}{2} \cdot \left(\frac{M - M_B}{M_A - M_B}\right)\right)^{1.35} \cdot \left(C_{DwA} - C_{DwB}\right) + C_{DwB} \qquad , M_B \le M \le M_A \qquad (6.39)$$

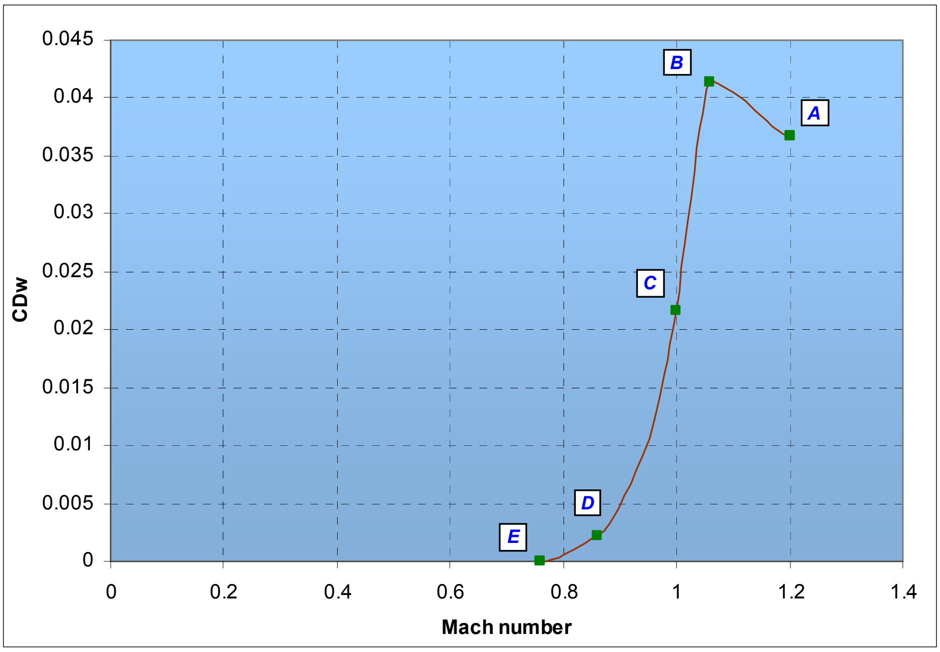

Figure 6.2: Transonic drag rise estimation

Figure 6.2 illustrates the transonic drag-rise curve produced by the above equations. Thus, for any given high-subsonic Mach numbers, the C_{D_w} incurred at the flight conditions can be readily determined.

6.2.3 Induced Drag

As mentioned at the beginning, the induced drag occurs as a result of the lift force generated by the aircraft. This drag due-to-lift is commonly written in the form shown below.

$$C_{D_i} = K \cdot C_L{}^2 \tag{6.40}$$

Although the Oswald span efficiency method could be applied in the T/W - W/S analysis to estimate the induced-drag factor K, such a method would not be able to provide sufficient accuracy for this detailed performance analysis due to the assumption of constant wing efficiency throughout the flight. For this reason, a method for approximating K based upon the leading-edge suction theory was selected instead. By accounting the variation of K due to the changes of the lift coefficient, the leading-edge-suction method is capable of estimating the induced drag accurately at any subsonic flight conditions. Since such a method requires the use of graphical data depicting a relationship between the leading-edge suction performance and the lift coefficient, this plot data has been converted into Eq. (6.41) shown below.

$$\begin{aligned} S = {} & 1.028 - 1.028 \cdot C_{L\mathrm{dsn}} - 0.546 \cdot C_L - 0.076 \cdot C_{L\mathrm{dsn}}{}^2 - 2.53 \cdot C_L{}^2 + 7.357 \cdot C_L \cdot C_{L\mathrm{dsn}} \\ & - 4.472 \cdot C_{L\mathrm{dsn}}{}^3 + 2.167 \cdot C_L{}^3 - 7.664 \cdot C_{L\mathrm{dsn}} \cdot C_L{}^2 + 6.053 \cdot C_{L\mathrm{dsn}}{}^2 \cdot C_L \end{aligned} \tag{6.41}$$

$$K = \frac{1}{C_{L\alpha} \cdot (1 - S) + S} \tag{6.42}$$

The value of the leading-edge suction parameter S varies from 0 to approximately 0.93. In general, the closer the current lift coefficient C_L of the aircraft to its design value $C_{L\mathrm{dsn}}$, the higher the S. Thus, resulting higher K and less induced drag for a given C_L.

Chapter 7

Weight and Stability

7.1 Refined Empty-weight Estimation

The detailed empty-weight predictions of both tanker and UCAV consist of empirical equations presented in references [44, 47]. These equations were selected primarily based on their input requirements subjected to the data available from the aircraft model. Also the number and the type of parameters used to formulate the equations were taken into consideration, and generally the equations which include greater number of relevant input parameters tend to deliver more accurate weight prediction. For example, refers to Appendix C, Eq. (C.2) for the wing weight estimation recommended by Raymer [47] takes a control-surface area into account as a multiplier. However, since such components are not installed on the fairing and the tip partitions, if a zero were to be input then the weight result would be undoubtedly incorrect. On the other hand, Roskam [44] suggested Eq. (C.1) for the same component featuring similar equation structure, but with an absence of the control surface area parameter. Thus for an optimal solution, it was decided that Eq. (C.2) would be applied to the wing partitions which are configured with the control surfaces, while the weights of other clean wing partitions would be evaluated using Eq. (C.1).

A complete list of the equations used for predicting the UCAV and the tanker empty weights can be found in Appendix C. Some of the adopted equations, however, need human-related parameters e.g. the number of crews N_c in Eq. (C.17) and Eq. (C.19). While $N_c = 0$ implying no-pilot factor in uninhabited aircraft can be appropriately applied to Eq. (C.19), the same value cannot be used in Eq. (C.17) due to its multiplication form, thus it is justifiable to assume $N_c = 1$ for such an equation. Also since the selected empirical weight equations were developed on a basis of existing aircraft database, some of the equations, in particular structure-related ones, would result over-predicted weights if an advanced technology such as lighter composite materials were employed in the designed aircraft. Therefore, fudge factors for major structural components, i.e. wing, fuselage, undercarriages and propulsion ducts, have been included into the corresponding equations in order to obtain accurate weights prediction that accounts for technology improvements.

7.2 Balance

As described earlier in the modelling of the airframe, for the majority of the aircraft's components, the volume distributions and hence their associated centre of gravity can be derived from the model coordinate data providing higher accuracy compared to the statistical approximations. Thus, the centre of fuselage's volume is deemed to be sufficiently accurate for representing the c.g. position. As far as the fixed shaped internal components such as weapon bays, undercarriages and APU are concerned, the c.g. locations can be evaluated according to their corresponding geometry models. Since the avionic compartments were assumed to be distributed in the nose area of the fuselage, its c.g. is approximated as that of the fuselage station A. As shown in Figure 7.1, due to the linear variation of propulsion system's cross-sectional area along the fuselage's length, their c.g. positions are calculated based on the centroid of each component's area formed under the graph.

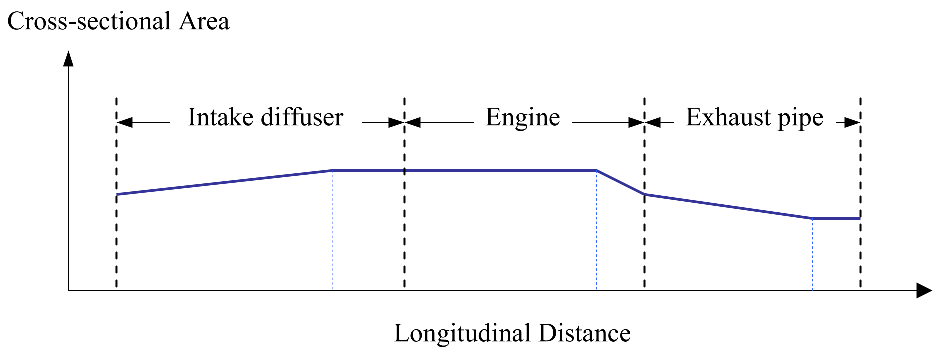

Figure 7.1: Overall volume distribution of the propulsion system

According to Torenbeek [51], the longitudinal c.g. location of a swept wing is approximately at 70% local distance between the front and the rear spars and at 35% semi-span from the main chord. Such conditions are applied to each partition of the aircraft's wing. The wing fuel tanks, on the other hand, are allocated in the wing-box space available between the spars; therefore, it is sufficiently rational to specify the c.g. location in middle between the spars at the spanwise distance measured from the inboard of y which can be calculated using Eq. (7.1) below.

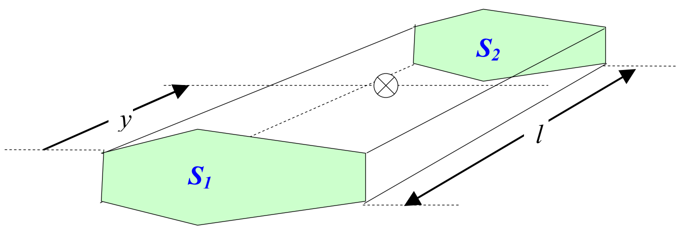

Figure 7.2: c.g. approximation of prismoid wing fuel tank

$$y = \frac{l}{4} \cdot \frac{S_1 + 3 \cdot S_2 + 2 \cdot \sqrt{S_1 \cdot S_2}}{S_1 + S_2 + \sqrt{S_1 \cdot S_2}} \tag{7.1}$$

Due to an assumption of distributed fuselage fuel tanks in the centre body (i.e. stations *B*, *C* and *D*), the volume's centre of these fuselage stations is used for representing the fuel tank's c.g. location. Also in order to reduce the complexity of aircraft's balance evaluations, the fuel transferring system between tanks is assumed to maintain the non-reserve fuel's c.g. position constant throughout the entire operation. On the other hand, the reserve fuel tanks locations are allowed to be shifted from the above c.g. location for a certain performance operation providing more flexible option to stabilise these flying-wing configuration aircraft from internal. Though this is not the case for the UCAV, the fuselage and the wing fuel tanks' c.g. locations of the tanker are separated for its own fuel use and the fuel payload carried. The approximated c.g. locations of the components defined in the detailed weights estimation of both aircraft are illustrated in Figure 7.3 and 7.4 below.

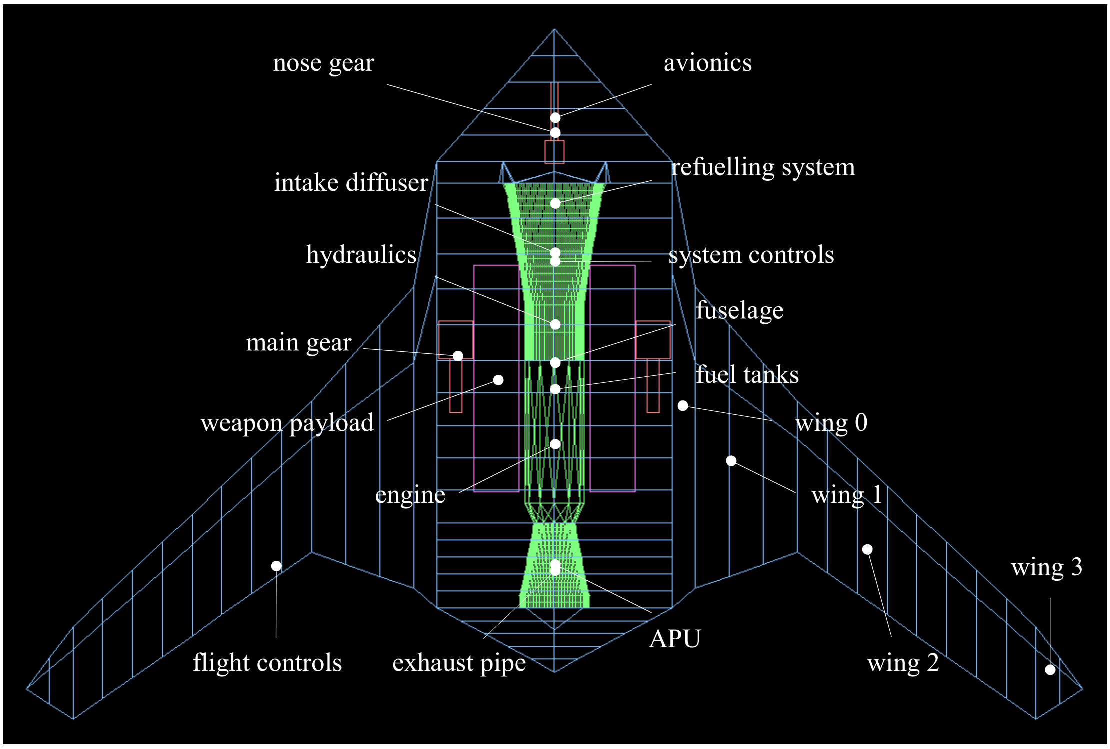

Figure 7.3: c.g. locations of UCAV's components

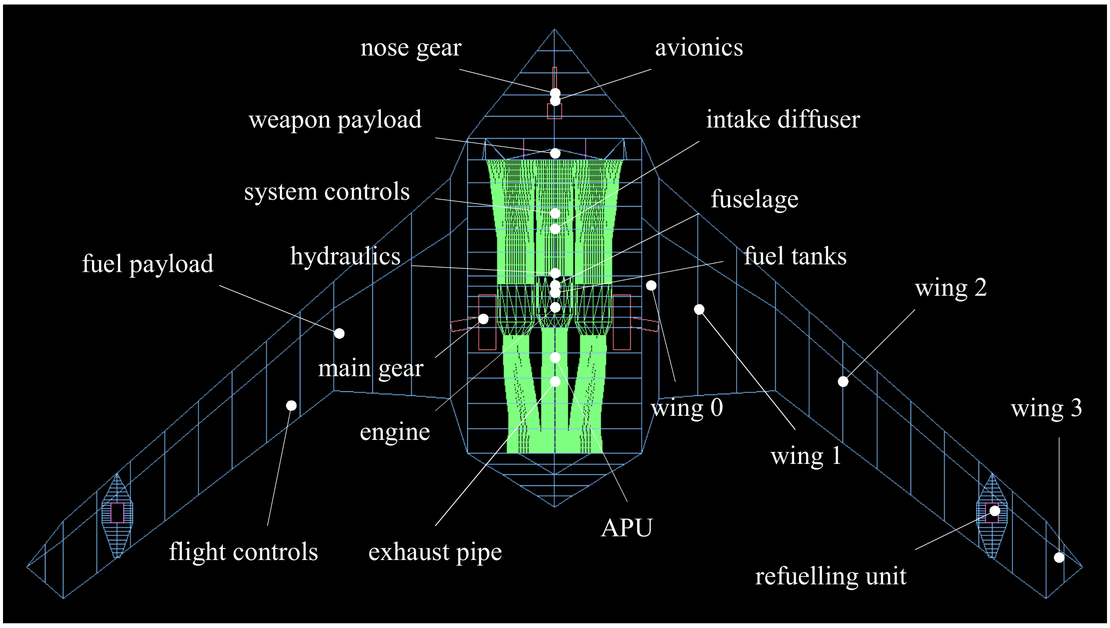

Figure 7.4: c.g. locations of tanker's components

7.3 Stability

In general, the stability analysis concerns how the designed aircraft response to the changes of various forces acting on during the flight and how the aircraft's balance can be achieved with appropriate angular orientation and control surface application. Within the contexts of this study, however, only longitudinal stability performance is focused due to the time limitation. As described previously in the baseline design considerations, due to the lack of powerful moment arms such as tail planes, the flying-wing aircraft needs to rely on the control surfaces available on the main wing for both stabilising and manoeuvring purposes. Therefore, these devices generally would not have sufficient rooms for supporting the lift-augmentation role at any points in the operation. Nonetheless, due to the low-aspect ratio and highly-swept wing configuration of the designed aircraft, the generated vortex induced effects substantially compensate the absence of high-lift device functions by enhancing the maximum lift coefficient and the stall angle of the aircraft which prove to be highly beneficial for takeoff and landing. The equations described in this section are taken from reference [47] unless individually specified.

7.3.1 Static Stability

The static pitch stability of both tanker and UCAV is derived as shown in Eq. (7.2). In order to stabilise these tailless aircraft, the first term needs to provide a negative pitching-moment derivative contribution, i.e. the c.g. must be located in front of the wing aerodynamic centre, to oppose the positive pitching tendency generated by the second term from the fuselage. The last term in the equation is a small contribution of the inlet normal force which can be neglected in the 'power-off' aircraft stability evaluation.

$$C_{m\alpha} = C_{L\alpha} \cdot \left(\frac{x_{\mathrm{cg}} - x_{\mathrm{acw}}}{c} \right) + C_{m\alpha F} + \frac{F_{p\alpha}}{q \cdot S_W} \cdot \frac{\partial \alpha_p}{\partial \alpha} \cdot \left(\frac{x_{\mathrm{cg}} - x_{\mathrm{p}}}{c} \right) \tag{7.2}$$

where,

$C_{m\alpha}$	- Total pitching-moment derivative	$C_{L\alpha}$	- Wing lift-curve slope
c	- Mean aerodynamic chord	q	- Dynamic pressure

Generally, the position of the aerodynamic centre of the wing x_{acw} is located at its quarter-chord point; however, such a position moves toward the trailing edge as the Mach number increases. This shift of this aerodynamic centre can be estimated using Eq. (7.3) shown below. The effect of the fuselage is considered later in this section in the estimation of the aircraft's neutral point (see Eq.7.7).

$$\Delta x_{\mathrm{acw}} = 0.25 \cdot c + \Delta x_{\mathrm{ac}} \cdot \sqrt{S_W} \tag{7.3}$$

when, $\Delta x_{\mathrm{ac}} = 0.26 \cdot (M - 0.4)^{2.5}$, $0.4 < M \leq 1.1$

$\Delta x_{\mathrm{ac}} = 0.112 - 0.004 \cdot M$, $M > 1.1$

where,

Δx_{acw} - Aerodynamic centre measured from the wing leading edge

The fuselage contribution to the pitching moment derivative can be obtained from the evaluation of Eq. (7.4) when w_F is the maximum width of the fuselage and l_F is the length. Eq. (7.5) provided for determining the empirical factor K_{fF} was developed from the corresponding graphical reference associated with Eq. (7.4).

$$C_{m\alpha F} = \frac{K_{fF} \cdot w_F^{\ 2} \cdot l_F}{c \cdot S_W} \tag{7.4}$$

when, $$K_{fF} = (6.1\times10^{-3}) - (1.64\times10^{-4}) \cdot x_{\mathrm{Q4}} + (1.86\times10^{-6}) \cdot x_{\mathrm{Q4}}^{\ 2.5} \tag{7.5}$$

where,

$C_{m\alpha F}$ - Fuselage pitching moment (deg)

x_{Q4} - Position of root quarter chord relative to total fuselage length (%)

The inlet normal force term in Eq. (7.2) occurs as a result of the air turning at the inlet front-face location x_{p}, hence providing a small contribution to the total pitching-moment derivative. The turning angle α_p coincides with the fuselage α; therefore, $\partial\alpha_p / \partial\alpha = 1$. Eq. (7.6) derived from the basic mass-flow rate formula is used for calculating the derivative of the normal force $F_{p\alpha}$ required in the main equation.

$$F_{p\alpha} = \rho \cdot V^2 \cdot A_{\mathrm{inlet}} \tag{7.6}$$

where,

A_{inlet} - Inlet area.

Eq. (7.2) can be rearranged into Eq. (7.7) for defining the neutral point x_{np} which refers to the position where the pitching moment is unchanged regardless of the angles of attack, i.e. $C_{m\alpha} = 0$. Also the total pitching-moment derivative equation described above is usually expressed in term of 'static margin' which can be derived from the x_{np} as shown in Eq. (7.8) below.

$$x_{\mathrm{np}} = \frac{C_{L\alpha} \cdot x_{\mathrm{acw}} - C_{m\alpha F} \cdot c + \dfrac{F_{P\alpha}}{q \cdot S_W} \cdot x_{\mathrm{p}}}{C_{L\alpha} + \dfrac{F_P}{q \cdot S_W}} \tag{7.7}$$

$$SM = \left(\frac{x_{\mathrm{np}} - x_{\mathrm{cg}}}{c} \right) \times 100 \tag{7.8}$$

where,

SM - Static margin (%)

The static margin generally provides an indication of whether the aircraft is stable. For an unmanned platform as such the designed tanker and UCAV, it is appropriate to assume that any instability occurring in cruise due to minor negative static margin can be accurately counteracted with the use of autonomous flight control systems.

7.3.2 Pitching Moment Equation

As far as the flying-wing configurations are concerned, the total pitching moment coefficient about an aircraft c.g. can be summarised as displayed in Eq. (7.9) below. The majority of the pitching-moment contributions are similar to those appeared in conventional aircraft with an exception of the tail lift contribution being excluded.

$$\begin{aligned} C_{m\mathrm{cg}} = {} & C_{L\ \mathrm{total}} \cdot \left(\frac{x_{\mathrm{cg}} - x_{\mathrm{acw}}}{c} \right) + (C_{mW\mathrm{i}} + C_{mW\mathrm{o}} + C_{mW\partial\mathrm{i}} \cdot \delta_{f\mathrm{i}} + C_{mW\partial\mathrm{o}} \cdot \delta_{f\mathrm{o}}) \\ & + (C_{m\alpha F} \cdot \alpha) - \frac{T \cdot z_t}{q \cdot S_W \cdot c} + \frac{F_{P\alpha} \cdot \alpha}{q \cdot S_W} \cdot \left(\frac{x_{\mathrm{cg}} - x_{\mathrm{p}}}{c} \right) \end{aligned} \tag{7.9}$$

when, $$C_{L\ \mathrm{total}} = C_{L\alpha} \cdot (\alpha + i_w - \alpha_{0L} - \Delta\alpha_{0L\ \mathrm{i}} - \Delta\alpha_{0L\ \mathrm{o}}) \tag{7.10}$$

where,

T	- Total thrust	α	- Angle of attack
α_{0L}	- Zero-lift angle	i_w	- Wing incidence relative to the fuselage
z_t	- Distance between the thrust-line and the vertical c.g. position		

From the above equations, the parameters required for the fuselage and the normal-force terms have been described in the previous section of static stability, while the pitching moment contribution due to the wing is separated for the inboard and the outboard wing partitions as denoted by the subscript character. Each wing partition consists of the pitching moment generated by the wing itself C_{mW} and its associated increment due to the flap deflection $C_{mW\partial}$. The C_{mW} value is primarily influenced by the zero-lift pitching moment of the aerofoil $C_{m0_{AF}}$ as shown in Eq. (7.11). Also due to the transonic effects, a 30% increment of the C_{mW} magnitude will be accounted for any speed regions in which the Mach number is greater 0.8.

$$C_{mW} = C_{m0_{AF}} \cdot \left(\frac{AR \cdot \cos^2 \Lambda_{LE}}{AR + 2 \cdot \cos \Lambda_{LE}} \right) - 0.01 \cdot \varepsilon \tag{7.11}$$

where,

ε - Wing twist (deg)

The contribution of the wing pitching moment due to the flap deflection is evaluated on a basis of the lift increment and the moment arm from the flap lift increment's centre of pressure x_{fcp} to the c.g. as depicted in Eq. (7.12). Nonetheless, from the graphical plot [64] accompanied with the equation, the x_{fcp} value varies linearly with flap-to-chord ratio (c_f / c) as shown in Eq. (7.13) below.

$$C_{mW\partial} = K_f \cdot \frac{\partial C_l}{\partial \delta_f} \cdot \left(\frac{x_{\text{fcp}} - x_{\text{cg}}}{c} \right) \tag{7.12}$$

when, $$\frac{\Delta x_{\text{fcp}}}{c'} = 0.5 - 0.25 \cdot \left(\frac{c_f}{c} \right) \tag{7.13}$$

where,

Δx_{fcp} - Centre of pressure of the flap lift increment measured from the hinge line.

c' - Flapped mean aerodynamic chord.

The lift increment per flap deflection $\partial C_l / \partial \delta_f$ can be calculated from its theoretical value $(\partial C_l / \partial \delta_f)_t$ using Eq. (7.14). The $(\partial C_l / \partial \delta_f)_t$ is a function of maximum aerofoil thickness and flap-to-chord ratio as shown in Eq. (7.15) which has been developed from the associated graphical plot provided by reference [64].

$$\frac{\partial C_l}{\partial \delta_f} = 0.9 \cdot K_f \cdot \left(\frac{\partial C_l}{\partial \delta_f}\right)_t \cdot \frac{S_{\text{flapped}}}{S_W} \cdot \cos \Lambda_{HL} \tag{7.14}$$

when,

$$\begin{aligned}\left(\frac{\partial C_l}{\partial \delta_f}\right)_t &= 6.909 + 2.748 \cdot \ln\left(\frac{c_f}{c}\right) + 5.374 \cdot tc + 0.356 \cdot \ln\left(\frac{c_f}{c}\right)^2 + 8.305 \cdot tc^2 \\ &\quad + 2.482 \cdot \ln\left(\frac{c_f}{c}\right) \cdot tc\end{aligned} \tag{7.15}$$

where,

S_{flapped}	- Flapped wing area	Λ_{HL}	- Hinge-line sweep angle
tc	- Maximum aerofoil thickness relative to the chord.		

The K_f parameters in both Eq. (7.12) and Eq. (7.14) refer to the same empirical correction for the lift increment due to the flap at large deflections. From the corresponding chart given by reference [37], the K_f value is 1.0 for the deflection ∂_f less than 10°, otherwise Eq. (7.16) which is a numerical expression created from the chart is applied.

$$\begin{aligned}K_f &= 0.24 + 1.701 \cdot \left(\frac{c_f}{c}\right) + 0.129 \cdot \delta_f - 3.212 \cdot \left(\frac{c_f}{c}\right)^2 - 0.007 \cdot \delta_f^{\,2} - 0.1 \cdot \left(\frac{c_f}{c}\right) \cdot \delta_f \\ &\quad + 3.159 \cdot \left(\frac{c_f}{c}\right)^3 + (1.12 \times 10^{-4}) \cdot \delta_f^{\,3} + (1.42 \times 10^{-3}) \cdot \left(\frac{c_f}{c}\right) \cdot \delta_f^{\,2} + 0.03 \cdot \left(\frac{c_f}{c}\right)^2 \cdot \delta_f\end{aligned} \tag{7.16}$$

With all above information acquired, the total wing contributions to the pitching moment about the aircraft c.g. can be found; nonetheless, the above lift increment due to the flap deflection $\partial C_l / \partial \delta_f$ is also accounted in the reduction of zero-lift angle $\Delta\alpha_{OL}$ in Eq. (7.10) used for evaluating the total lift coefficient. This $\Delta\alpha_{OL}$ can be expressed in the equation form shown below.

$$\Delta\alpha_{OL} = -\frac{1}{C_{l\alpha}} \cdot \frac{\partial C_l}{\partial \delta_f} \cdot \delta_f \tag{7.17}$$

$C_{l\alpha}$ is the aerofoil lift-curve slope while $\partial C_l / \partial \delta_f$ can be evaluated using the Eq. (7.14) described previously. Eq. (7.17), however, may result over-predicted control surface effectiveness, thus it is noted that the product of the first two parameters in the above equation cannot exceed the constraint value calculated below.

$$\frac{1}{C_{l\alpha}} \cdot \frac{\partial C_l}{\partial \delta_f} = 1.576 \cdot \left(\frac{c_f}{c}\right)^3 - 3.458 \cdot \left(\frac{c_f}{c}\right)^2 + 2.882 \cdot \left(\frac{c_f}{c}\right) \tag{7.18}$$

7.3.3 Trim Analysis

For a given flight condition, an aircraft is considered as 'trimmed' when the total moment about its c.g. is equal to zero which can be obtained by flying at an appropriate combination of the angle of attack α and the flap deflection δ_f. A graphical analysis technique called 'trim plot' is commonly used for determining the α and δ_f combination required to stabilise the aircraft. The trim plot employs certain ranges of the above parameters to compute the pitching moment coefficient $C_{m\,\mathrm{cg}}$ using Eq. (7.9) and the total lift coefficient $C_{L\,\mathrm{total}}$ from Eq. (7.10). Subsequently, the $C_{m\,\mathrm{cg}}$ will be plotted against $C_{L\,\mathrm{total}}$ according to the ranges of α and δ_f values as illustrated in Figure 7.5.

From the figure below, the trim plot data in general are linearly aligned in constant series except at large δ_f values when the lift correction factor K_f becomes active. And for a given value of the $C_{L\,\mathrm{total}}$, the trim point is located on the coordinate of $C_{m\,\mathrm{cg}} = 0$. Therefore, the solution of α and δ_f combination which precisely crosses at the trim point can be approximated using linear interpolations between the surrounding calculated trim points. For the purpose of simplifying the computational implementation of this trim plot analysis, the same magnitude of the flap deflection angle is applied to both inboard and outboard wings. However, the inboard-wing flap deflection would be employed in the opposite direction to the outboard wing if the x_{fcp} of the inboard-wing flap is located in front of the c.g. location of the aircraft. This is in order to counteract the pitching moment in the appropriate direction.

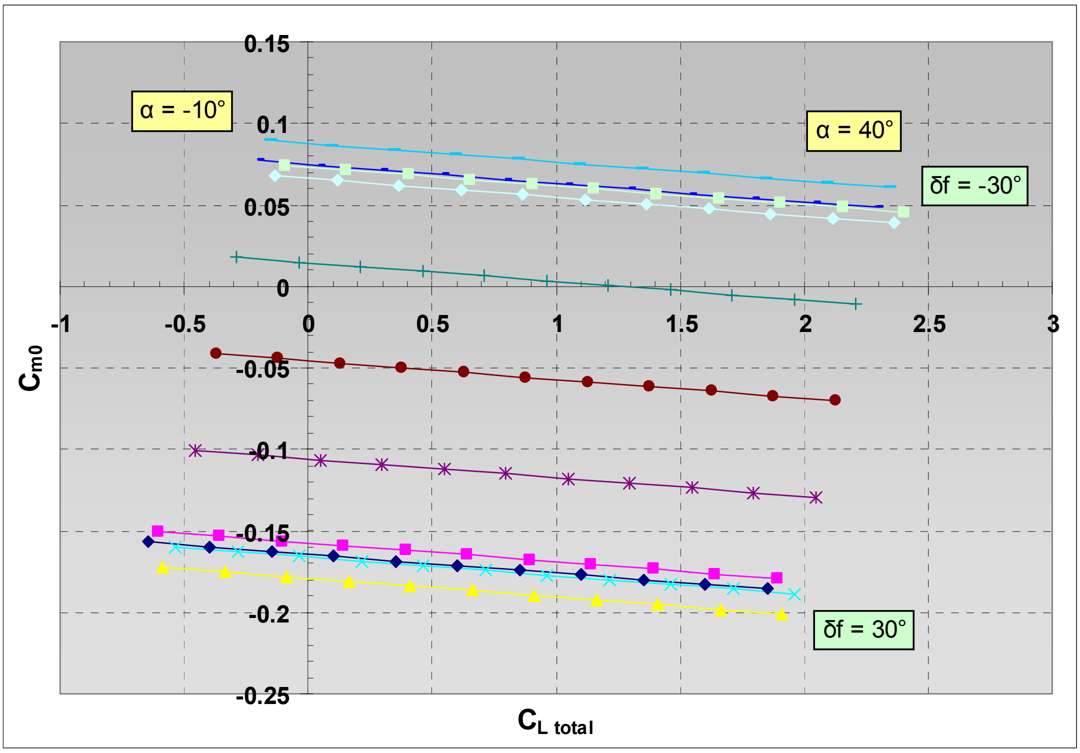

Figure 7.5: Trim plot example

Under steady flight assumptions, the total lift coefficient of an aircraft is equal to its current weight; therefore, the total induced drag coefficient including trim drag effects can be simply summarised as shown in the second term of the total drag equation below.

$$C_{D\ \text{trimmed}} = C_{D0} + K \cdot C_{L\ \text{total}}^2 \tag{7.19}$$

The trim drag effect on the profile drag coefficient C_{D0} is basically the total skin-friction drag increases due to flap deflection. This drag contribution can be evaluated using Eq. (6.27) described the previous chapter once the flap deflection angle required for stabilising the aircraft has been determined from the above trim analysis.

Chapter 8

Performance

8.1 Engine Performance

The uninstalled thrust parameter needed for sizing the physical dimensions of the aircraft's engine has already been described in section 4.1.1; however, the performances of the engine itself, such as the maximum thrust capability and specific fuel consumption, vary depending on operating flight conditions. In order to determine these performance variations with sufficient accuracy, the engine performance analysis methods developed by Mattingly [21] were selected for such purposes. The methods, in general, contain two evaluation sections, the on-design and the off-design cases. The on-design analysis is performed to identify the optimal performances of engine's components (e.g. compressor, burner, and turbine) at the design operating condition which is commonly referenced to the sea level. These optimum performances are required as reference parameters for the off-design analysis in which its objective is to evaluate the changes of the above engine components' performances and hence the output variations, for any other flight conditions in an operating envelope of the engine.

Although an executable FORTRAN-based program implementing the above engine performance analysis methods called 'ONX/OFFX' is provided together with the reference [21], the program was found to be substantially prone to errors. Also as far as the operation of the ONX/OFFX is concerned, developing an interface between such a program and other design synthesis modules written on Visual Basic.NET platform would be time-consuming. For these reasons, it was decided that the original on-design and off-design analysis methods would be written as part of the design synthesis modules providing more robust and more flexible methodology implementation. The engine performance analysis methods and their corresponding equations adopted from reference [21] are provided in Appendix D.

8.1.1 UCAV

Due to the UCAV's design requirement of low-bypass ratio engine, the methods for analysing a mixed-stream turbofan engine configuration were applied. The on-design cycle method is conducted by analysing airflow properties throughout the engine stations from the freestream entry at the fan to the exhaust nozzle exit as illustrated in Figure 8.1. The airflow properties evaluated at each station are mostly defined in non-dimensional forms such as the pressure ratio π and the temperature ratio τ ; and also including various mass-flow-related parameters e.g. bypass ratio α , bleeding air fraction β , fuel-to-air ratios f and etc. These parameters are used for evaluating the thrust (and hence the specific fuel consumption) generated as a result of the momentum and the total pressure changes over the component stations of the engine. A list of the equations for the analysis of the on-design engine performance can be found in Appendix D.1.1.

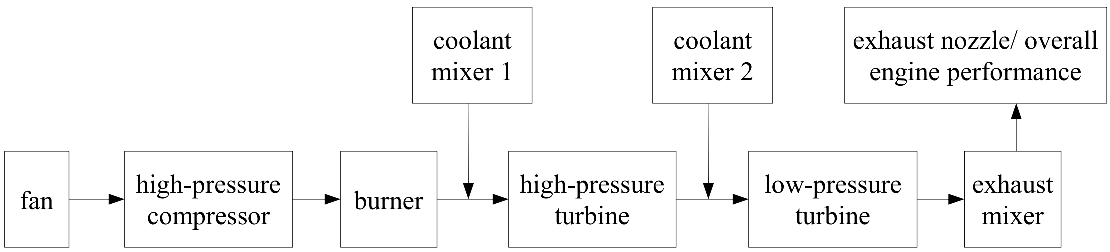

Figure 8.1: On-design cycle analysis process of the UCAV's engine

Since the original methods of the mixed-flow turbofan engine analysis provided in the reference [21] include an afterburner which is not required in the UCAV's engine; Eq. (D.41), Eq. (D.42) and Eq. (D.47) have been modified by eliminating any afterburner contributions from the equations. Without additional energy input from the afterburner, the ratio of specific heats γ for determining the exit Mach number M_9 in Eq. (D.43) would remain constant from the exhaust mixer station; therefore, γ of the afterburner was replaced by γ_6. Also due to an absence of the afterburner's temperature limitation, the total temperature ratio terms in Eq. (D.44) and Eq. (D.45) have been derived from the corresponding parameters determined in the prior engine stations.

A fudge factor for the specific fuel consumption fs is included to Eq. (D.48) in order to correct the output performance and to account for technology improvements. Nonetheless, this fudge factor is not required for calibrating the specific thrust value in Eq. (D.47) because the thrust performance has been improved over time in correspondent to the reduction of engine's physical dimensions. Therefore, providing that recent engine data have already been selected in the development of the size prediction equations; the modification to the above specific thrust equation is not necessary.

While the evaluations of the on-design analysis are generally performed in a straight order according to the sequence of the engine stations, the off-design analysis requires iterative procedures to verify and simultaneously calculate several unknown engine stations' performance parameters. The UCAV's off-design cycle evaluations can be summarised as illustrated in Figure 8.2. The initial values of the iteration parameters i.e. temperature ratio at low-pressure turbine τ_{tL}, mass flow rate m_0 and exhaust-mixer bypass ratio α' are specified to the reference values determined from the on-design analysis. These parameter values would be adjusted as the iterations advance until a fitting solution combination is found. The equations applied in the off-design cycle analysis as well as their evaluation order are listed in Appendix D.1.2.

With the original threshold accuracy values suggested in the reference [21] for verifying the above iteration parameters against their calculated counterpart, the off-design analysis would have a tendency of not being able to locate such a precise solution combination and thus repeating the evaluations infinitely. And if by any chances the solution is found, the overall execution time would be relatively long which is not desirable. For these reasons, the threshold accuracy values have been modified from the originals with more appropriate precisions in order to substantially reduce the running time and the aforementioned evaluation error.

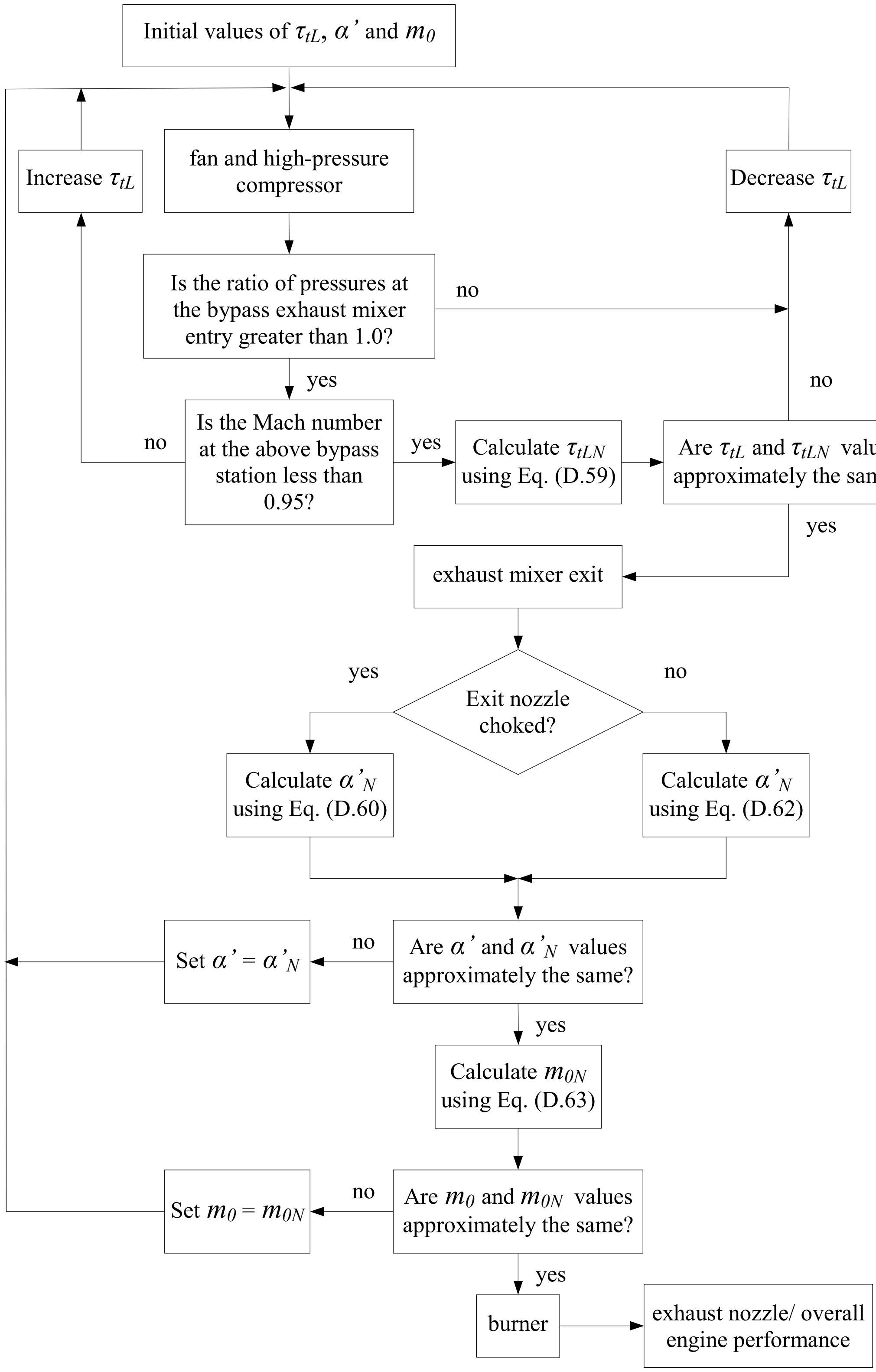

Figure 8.2: Off-design cycle analysis process of the UCAV's engine

8.1.2 Uninhabited Tanker

In order to minimise the fuel consumption of the tanker, a high-bypass ratio engine, and hence the corresponding analysis methods for such an engine category, have been selected. The majority of the on-design analysis processes remain the same as the previous mixed flow turbofan engine applied in the UCAV case; however, their primary difference is the absence of the exhaust mixer station (see Figure 8.1). Therefore, the fan-stream exhaust nozzle is separated from the core-stream section. Since the methods provided in the reference [21] for analysing high-bypass ratio engines already exclude the afterburner, the equations listed in Appendix D.2.1 were adopted directly with a minor modification of the specific fuel consumption correction due to the same reasons described in the UCAV section.

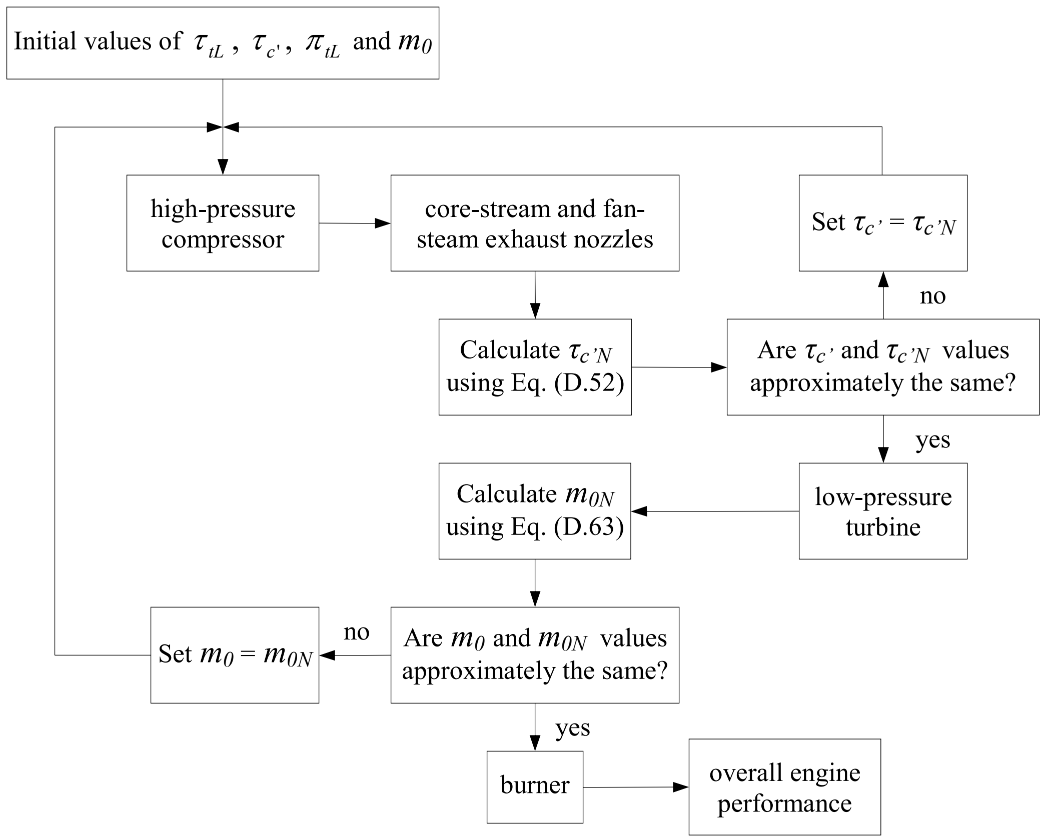

Figure 8.3: Off-design cycle analysis process of the tanker's engine

Figure 8.3 shows a summary of the off-design cycle evaluations for the high-bypass ratio engine. Despite the similarity in term of using an iterative approach to identify the solution, the evaluation process and the starting performance parameters are different from the off-design analysis shown in the Figure 8.2. The detailed procedures as well as the equations applied in the off-design cycle analysis for the high-bypass ratio engine can be found in Appendix D.2.2.

8.2 Field Performance

The field performance analysis primarily focuses on the evaluations of the takeoff and landing runway distances required for operating aircraft from an air base. Also the balanced field length, which is an important performance specification for the tanker, is included as part of the takeoff analysis. The equations and criteria used in this section are provided by reference [47].

8.2.1 Takeoff Analysis

The detailed analysis of the takeoff performance consists of multiple operation segments. These are the level ground roll, rotation to takeoff, transition to the climb and additional climb period if the height clearance at the end of the transition segment is not sufficient. The total takeoff distance can be found simply from an accumulation of the horizontal distances covered in the above operation segments.

Ground Roll and Rotation

Eq. (8.1) formulated for evaluating the ground-rolling distance S_G was originally developed from an integration of the velocity changes from V_i to V_f, when K_T and K_A are the functions of thrust and aerodynamic performances respectively.

$$S_G = \frac{1}{2 \cdot g \cdot K_A} \cdot \ln\left(\frac{K_T + K_A \cdot V_f^{\,2}}{K_T + K_A \cdot V_i^2} \right) \tag{8.1}$$

when, $$K_T = \left(\frac{T}{W}\right) - \mu \tag{8.2}$$

$$K_A = \frac{\rho}{2 \cdot (W/S)} \cdot \left(\mu \cdot C_L - C_{D0} - K \cdot C_L^{\ 2}\right) \tag{8.3}$$

where,

T/W	- Thrust-to-weight ratio	W/S	- Wing loading
ρ	- Air density	μ	- Ground rolling resistance
V_i	- Initial velocity = 0	V_f	- Final velocity = $1.1 \cdot V_{\text{stall}}$
C_L	- Lift coefficient	C_{D0}	- Zero-lift drag coefficient

The takeoff rolling friction coefficient μ for a dry-concrete runway is approximately 0.03. Also C_L and C_{D0} are the corresponding aerodynamic coefficients at the ground-rolling conditions with undercarriages deployed and no high-lift devices usage.

The time taken for the aircraft to rotate and lift-off from the ground varies from one to three seconds depending on the size of the aircraft. Due to this short time interval, it is reasonable to assume that there is no acceleration during this segment. Therefore, the rotation distance S_R can be simply calculated based on constant takeoff velocity as follows.

$$S_R = t_R \cdot V_{TO} \tag{8.4}$$

where,

t_R	- Rotation time	V_{TO}	- Takeoff velocity = $1.1 \cdot V_{\text{stall}}$

Transition to Climb

The horizontal distance travelled during the transition and possibly the initial climb segments are determined primarily on a basis of an altitude gained in the transition period comparing to the obstacle clearance requirement. This transition height h_{TR} can be evaluated in accordant with the equations shown below.

$$h_{TR} = R \cdot (1 - \cos\gamma_{CL}) \tag{8.5}$$

when, $$R = \frac{V_{TR}^{\;2}}{0.2 \cdot g} \tag{8.6}$$

$$\gamma_{CL} = \sin^{-1}\left(\frac{T}{W} - \frac{1}{L/D}\right) \tag{8.7}$$

where,

γ_{CL}	- Climb angle	L/D	- Lift-to-drag ratio
R	- Transition arc radius	V_{TR}	- Transition velocity = $1.15 \cdot V_{\text{stall}}$

The obstacle height clearance h_{obs} required for military aircraft is defined at 50 feet. The transition distance S_T is determined from one of the following equations depending on whether the above obstacle clearance is satisfied before the end of the transition segment.

$$S_T = R \cdot \sin\gamma_{CL} \qquad \text{, if } h_{\text{obs}} > h_{TR} \tag{8.8}$$

$$S_T = \sqrt{R^2 - (R - h_{TR})^2} \qquad \text{, otherwise} \tag{8.9}$$

An additional travelling distance would be required during the initial climb if the obstacle height was not met in the previous transition segment. This climb horizontal distance S_{CL} can be evaluated using Eq. (8.10).

$$S_{CL} = \frac{h_{\text{obs}} - h_{TR}}{\tan\gamma_{CL}} \qquad \text{, if } h_{\text{obs}} > h_{TR} \tag{8.10}$$

$$S_{CL} = 0 \qquad \text{, otherwise} \tag{8.11}$$

The γ_{CL} value used in this climb segment is calculated using Eq. (8.7) with the climb velocity $V_{CL} = 1.2 \cdot V_{\text{stall}}$ instead of the transition conditions applied earlier.

Balanced Field Length

The balanced field length is the total takeoff distance required if a pilot decides to bring an aircraft to stop when an engine failure occurs at the decision speed, otherwise the takeoff procedure must be continued. This performance specification is not applicable to the UCAV due to its single-engine configuration.

$$BFL = \left(\frac{0.863}{1+2.3\cdot G}\right)\cdot\left(\frac{W/S}{\rho\cdot g\cdot C_{LCL}}+h_{\text{obs}}\right)\cdot\left(\frac{1}{(T_{av}/W)-U}+2.7\right)+\left(\frac{655}{\sqrt{\rho/\rho_{SL}}}\right) \tag{8.11}$$

when, $U = 0.01\cdot C_{L\max} + 0.02$

$G = \gamma_{CL} - \gamma_{\min}$

$$T_{av} = 0.75\cdot T_{\substack{\text{takeoff}\\ \text{static}}}\cdot\left(\frac{5+BPR}{4+BPR}\right) \tag{8.12}$$

where,

BFL	- Balanced field length (ft)	BPR	- Engine bypass ratio
ρ/ρ_{SL}	- Air density ratio	C_{LCL}	- C_L at climb velocity

γ_{CL} refers to the climb condition in which the reduced thrust and the wind-mill drag rise due to one engine out of service must be taken into account. The value of $\gamma_{\min}$ varies according to the number of the engines, and for the three-engine configuration of the tanker $\gamma_{\min} = 0.027$.

8.2.2 Landing Analysis

The detailed landing analysis is fundamentally similar to the takeoff case except the entire operation segments are carried out in reverse. Also the maximum landing weight of the aircraft considered in the analysis is specified from the input as a function of the maximum takeoff weight.

Approach and Flare

The approach segment starts from the same obstacle height clearance h_{obs} described earlier in the takeoff section. In order to determine the horizontal distances travelled in the approach and the flare segments, the flare radius and the associated height must be obtained first using Eq. (8.13).

$$h_F = R \cdot (1 - \cos\gamma_A) \tag{8.13}$$

when, $$R = \frac{V_F^{\ 2}}{0.2 \cdot g} \tag{8.14}$$

where,

γ_A	- Approach angle	V_F	- Flare velocity $= 1.15 \cdot V_{\text{stall}}$
R	- Flare radius	h_F	- Flare height

An ideal approach-to-land angle of -3 degree is directly specified to the γ_A value. The approach and the flare horizontal distances can be calculated using Eq. (8.15) and Eq. (8.16) respectively.

$$S_A = \frac{h_{\text{obs}} - h_F}{\tan\gamma_A} \tag{8.15}$$

$$S_F = R \cdot \sin\gamma_A \tag{8.16}$$

Ground Roll

Once the aircraft touchdown, a few seconds are allowed for free rolling before brakes are applied. Under an assumption of no deceleration during this period, the free-rolling distance can be simply determined from Eq. (8.17), while the previous takeoff ground-roll equation is adopted for evaluating the braking distance in the landing operation as shown in Eq. (8.18).

$$S_{FR} = t_{FR} \cdot V_{TD} \tag{8.17}$$

$$S_B = \frac{1}{2 \cdot g \cdot K_A} \cdot \ln\left(\frac{K_T}{K_T + K_A \cdot V_{TD}{}^2}\right) \tag{8.18}$$

where,

t_{FR} - Free-roll time V_{TD} - Touchdown velocity = $1.1 \cdot V_{\text{stall}}$

The K_T and K_A values can be found from the Eq. (8.2) and Eq. (8.3) respectively using the parameter values in correspondent to the landing conditions. The landing thrust T is set to 'idle' which is approximately 5-10% of the maximum thrust and the ground rolling resistance μ value is considered for the applied brakes condition.

8.3 Point Performance

The performance of the aircraft any point in flight can be analysed using energy-manoeuvrability methods which describe the exchange of potential and kinetic energies to gain altitude or velocity. This point performance analysis, however, primarily focuses on a certain performance parameter, which is derived from the above energy methods, called 'specific excess power'. The specific excess power P_S, as the name implies, is the remaining thrust power of the aircraft divided by its weight as derived in Eq. (8.19) below.

$$P_S = \frac{V \cdot (T - D)}{W} = V \cdot \left[\frac{T}{W} - \frac{\rho \cdot V^2 \cdot C_{D0}}{2 \cdot (W/S)} - n^2 \cdot \frac{2 \cdot K}{\rho \cdot V^2} \cdot \frac{W}{S}\right] \tag{8.19}$$

where,

P_S - Specific excess power (ft/s) n - Load factor

For a given aircraft's operating condition, the above P_S equation can be applied for determining various performance figures such as the rate of climb, level turning and available manoeuvrability in cruise condition. The unit of P_S coincides with the velocity; therefore, under steady climb assumptions where the load factor $n = 1$, the P_S itself represents the rate of climb. From the manoeuvrability perspective, the maximum load factor for sustained turning at a certain point can be found when there is no excess power left in the aircraft, i.e. P_S is zero. Also since the maximum thrust produced by the engine decreases at high altitude, the power remaining for the aircraft to further accelerate, ascend or manoeuvre would become limited at such operating conditions. This maximum thrust variation can be determined from the off-design cycle analysis described previously in the engine performance section.

8.4 Cruise Performance

The analysis of cruise performance is governed by the evaluation of the Breguet range equation depicted in Eq. (8.20). Within the contexts of the initial sizing, this range equation was applied for evaluating the overall fuel weight reduction under a simplified assumption of the range parameters (i.e. V, sfc and L/D) being held constant throughout the cruise segments. However in a steady level-flight condition, the L/D values vary primarily depending on the aircraft weight at the moment. Thus, in order to improve the accuracy of the range equation in this detailed analysis, the total cruise segments are divided into several sub-segments and evaluated using the corresponding reduced weight due to fuel consumption, and hence the variation of the L/D values.

$$S = \frac{V}{sfc} \cdot \frac{L}{D} \cdot \ln\left(\frac{W_i}{W_f}\right) \tag{8.20}$$

where,

S	- Range	sfc	- Specific fuel consumption
W_i	- Initial aircraft weight	W_f	- Final aircraft weight

As far as the evaluation of the L/D is concerned, the lift part is equal to the current weight of the aircraft which can be approximated using an average of W_i and W_f values in each sub-segment. The drag part in the L/D refers to the total trimmed drag which can be obtained using the methods presented eariler in the aerodynamic drag and stability analyses. A summary of the evaluation process of this cruise performance analysis (i.e. the Breguet range equation) is illustrated in Figure 8.4, while the parenthesised number series represent the section in the thesis where the corresponding methods applied.

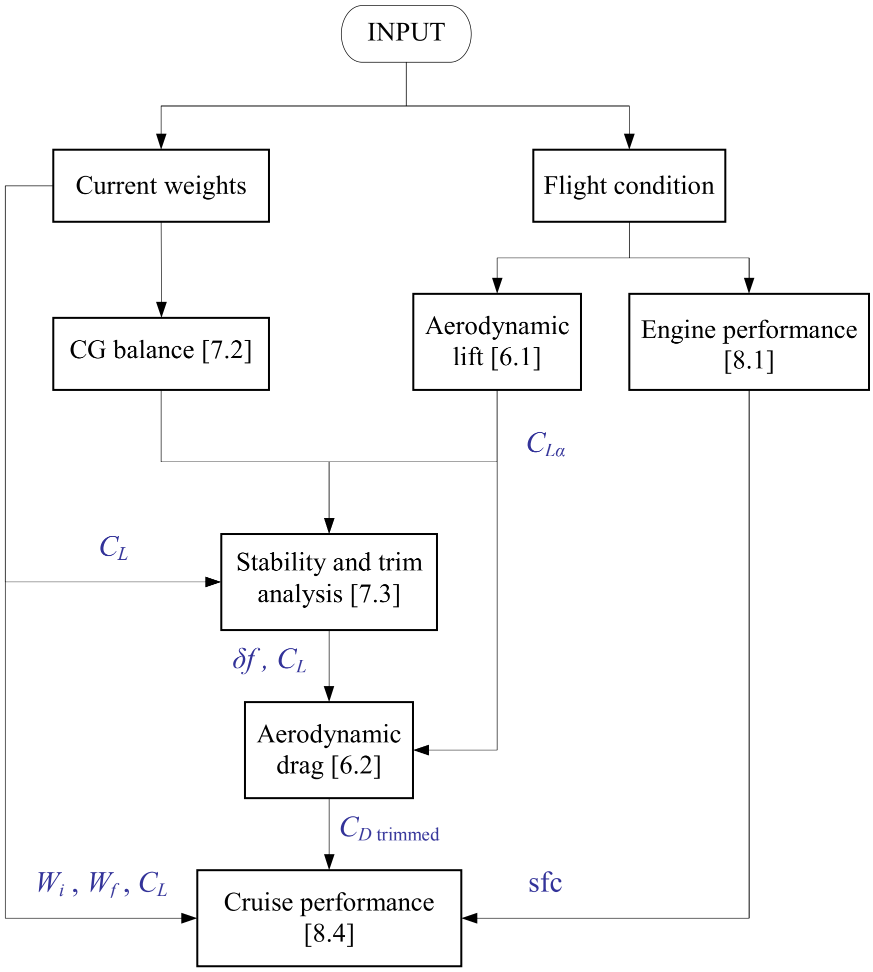

Figure 8.4: Evaluation process of cruise range performance

The specific fuel consumption at a given flight condition can be evaluated using the engine performance analysis described in section 8.1. It may seem that apart from the flight altitude and Mach number, there is no other factor in the range evaluation which directly induces the changes in the sfc value. However, as the aircraft weight drops, so does the lift, the induced drag, and hence the thrust required to maintain level flight. Generally this thrust reduction can be achieved by adjusting the throttle settings accordingly which, in turn, affecting the overall engine's operating performances, and hence the specific fuel consumption. Nonetheless, due to the unavailability of the direct relation between the throttle settings and the specific fuel consumption in the engine performance methods, and also for the purpose of this analysis, it is reasonable to assume that the value of the sfc remains constant throughout a certain cruise environment.

Chapter 9

Formation Flight

The methods used for synthesising the proposed tanker and UCAV from scratch as well as for analysing their performances in operations have been described early on. However, due to the unavailability of the methods which are capable of predicting the formation flight effects upon the aerodynamic performance of the trailing aircraft for a given dissimilar aircraft combination; the formation flight analysis is conducted separately prior to the design synthesis executions using a computational vortex-lattice program called 'Tornado'.

9.1 MATLAB Tornado Implementation

Tornado is a 3D-vortex lattice program written on MATLAB according to a standard vortex lattice theory. Due to its operational simplicity, the program is used primarily in the conceptual design stage of aircraft or in training and education. Similar to other existing vortex-lattice programs, Tornado only takes lifting surface components of the aircraft, e.g. wings, control surfaces and stabilisers, into consideration; therefore, the fuselage modelling function is generally not available. Even if a conventional aircraft were to be tested, only the reference wing and the vertical /horizontal tail planes may be modelled in the program. Although HASC95, a powerful vortex lattice code which has been widely used in many previous formation flight researches, allows the fuselage part to be built into the vortex-lattice model, it can only be applied in a form of horizontal and vertical planes intersecting at the aircraft's centreline. Therefore, realistically the code does not significantly provide superior modelling capability of actual 3D aircraft representation in comparison to other similar programs.

Since it is desirable for the tanker/UCAV combination to operate without being detected by radar signals, the stealth characteristics of flying-wing aircraft are taken as one of the main design considerations. And for this reason, the Boeing B-2 Spirit and Northrop Grumman X-47A were chosen as preliminary models of the tanker and the UCAV respectively for investigating the Tornado. Due to the genuine flying-wing configurations of both aircraft, it is rational to consider their entire airframe planform as a lifting surface, and thus can be fully modelled into the vortex-lattice program as shown in the figure below.

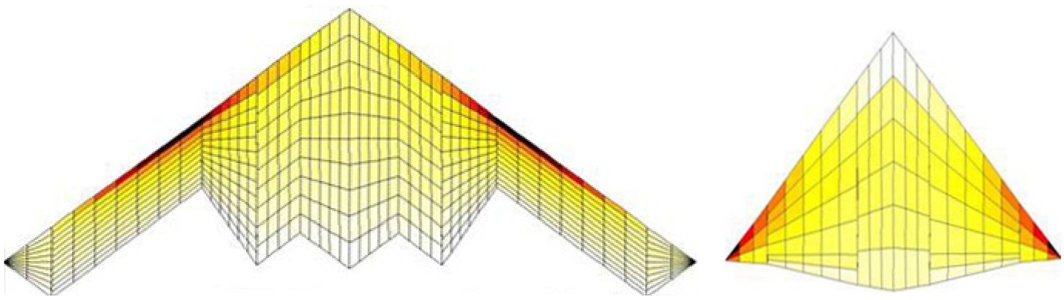

Figure 9.1: Vortex-lattice models of B-2 (left) and X-47A (right) generated in Tornado

Generally, a computational investigation of formation flight requires two or more aircraft models to be built in one flight space. The Tornado, however, was programmed to be used solely for testing single aircraft model, and thus preventing an input of multiple aircraft modelling data. Nonetheless, by exploiting the fact that finite numbers of wings are allowed to be placed into one model, the program can be adapted for generating more than one aircraft in the same flight space by considering each wing model as an individual aircraft. The leading aircraft (tanker) would be registered in the program as 'main wing' while other trailing aircraft (UCAVs) would be regarded as miscellaneous wings e.g. the tail planes from conventional aircraft perspective. The positions of these wings can be literally located at any point in the flight space, thus providing high flexibility for setting various aircraft formation arrangements.

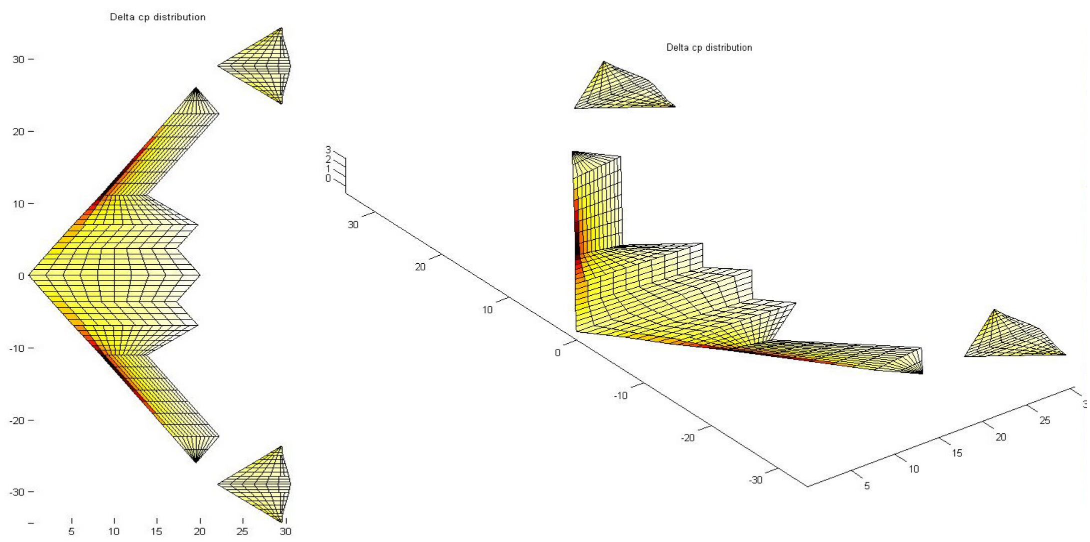

Figure 9.2: A formation of Tanker (B-2) and two UCAVs (X-47A) generated in Tornado

Tornado version 1.32 has been selected for the formation flight analysis and the associated program modifications despite the availability of more recent versions of the Tornado. This is primarily because the new versions have a tendency to fail to evaluate the aircraft formation models as a result of insufficient computational memories, thus causing the program to terminate prematurely. The memory overloading problem occurs due to a large number of vortex-lattice elements, generated by several aircraft models, being executed in a single batch as well as additional result evaluations included in the new versions which increase computer's resource consumption. Nonetheless, for the program version 1.32 and below, this execution failure may still present if highly-refined vortex-lattice grids are applied to complex-configuration aircraft models. Therefore, the numbers of vortex-lattice elements are appropriately specified by considering the number of the aircraft models in the formation and their airframe configurations.

9.2 Aircraft Formation Arrangement

The majority of the previous formation flight studies described the aerodynamic benefits gained from the upwash regions in the forms of drag reduction and fuel savings. However, for the purpose of optimising the formation range of the developed tanker/UCAV combination according to Breguet range equation, an increment in the lift performance and hence the overall lift-to-drag ratio would be considered instead. Though whether it is the drag reduction, fuel savings, or lift-to-drag ratio increment, these parameters are related to each other from the aerodynamic and range performances' perspective, and therefore, implying the same benefit.

Generally in order for the trailing aircraft to gain 'free lift', its lateral position during the close-formation flight should be located in the vicinity behind the wingtips of the leading aircraft. However, the upwash region due to the vortices produces greater lift on one wing which tends to roll the trailing aircraft away from the leading one. This rolling moment must be counteracted by an opposing aileron input which, in turn, generates additional drag resulted from trimming the aircraft during cruise, and more thrust would be required to overcome this trimmed drag increment. And eventually the overall fuel consumption of the trailing aircraft may not reduce as expected from the technique. In attempt to prevent that from occurring and hence eliminate the need for asymmetry control surface deflections which is the cause of the trim drag, this research programme aims to investigate and quantify the effects of the formation flight from a new perspective by considering the minimum rolling-moment position, which is identified according to the distribution of pressure coefficients ΔC_P across the span of the aircraft.

To determine such a position, the ΔC_P distribution diagram obtained from Tornado is used as a criterion. The rolling moment is considered to be minimised if the ΔC_P distribution is nearly balanced about the centreline of the trailing aircraft. Figure 9.3 shows a comparison between typical and optimal positions in close-formation flight. The ΔC_P distribution of the typical formation is not balanced between both sides of the trailing aircraft's wings as shown by the colour scales. Therefore, it can be concluded that, without additional control surface usage, the aircraft would have a tendency to be laterally unstable due to the rolling moment generated from asymmetric lift distribution across the span. On the other hand, in the optimal formation, it is reasonable to assume that the trailing aircraft is laterally stable during the formation and hence no further control surface input is needed. Although the lift increment gained from the optimal position might be less than the typical one, this optimal position is more desirable due to the elimination of the aileron input and its associated trim drag.

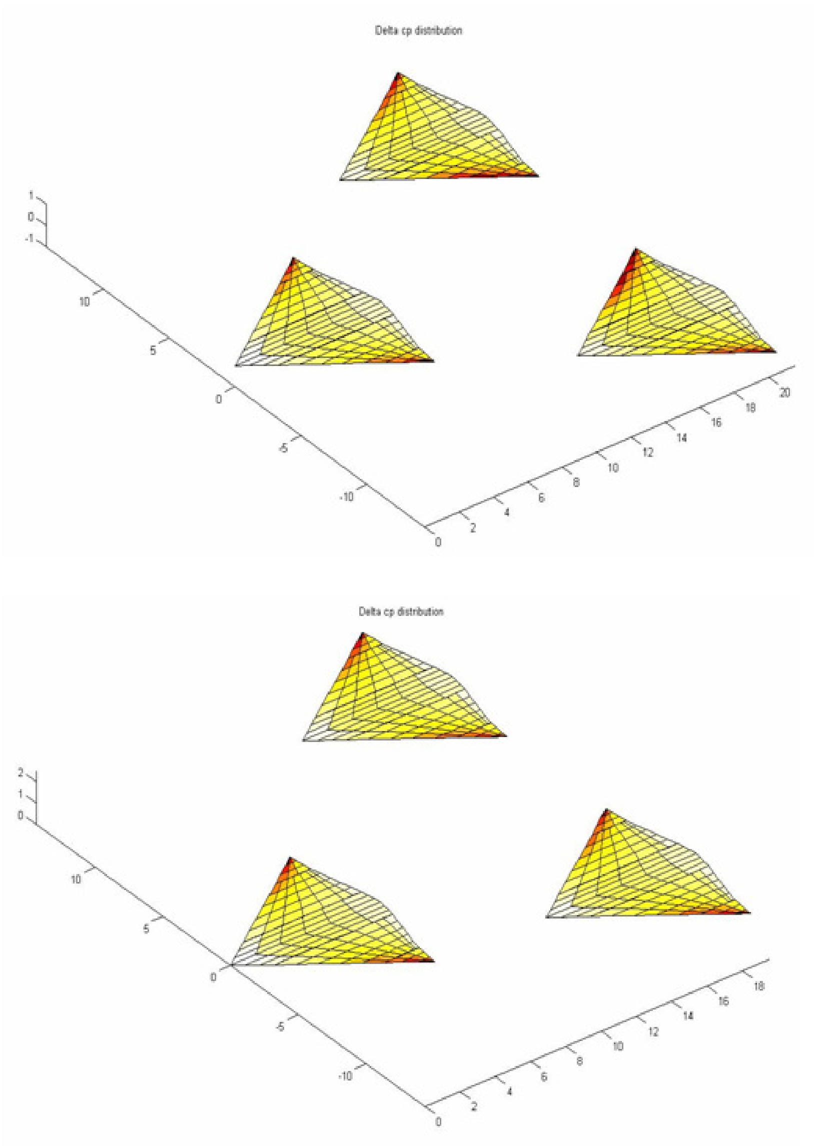

Figure 9.3: Typical (top) and optimal (bottom) formations

The optimal formation shown in Figure 9.3 was manually adjusted and justified based on a visual estimation of the ΔC_P distribution across the aircraft span. The aerodynamic effects upon the trailing aircraft due to formation flying also depend on the leading aircraft configuration. In a multi-row formation of the tanker and UCAVs as depicted in Figure 9.4, the leading aircraft term refers to the tanker and any UCAVs which are located in front of the considered trailing aircraft. Hence, before attempting to locate for an optimal position of a certain UCAV formation row, the formation arrangement of the aircraft in the prior rows must be optimised first.

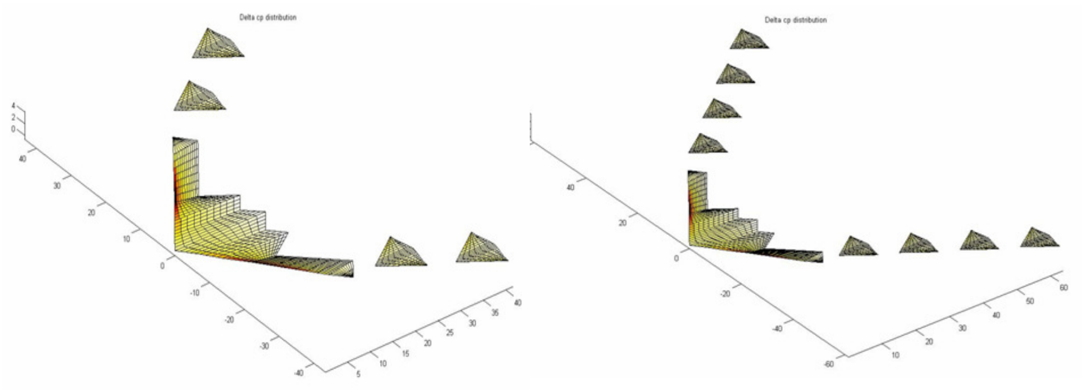

Figure 9.4: Tanker and UCAVs flying in optimal formation

Although the adjustment and the justification for an optimal formation position of the trailing aircraft which possess a simple kite-shaped airframe could be manually performed as shown above; the entire investigation was undoubtedly time-consuming. Due to such laborious tasks involved, this manual formation arrangement proved to be limited especially in term of expanding the investigation envelope of formation positions. Also the visualising-based method used for comparing the ΔC_P distribution balance between both sides of the wing, and also recognising minor differences between individual formation cases would pose difficulties when the actual UCAV configuration, which contains more airframe details, is applied in the lattice model. This problem became more severe in a large aircraft formation in which the colour scales of the ΔC_P distribution cannot be clearly illustrated to begin with. For these reasons, Tornado has been modified to accommodate such problems as well as to perform the analysis of the optimal formation arrangement for a given combination of tanker and UCAV configurations.

As far as common vortex lattice programs are concerned, Tornado is relatively user-friendly with interactive selection procedures and clear presentation. However, if the program is to be applied for the formation flight analysis, the aircraft formation's adjustment processes would become unfavourably repetitive especially in point-matrix pattern which requires the formation positions to be changed uniformly several times. Therefore, additional scripts have been integrated to the Tornado in order to bypass the aforementioned selection procedures and directly execute the vortex-lattice computation codes multiple times on account of changing the trailing aircraft's formation position in three dimensions. Also the ΔC_P distribution and the total lift coefficient results will be extracted and compared for every point generated in the flight matrix to identify the optimal formation position based on the method described in the section below.

9.3 Optimal Aircraft Formation Analysis

Prior to performing the investigation of the optimal formation positions between the tanker and the UCAVs, the vortex-lattice model of each aircraft category must be tested individually under the same flight condition as the formation cruise first. This is to obtain their corresponding aerodynamic performances in a solo flight which are necessary to determine how much the performances have changed in the formation flight compared to the normal cruise condition. For the purposes of this formation flight analysis, the following operational criteria and assumptions have been considered.

For a given range requirement of the tanker/UCAV combination, the size of the designed tanker increases according to the amount of fuel payload carried which is directly proportional to the number of UCAVs assigned per tanker. Although it is desirable to keep the tanker's size minimal in order to reduce the overall weight and thus the fuel consumption, the number of UCAVs assigned per tanker should be also sufficiently great for combat effectiveness. As far as the long-range operations focused on this research are concerned, it was decided that the tanker would accompany six UCAVs in total, and thus can be arranged into three trailing aircraft formation rows in 'V' formation.

As described earlier, in order to apply Tornado for modelling aircraft formations, the tanker airframe would represent the main wing and hence the reference area of the formation model, while the UCAVs in any formation positions would be considered as the miscellaneous wings. For this reason, in order to correctly evaluate the aerodynamic results obtained from the formation model, the entire aircraft formation must be viewed as a single aircraft unit with multiple wings as it was regarded in the modelling principles and vortex-lattice computations of the Tornado. Thus, for a given total lift coefficient value generated by the aircraft formation model, the actual lift coefficient of a single UCAV in the formation must be evaluated based on the wing-area ratio approach which is commonly used for calibrating the lift contribution of the tail planes relative to the main wing. The lift coefficient increment of the UCAV positioned on a certain formation row can be calculated according to the equations shown below.

1st row: $$\Delta C_{L1} = \frac{1}{2} \cdot \frac{S_{\text{tanker}}}{S_{\text{ucav}}} \cdot (C_{L\,FF} - C_{L\ \text{total}}) \tag{9.1}$$

2nd row: $$\Delta C_{L2} = \frac{1}{2} \cdot \frac{S_{\text{tanker}}}{S_{\text{ucav}}} \cdot (C_{L\,FF} - C_{L\ \text{total}}) - \Delta C_{L1} \tag{9.2}$$

3rd row: $$\Delta C_{L3} = \frac{1}{2} \cdot \frac{S_{\text{tanker}}}{S_{\text{ucav}}} \cdot (C_{L\,FF} - C_{L\ \text{total}}) - (\Delta C_{L1} + \Delta C_{L2}) \tag{9.3}$$

nth row: $$\Delta C_{L\,n} = \frac{1}{2} \cdot \frac{S_{\text{tanker}}}{S_{\text{ucav}}} \cdot (C_{L\,FF} - C_{L\ \text{total}}) - \sum_{n=1}^{n} \Delta C_{L\,n-1} \tag{9.4}$$

when, $$C_{L\ \text{total}} = C_{L\ \text{tanker}} + 2 \cdot n \cdot \frac{S_{\text{ucav}}}{S_{\text{tanker}}} \cdot C_{L\ \text{ucav}} \tag{9.5}$$

where,

n - Formation row number

$\Delta C_{L\,n}$ - C_L increment of a UCAV locating at the n^{th} row

S_{tanker} - Reference area of the tanker

S_{ucav} - Reference area of the UCAV

C_{LFF} - C_L obtained from the airframe formation results

$C_{L\ \mathrm{total}}$ - Total C_L accumulated from individual aircraft in the formation

S_{tanker} is the reference area result obtained from either the aircraft formation or the sole tanker models while S_{ucav} can be found from the results of the solo-flight UCAV model generated prior to the analysis of the aircraft formation. As mentioned earlier, the optimisation of aircraft formation must be conducted in sequence from the first to the last rows. For example,

To determine an optimal formation solution for a combination of one tanker and six UCAVs, Eq. (9.1) must be applied to an initial formation model consisting of one tanker and two UCAVs while the values of C_{LFF} and $C_{L\ \mathrm{total}}$ are corresponding to this three-aircraft formation model. The C_{LFF} values produced by Tornado's vortex-lattice methods vary depending on UCAV formation positions in the matrix of flight envelope. The ΔC_{L1} values deduced from every point in the above formation-position matrix are used in the optimal formation evaluation which will be described in the next paragraph. Afterward the second row of UCAVs would be included into the formation model (i.e. five aircraft in total) in which the tanker and the first-row UCAVs are now fixed at their optimal positions. And then Eq. (9.2) would be applied in a similar way to the previous first-row formation analysis while the ΔC_{L1} value used in the above equation is the corresponding result of the leading UCAVs. Once the optimal position of the second-row UCAVs has been found, the same approach will be used for the third formation row and so on.

The above ΔC_L value in any formation positions can be presented in a form of the percentage increase from the original UCAV's lift coefficient as shown in Eq. (9.6). After the flight matrix of a certain formation row has been entirely evaluated, for every point in the matrix, the ΔC_P results generated on each side of the analysed trailing UCAV will be accumulated and compared to estimate the overall balance of the ΔC_P results between both sides of the UCAV. Subsequently, the optimal solution will be selected from the formation position where the ratio between the lift increment and the total ΔC_P difference, presented in Eq. (9.7), is maximised. This function ratio is used instead of simply the minimisation of the ΔC_P difference across the UCAV's span to ensure that the solution gained does not solely focus on optimising the ΔC_P balance while the aerodynamic benefit deduced from such a solution could be, in fact, close to idle or even negative.

$$f_{CL} = \frac{\Delta C_L}{C_{L\ \mathrm{ucav}}} \times 100 \qquad (9.6)$$

$$x_{FF} = \frac{f_{CL}}{\left|\Sigma(\Delta C_P)_R - \Sigma(\Delta C_P)_L\right|} \qquad (9.7)$$

where,

f_{CL} - Increment of UCAV C_L in formation flight (%)

$\Sigma(\Delta C_P)_R$ - Total ΔC_p on the right side of the UCAV

$\Sigma(\Delta C_P)_L$ - Total ΔC_p on the left side of the UCAV

The f_{CL} value obtained from the above optimal formation evaluation is required for appropriately developing the preliminary refuelling sequence, and hence the design synthesis of the tanker. Thus, this formation flight analysis actually becomes part of the main design synthesis operations that require iterative procedures to arrive at a converged solution. And originally it was intended to do so by integrating the Tornado to the design synthesis program to perform the formation flight analysis as the design synthesis execution progresses. However, time was not permitted for such a development due to the extensive and complex computational works involved. Furthermore, despite the developments of the automated scripts and additional functions for the Tornado to reduce the repetitive workloads of manually performing the formation flight analysis, the time taken to generate the matrices of formation flight results varies from three to six weeks depending on how small the point intervals in the matrices are specified. And for this reason, it is not viable to perform such an analysis repetitively along with the design synthesis operations due to the execution time stated.

As far as the design synthesis results are concerned, the effects of the UCAV's formation-flight lift increment to the tanker's total offload fuel required, and therefore, the size of the tanker itself, are not substantial in comparison to other changes in geometry and performance design requirements. Therefore, as long as the aircraft configurations are not significantly different from the initial models used in the preliminary analysis of the formation flight, it is reasonable to assume that the changes in the formation-flight positions and their associated lift increments are negligible. Also from the aircraft design's point of view, the accuracy of the end results is primarily determined by the methods implemented in the design synthesis and any rational assumptions being made throughout. As mentioned above, due to a comparatively small effect of the formation-flight lift increment onto the overall picture of the results, it is possible to allow the error margin of 10-25% for such parameter.

According to the results obtained from the preliminary analysis of the formation flight, the optimal lift increment values for all three formation rows are 26%, 20% and 34% respectively. However, the highest value provided by the third formation row came with a relatively large ΔC_P difference compared to the first two rows. Since the design synthesis has been developed under the assumption of equivalent formation flight effect for all UCAVs in the fleet, and due to the error margin specified above, if the UCAVs are to swap their formation rows after every refuelling operation, it is sufficiently reasonable to assume that the average lift-coefficient increments of all three formation rows are approximately the same while this averaged value would be on account of the first two formation row in which the rolling moments are close to idle.

From the lift-to-drag ratio perspective, the lift coefficient increment ΔC_L due to formation flying effectively reduces the total lift force need to be produced by the aircraft in order to maintain steady flight conditions. Therefore, this additional lift would contribute to a reduction of the induced drag term while the total lift would remain the same. The improved lift-to-drag ratio of the UCAV in formation flight can be derived as shown in below.

$$\left(\frac{L}{D}\right)_{FF} = \frac{C_L}{C_{D0} + K \cdot (C_L - \Delta C_L)^2} = \frac{C_L}{C_{D0} + K \cdot {C_{L\,FF}}^2} \qquad (9.8)$$

when, $\qquad C_{L\,FF} = C_L \cdot \left(1 - \frac{f_{CL}}{100}\right)$

The above equation is applied to the UCAV's range evaluation in the development of the preliminary refuelling sequence and the final optimisation of the formation range.

Chapter 10

Optimisation

Since the tanker and the UCAV have been designed and synthesised according to certain refuelling provision sequence and flight conditions, this may imply a promising solution to their best performances if this particular tanker/UCAV combination were to operate under such criteria. However, there is in fact a chance that the aircraft combination could demonstrate better performances compared to the design solution if other sets of operating criteria are used. Therefore, in order to investigate the possibility of aircraft combination performances improvement as well as identifying the solution to it, an optimisation study has been conducted and implemented to the design problem.

10.1 Background

The term optimisation is defined as a process or rationale used for achieving an improved solution to a problem. Although the best or perfect solution for the problem is desirable, it is common to settle for a satisfied improvement rather than trying to obtain an absolute optimal solution. The fundamental definitions in the area of the optimisation are, *design variables*, *merit function*, *design space*, *constraints* and *the type of extremum problem*. The *design variables* are described as a group of independent variable parameters which define the considered problem. The values of these parameters are meant to be solved in an optimisation process in order to obtain better or locally optimal solutions. The *merit function* is an equation or evaluation procedure, in which the solution is meant to be solved according to its *type of extremum* (i.e. minimisation or maximisation). The total exploration space that the optimisation search can be conducted is called the *design space*. The size of this space depends on the number of the design variables and the specified *constraint* boundaries.

In general, the techniques used for performing optimisation searches can be categorised into one-dimensional and multi-dimensional types. As the name implies, one-dimensional optimisation techniques refer to the search algorithm for solving an objective function that contains only one design variable, in other words, the function that can usually be written in a form of $y = f(x)$. Multi-dimensional optimisation techniques, on the other hand, are used for the case where there is more than one design variable involved. The methods which are commonly used for solving multi-dimensional optimisation problems are the gradient and the pattern search methods. The fundamental principles of the gradient methods rely on an evaluation of partial derivatives at the point being considered; however, many optimisation problems contain a merit function which the mathematical derivation cannot be performed. On the contrary, the pattern search methods are recommended for the above problems since their search algorithms are not involved with the function derivative. Also if the merit surfaces of the objective function contain sharp ridges due to the applied boundary constraints, the pattern search methods prove to be superior in comparison to the gradient methods in term of finding the solution.

10.2 Optimisation Algorithm Implementation

Originally it was intended to locate for a third-party Visual Basic.NET optimiser for solving this refuelling sequence optimisation problem; however, all of the compatible optimisers found were available for commercial use. They also employed the gradient-based methods for multi-dimensional optimisation which are not practical for this research problem due to the reasons explained above. Another option being considered was to use the built-in Microsoft Excel optimiser, Excel Solver. Although the Excel Solver itself is relatively user-friendly, interfacing and sending roundtrip data between the optimiser and the design synthesis program would pose development difficulties. For these reasons, it was decided that an optimiser algorithm would be selected from one of the multi-dimensional optimisation techniques described earlier, and implemented into the design synthesis program directly. The built-in optimiser would provide the flexibility of accommodating the design optimisation problem and also the fidelity of interfacing with various design synthesis modules.

Since the objective function developed in this optimisation problem primarily concerns with the range evaluations of the tanker and the UCAVs flying in combination, several complex performance analysis modules varied from computation iterations to regression models are employed. The results obtained from these analyses possess intricate non-linear behaviours which are not possible to predict and formulate into mathematical equations. Therefore, the gradient methods which rely on partial derivatives to search for the solution cannot be used for this type of objective function. Thus, the pattern search methods are selected. There have been a number of pattern search algorithms available up to date; however, the majority of them were developed specifically for applying to their own problem, and thus may not be fully compatible to other applications. For this reason, the following fundamental pattern search methods recommended by Shoup and Mistree [22]; Hooke and Jeeves, Rosenbrock and Simplex methods were investigated. Subsequently, the Hooke and Jeeves algorithm was selected for using with this research optimisation problem due to its robustness and simplicity. These advantages result the algorithm being more flexible to accommodate additional modifications of constraint boundary handlings and different ranges of design variable values in comparison to the other two investigated pattern search methods.

Figures 10.1 and 10.2 illustrate the main algorithm and the exploration process of the Hooke and Jeeves method. Since the original method described in reference [22] was provided for solving unconstrained optimisation problems, boundary constraint verification procedures have been included to the implemented search algorithm codes, generally at the point where the values of the design variables change. Also the original algorithm used one step size parameter for all design variables which would be convenient only if such variables possess the same range of values. Though, in most of practical optimisation problems, the design variables are generally in different value spectrums various from decimals to large-scale numbers or in some cases only limited to integers. Thus, in order to apply these range variations to the step size processes while maintaining the original structure of the algorithm, the step size parameter has been changed to an equivalent scaling factor which ranged from 0 to 1. This scaling factor works the same way as its predecessor in terms of step adjustment and pattern records; however, the parameter would be multiplied by corresponding range intervals of the design variables to provide the actual stepped values before the objective function evaluation is called in the algorithm.

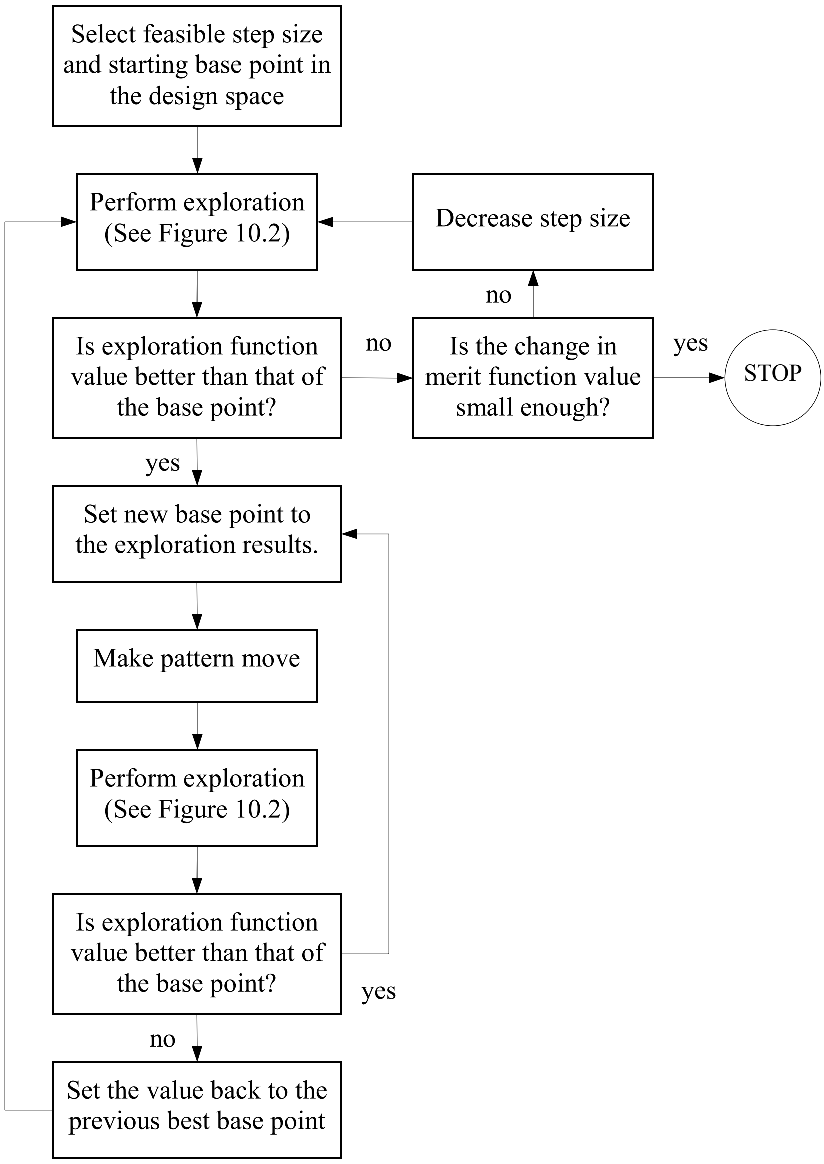

Figure 10.1: Hooke and Jeeves pattern search algorithm

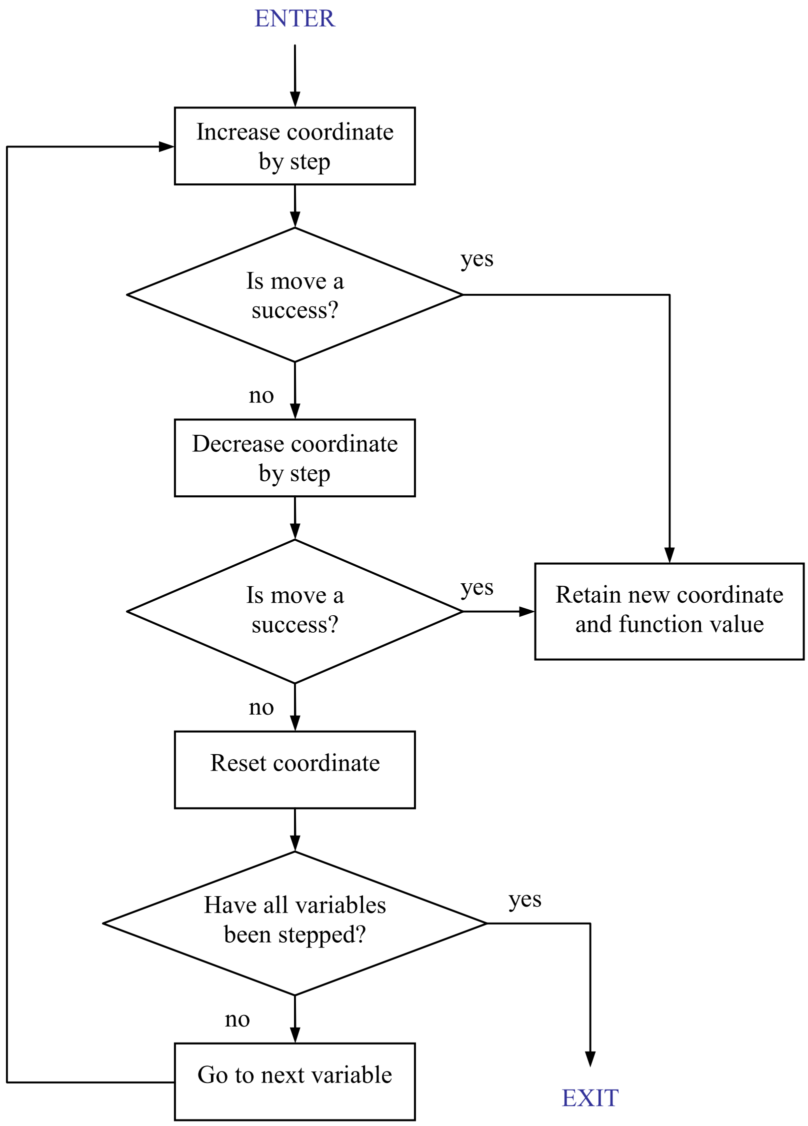

Figure 10.2: The exploration method used in Hooke and Jeeves algorithm

10.3 Refuelling Sequence Optimisation

As far as the optimisation of the refuelling sequence is concerned, solely maximising the overall combat radius of the tanker/UCAV combination seems rational for representing an objective function. However, the solution obtained from optimising the range parameter alone may not be effective in actual operations. Since there is a possibility that the aircraft combination would choose to fly at mid subsonic speed in order to improve the range performance, which eventually, despite the fleet's capability of achieving global combat radius, it could take several days to complete the mission. This long operating time is not desirable from combat effectiveness' point of view, and in fact it defiles the original purpose of designing the tanker/UCAV combination for swift response to time-critical missions. Furthermore, an ideal operation of the aircraft combination should be economical in fuel consumption in order to maintain the fundamental cost benefit of using unmanned systems.

Upon considering the above criteria, they clearly suggest that for operational effectiveness, both the fuel consumption and the operating time of the aircraft combination should be minimised while maximising the range proceeded. Thus, the objective function of this refuelling sequence optimisation problem MF, subjected to the maximisation, can be formulated as shown in Eq. (10.1). Although this function may not provide an answer to the maximum possible range obtained from a particular aircraft combination, the formulated operational effectiveness term was considered to be more appropriate due to the aforementioned reasons.

$$MF = 1 + \frac{\text{additional combat radius}}{\text{total fuel consumption} \times \text{operating time}} \quad \text{, m/lb-hr} \tag{10.1}$$

From the above equation, if the total combat radius achieved by the aircraft combination was being used as a numerator in the division term, then there would be a great tendency that the optimisation algorithm would return high merit values which, however, have the total combat radius result being less than one specified in the original design requirements. Since this refuelling sequence optimisation aims to search for an improved solution which does not only provide operational effectiveness, but also extends the combat radius further from the original design value, the term 'addition combat radius' is used in the equation instead. This would cause the entire division term being negative if a combination of design variable values could not produce greater combat radius than the original one. An additional value of 1 in the Eq. (10.1) was applied for calibrating the merit value to the figure which relates to the total combat radius, thus $MF = 1$ for the original design range value.

Within the contexts of this research study, for any given designs of tanker and UCAV, the total combat radius produced by a combination of these aircraft primarily depends on how their flight-refuelling routines are performed in the cruise legs. In the preliminary refuelling sequence established for designing the tanker, the refuelling profile parameters e.g. the numbers of air refuelling and the offloaded fuel amounts were determined primarily based on operational considerations, while the associated flight conditions were specified from the design requirements. Therefore, in order to investigate the possibility of range performance improvements obtained from different combinations of refuelling and flight profiles, the following parameters were selected for using as the design variables in this refuelling sequence optimisation problem.

- Inbound and outbound offload fuel ratios
- Cruise Mach number and altitude
- Refuelling air speed

The ratios of offload fuel refer to the amount of the fuel offloaded from the tanker to the UCAV divided by the UCAV's maximum fuel capacity. This non-dimensional term is considered to be more appropriate for representing the fuel weight parameter due to the flexibility of accommodating the synthesised aircraft results. An air speed is used for representing the flight velocity during air refuelling operations instead of Mach number to conveniently follow the standard unit provided by the flight envelope data of refuelling equipments in general [47].

Since practically it is inappropriate to alternate an operating altitude frequently due to various issues, such as traffic controls, enemy's detection and increase fuel consumption, the refuelling altitude would be coincided with the cruise condition as initially assumed for the design case. As far as the investigations of this refuelling sequence optimisation are concerned, the numbers of refuelling which provide optimal solutions are always the same as those originally specified for the design condition. Thus, in order to narrow down the design space and hence eliminate any unnecessary optimisation searches, the numbers of refuelling were excluded from the design variables.

The evaluation processes for determining the combat radius from the aforementioned design variables are carried out according to the detailed mission profiles similar to the second initial sizing of the tanker. However, since at this point both the tanker and the UCAV have been completely synthesised, many aircraft performance parameters which were assumed at the beginning, e.g. weights, lift-to-drag ratios and specific fuel consumptions, can now be calculated accurately using their corresponding performance and weight analysis methods described in the previous chapters.

In order to establish uniform refuelling sequence based on given number of refuelling and offload fuel ratio, the operational criteria considered eariler in the preliminary refuelling sequence for designing the tanker are still applied. The takeoff range segment would be maximised by advancing the aircraft combination until UCAV's fuel level reaches its reserve value which indicates the time for the first refuelling operation. The amount of fuel being offloaded to the UCAVs before departing from the tanker is up to the maximum capacity due to the reasons explained in the preliminary refuelling sequence (see section 3.2.2.1). Once the aircraft combination arrives at the designate point for UCAV deployment, the total formation cruise distance required to fly back has already been established by the outbound-leg value. Therefore, the landing range segment can be found from the remaining distance to the departed air base after the last inbound refuelling operation has been performed.

The uniform range travelled by the UCAVs per refuelling is no longer determined by the division criterion of minimum number of refuelling operations. However, they would be evaluated based on the offload fuel received from the tanker using the formation-flight range equation shown in Eq. (10.2). And then the range value obtained would be used for reversely calculating the fuel consumption of the tanker over the same segment using Eq. (10.3). Also to improve the accuracy of the solution, the evaluations of both equations are broken into several sub-segments as described in the cruise performance analysis (see section 8.4).

$$S = \frac{V}{\text{sfc}} \cdot \left(\frac{L}{D}\right)_{FF} \cdot \ln\left(\frac{W_{\text{initial}}}{W_{\text{final}}}\right) \tag{10.2}$$

$$W_{\text{fuel}} = \left[1 - \exp\left(-\frac{S \cdot \text{sfc}}{V \cdot L/D}\right)\right] \cdot W_{\text{initial}} \tag{10.3}$$

$(L/D)_{FF}$ is the lift-to-drag ratio of UCAV increased due to formation flying which can be evaluated according to Eq. (9.8) for a given UCAV's lift increment (see section 9.3). Although it was found that the lift increment values vary between three UCAV formation rows, time was not permitted for the development of individual refuelling sequence optimisation. Nonetheless, as mentioned in the previous chapter, it is sufficiently reasonable to apply the same lift increment for all UCAVs using an average-value assumption. Therefore, in the optimisation problem, the UCAVs can all be treated as a single entity instead of three (or six) individuals. This substantially reduces the complexity of the range and refuelling sequence evaluations, and also increases the chance for the optimisation search to find an improved solution.

The refuelling sequence optimisation is a uniquely difficult problem due to the fact that the range solution is presented in a form of 'combat radius'. This implies that the solution is only valid when both tanker and UCAVs successfully return to the departed air base. Although it might not be the case for the outboard leg, during the optimisation process, there is a high probability that the tanker would run out of fuel either on itself or its payload before the fleet can complete the return trip primarily due to over fuel consumptions in the outbound leg or ineffective inbound refuelling profiles. If such cases rise then the solution is considered to be invalid, and thus a *penalty function* would be imposed directly onto the merit value MF. The values of the penalty function applied in this optimisation problem vary from zero to negative numbers depending on at which point the operation fails to complete due to the fuel tanks emptied beforehand. And the sooner this operation failure occurs, the more negative the penalty value would be imposed. This variation of penalty function values is developed to allow the search algorithm to detect how much the solution is far from being valid, and hence inducing the searching direction to a feasible area.

Chapter 11

Full Methodology Implementation

11.1 Operations of Design Methodology

The complete design methodology developed in this research programme does not only contain the aircraft design synthesis methods, but also various external modules e.g. formation flight analysis, refuelling sequence optimisation, and graphical generation of aircraft models. These modules must be performed in rational sequence to deliver the aircraft that reflect the initially set design and mission specifications, in an optimised and practically feasible solution. The main operation of the design methodology and its procedure are illustrated in Figure 11.1.

Due to the significance of the selected thrust-to-weight ratio T/W and wing loading W/S values on the synthesised aircraft, the T/W-W/S analysis of individual platform (see section 3.2.3) must be performed prior to their corresponding design synthesis evaluations to approximate an optimal combination of the T/W and W/S values according to given design requirements and estimated aircraft performances at various specific operating conditions.

The analysis of tanker/UCAV formation flight is conducted primarily to obtain an approximated value of the UCAV's lift increment which is part of the inputs required for evaluating the operating performances of the synthesised UCAV. This lift increment due to formation flying does not, by all means, account in the actual design synthesis calculations for sizing the UCAV. However, the parameter will be used toward the end of the synthesis operations to determine the formation range performance which will affect how the design refuelling sequence is developed, and hence the design mission profile of the tanker.

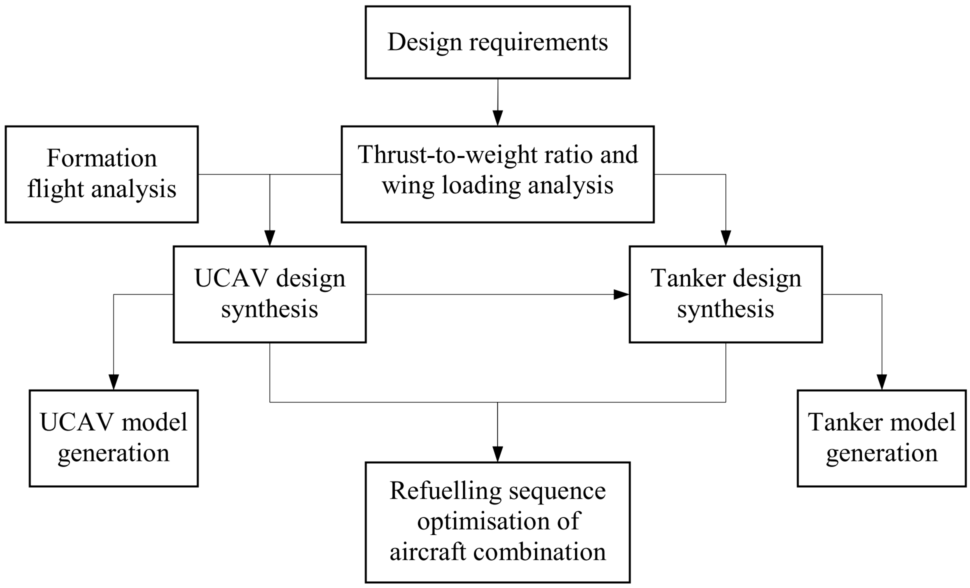

Figure 11.1: Main operation of the design methodology

The model data of the aircraft obtained from their corresponding design synthesis results will be sent to the individual model generation modules for visualising the resulted aircraft configuration as well as verifying its validity. The refuelling sequence optimisation, located at the very end of the main operation process, uses the design synthesis results of both tanker and UCAV, particularly the parameters which are related to the range performance evaluation, to accurately determine an optimisation merit value using Eq. (10.1), and thus an optimal combat radius improved from the original design condition.

The aircraft modelling and various performance analysis methods described in previous chapters are parts of the design synthesis methodologies of the tanker and the UCAV. Although the methods' details and the evaluations of each aircraft may be different, their main operation procedures are fundamentally similar.

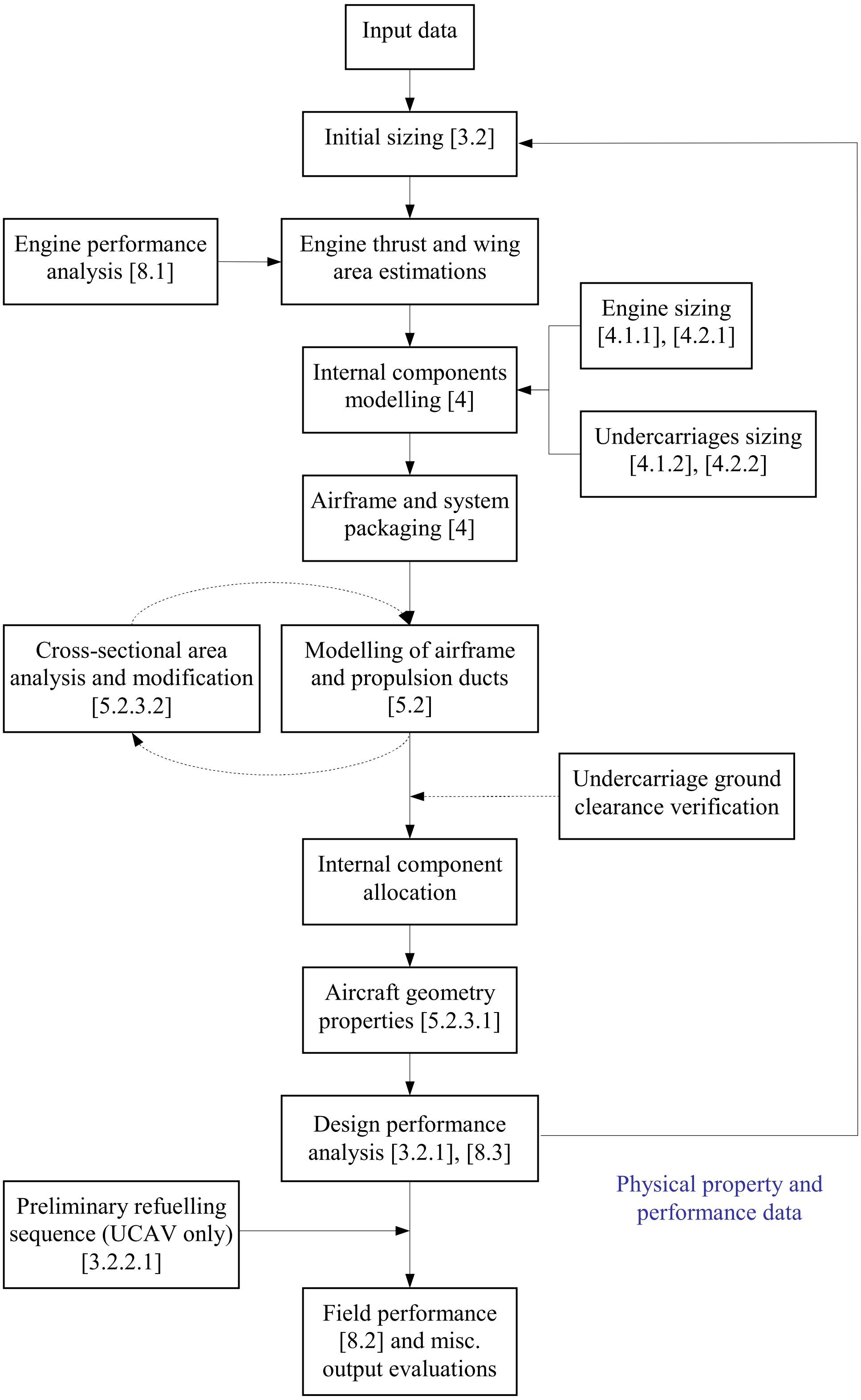

Figure 11.2: Main operation of the design synthesis

Figure 11.2 illustrates how the design synthesises of the tanker and the UCAV are operated in general. The number series in parenthesises indicate the chapter/section in this thesis where the corresponding methods are implemented, whereas the remaining unspecified-number modules are self-explanatory operations which do not follow specific evaluation methods.

The primary objective of the initial sizing module is to estimate the maximum takeoff weight of the aircraft according to given input parameter values. In subsequent iterations of the design synthesis execution, some of the input values which were initially approximated based on empirical data, e.g. lift-to-drag ratios, specific fuel consumptions and empty-weight fractions, would be replaced by the values calculated in the previous synthesis iteration in order to employ more accurate figures of the sizing parameters, and thus achieving a convergence of the results as the evaluation iterations progress.

The maximum thrust and the wing area required for appropriately designing the aircraft are simply the multiplication products of the estimated takeoff weight obtained from the above initial sizing module together with the T/W and W/S values. The maximum thrust is then converted into an uninstalled thrust using Eq. (4.1), which is necessary for sizing the physical properties of the engine as well as analysing its performance. Since the design operating environment of the engine is set at sea-level conditions, the performance of the engine at other flight conditions, e.g. cruise, refuelling and loiter, must be evaluated using the off-design cycle analysis methods. The estimated weights and the wing area known at this stage can be used for calculating the design lift coefficient of the aircraft based on a simplified assumption of half payload and fuel weights carried at the cruise condition.

The internal-components modelling module contains the sizing and the packaging of the fixed components allocated in the aircraft. The takeoff weight and the design engine performance data are carried over from the previous operation for evaluating the physical dimensions of the undercarriage and the engine models. Similar to the initial sizing module, for any subsequent iterations of the design synthesis execution, the aircraft's c.g-related parameter values, which are required in the dynamic braking load evaluation according to Eq. (4.9), would be substituted with those obtained from the detailed balance analysis of the previous synthesis iteration.

The above fixed components' dimensions together with various non-dimensional geometry inputs are used for establishing the packaging constraints of the fuselage airframe's cross-sections and longitudinal stations. The wing section of the airframe packaging is then developed afterward due to the prerequisite geometry data of the fairing's length and location which must be obtained from the fuselage packaging results. Subsequently, surface models of the airframe and variable-shaped propulsion ducts will be established according to the above packaging constraints and the mathematical modelling equations described in chapter 5.

Once the surface coordinates of the airframe model has been completely evaluated, the cross-sectional area of the aircraft at any longitudinal position can be derived from such results. The cross-sectional area analysis module is performed by producing an actual area distribution of the aircraft, and compared the figure with its ideal Sears-Haack body generated by Eq. (6.40) and Eq. (6.41) assuming that the starting, the peak, and the final coordinates are the same as the actual distribution. At every defined fuselage station, if the difference between the actual and the ideal cross-sectional areas is greater than ±5% tolerance of the cross-sectional area, then the size of the fuselage station's cross-section will be adjusted toward the ideal value direction by changing the values of fuselage packaging parameters within the boundary limits. However, since the majority of such parameters are inter-dependant especially the top part of the fuselage model, to maintain appropriate figure of the overall aircraft model generated, only the bottom depth parameters of the fuselage stations are used in this area adjustment.

After a step change has been made in the cross-sectional area analysis, a new set of packaging parameter values will be fed back to the airframe model evaluations as shown in the Figure 11.2. The process is repeated until either the area difference is within the above specified tolerance or the altering parameter values encounter the boundary limit. Afterward this cross-sectional area verification process will move on to the next fuselage station and carry out until the last one. Despite an extensive procedure, this cross-sectional area analysis operation does not actual provide significant changes to the overall aircraft model not to mention its very small effects on the convergent direction of design synthesis results. The entire operation, however, consumes a considerable amount of time to complete. Thus, in order to reduce the overall execution time, this analysis module is included in the last few iterations of the design synthesis execution after the overall aircraft specifications have been substantially converged.

The verification of undercarriage's ground clearance involves a number of operational criteria e.g. rake angle, track limitation, and taildown angle. If the clearance of any above criteria is not met then the strut length and thus the associated model dimensions would be increased accordingly. Also the length of the nose undercarriage's strut will be adjusted to balance with the overall height of the main undercarriage once deployed. This operation is separated from the previous fixed components modelling due to the need of fuselage and wing model geometry data for verifying the track limitation and the taildown angle. Since this clearance verification process requires the pivot locations of the undercarriages which will be determined in the next step of the component allocation, this operation module will be performed from the second design synthesis iterations onward using the undercarriages' locations of the previous evaluation iteration.

As far as the allocations of internal component are concerned, their lateral locations have been defined earlier in the system packaging, whereas the longitudinal and the vertical locations of the objects will be positioned within the modelled airframe surfaces using an automated component allocation algorithm illustrated in Figure 5.8. At this point, the aircraft model has now been completely developed, thus the surface area and the internal volume of the aircraft can be directly derived from the model results by integrating airframe coordinate data in appropriate directions. Furthermore, due to the cranked-wing configuration employed in the designed aircraft, equivalent wing geometry parameters are also computed at this stage.

The design performance analysis module primarily contains the detailed evaluations of the aircraft's physical properties and performances which will be sent back to the next evaluation iteration replacing the value of the same parameters previously used in the initial sizing and a few other modules described above. After a certain number of iterations have been performed, the empty weight of the aircraft calculated by the initial sizing and the refined weights estimation method (see section 7.1) will be converged to approximately the same value, and so do other coherent results. The analysis of the preliminary refuelling sequence is only applied to the design synthesis of the UCAV once the evaluation iterations have been entirely completed. Hence such a module could be considered as part of the performance output computations.

11.2 Computer Program Architecture

11.2.1 Development of Computational Works

Due to the complexity of the design methodology described in the previous section and the variations of modelling and analysis modules involved, the development of computational programs is essential in order to assist the operations of the design methodology at various stages. This would provide rapid execution of the methodology procedures and hence accelerate the verification of results' validity. The following programs have been created for serving such purposes.

11.2.1.1 Thrust-to-weight and Wing Loading Analysis

In contrast to the design synthesis and optimisation operations, the T/W-W/S analysis does not use iterative procedures to attend the solution. However, apart from a number of performance plot data which need to be evaluated, this analysis also generally requires multiple tests of input values combination to adjust the performance criteria to achieve an optimal solution of T/W and W/S. Thus, without computational assistances, this analysis would be highly time-consuming to perform. To minimise the time spent on the T/W-W/S calculations and the subsequent analysis, the performance function results should be rapidly evaluated and promptly presented for solution verification. For this reason, an executable program written in Visual Basic.NET language has been developed particularly for computing the T/W and the W/S of the considered performance criteria.

One of Visual Basic.NET advantages over other programming languages is the capability of interfacing with other code formats and various commercial programs via the use of dynamically-linked library (DLL). The DLL is a type of library files which normally contains functions of the software or the compiled codes. The levels of interface compatibility and complexity vary depending on how these functions are programmed and organised internally. Generally in the software case, DLL function manuals and descriptions are not available in any reading materials neither they are clearly stated in the function codes' abstract comment. This may pose a significant difficulty for inexperienced users to understand and appropriately implement the software's functions. Nonetheless, the Microsoft-developed software tend to provide the aforementioned interface environment better than other commercial programs with similar DLL-interfaced capability.

Since Visual Basic.NET does not include a built-in function for generating graphical plot results neither there is decent third-party subroutine available for such a purpose, Microsoft Excel spreadsheet was selected to be interfaced as part of the developed T/W-W/S analysis program (see Figure 11.4) via the aforementioned DLL method. After the T/W-W/S evaluations of all performance criteria are completed, the spreadsheet accompanied with the above program, which has been prepared for corresponding data presentations, will be initiated and generate all graphical plots automatically as shown in Figure 11.5. In addition, turn rates and climb angle will be calculated and displayed in the program as output parameters also.

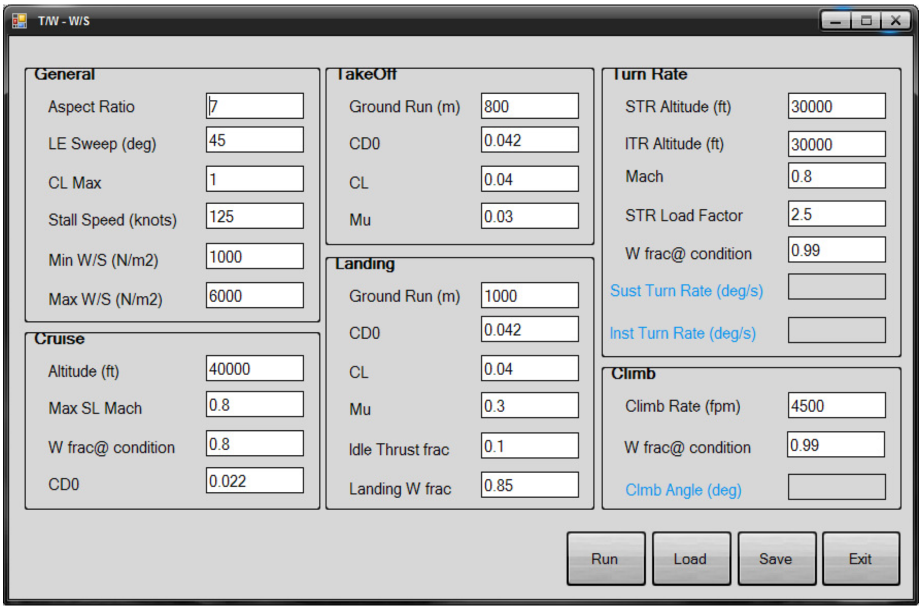

Figure 11.4: T/W-W/S program developed on Visual Basic.NET

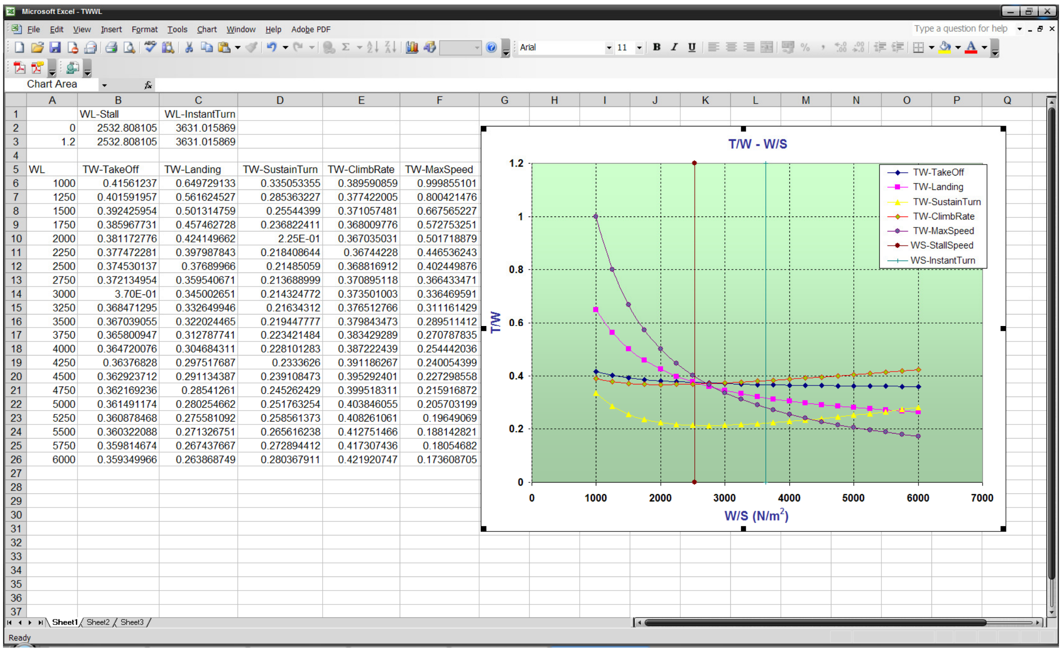

Figure 11.5: Microsoft Excel spreadsheet interfaced with T/W-W/S program

The direct interface of Microsoft Excel spreadsheet allows the user to rapidly generate and verify the results for an optimal T/W - W/S solution without the need of creating export data files and manually importing them to the spreadsheet. This together with a simple-designed T/W - W/S evaluation program provide a convenient tool for assisting the investigation and analysis tasks of the subject. The optimal T/W and W/S values determined in this analysis will be used as approximated inputs for the following design synthesis and optimisation program.

11.2.1.2 Design Synthesis and Optimisation

The design synthesis methodology developed in this research programme contains various evaluation and analysis methods, and initially it was planned to integrate existing performance analysis programs such as Datcom and ONX-OFFX, as part of the computational design synthesis modules. For these reasons, Visual Basic.NET was selected as the programming language platform for developing the design synthesis and optimisation program primarily on account of the language structure simplicity compared to other major platforms, e.g. Java, C++ and FORTRAN, as well as the aforementioned interface capability. Furthermore, Visual Basic.NET provides a great tool for developing Graphical User Interfaces (GUIs) which is an important feature for a large complex program such as this to be operational simplicity.

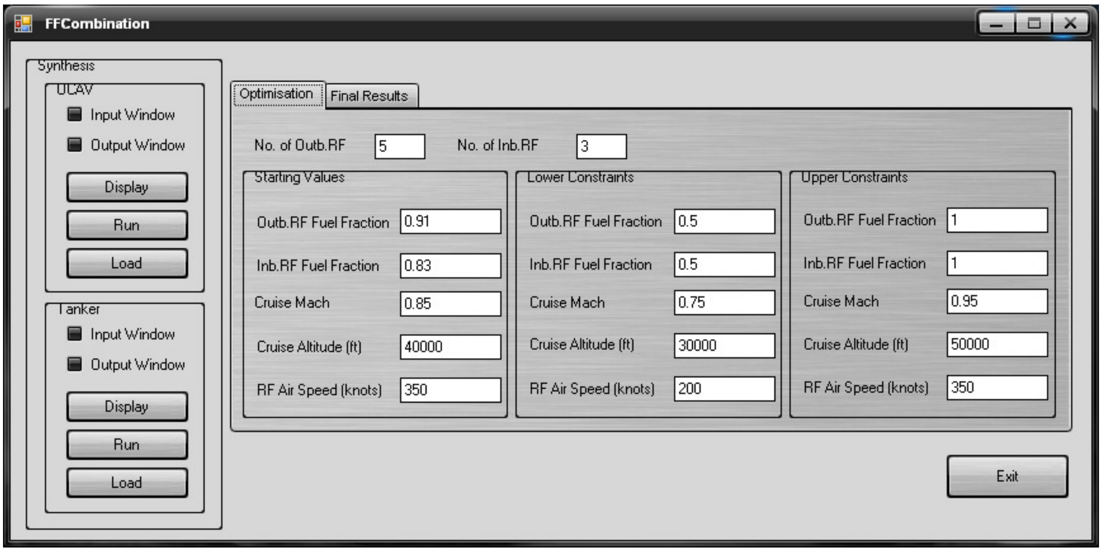

Figure 11.6: Design synthesis and optimisation program developed on Visual Basic.NET

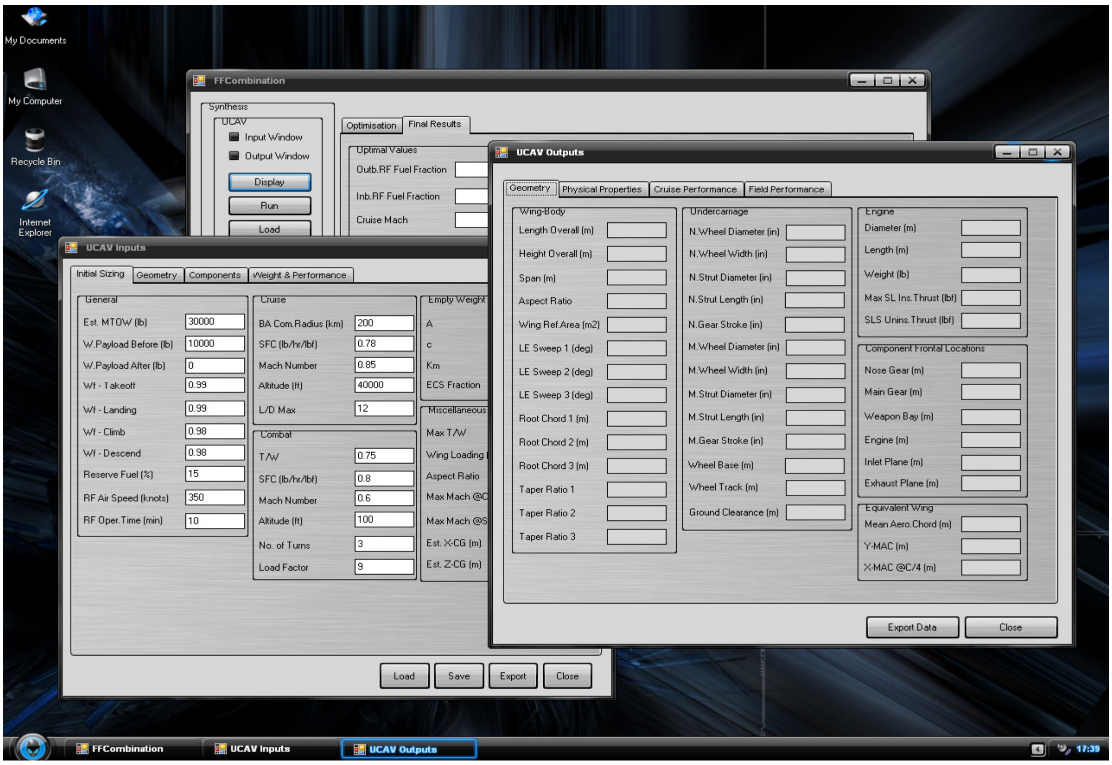

Figure 11.7: Sub-window forms of the design synthesis and optimisation program

Figure 11.6 illustrates the main operating window of the developed design synthesis and optimisation program. Since the program contains three extensive evaluations of the UCAV and tanker design synthesises and the refuelling sequence optimisation, it has been designed to operate in multiple sub-window forms and tab pages as shown in Figure 11.7 for the purpose of categorising input and output data of the corresponding evaluations. In addition, data storage and retrieval functions were also integrated to significantly improve operational facilities of the program. A user manual which briefly describes how to operate the program and its functions can be found in Appendix E.

11.2.1.3 Aircraft Model Generation

Since Visual Basic.NET does not supply a built-in function for producing 3D visualisation of the graphical output, it was decided to export the surface point data along with the internal component specifications to text files and then importing to a dedicated CAD program. AutoCAD has been selected for this purpose due to its capability of rapidly generating 3D drawing objects by reading the exported data files via the use of its own programming language, AutoLISP.

In general, the AutoLISP language features an execution of non-compilation file scripts similar to MATLAB. The majority of AutoLISP command lines represent the drawing and the action functions of the AutoCAD itself which makes the language suitable for automating the model generation. Nonetheless, sufficient knowledge of both AutoCAD and AutoLISP operations is required in order to appropriately select and utilise drawing tool commands, and also to supply optimal contexts of the exported data files to the AutoLISP for effectively extracting and producing the graphical results.

The initial part of the AutoLISP code is developed to perform the following procedures; read and categorise aircraft's station sections from within the text files, then assign series of point numbers stored in the station sections to appropriate drawing types e.g. poly-line, line and 3D objects. Figure 11.8 (upper section) shows the wireframe modelling of UCAV's fuselage and wing cross-sections together with their associated planform shape, which are generated by a combination of the poly-line and the line drawing tools. Due to the variable-shaped geometry of the propulsion duct models, the components are also drawn using the same approach as above. On the other hand, other internal component models (lower left) are created using the 3D-object tools which only require the input data of the location and the dimensions of the object.

In the same figure (lower right), the aircraft's surface is generated by the latter part of the AutoLISP code using the 'Edge Surface' command which creates a mesh in any selected quadrilateral frame formed by two adjacent cross-section stations and two other perpendicular boundary lines. The command is called repeatedly in order to generate the surface for the entire aircraft. However, this AutoCAD mesh generation is not appropriate for directly applying to the boundary lines which contain sharp deflections, e.g. perpendicular corners of the fuselage cross-section, since the program would create a round-transition mesh despite the shape changes of the boundary lines. This is due to the fundamentals of the program's mesh evaluation which produce the shape of the mesh surface according to an approximated boundary lines' trend rather than following their exact course. In order to rectify such an issue, the aircraft's cross-sectional frames are split into the top, side and bottom parts in which the mesh command is individually applied. Therefore, the perpendicular corners of the cross-section frames would not be presented in any part of the selected boundary lines, and thus the mesh surface can be generated more precisely in accordant with the frame structure of the model.

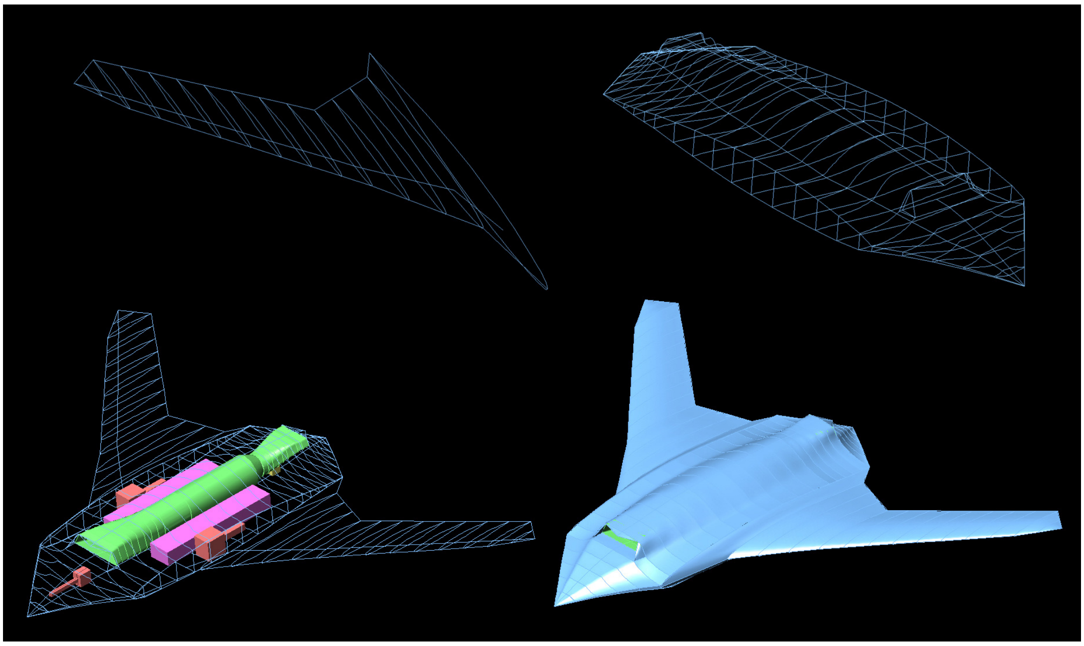

Figure 11.8: Aircraft model results generated by AutoCAD

Since the aircraft model contains various pointed sections e.g. the apex of the fuselage, saw-tooth sheath plates and wing tips, where the component's size is mathematically zero, thus any associated surface facets in the aforementioned sections consist of three edges (i.e. a triangular plane). However, the AutoCAD's 'Edge Surface' command can only be applied to quadrilateral-facet structure; therefore, a very small magnitude is included to the above zero-distance locations before exporting the modelling data from the design synthesis program. This would create additional virtual edge at the apex of the triangle facets and hence allowing the above mesh generation command to be applied. Finally, since both tanker and UCAV designs are symmetrical about the centreline, the exported data from the design synthesis program and the drawing codes were developed to generate half of the aircraft model, and then the 'Mirror' command would be called at the end of the drawing codes after the mesh generation to instantaneously create the other half. This mirror technique substantially reduces the amount of modelling point data required to be evaluated and exported from the design synthesis program, and so does the drawing procedure.

11.2.1.4 MATLAB Tornado Integrations

As far as the formation flight analysis is concerned, although it is possible to arrange, investigate and optimise the aircraft formation positions manually, the entire process would be extremely laborious and time-consuming due to the reasons stated in chapter 9. Therefore, additional MATLAB scripts were integrated into Tornado version 1.32 to assist formation flight analysis operations as follows.

`tloop#.m`, the bypass execution scripts, were embedded into the Tornado as additional options available for selecting in the main menu. The script character '`#`' represents the formation row number for which the results matrix will be generated. Since the development of these additional function scripts was focused on rapid evaluations of the formation flight analysis rather than retaining Tornado's interactive user-friendly features, any amendments regarding the flight-matrix envelopes as well as the selections of the aircraft model and the flight condition data files must be done in the scripts themselves. After the corresponding aircraft and flight condition data files have been selected, the script will re-configure the position of the trailing aircraft within the flight-matrix envelope specified by the user. For every formation position changes, the vortex-lattice model of the aircraft formation will be created and will be computed for aerodynamic performance outputs under the selected flight condition. The Tornado result file generated after every evaluation will then be stored in the result folder '`formation#`'.

Once the results matrix of a certain formation row has been entirely computed, the formation flight analysis function called `cpdist.m` can then be used separately outside the Tornado program for determining which formation position in the above results matrix yields the best solution according to the method described in section 9.3. The formation C_L and ΔC_P distribution data of the evaluated trailing aircraft will be extracted from each result data file, and then the function script `incL.m`, implementing Eq. (9.6) and its corresponding pre-computations, will be called for calculating the lift increment of the investigated formation row based on a given value of the formation C_L result. The difference between the total ΔC_P results about the above UCAV's centreline will be calculated for determining the merit value defined in Eq. (9.7). Afterward the function in `cpdist.m` will search for the results file which gives the maximum merit value, and then `regeo.m` will be called at the end of the operation to automatically set the UCAV positions in the original aircraft-formation model files to the optimal arrangement obtained above. This will eliminate the need for the user to manually do so every time the solution changes.

11.2.2 Programming Assessments

The computational design synthesis program contains a number of performance analysis and modelling evaluation subroutines executed for several iterations to achieve a convergence. Thus, despite recent computer technologies, a certain period of execution time is somehow inevitable. The speed at which the design synthesis operation is completed partially depends on the robustness of the programming structure especially in terms of subroutine and data organisation. However, the primary contributions to the overall execution time are, in fact, the numbers of iterations specified for certain procedures and their evaluations' complexity. For example,

Although the design synthesises of both tanker and UCAVs share similar design methodologies and computational structures, the tanker's evaluation takes much longer time to complete compared to the UCAV's. This is mainly because the design mission profile of the tanker, unlike the UCAV and many other aircraft, contains several range sub-segments which are established according to the preliminary refuelling sequence. Each of such segments is evaluated using the detailed range calculation that spans through various performance analysis modules (see section 8.4) in order to obtain accurate results. The overall computation time can actually be improved by reducing the number of evaluation segments divided for the range performance calculation; however, the decreased total time should be also compromised with the loss of accuracy due to fewer evaluation segments.

One of the main considerations for implementing the design methodology computationally is to develop small subroutines which carry out a specific task rather than the large ones that cover multiple operations together. This is to provide flexibility for each subroutine to be individually accessed and utilised while also eliminating the executions of other unrelated tasks as well as their associated input requirements. Thus, significantly reducing the computation time and computer's resources. In addition, the validation of small subroutines by comparing against manual evaluations and tracking any errors can be performed more conveniently.

Any parameters which share similar properties in common, such as XYZ coordinates of internal components or their geometry dimensions, are categorised and grouped in multiple levels of data structure to minimise the number of individual settings of input/output data. This increases portability of the data carried over between subroutines and also reduces the definition of long variable names which can be difficult to invent and recognise easily afterward. Nonetheless, for the modelling and other graphical plot data, multi-dimensional arrays are used for the storage since these data are normally called for the entire array and evaluated in iterations rather than doing so for specific coordinates in the array.

As far as the design synthesis methodology is concerned, many performance calculation methods, which are called several times throughout the design synthesis processes, contain graphical analyses that are favourable for manual evaluation. However, this is not the case if such methods are to be computationally implemented primarily due to the programming efforts involved in the imitation of the above manual analysis. For this reason, instead of following typical programming approaches of reading and interpolating results from data files, any graphical plots needed were converted into numerical equations using regression analysis program, Datafit. This conversion approach effectively produces faster execution time to the design synthesis program overall due to the substantial reduction of programming works and hence the computational procedures required to achieve a certain task. Numerical equations are also desirable from computational operation's point of view since their executions consume less computer's resource compared to typical data-scanning procedures. Furthermore, by eliminating the storage of graphical coordinate data, the entire program becomes smaller in size and more independent from other associated files.

Due to the reasons stated above, the International Standard Atmosphere (ISA) data, which are fundamental materials in the aeronautics field used for providing air properties at various altitudes, were programmed using to the equation forms provided by ESDU 77021 [62] instead of storing the entire table of the atmospheric data. Since the implemented design methods came from various sources and a number of them used their individual units as convenience, thus conversion functions between Imperial, Standard International, and other common units such as degree-radian, were created to swiftly change the parameter units for any methods. Also the subroutine functions for determining the maximum and the minimum values between a given set of input data or such within an array were developed to assist any magnitude comparison works.

A linear interpolation technique is applied in various subroutine tasks particularly the array coordinate approximation, e.g. estimating the aerofoil thickness at any given chord-wise position. Another application of this technique is for constructing an array of continuous data series (i.e. cross-sectional area distributions) with a uniform coordinate interval for the purpose of data superposition. In general the aforementioned array interpolation is performed by locating the coordinate interval where the subjected value falls in-between and then the result can be found by linearly interpolating the above value within the two associated boundary coordinates.

Although it is possible to export the design synthesis data after every certain number of iterations for tracking results convergence and storing previous data in case of the execution is terminated prematurely due to any reasons. Such features were not particularly necessary since the design synthesis results become converged after approximately 10 iterations while the overall computation time is somehow dispensable and much smaller in comparison to the subsequent optimisation process. Also the synthesised aircraft data contain a large number of variables which would unnecessarily increase computer's works if such data were consistently recorded by the means of designated data file or text format.

An optimisation procedure, on the other hand, usually takes 200-400 search iterations and approximately 3-7 hours to arrive at a solution. In contrast to the design synthesis case, despite a relatively large number of iterations, the optimisation results are essentially the design variables, range, and merit function value. Due to the small amount of data exported and the necessity of tracking optimisation behaviour and progress over a period of time, two separated log files are created in the operation, one for recording all optimisation search attempts and the other for only the best search results. Furthermore, the log time is also noted for the purpose of verifying whether the optimisation progress is hauled or trapped at some point due to unhandled errors.

A programming technique used for interfacing between the input/output data and the actual computation subroutines is commonly done by the means of data file and specific text form. Although such a technique is generally an effective solution when there are a large number of data need to be linked, it may prove to be time-consuming for new users to familiarise with the format and the contexts of the interfaced data. Also unlike the modelling data exported to AutoCAD, in which the contexts were constructed only meant for another computational code to decipher and execute accordingly, the user-interface data require a lot of efforts to develop the contexts in such a way that both the user and the computational code could comprehend. In order to provide the program which is simple for the user to understand and operate, GUIs have been created as illustrated previously in the Figure 11.6. Similar to the aforementioned data file approach, the values of the GUI-interface parameters are linked to the computation parts via the use of string-to-number conversion and vice versa. Since the program incorporates a large number of input and output parameters, sub-window forms and tab pages were employed in the GUI design to maintain the appropriate size of the main window and also to categorise the data types clearly in levels with an assistance of parameter group labels. This would help the user getting used to the program as well as locating for certain input/output parameters much more quickly.

Due to a substantial number of design parameters input to the GUIs, it would be difficult to manually track and change all the input values back to a certain combination setting. Thus, the following functions have been integrated to assist such an issue. A set of input values can be saved and loaded from a designated data file. This allows the user to record and recall any input value settings providing convenience and flexibility to the design investigation and manual optimisation of the aircraft. The save function procedure is carried out by converting a collection of input parameter values to a serial form and then writing these serialised data to a file, and the procedure of loading the input values from the data file is performed in reverse. The input value settings in the GUIs are also dynamically stored in the computer's resource and would be retrieved the next time the program opens. This internal data storage function was included to allow the user to resume their investigation with the value settings before the program being terminated due to any circumstances. Apart from the above functions of the GUI program, the output data can also be exported to a readable text format providing a swift note of the results.

The operations of the UCAV design synthesis, the tanker design synthesis, and the refuelling sequence optimisation have been developed to perform separately in order. The design synthesises of the UCAV and the tanker would be saved in the associated file format after the execution is completed. This is to allow the user to access to any of the above operation stages directly by loading the synthesised aircraft data from their corresponding save files. Without the need of repeating the execution in prior stages, the total time taken to complete the subsequent-stage runs would reduce due to the bypassed operations, and hence an investigation of a particular execution stage can be performed more efficiently. Also this operation scheme allows the user to select any UCAV and tanker files generated from different design conditions and couple them in the refuelling sequence optimisation, thus providing the capability of expanding the area of investigation.

The design synthesis and optimisation program itself can be potentially installed in any computer's directory due to one of the Visual Basic.NET functions which is capable of detecting the current location of the program. Thus, the output file paths of the spontaneous results, e.g. aircraft modelling data, would adapt automatically according to the program's location. However, since such a luxury function is not available in AutoLISP, the modelling data can only be read from fixed file paths, and hence indirectly forces the program package to be installed to a certain location. For this reason, the directory `C:\` was selected as an installation folder of the package due to the fact that this directory is commonly available in any computer personals.

By understanding the natures of the programming language and the implemented design methods, the subroutine created for performing a certain task can be developed with less redundancy and complexity. Hence, reducing the overall size of the codes as well as providing more efficient computer's resource consumption and faster execution time. Furthermore, appropriate designs of the data interface and data storage increase the flexibility of the program's utilisation as well as its operation simplicity.

Chapter 12

Case Study

This chapter will provide an example of the design and operational requirements used for synthesising individual aircraft, and also for verifying the results produced by the design methodology developed in this research project. An optimal cruise formation arrangement between the tanker and the UCAVs obtained from the formation flight analysis on Tornado will be presented. And finally the results generated by the optimisation of refuelling sequence will be shown and compared to the preliminary sequence used initially for designing the tanker.

12.1 UCAV Design Synthesis

As stated in the UCAV mission profile (see section 3.2.1.1), the design operations of the UCAV were considered based on a simple hi-lo-hi combat profile after breaking off from the formation with the tanker. Although in general it is desirable to deploy the UCAVs as close to the target as possible, in order for the tanker to avoid being involved in any conflicts, the aircraft needs to remain outside the enemy's hostile range. This distance is used for determining the deployment combat radius of the UCAVs. The high subsonic speed and high altitude selected for designing the UCAV are not justified based on the combat profile; however, from the optimal cruise and refuelling conditions during the formation with the tanker. The reason for this is to design the UCAV which is suitable for operating in both combat and formation sections.

As far as the current UCAV developments are concerned, their mission objectives generally focus on suppressing ground targets rather than performing aerial combat operations. Therefore, the weapon payloads carried could range from sophisticated air-to-ground missiles, e.g. AGM-65 Maverick, to guided general-purpose bombs such as JDAM-84 which is in fact a primary weapon payload of the developing X-47B [11]. Also a small-diameter bomb series GBU-39 which has been recently produced to allow strike aircraft to carry greater number of munitions may be considered for this UCAV. Figure 12.1 illustrates the design mission profile of the UCAV used in this case study while the descriptions of mission segment numbers can be found in section 3.2.1.

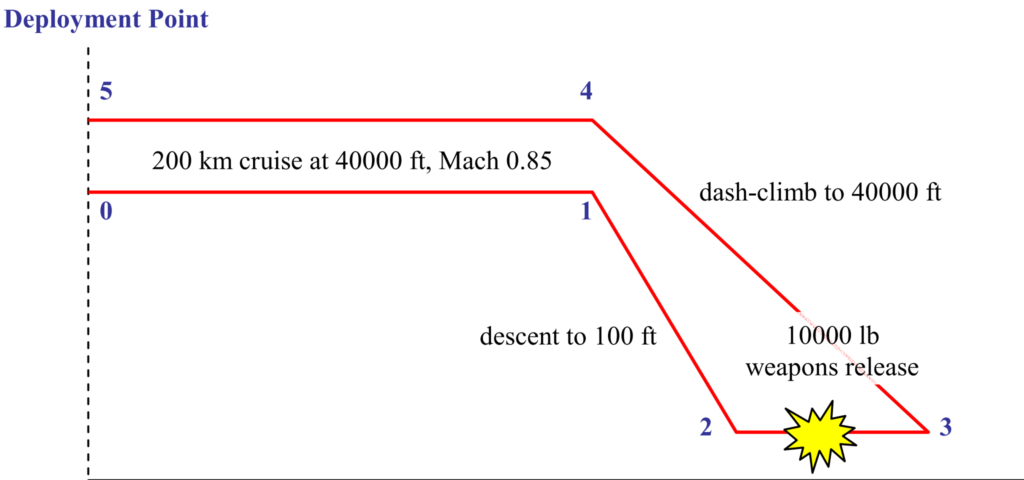

Figure 12.1: Design mission profile example of UCAV

Table 12.1: UCAV executive design requirements

Deployment combat radius	200 km	Payload weight (lb)	10000 lb
Wing aspect ratio	4	Max Load factor	9
Thrust-to-weight ratio	0.75	Cruise altitude	40000 ft
Wing loading	2000 N/m^2	Cruise Mach number	0.85
Landing-weight fraction	1.0		

From Table 12.1, the payload weight of 10000 lb is assumed for this particular case study primarily to demonstrate the enhanced payload carrying capability of UCAVs when the air refuelling technique is incorporated in a long-range mission. In a more detailed iteration of the design, the weight of the payload would be matched to the weapon bay dimensions by considering an appropriate armament installation density and the geometric constraints of the actual weapon.

Time was not permitted to develop a computational optimisation for the aircraft geometry and performances. Therefore, the general performances of the UCAV have been fully validated and manually optimised from the original baseline settings particularly in terms of aerodynamic and stability. The manual optimisation, performed by Dr Serghides, was conducted by primarily altering the wing planform and utilising reserve fuel c.g. shift provisions to achieve the aircraft which is operationally feasible and adequately robust for the purposes of this case study.

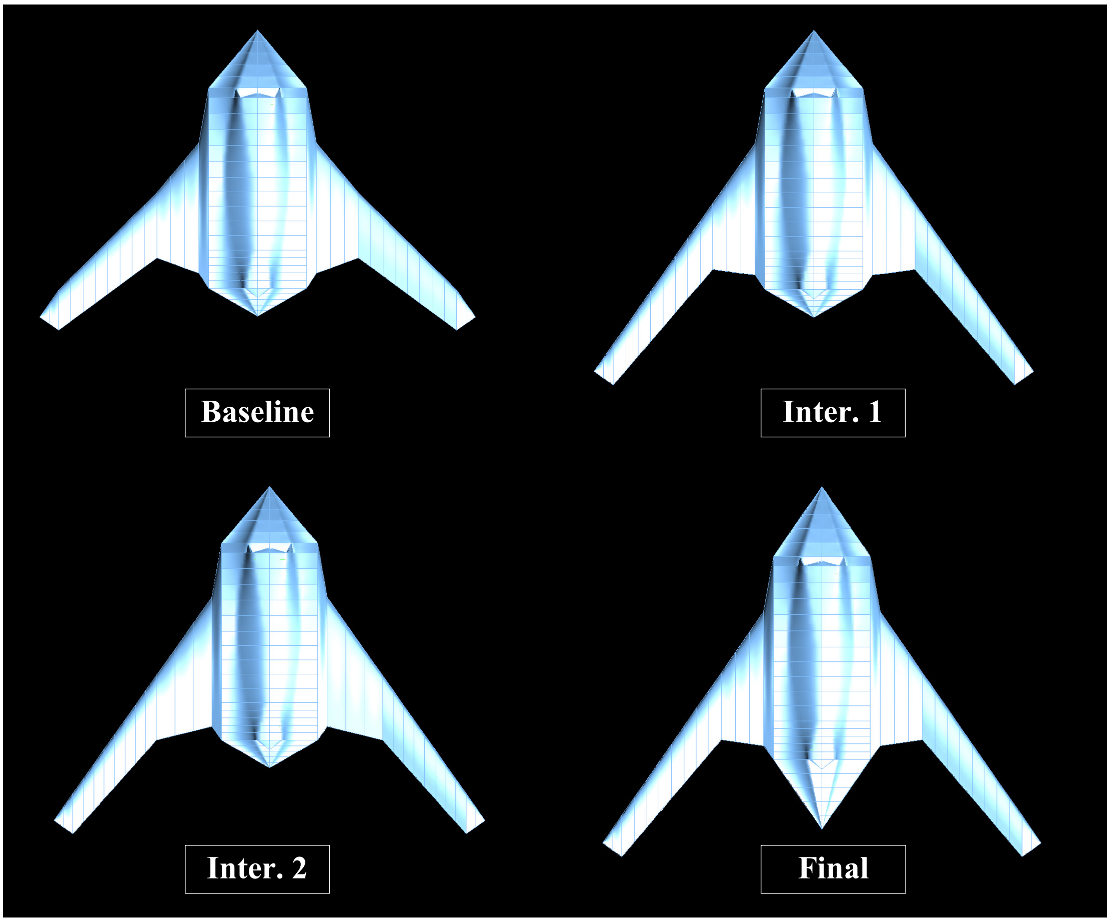

Figure 12.2: Validation and optimisation of the UCAV

Table 12.2: Overall UCAV specification changes

Configuration	Baseline	Inter. 1	Inter. 2	Final
T-O weight (lb)	26008	27000	26828	27805
Empty weight (lb)	14016	14932	14733	15697
Fuel weight (lb)	1992	2068	2095	2108
Length overall (m)	11.04	11.19	11.16	13.39
Height overall (m)	2.40	2.44	2.43	2.56
Wing span (m)	15.21	15.50	15.45	15.73
Wing reference area (m^2)	57.84	60.05	59.67	61.84
LE sweep – fairing (deg)	80	80	80	80
LE sweep – inboard (deg)	50	55	55	55
LE sweep – outboard (deg)	45	55	55	55
LE sweep – tip (deg)	55	55	55	55
Cruise lift-to-drag ratio	12.22	12.63	11.91	13.07
Cruise static margin (%)	1.15	7.94	17.31	6.72
Max sea-level thrust (lb)	15356	15942	15840	16417
Ferry range (km)	2957	3119	3008	3126

From Figure 12.2, the most obvious change in the final configuration of the UCAV compared to the baseline is a highly-swept wing with straight leading edge to enhance the longitudinal stability during various key flight conditions i.e. cruise, takeoff and landing. Despite a sacrifice in lift performance due to the high sweep in general, the effectiveness of the outboard control surfaces increases as they are swept further to the back. This provides a greater moment arm to produce counteracting lift forces, and hence lower the deflection angle required to trim the aircraft. The lift-to-drag ratio is also improved from this trim drag reduction. Furthermore the tail length of the fuselage was deliberately increased to align with the leading-edge sweep angle to enhance stealth characteristics of the aircraft. In this particular case study the incorporated edge alignment for stealth was rather limited in order to allow sufficient flexibility for the airframe geometry model to vary in accordance to the imposed optimisation requirements. The configuration geometry may be controlled through specific constraints set for each design case. The compressor might also be visible through a very small range of azimuth and elevation angles as shown in Figure 12.3

(front view); this, however, depends on the location of the aircraft relative to the radar at that particular moment

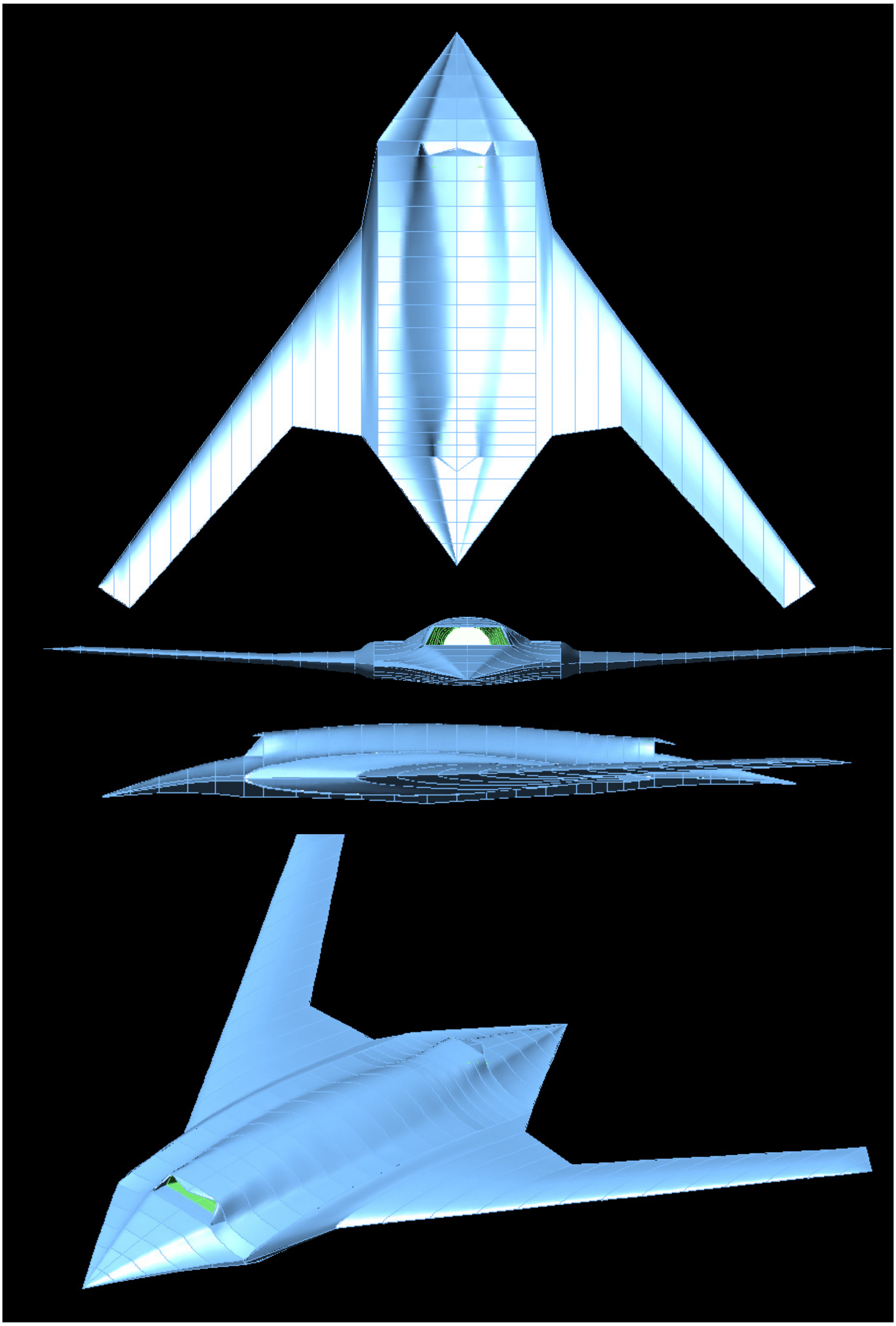

Figure 12.3: Three-view drawing of the UCAV model result generated by AutoCAD

Table 12.3: UCAV executive output summary

Length overall	13.39 m	Max T-O weight	27805 lb
Height overall	2.56 m	Empty weight	15697 lb
Wing span	15.73 m	Fuel weight	2108 lb
Wheel track	3.02 m	Payload weight	10000 lb
Wheelbase	6.24 m	Max sea-level thrust	16418 lb
Wing reference area	61.84 m^2	X-c.g. @MTOW	6.849 m
Deployment combat radius	200.55 km	Z-c.g. @MTOW	1.765 m
MTOW range	62.9 km	MAC	4.55 m
Ferry range	3126 km	Spanwise MAC location	3.55 m

Table 12.3 contains a summary of important UCAV's geometry and performance specifications obtained at the end of the design synthesis for results examination and justification. In general, the size and the weight of the developed UCAV are smaller than X-47B; nonetheless, the overall specifications of the aircraft are still much larger in comparison to its predecessor i.e. X-47A. Since the UCAV has been designed to perform a mission in group with an assistance of periodical refuelling operations from the tanker, the individual aircraft carries a relatively small amount of fuel compared to its weapon carriage capability as depicted in the output results.

The above advantageous characteristic of the aircraft; however, comes with the range performance trade-off which is to be expected considering the design requirement of 200-km combat radius. The design synthesis methodology has been developed in such a way that it would size the aircraft to precisely match a given design mission profile. Hence, the reason the combat radius result reflects approximately the same value as the design requirement. The output range evaluations are accounted for the distance produced in the level-flight segment only. And for this reason, the low range at the maximum takeoff weight condition is the results of both of heavy payload carriage and decent amounts of fuel being consumed in the non-level-flight segments. On the other hand, the ferry range is calculated under the assumption of the UCAV carrying additional fuel in the weapon bays; therefore, the aircraft exhibits much greater range performance compared to the previous maximum weight condition.

Table 12.4: UCAV in-flight performance – 1

Cruise Conditions			
Mach number	0.85	Max cruise thrust	6141 lb
Altitude	40000 ft	SFC	0.839 lb/hr/lb
C_L Alpha	2.42 rad^{-1}	Fwd X-c.g. limit	6.87 m
C_L Max	1.43	Aft X-c.g. limit	7.14 m
Stall angle	41.47°		
Outbound Leg		**Inbound Leg**	
Thrust	2112 lb	Thrust	1537 lb
Aircraft weight	27607 lb	Aircraft weight	16197 lb
C_L	0.209	C_L	0.122
C_{D0}	0.011	C_{D0}	0.010
L /D	13.07	L /D	10.53
Specific excess power	120.07 ft/s	Specific excess power	233.86 ft/s
Stall speed	186.44 knots	Stall speed	142.81 knots
Static margin	6.719 %	Static margin	1.213 %
Trim alpha	1.00°	Trim alpha	-0.89°
Inboard control deflection	4.45°	Inboard control deflection	3.83°
Outboard control deflection	4.45°	Outboard control deflection	3.83°

The 5.5% difference in the static margin between the outboard and the inbound legs occurs due to the c.g. shift from the payload release. Although it is desirable to allocate the weapon very close to the overall c.g. of the aircraft so that the release of the payload would not have significant effect on the aircraft's stability. For this blended flying-wing design aircraft, such an ideal is difficult to achieve due to the internal payload bay installation. This causes the allocation of the item to be highly constrained by the airframe surface and other internal components; nonetheless, in this design example, the resulted static margin range is within reasonable limits.

The above C_{D0} outputs comprise the wave drag and skin-friction drag including one due to the control surface deflection. Therefore, a minor C_{D0} difference between both cruise legs is shown despite operating at the same flight condition. The reduction of the lift-to-drag ratio in the inbound leg occurs primarily as a result of the lower aircraft weight and hence the lift force needed to maintain the UCAV in a steady level flight which is clearly shown in the resulted trim alpha (i.e. the aircraft's angle of attack). The trim alpha in cruise is maintained within the maximum of ±1°, thus it can be rationally assumed that any additional frontal drag of the aircraft due to the angle of attack is negligible.

Table 12.5: UCAV in-flight performance – 2

Climb		**Descend**	
Mach number	0.5	Mach number	0.5
Climb rate	9844 fpm	Descend rate	2101 fpm
Climb angle	18.45°	Descend angle	-3.87°
Throttle setting	100 %	Throttle setting	10 %
Covered range	36.54 km	Covered range	179.60 km

The climb and the descend conditions depicted in Table 12.5 are evaluated at the middle between the cruise and sea-level altitudes. Due to a relatively powerful thrust and low-drag characteristic of the UCAV, an air brake application is required for the aircraft in order to properly descend in the near-empty weight landing situation.

Table 12.6: UCAV field performance

Takeoff		**Landing**	
Ground run	574.68 m	Ground run	998.79 m
Total distance	1304 m	Total distance	1604 m
Takeoff speed	148.77 knots	Touchdown speed	148.77 knots
Static margin	0.492 %	Static margin	0.492 %
Takeoff alpha	10.66°	Touchdown alpha	10.66°
Inboard control deflection	4.94°	Inboard control deflection	4.94°
Outboard control deflection	4.94°	Outboard control deflection	4.94°
T-O Climb angle	18.31°	Approach angle	-3°

It is commonly stated that combat aircraft should be designed to be unstable for manoeuvrability and agility purposes; however, this is only the case for conventional fighters which possess tail planes to stabilise themselves efficiently. Although it is rather common to fly an aircraft with negative static margins in flight, for the takeoff and landing operations, it is dangerous for a highly unstable aircraft to operate due to its natural tendency to pitch up in the takeoff rotation and touchdown flaring. Hence causing the platform to become sensitive to external disturbances and may lead to losing control. Therefore, the reserve fuel c.g. is managed in such a way that the static margin of the UCAV is maintained in a positive region during the above takeoff and landing operations.

According to military regulations, the takeoff and touchdown speeds are coincided at $1.1 \cdot V_{\text{stall}}$. With the maximum landing weight fraction of 1 for the UCAV, there is no doubt that the aircraft would reflect the same flight characteristics in the transition segments of both takeoff and landing operations.

The design synthesis results of the UCAV presented so far are evaluated solely based on the aircraft's mission profile in the combat section of the entire tanker/UCAV combination scenario (see Figure 3.3). Hence the resulted UCAV is naturally independent from the formation cruise section with the tanker. In order to establish a preliminary refuelling sequence of the UCAVs which is necessary for sizing the tanker, the overall operational requirements of the above aircraft combination shown in Table 12.7 below are used.

Table 12.7: Tanker/UCAV combination operational requirements

Formation cruise radius	5000 km
Number of UCAVs per tanker	6
Formation-flight lift increment	20%
Refuelling air speed	350 knots
Refuelling operation time	10 min

The total combat radius capability of the tanker/UCAV combination measured from the air base to the actual target is governed by the formation cruise section. As mentioned in the introduction chapter, this aircraft combination concept is developed to serve a long-range mission without making a stop. Thus, for the purpose of this study example, a medium-intercontinental distance which is somehow comparable to a sophisticated bomber aircraft such as B-2 Spirit is applied. The justifications for the number of UCAVs per tanker have already been described in section 9.3 while the UCAV's lift increment of 20% due to the formation flight is set as an example value considered from the analysis results shown in Table 12.15.

Since it is desirable to reach the target and hence complete the mission as quickly as possible, the speed at which the aircraft combination needs to slow down for refuelling should be maximised. And as far as the operational envelopes of various refuelling hose drum units are concerned, the maximum air speed allowed during the refuelling operation is 350 knots [49] while the ceiling altitude of the same component is 40000 feet. In attempt to minimise the flight condition changes in the formation section, the cruise altitude of both aircraft was specified to the above refuelling envelope value. The total refuelling time of 10 minutes is approximated based on the offload rate of the hose drum unit and the maximum fuel capacity of the UCAV. Sufficient time is also allowed for air refuelling contact procedures and the interval between three UCAV formation rows.

Table 12.8: Refuelling provision analysis results

Outbound Leg		**Inbound Leg**	
Number of refuelling	5	Number of refuelling	4
Uniform segment fuel	11656 lb	Uniform segment fuel	10963 lb
Pre-combat segment fuel	12520 lb	Pre-landing segment fuel	11447 lb
Takeoff segment range	563.50 km	Landing segment range	914.93 km
Uniform segment range	974.08 km	Uniform segment range	1217.6 km
General			
Total offload fuel required		103485 lb	
Refuelling range		108.03 km	
Combat operation time		1.16 hr	

Table 12.8 contains the preliminary refuelling sequence results evaluated according to the design requirements given in Table 12.7. Due to the payload carried during the outbound leg, the UCAV undoubtedly demands greater amount of fuel and more frequent refuelling compared to the inbound leg for the same total distance. Also clearly by excluding the takeoff and landing processes from the system, the UCAV's

fuel can be consumed more efficiently during cruise, and thus producing much further range in level-flight segments in general. The above refuelling sequence results will be used for generating the detailed mission profile segments (see Figure 12.4) for appropriately designing the tanker.

12.2 Uninhabited Tanker Design Synthesis

In contrast to the UCAV, the design mission profile of the tanker follows a common takeoff-landing operation as illustrated in Figure 12.4 where the majority of the design requirements specified for the tanker operation have already been described in the previous UCAV section.

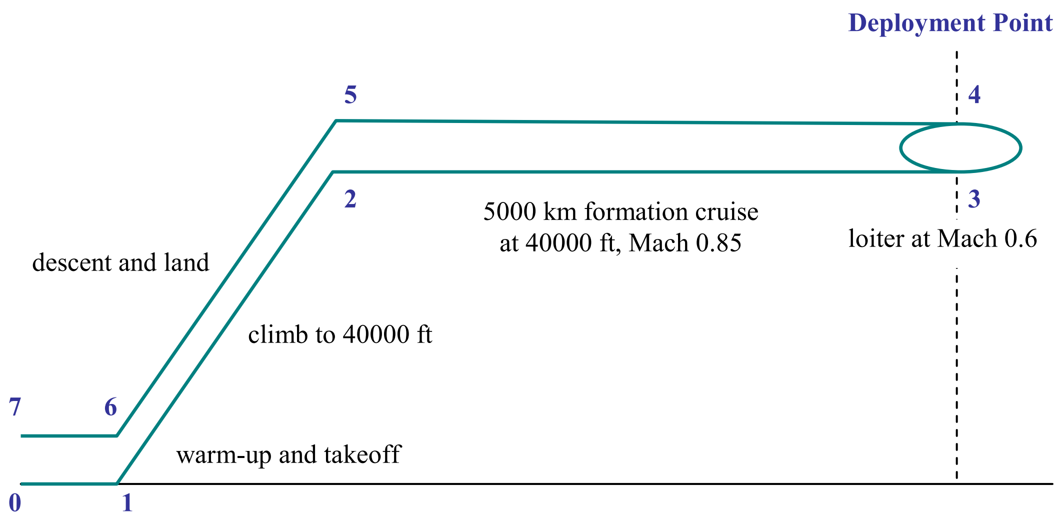

Figure 12.4: Design mission profile example of tanker

The loiter altitude is maintained from the cruise condition, while a lower cruise Mach number is selected for this segment in order to eliminate the wave drag rise occurring at high-subsonic speed. The reduced total drag would result lower thrust required to sustain a level flight, and hence reducing the overall fuel usage on top of the decreased specific fuel consumption which is proportional to the air speed. The outbound and the inbound formation cruise sections, denoted by the segments 2-3 and 4-5 respectively, contain sub-mission profiles constructed as shown in Figure 12.5 below.

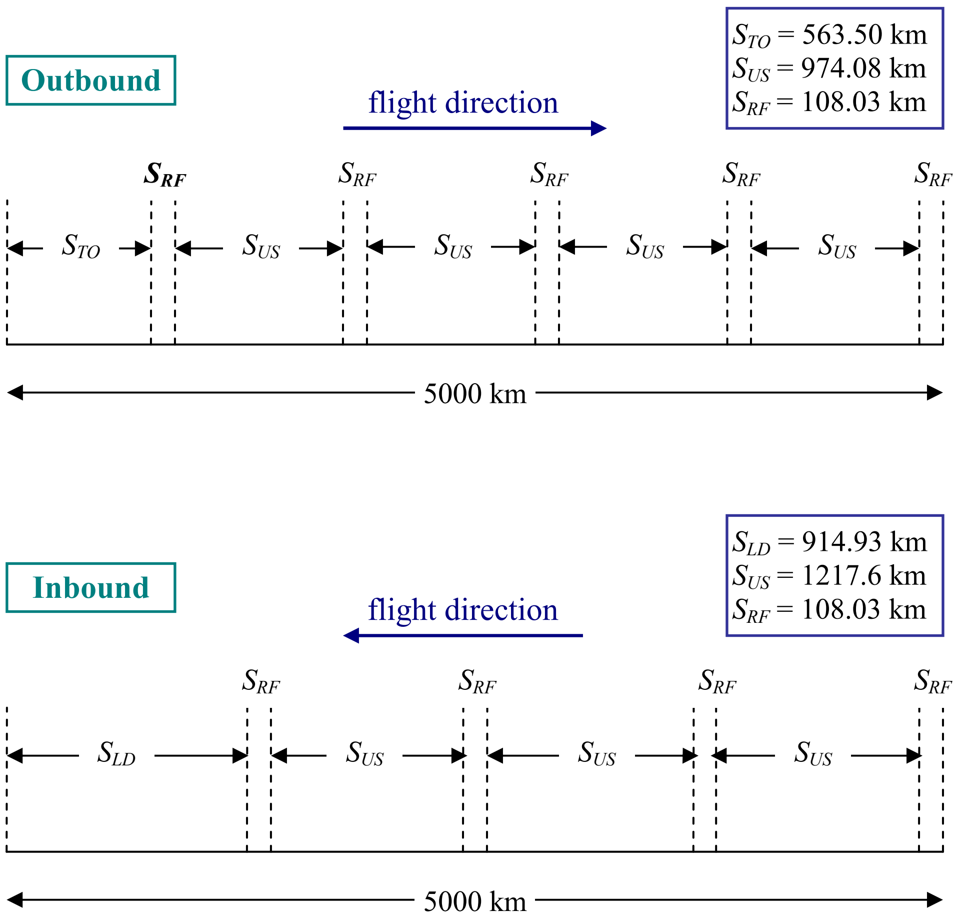

Figure 12.5: Refuelling sequence sub-mission profiles

The range segments S_{TO}, S_{LD}, and S_{US} displayed in the figure above are proceeded according to the design cruise conditions, whereas for every S_{RF} range segment, the tanker would slow down to 350 knots (as specified in the Table 12.7) to perform an air refuelling operation.

The tanker's weapons are installed for the purpose of providing a sufficient self-defence capability rather than utilising them for purely offensive roles; therefore, the defensive package considered consists of air-to-air missiles e.g. AIM-120 AMRAAM in combination with radar/infrared countermeasures such as chaffs and flares. The tanker is also designed for sustaining a load factor of 2.5 g since it is primarily designed as a cruiser. On the other hand, the UCAV is designed to sustain

9 g manoeuvres. This is because its primary mission is the suppression of enemy air defences (SEAD) in which the aircraft is expected to be highly manoeuvrable in order to avoid a high density of ground-to-air missiles.

Table 12.9: Tanker executive design requirements

Formation cruise radius	5000 km	Wing aspect ratio	7
Fuel payload weight	103485 lb	Thrust-to-weight ratio	0.4
Weapon payload weight	2500 lb	Wing loading	3000 N/m^2
Refuelling air speed	350 knots	Cruise altitude	40000 ft
Max sea-level Mach number	0.9	Cruise Mach number	0.85
Max cruise Mach number	1.0	Loiter Mach number	0.6
Landing weight fraction	0.85		

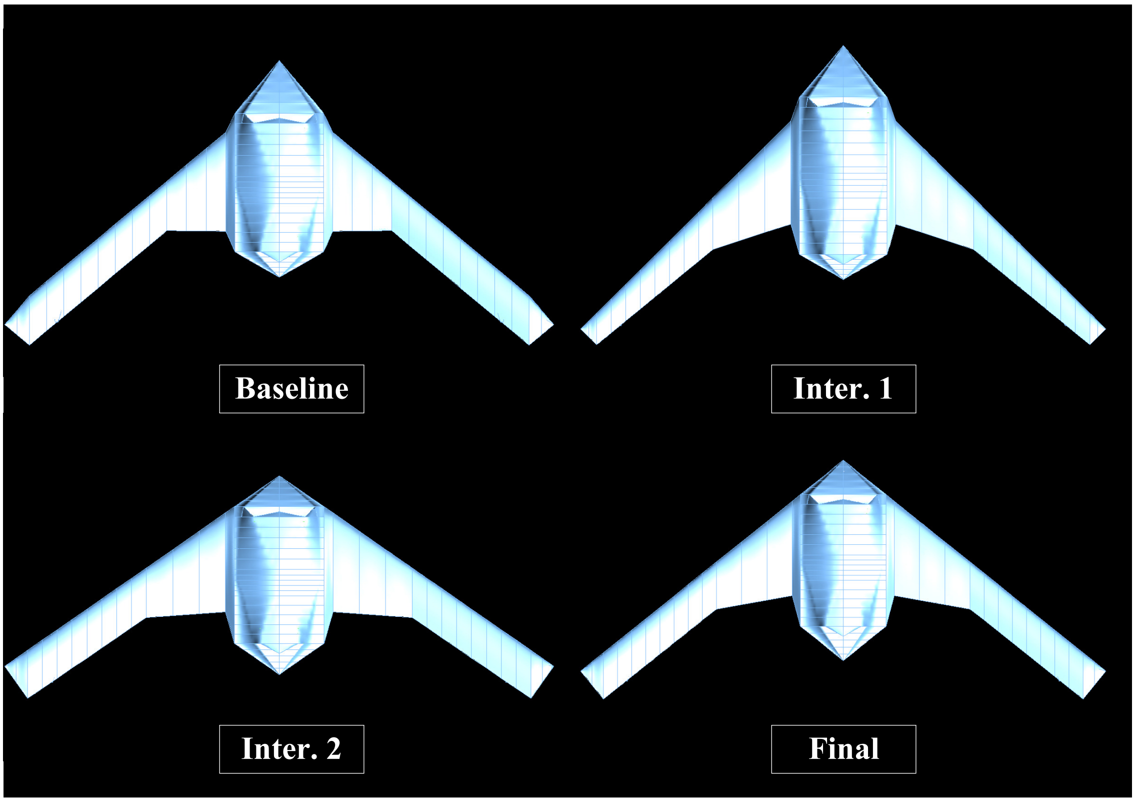

Figure 12.6: Validation and optimisation of the tanker

An optimisation of the uninhabited tanker has been performed in the same way as the UCAV. However, in the baseline design, the static margin of the aircraft in cruise was somehow over stable, whereas for the takeoff/landing case, the aircraft become unstable during the rotation. Thus, in order to rectify and compromise such issues, the reserve fuel c.g. is pumped toward the aft of the fuselage in cruise and controversy shifting forward during the takeoff/landing to stabilise the aircraft for all important operation points. The leading-edge sweep has been reduced to improve aerodynamic efficiency as well as providing larger outboard-wing chord increasing the partition stiffness and thus preventing it from being twisted at high speed.

Table 12.10: Overall tanker specification changes

Configuration	Baseline	Inter. 1	Inter. 2	Final
T-O weight (lb)	471546	514381	422887	452473
Empty weight (lb)	152891	170886	132602	145995
Fuel weight (lb)	209002	239040	185829	200494
Fuel Payload (lb)	107154	101955	101955	103485
Length overall (m)	30.96	33.81	26.06	28.91
Height overall (m)	5.72	6.60	5.69	6.13
Wing span (m)	69.96	73.06	66.25	68.52
Wing reference area (m^2)	699.16	762.68	626.93	670.72
LE sweep – fairing (deg)	65	70	35	39
LE sweep – inboard (deg)	40	45	35	39
LE sweep – outboard (deg)	40	45	35	39
LE sweep – tip (deg)	50	45	35	39
Cruise lift-to-drag ratio	14.68	13.12	14.27	14.62
Cruise static margin (%)	11.62	22.77	5.11	9.99
Total sea-level thrust (lb)	61951	67578	55550	59431
Ferry range (km)	18530	16651	18433	18801

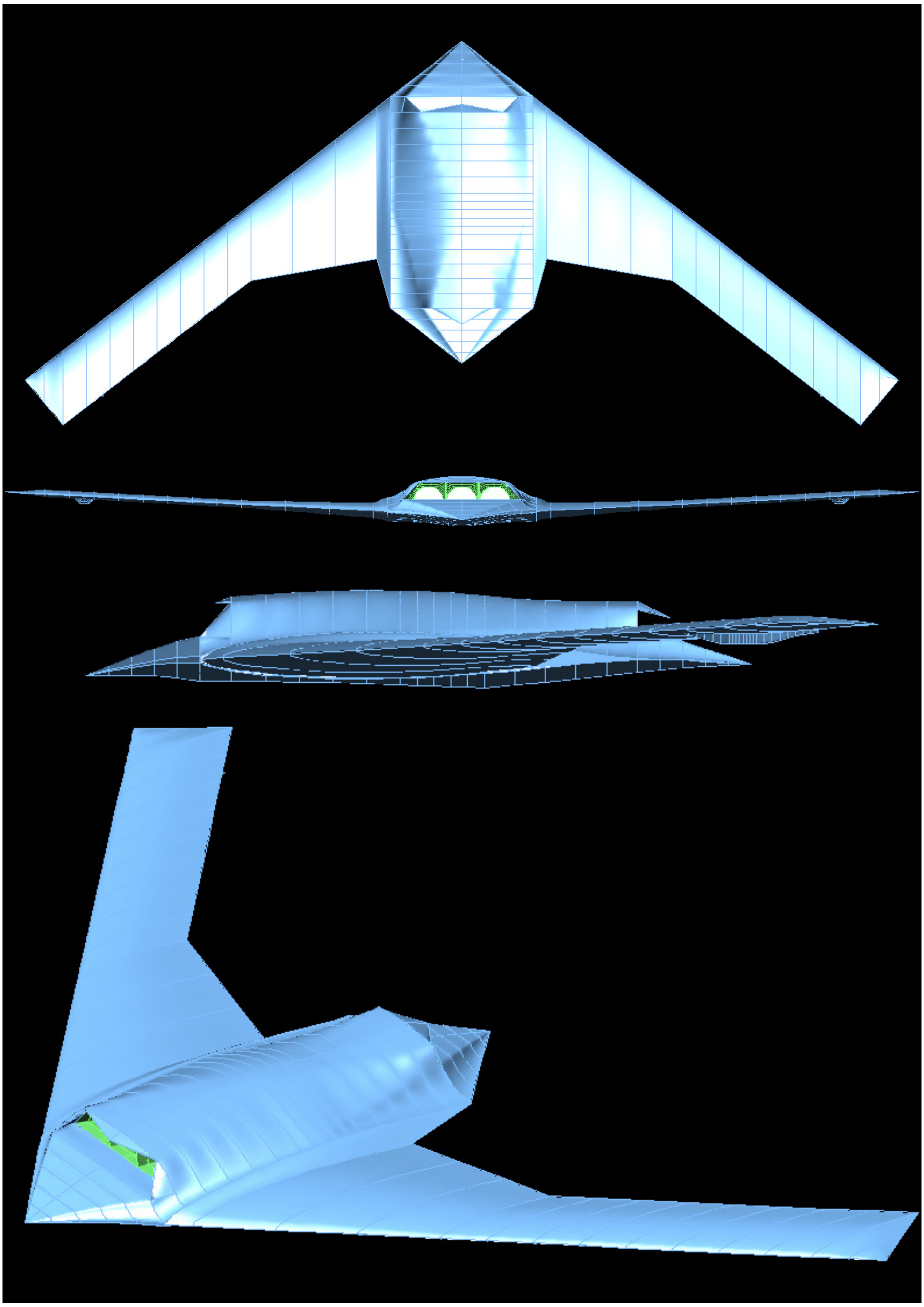

Figure 12.7: Three-view drawing of the tanker model result generated by AutoCAD

Table 12.11: Tanker executive output summary

Length overall	28.91 m	Formation cruise radius	4999.85 km
Height overall	6.13 m	Max T-O weight range	9195 km
Wing span	68.52 m	Ferry range	18800 km
Wheel track	14.83 m	T-O distance	1578.8 m
Wheelbase	12.87 m	Balance field length	1300.8 m
Wing reference area	670.72 m^2	Landing distance	1545.5 m
Max T-O weight	452473 lb	Climb rate	6182.5 fpm
Empty weight	145995 lb	Max sea-level thrust	178290 lb
Max fuel weight	200493 lb		

Since the design synthesis of the tanker has been developed using the same approach as the UCAV, the calculated value of the formation cruise radius reflects approximately the same value as that specified in the design requirements. As far as the takeoff weight result is concerned, the exampled uninhabited tanker could be compared to the current U.S. Air Force tanker, KC-10 Extender. Undoubtedly due to a dedicated design, the uninhabited tanker possesses lighter empty weight and better range performances while carrying greater fuel capacities for both individual consumption and offloading purposes. Due to the tailless flying-wing configuration, the sizes of the uninhabited tanker airframe prove to be much smaller in the longitudinal and vertical dimensions. However, the wing span of the developed tanker, hence the overall lateral dimension, is greater than the KC-10 Extender as a result of lower wing loading in comparison. The above ferry range was evaluated under an assumption of the tanker carrying its own additional fuel in the payload tanks.

Table 12.12: Tanker in-flight performance – 1

Outbound Cruise		**Inbound Cruise**	
Thrust	24724 lb	Thrust	17288 lb
Aircraft weight	361399 lb	Aircraft weight	225912 lb
C_L	0.253	C_L	0.158
C_{D0}	0.013	C_{D0}	0.010
L /D	14.62	L /D	13.07

Specific excess power	114.72 ft/s	Specific excess power	210.60 ft/s
Stall speed	211.18 knots	Stall speed	166.97 knots
Static Margin	9.991 %	Static Margin	0.404 %
Trim alpha	0.76°	Trim alpha	-0.65°
Inboard control deflection	-3.99°	Inboard control deflection	-2.57°
Outboard control deflection	3.99°	Outboard control deflection	2.57°

The difference deflection between the inboard and the outboard control surfaces is observed in cruise while it is not the case during takeoff and landing. This is because the overall c.g. of the tanker in cruise is located behind the inboard device. Therefore, an opposite deflection is required to generate a correct balancing force and hence appropriately trim the aircraft. The majority of other performance results show similar behaviours to the previous UCAV case, thus will not be discussed in details.

Table 12.13: Tanker in-flight performance – 2

Climb		**Descend**	
Mach number	0.4	Mach number	0.5
Climb rate	6183 fpm	Descend rate	2593 fpm
Climb angle	14.39°	Descend angle	-4.78°
Throttle setting	100 %	Throttle setting	10 %
Covered range	47.53 km	Covered range	145.71 km

Table 12.14: Tanker field performance

Takeoff		**Landing**	
Ground run	897.68 m	Ground run	961.15 m
Total distance	1353 m	Total distance	1545 m
Balance field length	1301 m	Touchdown speed	140.67 knots
Takeoff speed	152.58 knots	Static margin	7.772 %
Static margin	7.576 %	Touchdown alpha	7.49°
Takeoff alpha	7.58°	Inboard control deflection	7.32°
Inboard control deflection	7.04°	Outboard control deflection	7.32°
Outboard control deflection	7.04°	Approach angle	-3°
T-O Climb angle	8.67°		

The maximum landing weight fraction of the designed tanker was specified at 85% similar conventional airliners. This requires fuel jettison to reduce its total weight if the aircraft attempts to land immediately after the takeoff with maximum loads. In contrast to the UCAV, as a result of this different takeoff and landing conditions, the operational air speeds and their associated stability performances are also different.

12.3 Formation Flight Analysis

The formation flight analysis has been conducted prior to the above design synthesis evaluations, using the tanker and UCAV airframe configurations obtained from the preliminary runs of corresponding aircraft design synthesis, to determine an approximated optimal formation arrangement of the designed aircraft flying in combination as well as their associated aerodynamic performance improvements. A summary of these analysis results is shown in Table 12.15 below.

Table 12.15: Formation flight analysis results

Parameter	**1st Row**	**2nd Row**	**3rd Row**
Longitudinal position (X)	60.61 m	80.81 m	111.11 m
Lateral position (Y)	37.04 m	47.13 m	57.24 m
Vertical position (Z)	0 m	3.36 m	5.05 m
Lift increment (%)	21.1%	16.4%	27.79%
Total ΔC_p difference	0.009	0.024	12.12
Merit function value	2312.41	673.81	2.29

The additional lifts gained in each aircraft formation row are the important figures used for justifying the average value of the same parameter inputted in the preliminary refuelling sequence development (see Table 12.7). As far the above formation flight results are concerned, the ΔC_P differences of the UCAVs in the first and the second rows of formation coordinate are very close to zero. This indicates that the aircraft flying at such positions can exploit the formation-flight upwash benefit without the need of appended control surfaces to counteract the rolling moment. Within the first two stabilised formation rows, the first row gain higher lift increment in comparison to second one, which is most likely due to its closer proximity and directly behind the large aircraft as the tanker. Although the lift increment resulted from the third formation row is rather prominent relative to the first two cases, the associated ΔC_P difference of such a formation coordinate is not small enough to become negligible. Therefore in practice, minor control surface usage might be needed in order to trim the aircraft from gradually rolling away from the formation.

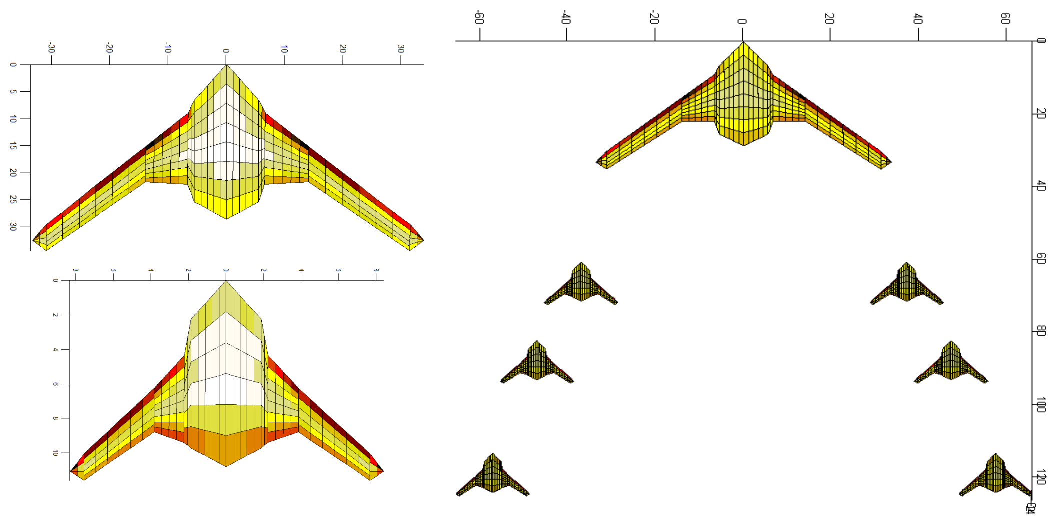

Figure 12.8: Vortex lattice models of tanker and UCAV and their optimal formation result

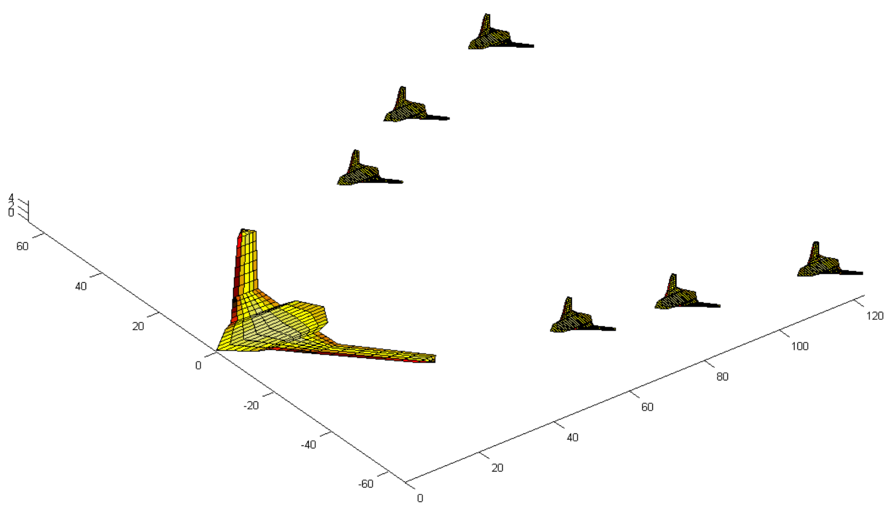

Figure 12.9: Optimal aircraft formation arrangement from an isometric view direction

Figures 12.8 and 12.9 together depict the tanker and UCAV vortex-lattice models used in the formation flight analysis as well as their optimal formation arrangement. In general, the positions of the UCAVs in the formation laterally expand as the row numbers become further. This creates a resembling V-shaped formation which is rational considering the fact that the upwash regions are produced in the outboard proximity of the leading aircraft. Although the relative positions between aircraft formation rows are not consistently uniform similar to typical formation arrangements performed in military and various air shows, it should be noted that this aircraft formation result has been analysed according to optimal aerodynamic performance criteria, not the regulation or demonstration of flight commanding operations. Therefore, the variation of the aforementioned relative formation positions has been anticipated.

The vertical positions of each aircraft in the above optimal formation appear to be rising as depicted in the Figure 12.9. Normally, in a close formation flight between manned aircraft, the pilots rely on visual references of the leading aircraft to position and preserve their aircraft's coordinate in the formation. However, with an upward echelon arrangement shown in the above optimal formation result, it is practically not feasible for the piloted aircraft to perform and maintain such a formation precisely. This is primarily due to the difficulty of the trailing aircraft's pilot to obtain a clear reference view when the leading aircraft is underneath. Not to mention the risk of mid-air collision due to a long-haul formation flight in obscure visual conditions of the nearby aircraft. In order for the UCAV to be capable of flying in this upward formation arrangement with high precision, a sensor package may be installed under the fuselage's nose area to receive accurate optical data of the current relative formation position from the leading aircraft flying beneath.

Within the contexts of this research study, by increasing the additional lift which the UCAV gained from flying in formation with the tanker, a reduction of the total offload fuel, and hence the weights of the designed tanker, required to complete a given operating range, were observed as shown in Table 12.16 below. The test was conducted by solely changing the formation-flight lift increment value used for synthesising the tanker while the other required inputs were fixed at the original optimised condition for 20% lift increment.

Table 12.16: Effects of the formation-flight lift increment on the tanker weights

FF Lift Increment	0%	5%	10%	15%	20%	25%	30%
MTOW (lb)	485639	479959	472846	464144	452473	446184	435634
Empty weight (lb)	157127	155293	153114	150462	145995	143828	140143
Tanker fuel (lb)	212273	211077	208460	205459	200494	198451	190084
Fuel payload (lb)	113739	111089	108772	105722	103485	101405	99474

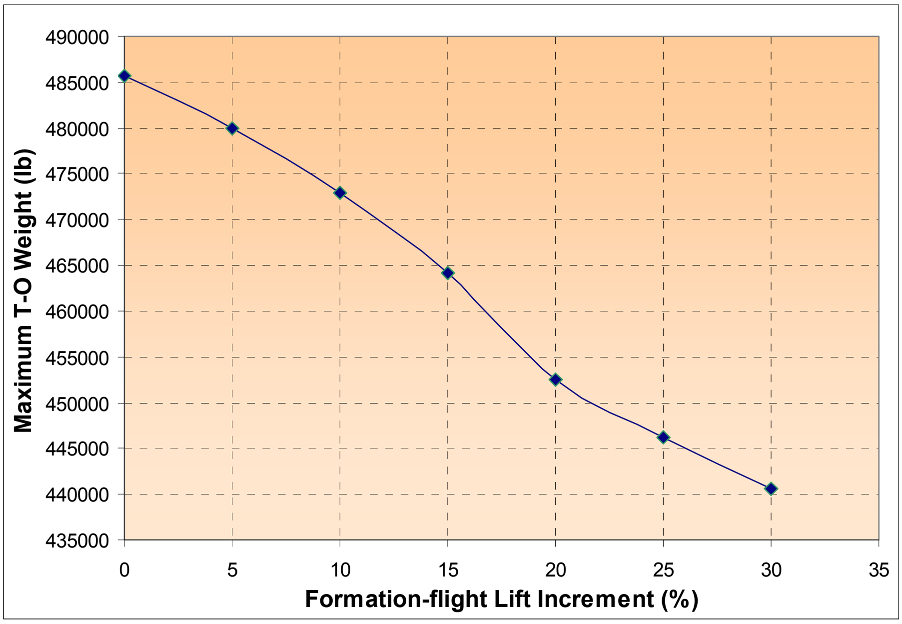

Figure 12.10: Tanker's MTOW vs. UCAV's lift increment due to formation flight

As far as the above table is concerned, it is clear that the overall weights of the designed tanker reduce accordingly as the formation-flight aerodynamic effect increases. Since the cost of developing an aircraft in general is proportional to its design weight, the above data shows that apart from saving the operating and fuel costs, the cost of the aircraft development would go down as a result of the formation flight benefit. From Figure 12.10, a slight drop in the tanker's takeoff weight relation is presented at 20% lift increment. This is most likely due to the fact that the aircraft configuration tested was optimised particularly for such a point.

12.4 Refuelling Sequence Optimisation

An optimisation of the refuelling sequence between a given combination of the designed tanker and UCAVs is performed at the end to explore a possibility of enhancing the combination range performance, which is done by changing the operational and refuelling procedures in the formation section from the original design conditions. Table 12.17 shows a list of the design variables used, specified boundary constraints, and a comparison between the values applied for designing the preliminary refuelling sequence and the best results achieved by the optimisation.

Table 12.17: Optimisation results – Design variable

Design Variable	Lower Limit	Upper Limit	Design Con.	Optimum
Outbound fuel fraction	0.5	1.0	0.921	0.946
Inbound fuel fraction	0.5	1.0	0.905	0.895
Cruise Mach number	0.75	0.95	0.85	0.8
Cruise altitude (ft)	25000	40000	40000	40000
Refuelling air speed (knots)	250	350	350	350

From the above results, the optimal values of the offload fuel fraction are relatively close to the original design conditions. This implies that the preliminary refuelling sequence analysis (see section 3.2.2.1) itself provides an effective solution close to an absolute optimum to start with. On the other hand, the design variables which provide a decent contribution to the changes of overall aircraft combination's performances are the cruise Mach number and altitude due to their direct influences on both aerodynamic and propulsion characteristics of the aircraft.

Due to the natures of this refuelling sequence optimisation problem and the pattern search technique applied, multiple optimisation runs were performed using various starting design variables conditions (i.e. base points). This is primarily to increase the chance of locating and verifying for superior solutions since the Hooke and Jeeves algorithm was originally developed to explore a solution in specific directions rather than searching through an entire design space. Table 12.18 presented below contains three different base point inputs and the optimisation results obtained from each case.

This shows that, while the third case produced the best merit function value despite its most distanced starting point of all.

Table 12.18: Optimisation results – Base point comparison

Base Point	**Case 1**	**Case 2**	**Case 3**
Outbound fuel fraction	0.92	0.85	0.8
Inbound fuel fraction	0.86	0.82	0.8
Cruise Mach number	0.83	0.85	0.8
Cruise altitude (ft)	40000	38000	30000
Refuelling air speed (knots)	350	300	280
Optimal Point			
Outbound fuel fraction	0.936	0.936	0.946
Inbound fuel fraction	0.998	0.893	0.895
Cruise Mach number	0.803	0.801	0.8
Cruise altitude (ft)	39250	38509	40000
Refuelling air speed (knots)	350	335.07	350
Performance Results			
Formation cruise radius (km)	5417.80	5317.60	5453.62
Total fuel consumption (lb)	311935	310595	311518
Total operation time (hr)	14.22	14.07	14.35
Merit function value (km /lb-hr)	1.094	1.073	1.101

An optimisation path and merit function improvement of the above best search result, i.e. Case 3, are plotted in Figures 12.11 and 12.12. With an exception of the cruise Mach number, the majority of the design variables went through drastic changes during the first 45 iterations and afterward these parameters began to converged and minor improvements were achieved. The reason for this was because, despite multiple search attempts during this phase, the optimisation could not find any leads to a better result area. Also an encounter of the tanker and payload fuel constraints prevented the offload fuel fractions from rising higher or flying at faster speed due to a greater drag penalised and increase fuel consumption.

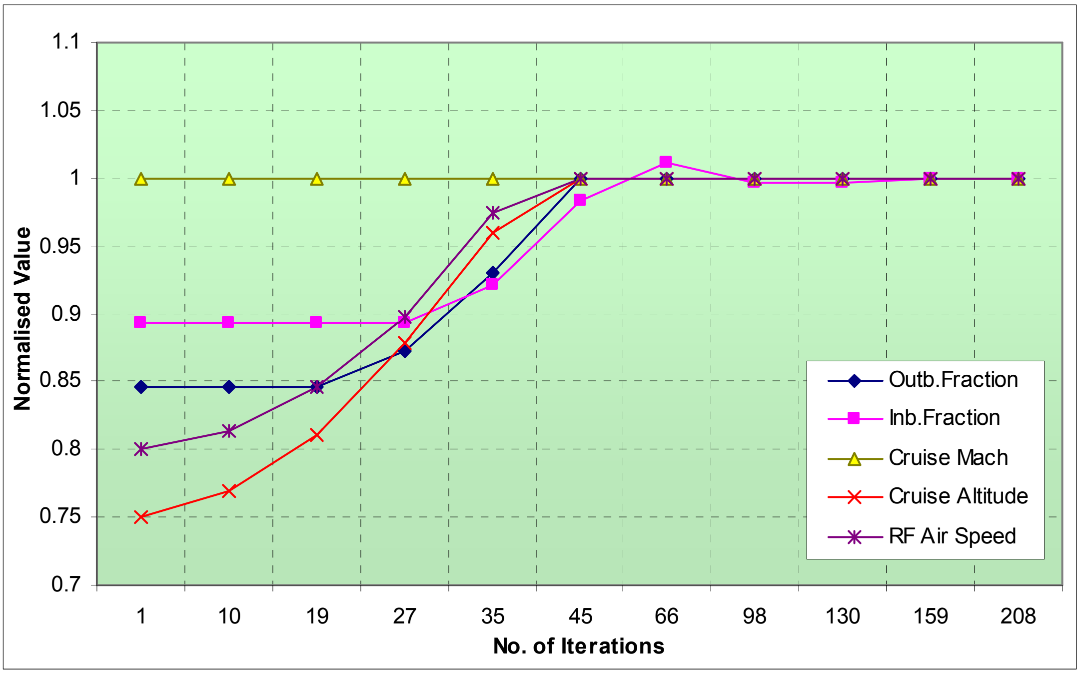

Figure 12.11: Optimisation path of the design variables

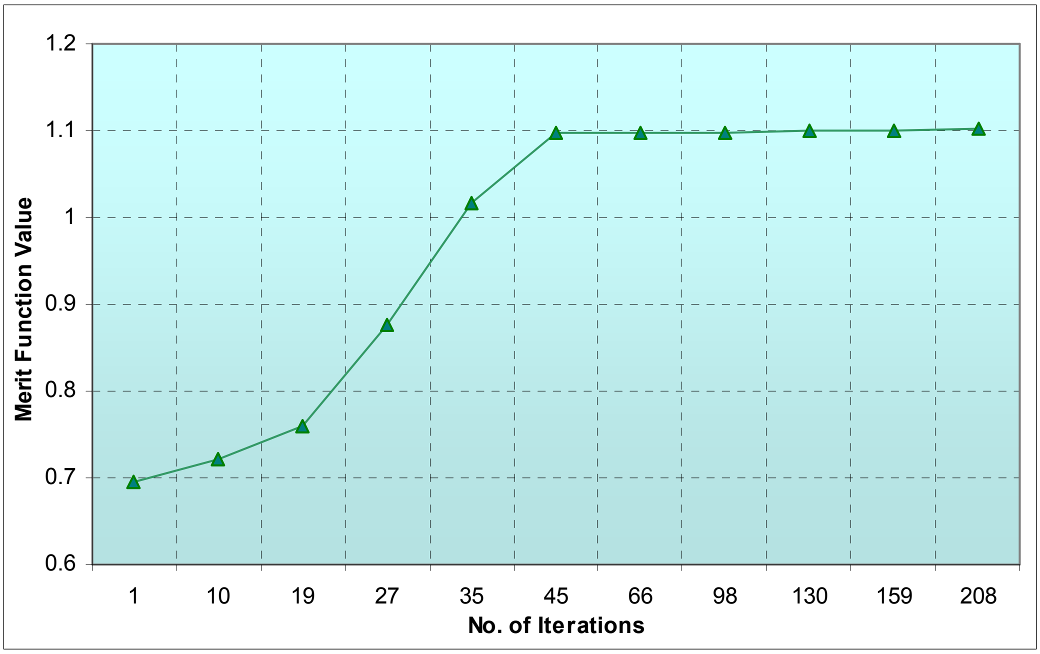

Figure 12.12: Convergence of merit function value

A comparison between the optimal performances of the tanker/UCAV combination and those at the design conditions are presented in Table 12.19 together with two additional experiments which will be described subsequently below.

Table 12.19: Optimisation results – Additional analyses

Parameter	Design Con.	Optimum	RF 6/5	FF zero
Formation cruise radius (km)	4999.85	5453.62	5329.45	4721.73
Total fuel consumption (lb)	314326	311518	312208	301052
Total operation time (hr)	12.66	14.35	14.13	12.53
Merit function value (km /lb-hr)	1.0	1.101	1.075	0.926

As far as the optimum results are concerned, an increase in total operation time was not only a consequence of slower cruising speed, but also an extended formation cruise radius by which the aircraft combination was capable of proceeding with the same limited amounts of fuel. The total fuel consumption value in the design synthesis case reflects a situation when both the usable and the payload fuel amounts in the tanker were entirely consumed. Hence, indicates that in the optimal case, there is a small amount of usable fuel left at the end of the operation. Such remaining fuel came from the usable amount of the tanker due to the fact that the fuel payload had reached its limit, which is different from the design synthesis condition where both of the fuel categories were depleted simultaneously. For this reason, despite the residual total fuel, a further range improvement cannot be achieved from this aircraft combination.

Since the numbers of refuelling were fixed to the design values primarily in order to improve the overall execution time and optimisation search effectiveness. Nonetheless, a further investigation has been conducted by deliberately increasing the numbers of refuelling applied in the optimisation by one for both cruise legs. Hence the refuelling number is six for the outbound and five the inbound legs as denoted by 'RF 6/5' column in the above tabulated data. The reason for this analysis is the fact that there was a possibility that the aircraft system could gain further range due to small range segments resulting less fuel weight carried by UCAVs, and therefore lower the fuel consumption The 'RF 6/5' results clearly show merit function value improvement from the initial design synthesis conditions. However, the overall performances gained are still inferior compared to the optimum case with the original numbers of refuelling '5/4'.

In order to investigate the actual effect of formation flying on a certain tanker/UCAV combination, an additional analysis was performed by using the same aircraft system, designed at 20% formation-flight lift increment, to operate at the conditions in which assumed that the UCAVs flew independently, and thus did not gain any aerodynamic benefit (i.e. zero additional lift). The optimisation results of this analysis are shown in the 'FF zero' case. Undoubtedly its optimal cruise radius is shorter compared to any other refuelling cases. Nonetheless, as applied to all optimisation runs, the above 'FF zero' results do not, by all means, indicate that the aircraft system would not be able to fly any further. Since, apart from the range parameter, the optimisation merit function takes the fuel consumption and operating time into account, thus the cruise radius result represents the most efficient operating distance, not the maximum one.

Chapter 13

Concluding Remarks

13.1 Discussion

The concept of incorporating UCAVs with an air refuelling capability to extend their range and enhance their overall combat capabilities has been considered in current UCAV developments. This research programme aimed to provide a more advanced solution to increase the UCAV performance far beyond the above concept by utilising a combination of the following three features; uninhabited aircraft system, air refuelling and formation flying techniques. Such a solution, however, required various new investigations particularly in the areas of design synthesis methodology, formation flight analysis and optimisation of the refuelling process.

The design syntheses of both aircraft contained complex iterative procedures; hence any evaluation methods selected were deliberately developed to be suitable for computational programming implementation. Therefore, various graphical analysis tasks have been translated into numerical equations with corresponding evaluation sequences.

Although the theory of formation flight aerodynamics has been established for a long time, and a number of research investigations have been performed in this particular area, the behaviour of the aircraft's aerodynamic performance concerning in relation to variations of airframe configurations and formation positions still cannot be accurately predicted. Due to an extensive investigation and its associated expenditures required in the formation flight research field in general, the majority of previous work focused on very specific experiments and on certain aircraft combinations. Hence the results obtained from those research programmes were somehow insufficient to be applied for any further analysis.

As far as the formation flight investigation methods are concerned, the flight testing, while being the most accurate, is the most expensive and requires additional instruments to measure the changes in performance as well as skilled pilots to position and maintain the aircraft precisely at specific formation test points. A wind-tunnel testing method is capable of providing some useful data; however, due to the amount of experimental work involved especially regarding scale model construction, it is normally performed to a limited extent. For these reasons, on account of resource availability and investigation flexibility, a computational vortex-lattice method proves to be favourable for investigating general formation flight effects which are not concerned with in-depth vortex flow analysis and mainly focus on the aerodynamic performance of the aircraft.

The formation flight analysis method developed in this research project provided a wide scope of work compared to previous research in the same area, particularly in terms of novel aircraft configurations and multi-row aircraft formation analysis. The optimal formation result obtained from the analysis appeared to be unique in comparison to typical military aircraft formations. However, such uniform formation arrangements which are conducted primarily for operational reasons, demand the pilots to focus on maintaining the aircraft precisely in the formation without considering aerodynamic performance benefits as their first priority.

From the design synthesis perspective, the aerodynamic performance improvement obtained from the above formation flight analysis is used as part of the input requirements, and hence the analysis itself may be considered as a separate element from the main design operations. Since this research project emphasises the development of the design methodology which implies the flexibility of the methods applied, the above formation-flight aerodynamic effects could also be determined from other analytical methods or appropriate assumptions could be made.

Although the formation flight analysis is one of the primary research aspects, accurate results are very difficult to deduce due to the available means of investigation and the feasible approach for incorporating the results with the design synthesis. Nonetheless, as far as the UCAV's overall aerodynamic performance is concerned, the effect of formation flight is not very significant in comparison to the basic aerodynamic characteristics of the aircraft which are determined by the overall design configuration and implemented by design synthesis methods. For this reason, a reasonably large error margin of the formation flight results and hence an assumption of the average lift-increment for all UCAV formation rows could be allowed. Furthermore, due to the time limitation and a number of complicated research areas involved in this project, the development of the methodologies for accuracy were focused on the design synthesis part rather than on the formation flight analysis.

The design methodology of the tanker/UCAV combination may imply the development of parallel design synthesis executions for each aircraft. However, since the initial sizing of the tanker needs the UCAV operational performance as part of the design requirements, these performance values should be taken from the finalised UCAV, in which all parameters have been converged instead of those from the parallel initial sizing stage. This would also prevent the synthesised tanker results from being incoherent with the designed UCAV.

The size of the tanker primarily depends on the range requirement and the number of UCAVs assigned to the fleet. Generally the fuel payload could be considered as one of the major contributions to the tanker's size; however, within the context of this research, this fuel parameter is, in fact, also determined by the above range requirement by which the UCAVs need to travel in the mission. In order to maintain the appropriate size of the tanker for flexible operating airbases, the aforementioned influential criteria should be optimal. Nonetheless, if the range requirement is extremely great while the UCAVs number is small then, despite the ultra long-reach capability, the overall combat effectiveness of the fleet which is the key to succeeding the campaign would be undoubtedly reduced. This airpower issue can be rectified by launching multiple fleets of aircraft system all together as long as the significance of the mission takes priority over ineffective resource consumption. On the other hand, regardless the number of UCAVs, if the range requirement is relative short then the design operation could be arguably overlapped by large combat aircraft.

In order to minimise any sudden transformations occur on the airframe and other airflow-interacting components, multiple combinations of spline-type equations were applied in 2D modelling. These equation combinations are capable of producing various geometry shapes with high flexibility, which is especially useful for modelling the fuselage of the aircraft. This is due to the requirement of the fuselage model to be capable of adapting the cross-section figures along its length in order to accommodate various sizes of internal components while maintaining appropriate external shape for aerodynamic efficiency.

The development of tanker and UCAV models has demonstrated the flexibility of the mathematical modelling approach. Although the airframes of both aircraft contained very similar equation structures, each aircraft displayed a rather distinctive appearance at the end. This is primarily due to the differences of the design requirements, internal component layouts and design synthesis methodologies applied to respective aircraft categories.

The mathematical equations used for representing the behaviours of lift-curve slope and wave drag rise associated to the Mach number are only applicable in the transonic flight regime. Any further approximation produced in the latter supersonic region would be likely to contain significant errors due to the deviation of the equation shape from the general trend. Nonetheless, since both tanker and UCAV were designed to be operated specifically at high subsonic speed, it is reasonable to neglect the accuracy of any aerodynamic performance evaluations beyond the transonic region.

As far as the overall tanker and UCAV configurations are concerned, the fairing partition is essential for optimising these tailless flying-wing aircraft. This is by allowing the wing position to shift and adjust for aerodynamic and stability performances, while preserving the blended-wing-body airframe. Since the control surfaces of the designed aircraft were dedicatedly configured for the stability and manoeuvrability purposes, it was assumed that they did not serve any lift-augmentation role during takeoff and landing. Despite the absence of high-lift devices usage, the field performances of the aircraft exhibited in a common range. This was mainly the results of the relatively large wing area and the enhanced maximum lift capability due to the vortex induced effects generated on the highly swept low-aspect-ratio wing configuration.

Due to the above vortex induced effects, both tanker and UCAV have a rather high maximum lift coefficient and stall angle. Therefore, at takeoff and landing, the actual stall speed derived from the maximum lift coefficient value is not appropriate for using to determine the takeoff and touchdown speeds due to the limitation of the maximum taildown angle for ground rotation. Thus, the stall speed evaluated at such points reflects the condition by which the aircraft's angle of attack is rotated up to the above specified taildown angle.

Generally it is desirable to design an aircraft which possesses low drag characteristic to increase the aerodynamic performance particularly in cruise, thus providing greater fuel savings for a given distance. However, such a low-drag aircraft may also need additional drag forces in order to improve its operational performance at certain conditions e.g. light-weight descent and high-speed landing. Air brakes integration is an effective mean of rectifying the above issue since these devices can be activated as necessary at specific points in the operation.

From the aircraft design perspective, the leading-edge sweeps highly influence the stability performance of the synthesised aircraft since they simultaneously change the locations of the wing aerodynamic centre, overall aircraft c.g. and control surfaces. Due to the above reasons, these wing geometry parameters are suitable for largely optimising the aircraft's stability performance in general without changing overall sizes. Also fuel c.g. shifted between tanks is highly essential especially for flying-wing aircraft to stabilise themselves at specific conditions.

The refuelling sequence optimisation problem is a difficult task for an optimisation search algorithm to locate for a solution primarily due to the limits of tanker's usable and the payload fuel amounts carried. Thus the design variables constraints and the penalty function scheme must be imposed appropriately in order to guide the search direction to feasible areas. Nonetheless, throughout the optimisation process, the penalty function was likely to incur for over one-third of the total search attempts due to insufficient fuel for the aircraft to complete the entire mission, while the search results tended to be valid only for the case when the outbound refuelling provisions were somehow compromised with the inbound leg.

The design variables selected for the refuelling sequence optimisation problem must be appropriately considered in order to provide an effective solution search. The numbers of refuelling are one of the primary factors that determine the refuelling provision sequence. However, as far as the optimisation results were concerned, the search variation of these parameters tended to give significantly inferior results compared to other solutions in the same exploration iteration, and hence being discarded by the optimiser. This was due to the fact that the refuelling numbers highly influenced the total fuel consumption in a cruise leg, and thus causing the aircraft to either run out of fuel before completing the mission if the number had increased by one, or became under performance in term of range if it was the other way around. Thus, eliminating such parameters from the optimisation design variable list narrowed down the search directions. The total optimisation time was reduced as a result of the optimisation being able to focus on to other design variables which effectively contribute to the changes in the aircraft combination performances.

For a given range requirement, the lift increment of the UCAV due to formation flight is inversely proportional to the reduction of the designed tanker's weights as a result of less fuel payload carriage needed. And in general, the weight of the aircraft is directly related to the developing cost as well as subsequent maintenance and operating expenditures. Therefore, apart from the overall fuel saving benefits, the formation flight technique reduce the total costs of the tanker's development and utilisations, while a prolonged service life due to the rid of flight training operations would also contribute to this long-term cost reduction.

13.2 Conclusions

Due to the currently advancing technologies, a combat version of uninhabited aerial vehicles known as UCAV has been widely developed for armed operation purposes. Since various performance capabilities of such aircraft are not limited by pilot tolerance factors, the demands of certain performance aspects in particular the range also increase accordingly. This research programme concerned the development of a design methodology for an autonomous aircraft system comprising a number of UCAVs accompanied by an uninhibited tanker. By incorporating the close-formation flight and air refuelling techniques, tremendous improvements in the range performance as well as various operational benefits could be obtained from such an aircraft combination.

An uninhabited tanker is a novel aircraft concept which would eliminate the problems facing existing conventional tankers particularly regarding the fleet crewing and operational effectiveness issues, while also comparatively being superior in various aspects as a result of unmanned system benefits. It is difficult and resource consuming to train qualified tanker operators, and for this reason, an air crew shortfall may occur if the tankers have been called for a mission frequently for a certain period of time. The lack of the operational effectiveness is somehow a direct problem from the fact that the current tankers were modified from the previous generation of commercial aircraft which were originally designed and optimised solely for air transporting purposes. Thus the modification of such aircraft for an alternate role of air refuelling operations could only be conducted to a certain extent. The selection process of the tanker is also one of the major concerns due to the demanding tanker's operational requirements, whereas the available choices of the commercial aircraft which can be modified are limited to begin with. Thus, normally the final selection would end up as a compromise of overall specifications rather than meeting all of the original requirements.

As far as previous formation flight research works are concerned, although the improvement of the trailing aircraft performances was detected and variously defined in terms of aerodynamic and propulsion, none of the researches provided proper methods for evaluating such benefits universally. The benefits of flying in formation usually associate with the trim drag penalty which occurs as a result of the applied control surfaces in order to counteract the rolling moment generated due to an unbalanced lift force acting on the aircraft's wings. For this reason, the formation flight analysis developed in this research was conducted based on an alternate approach by considering an optimal rolling moment position. The effects of formation flight are dependent upon the configurations of both leading and trailing aircraft; therefore, ideally individual experiments should be carried out for every new aircraft combination to determine such effects with sufficient accuracy. A computational vortex-lattice method has been widely used in the formation flight research area, and a MATLAB vortex lattice program 'Tornado' was selected for conducting this investigation.

Since Tornado contains interactive input procedures and basic evaluation options, additional function scripts were included to the original program to accommodate the formation flight analysis tasks. This was to bypass the majority of the above interactive procedures and directly executed the computation parts rapidly creating a matrix of aircraft formation positions together with the associated vortex-lattice results. Another function script was developed to identify the formation position which yields an optimal result between the lift increment and the total pressure coefficient balance about the aircraft's centreline.

The formation flight benefit deduced from the above analysis was presented in the form of lift increment. For a steady level flight, this additional lift changed the overall lift-to-drag ratio of the aircraft by effectively reducing the lift contribution in the induced drag term whereas the total lift force acting on the aircraft to sustain its current weight remains the same.

The baseline configuration of aircraft was created for the purpose of outlining overall internal arrangement and airframe appearance which would help the designer to justify appropriate design methodologies as well as, in the contexts of this research, selecting the mathematical equations used for modelling specific parts of the aircraft. The baseline designs of the tanker and UCAV were originally portrayed from existing aircraft; however, they subsequently evolved into a unique blended-wing-body configuration in order to satisfy operational feasibilities and modelling flexibility.

The development of new methods was required for creating a design methodology for the tanker/UCAV combination. Their overall design mission profiles contained two operation parts; the formation part in which both aircraft operated together on the same route, and the combat part where the UCAVs broke away from the tanker and operated independently. The UCAVs were synthesised in accordant with the design mission profiles in the combat part. The tanker, on the other hand, required two initial sizing procedures; the first sizing process, in which each formation cruise leg was defined as a single segment to crudely estimate the tanker's weights and the fuel consumption. And the second sizing included the breakdown refuelling segments in order to account for fuel payload dropped over the formation cruise legs and hence the sizing weights reduction. Since the refuelling sequence provision used for designing the tanker is dependent on UCAV's performances, the design synthesis operation of the UCAV must be carried out prior to the tanker.

The aircraft models must be sufficiently flexible in order to accommodate a certain variation of design requirements; therefore, mathematical modelling methods were selected. To answer the above model flexibility, aircraft's internal components were allowed to be freely positioned within their corresponding packaging constraints which were primarily defined in a form of longitudinal fuselage station. The 2D modelling study was conducted to investigate the behaviour of mathematical equations in general and subsequently selected appropriate ones to represent certain geometry aspects of aircraft's components. The principle of 3D mathematical modelling of aircraft in general could be described as a product of 2D cross-sectional model variations generated in the direction perpendicular to the cross-section plane. These variations were controlled by several 2D mathematical equations which individually defined other geometry aspects of the same component.

The study of 3D modelling focused on realistic visualisation of the aircraft; therefore, AutoCAD was considered for using as a drawing platform. With the assistance of its programming language, AutoLISP, the AutoCAD demonstrated capabilities of reading the aircraft model's coordinate data exported from the design synthesis program and then rapidly generating the 3D model accordingly. Within the design synthesis, these model coordinate data were also used for evaluating various aircraft's geometry specifications such as surface areas, volumes and centres of gravity, providing greater accuracy in comparison those obtained from statistical estimations. Furthermore, the 3D presentation of the aircraft model also assisted the verification of configuration validity as well as justified any necessary additional modifications to the aircraft.

Existing aerodynamic analysis methods were used in conjunction with numerical equation approximations to simulate the behaviours of the lift-curve slope and wave drag rise in the transonic flight regime. Due to the need for the design synthesis methods to be accommodated for computational implementation, several graphical data applied in the above methods were converted into numerical equations using a regression analysis program, DataFit. The cross-sectional area distributions of trapezium wings referenced to the fuselage's downstream direction were found to always resemble a bell shape with a variation of the maximum cross-sectional area coordinates. Such coordinates could be predicted with the use of position-shifting methods which had been developed from the area distribution data of several wing model specimens. Subsequently the mathematical spline-typed equations used in the airframe modelling were applied to generate a complete distribution curve according to the predicted location of the maximum area coordinates.

Several numerical equations were developed from graphical plot data used in the stability analysis methods. The detailed engine performance analysis contains two separated methods for the on-design and the off-design operating conditions. Some original equations were modified to exclude the afterburner station from the system evaluations. Also a fudge factor for correcting the specific fuel consumption value was included on account of result calibration and technology improvements. In addition, new equations were created to predict physical properties of a medium-high bypass ratio engine for given requirements of the engine thrust and bypass ratio.

Hooke and Jeeves pattern search method was selected for applying to the refuelling sequence optimisation problem due to its algorithm simplicity and robustness. However, additional modifications of constraint boundary handlings and individual step adjustments were necessary in order to envelope an optimisation search within a given design space, and also to accommodate different spectrums of the design variables used in the optimisation problem. The mission radius, overall fuel consumption and total operating time of the tanker/UCAV combination were taken into account for the optimisation objective function. Despite the initial objective of maximising this mission radius, time and resource consumption were also included to ensure that the solution obtained was operationally effective.

13.3 Suggestion for Further works

As far as the end results of this research project are concerned, all important investigations and developments of new design methodologies had been delivered. Nonetheless, due to a number of difficult research fields involved, and since time was not permitted to conduct certain investigations in details, simplified assumptions were reasonably made at some points. The initial further work recommended for this project is a fully automated optimisation for the aircraft. An optimiser could be incorporated at the execution level of the design inputs and the output results. Thus, the search algorithm would not disrupt the original design synthesis operations. Nonetheless, due to a tailless flying-wing configuration of both tanker and UCAV, feasible solutions are limited due to geometry and performance constraints particularly regarding the aircraft stability. Therefore, the optimisation design variables, merit functions and boundary constraints must be carefully considered.

In this research work, the formation flight analysis on Tornado was conducted separately from the design synthesis instead coupling them together due to several significant limitations. Though initially it was planned to integrate this Tornado to the design synthesis and the above optimisation which would result a complete picture of this tanker/UCAV combination synthesis. The process is to run the design synthesises optimisation for both aircraft, and then send the data of the optimised aircraft configurations to the Tornado. Subsequently an aerodynamic benefit deduced from the formation flight analysis would be fed back to the design synthesis and repeat the process until a total convergence is achieved.

The refuelling sequence analysis for each UCAV in the fleet would be necessary if a variation of formation-flight effect between different aircraft rows were considered instead of the current assumption of same aerodynamic effect for all UCAVs. The development of more complex methodologies would be required especially for the initial sizing of the tanker and the final refuelling sequence optimisation. Also this would generate another problem regarding the number of GUI input slots which must be correspondent to the UCAVs number in the formation. Nonetheless, such an issue is supposed to be handled from the computational programming perspective rather than the design methodology itself.

As mentioned earlier in the discussion part, in order to maintain the size of the tanker within appropriate limits, deploying several fleets of the tanker/UCAV combination may be considered as a solution to compensate the loss of overall combat effectiveness in an ultra-long-range operation. Therefore, a study of multiple numbers of the tankers and UCAVs flying in close formation could be conducted to explore a possibility of improving the performance of the tankers. Also the aerodynamic effects produced by unconventional formation arrangements, e.g. W-formation, would be worth studying especially on the trailing aircraft which positioned in a mutual upwash region generated by two of the side-by-side leading aircraft.

Finally, an optimal UCAVs refuelling approach during the air refuelling operation could be investigated to determine how the UCAV would break off from the cruise formation, move to the refuelling position behind the tanker and so on. The main objective of this investigation should be to optimise the total time spent to complete the refuelling operation and also possibly to establish the queuing formation arrangement and the approaching/departing routes of the UCAVs which maximise positive aerodynamic effects.

References

1. John M. Borky, *Payload Technologies and Applications for UAVs*, Aerospace Conference 1997 Proceedings Vol.3, pp. 267-283, IEEE, 1997.

2. Peter V. Blyenburgh, *UAVs: an Overview*, Air & Space Europe Vol.1 No. 5/6, pp. 43-47, Elsevier, 1999.

3. Robert C. Nolan II, *The Pilotless Air Force? A Look at Replacing Human Operators with Advanced Technology*, USAF Air Universty: Air Command and Staff College, 1997.

4. Dossier, *Civilian Applications: the Challenges Facing the UAV Industry*, Air & Space Europe Vol.1 No. 5/6, pp. 63-66, Elsevier, 1999.

5. Mike Carabajal, *U.S. Air Force Fact Sheet – Global Hawk*, http://www.af.mil/ information/factsheets /factsheet.asp?id=13225, U.S. Air Force, 2005.

6. Mike Carabajal, *U.S. Air Force Fact Sheet – MQ-1 Predator*, http://www.af.mil/ information/factsheets/factsheet.asp?fsID=122, U.S. Air Force, 2005.

7. Jan Walker, *DAPRA Fact Sheet - J-UCAS Overview*, http://www.darpa.mil/j-ucas/ fact_sheet.htm, Defence Advanced Research Projects Agency, 2005.

8. John A. Tirpak, *Toward an Unmanned Bomber*, Air Force Magazine/ June 05, the Air Force Association, 2005.

9. Timothy A. Kinnan, *Air Refueling*, Air Force Doctrine Document 2-6.2, U.S. Air Force, 1999.

10. Carlo Kopp, *Expanding the Tanker Fleet*, http://www.ausairpower.net/TE-AAR-Expand.html, Air Power Australia, 2005.

11. Rick Ludwig, *J-UCAS (X-47B) Overview*, Northrop Grumman Public Release, 2004.

12. Jacob L. Hinchman, *An Equivalent Model for UAV Automated Aerial Refueling Research*, AIAA 2005-6006, AIAA Modelling and Simulation Technologies Conference and Exhibit, 2005.

13. Defence Science Board, *Aerial Refueling Requirements*, Defence Science Board Task Force Report, U.S. Office of the Secretary of Defence, 2004.

14. Carlo Kopp, *Aerial Refueling for the ADF: Strategic, Operational and Technical Issues*, Unclassified Discussion Paper, Air Power Australia, 2002.

15. North Atlantic Treaty Oganisation, *Annex 10R AAR Capabilities*, ATP56 Air-to-Air Refuelling, NATO Unclassified Publication, 2000.

16. Dietrich Hummel, *The Use of Aircraft Wakes to Achieve Power Reductions in Formation Flight*, Proceedings of the FDP Symposium on The Characterisation and Modification of Wakes from Lifing Vehicle in Fluid, Paper No.36 pp. 1-13, AGARD, 1996.

17. Blake, William and Dieter Multhopp, *Design, Performance and Modelling Consideration for Close Formation Flight*, AIAA 98-4343, AIAA, 1998.

18. Ronald J. Ray, Brent R. Cobleigh, M. Jake Vachon, and Clinton St. John, *Flight Test Technique Used to Evaluate Performance Benefits during Formation Flight*, NASA/TP 2002-210730, NASA Dryden flight Research Centre, 2002

19. Ronald J. Ray, Kevin R. Walsh, M. Jake Vachon, and Kimberly Ennix, *F/A-18 Performance Benefits Measured during the Autonomous Formation Flight*, AIAA 2002-4490, Proceeding of the AIAA Flight Mechanics Conference and Exhibit, 2002.

20. Michael T. Morgan, *A Study in Drag Reduction of Close Formation Flight Accounting for Flight Control Trim Positions and dissimilar Formations*, Air Force Institute of Technology, 2005.

21. Jack D. Mattingly, *Aircraft Engine Design 1st Edition*, AIAA Education Series, 1987

22. Terry E. Shoup, and Farrokh Mistree, *Optimization Methods with Applications for Personal Computers*, Prentice-Hall Inc., 1987.

23. Kenneth Munson, *Jane's Unmanned Aerial Vehicles and Targets*, Jane's Information Group Limited, 1996.

24. Christopher A. Jones, *UAVs – An Assessment of Historical Operations and Future Possibilities*, USAF Air Universty: Air Command and Staff College, 1997.

25. Gene H. McCall, *New World Vistas: Air and Space Power for the 21st Century, Summary Volume*, USAF Scientific Advisory Board, 1995.

26. David Glade, *UAVs – Implications for Military Operations*, USAF Air Universty: Air War College, 2000.

27. U.S. Office of the Secretary of Defence, *Unmanned Aerial Vehicle Reliability Study*, Office of the Under Secretary of Defence for Acquisition, Technology and Logistics, 2003.

28. Andreas Parsch, *Undesignated Vehicles: Sperry "Flying Bomb"*, http://www.designat ion-systems.net/dusrm/app4/sperry-fb.html, Directory of U.S. Military Rockets and Missiles, 2008.

29. Andreas Parsch, *Early Missile and Drones: Radioplane OQ-14/TDD*, http://www.designation-systems.net/dusrm/app1/oq-14.html, Directory of U.S. Military Rockets and Missiles, 2008.

30. William K. Lewis, *UCAV – The Next Generation Air-Superiority Fighter*, USAF Air University, 2002.

31. Andreas Parsch, *Modern UAVs*, http://www.designation-systems.net/dusrm/app2/index.html, Directory of U.S. Military Rocket and Missiles, 2008.

32. Andreas Parsch, *Teledyne Ryan AQM/BQM/MQM-34 Firebee*, http://www.designation-systems.net/dusrm/m-34.html, Directory of U.S. Military Rocket and Missiles, 2008.

33. Richard M. Clark, *UCAV – Airpower by the People, for the People, but not with the People*, USAF Air University, 1999.

34. Brian P. Tice, 1991, *UAVs, Force Multiplier of the 1990s*, Airpower Journal Vol.5, pp. 41-55, 1991.

35. Maj. Jim Shane, *An Interview by Richard M. Clark on 22 February 1999*, UAV Battle Lab, Eglin Air Force Base, 1999.

36. Andy Bunce, *BAE Systems to Lead £124 Million UAV Technology Demonstrator Programme*, http:// 147.29.80.132 / newsroom / 2006 / dec / 071206news1 .htm, BAE Systems, 2006.

37. Steven M. Ross, *Formation Flight Control for Aerial Refuelling*, Air Force Institute of Technology, 2006.

38. Carlo Kopp, *A Strategic Tanker /Transport Force for the ADF*, Air Power Studies Centre, 2000.

39. Michael Bruno, *Pentagon to a Rebid Air Tanker Contract*, Aviation Week/ July 08, 2008.

40. Royal Air Force, *Royal Air Force Flying Training Manual Part I - Landplanes*, Air Publication 129, Air Ministry, 1940.

41. Dietrich Hummel, *Aerodynamic Aspect of Formation Flight in Birds*, Journal of Experimental Biology Vol.104, pp. 321-347, 1983.

42. Jennifer L., Hansen and Brent R. Cobleigh, *Induced Moment Effects of Formation Flight Using Two F/A-18 Aircraft*, NASA/TM 2002-210732, NASA Dryden flight Research Centre, 2002.

43. Eugene H. Wagner, *An Analytical Study of T-38 Drag Reduction in Tight Formation Flight*, Air Force Institute of Technology, 2002.

44. Jan Roskam, *Airplane Design/Part 1-8*, Design Analysis & Research Corporation, 1985.

45. David R. Gingras, *Experimental Investigation of a Multi-Aircraft Formation*, AIAA 99-3143, the 17th Applied Aerodynamic Conference, 1999.

46. Varnavas C. Serghides, *Design Synthesis for Canard-Delta Combat Aircraft*, Cranfield University, 1987.

47. Daniel P. Raymer, *Aircraft Design: A Conceptual Approach 4th Edition*, AIAA Education Series, 2006.

48. Cavallo B., *Subsonic Drag Estimation Methods*, U.S. Naval Air Development Centre, 1966.

49. Ken Eaton, *Aerial Refueling Hose Drum Unit Model FR-600*, Aerial Refuelling Informational Flyers, Sargent Fletcher Inc., 2008.

50. Richard G. Whittle, *the Development of Preliminary Design and Assessment Methodologies for Enhanced Combat Aircraft Supportability*, Imperial College London, 1997.

51. Egbert Torenbeek, *Synthesis of Subsonic Airplane Design*, Delft University Press, 1982.

52. Douglas Barrie, *Skat Attack*, Aviation Week/ August 07, 2007.

53. Aviation Safety Network Database, *British Aerospace Nimrod MR.2 XV230 Kandahar*, http://aviation-safety.net/database/record.php?id=20060902-0, 2008.

54. David J. Hall, *Interactive Preliminary Design Assessment of Advanced Technologies on Combat Aircraft Configurations*, Imperial College London, 1999.

55. Nikolaos L. Tirovolis, *Integration of Commercial Aircraft Economic Targets into the Initial Design Process*, Imperial College London, 2005.

56. John P. Fielding, *Introduction to Aircraft Design*, Cambridge University Press, 1999.

57. Black World Declassified, *the Crash of XB-70 Valkyrie*, http://area51specialprojects .com/xb70_crash.html, 2008.

58. International Civil Aviation Organisation, *Aerodrome Manual - Part 2*, Doc. 7920-AN/865/2, ICAO, 1965

59. O' Conner, W., *Lift and Drag Prediction in Computer-Aided Design*, U.S. Air Force ASD/XR-73-8, 1983.

60. Vicent G. Tormo, *Development of Initial Design Methodologies for Reusable Small-Payload Uninhabited Aerospace Vehicle*, Imperial College London, 2006.

61. North Atlantic Treaty Oganisation, *Annex 10Q National Annex – United States of America*, ATP56 Air-to-Air Refueling, NATO Unclassified Publication, 2000.

62. ESDU, *Properties of a Standard Atmosphere*, Item No. 77021, ESDU International, 1977.

63. Michael J. Vachon and Ronald J. Ray, *Calculated Drag of an Air refuelling Assembly through Airplane Performance Analysis*, NASA Dryden flight Research Centre, 2004.

64. Hoak D., Ellison D., et al., *USAF DATCOM*, Air Force Flight Dynamics Laboratory, Wright-Patterson Air Force Base, 1979.

65. Varnavas C. Serghides, *Aerospace Vehicle Design course materials*, Imperial College London, 2009.

66. U.S. Department of Defence, *DoD Announces Termination of KC-X Tanker Solicitation*, http://www.defense.gov/releases/release.aspx?releaseid=12195, 2008

67. Varnavas C. Serghides, *Advanced Combat Aircraft Design Optimization*, CoA Report No.8814, Cranfield University, 1988.

68. Noah Shachtman, *Killer Drone's Big Brother*, http://www.noahshachtman.com/archi ves/002005.html, 2008.

69. Anonymous, *X-Series Planes*, http://www.coldstares.com/X%20Series.htm, 2008.

70. Anonymous, *Dassault nEUROn*, http://en.wikipedia.org/wiki/Dassault_nEUROn, Wikipedia.org, 2006.

71. Sonia Bauchadie, *Additional Centre Tanks: Upgrading your Airbus fleet for enhanced operational flexibility*, http://www.airbus.com, Airbus, 2006.

72. Carla Thomas, *NASA Dryden Flight Research Centre Collection*, http://www.nasa images.org, NASA Dryden Flight Research Centre, 2008.

73. Jimmy C. Pan, *United States Department of Defence images*, http://www.defense .gov, United States Department of Defence, 2008.

74. Jeffrey A. Scott, *V-Formation Flight of Birds*, http://www.aerospaceweb.org/ quest ion/nature/q0237.shtml, Aerospaceweb.org, 2006.

75. Julian Hellebrand, *Wing Air Refuelling Pod 34" Series*, http://www.cobham.com/ missionequipment, Cobham plc, 2009.

76. Tomas Merlin, *A Vortex-Lattice MATLAB Implementation for Linear Aerodynamic Wing Applications*, Royal Institute of Technology, Department of Aeronautics, 2000.

77. Mark Daly, *Jane's Aero-Engines*, http://jae.janes.com/public/jae/index.shtml, Jane's Information Group Limited, 2006.

78. Paul Jackson, *Jane's All the World's Aircraft*, Jane's Information Group Limited, 2000.

79. Anonymous, *B-2 Spirit*, http://en.wikipedia.org/wiki/B-2, Wikipedia.org, 2010.

80. Jeffrey A. Scott, *Aircraft Museum B-2 Spirit*, http://www.aerospaceweb.org/aircraft /bomber/b2/, Aerospaceweb.org, 2010.

81. Federal Aviation Administration, *Digital Terminal Procedures/ Airport Diagram*, http://www.naco.faa.gov/index.asp?xml=naco/online/d_tpp, FAA, 2010.

Appendix A – System Packaging

A.1 UCAV Propulsion Ducts

Exhaust Pipe

$$l_{\text{exs}} = R_{LEC} \cdot l_{\text{en}} \tag{A.1}$$

$$l_{\text{ex}} = l_{\text{exs}} + h_{\text{ex}} \tag{A.2}$$

$$z_{\text{exs}} = l_{\text{exs}} \cdot \frac{2}{\pi} \cdot \tan(\theta_{\text{sd}}) \tag{A.3}$$

$$b_{\text{el}} = \sqrt{\frac{AR_{\text{ex}} \cdot R_{IE} \cdot R_{IC} \cdot \pi \cdot \left(\frac{d_{\text{en}}}{2}\right)^2}{(1+R_{\text{eb}})^2}} \tag{A.4}$$

$$b_{\text{eu}} = b_{\text{el}} \cdot R_{\text{eb}} \tag{A.5}$$

$$h_{\text{ex}} = (b_{\text{el}} + b_{\text{eu}}) \cdot AR_{\text{ex}} \tag{A.6}$$

when, $$R_{\text{eb}} = \frac{1 - 0.5 \cdot AR_{\text{ex}} \cdot \tan(\theta_{\text{tp}})}{1 + 0.5 \cdot AR_{\text{ex}} \cdot \tan(\theta_{\text{tp}})} \tag{A.7}$$

where,

R_{LEC} - Ratio between the lengths of the exhaust pipe and the engine

R_{IE} - Area ratio between the exhaust and the inlet planes

A.2 UCAV Fuselage

Station B

$$xB_0 = xA_E + l_{\text{stg}} \tag{A.8}$$

$$xB_E = xB_0 + (l_{\text{ins}} + d_{\text{en}}) \tag{A.9}$$

$$yB_b = yA_b \tag{A.10}$$

$$yB_{bu} = b_{\text{iu}} \tag{A.11}$$

$$yB_{bm} = yB_b \cdot R_{\text{bm}} \tag{A.12}$$

$$yB_{\max} = yA_{\max} \tag{A.13}$$

$$zB_b = zA_b \tag{A.14}$$

$$zB_d = zA_d \tag{A.15}$$

$$zB_h = (xB_E - xB_0) \cdot \tan(\theta_{\text{zt}}) \tag{A.16}$$

$$zB_e = 0.05 \cdot yB_{bu} \tag{A.17}$$

$$zB_c = 0.05 \cdot h_{\text{in}} \tag{A.18}$$

$$zB_u = zB_b + zB_h + zB_e + zB_{sc} + h_{\text{in}} \tag{A.19}$$

where,

θ_{zt} - Top-fuselage curvature angle

Station C

$$yD_b = b_{\text{el}} \tag{A.20}$$

$$yD_{bu} = b_{\text{eu}} \tag{A.21}$$

$$zD_b = z_{\text{exs}} + z_{\text{en}} \tag{A.22}$$

$$zD_e = zB_e \tag{A.23}$$

$$zD_c = 0.1 \cdot h_{\text{ex}} \tag{A.24}$$

$$zD_u = zD_b + zD_e + zD_{sc} + h_{\text{ex}} \tag{A.25}$$

$$xC_0 = xB_E \tag{A.26}$$

$$xC_E = xC_0 + l_{\text{en}} \tag{A.27}$$

$$yC_{\max} = yB_{\max} \tag{A.28}$$

$$yC_b = yB_{bm} \tag{A.29}$$

$$yC_{bn} = yC_b - \left(\frac{xC_E - xC_0}{xD_E - xC_0} \right) \cdot (yC_b - yD_b) \tag{A.30}$$

$$zC_b = zB_b - \left(\frac{xC_E - xC_0}{xD_E - xC_0} \right) \cdot (zB_b - zD_b) \tag{A.31}$$

$$zC_u = zB_u - \left(\frac{xC_E - xC_0}{xD_E - xC_0} \right) \cdot (zB_u - zD_u) \tag{A.32}$$

$$zC_d = zB_d \tag{A.33}$$

Station D

$$xD_0 = xC_E \tag{A.34}$$

$$xD_E = xD_0 + l_{\text{ex}} \tag{A.35}$$

$$zD_d = \left(\frac{xD_E - xD_0}{xE_E - xD_0} \right) \cdot zC_d \tag{A.36}$$

Station E

$$xE_0 = xD_E \tag{A.37}$$

$$xE_E = xE_0 + yD_{\max} \cdot \tan(\Lambda_{\text{ft}}) \tag{A.38}$$

The cross-section parameters of the stations *A* and *B* can be directly applied for evaluating the cross-section model of the station *S*; therefore, additional parameter definitions for the station are not required.

A.3 Tanker Propulsion Ducts

Exhaust Pipe

Centre duct

$$b_{\mathrm{ec}} = \sqrt{\frac{R_{IE} \cdot R_{IC} \cdot \pi \cdot \left(\frac{d_{\mathrm{en}}}{2}\right)^2}{4 \cdot AR_{\mathrm{ex}}}} \tag{A.39}$$

$$h_{\mathrm{ex}} = 2 \cdot b_{\mathrm{ec}} \cdot AR_{\mathrm{ex}} \tag{A.40}$$

Side duct

$$b_{\mathrm{es}} = b_{\mathrm{eu}} = \frac{2 \cdot b_{\mathrm{ec}} \cdot R_{\mathrm{eb}}}{R_{\mathrm{eb}} + 1} \tag{A.41}$$

$$b_{\mathrm{el}} = b_{\mathrm{eu}} \cdot \left(\frac{2}{R_{\mathrm{eb}}} - 1\right) \tag{A.42}$$

$$l_{\mathrm{ess}} = l_{\mathrm{ecs}} - x_{\mathrm{stg}} \cdot l_{\mathrm{en}} \tag{A.43}$$

$$l_{\mathrm{es}} = l_{\mathrm{ess}} + h_{\mathrm{ex}} \tag{A.44}$$

$$y_{\mathrm{ess}} = (d_{\mathrm{en}} + 2 \cdot w_{\mathrm{fw}}) - (b_{\mathrm{ec}} + b_{\mathrm{es}}) \tag{A.45}$$

Appendix B – Airframe Geometry

B.1 UCAV Fuselage

Station A

***XY* Plane:** for $0 \le x_i \le xA_E$

$$ybA_i = \left(\frac{x_i}{xA_E}\right) \cdot yA_b \tag{B.1}$$

$$ymA_i = \left(\frac{x_i}{xA_E}\right) \cdot yA_{\max} \tag{B.2}$$

***XZ* Plane:** for $0 \le x_i \le xA_E$

$$zbA_i = \left(\frac{x_i}{xA_E}\right) \cdot zA_b \tag{B.3}$$

$$zdA_i = \left(\frac{x_i}{xA_E}\right) \cdot zA_d \tag{B.4}$$

$$zsA_i = \left(\frac{x_i}{xA_E}\right) \cdot zA_s \tag{B.5}$$

Cambered fuselage:

$$f_{SC}(x_i) = \cos\left(\frac{\pi}{2} \cdot \left(\frac{xA_E - x_i}{xA_E}\right)\right) \cdot (z_{SC}(1) - z_{SC}(0)) + z_{SC}(0) \tag{B.6}$$

***YZ* Plane:** for $0 \le y_j \le ymA_i$

Upper surface

$$zAu_{\mathrm{i,j}} = zbA_i + f_{SC}(x_i) \qquad , \; 0 \le y_j < ybA_i \tag{B.7}$$

$$zAu_{\mathrm{i,j}} = \tan\left(\frac{\pi}{4}\cdot\left(\frac{ymA_i - y_j}{ymA_i - ybA_i}\right)\right)^2 \cdot \left(zbA_i - \frac{zsA_i}{2}\right) + \frac{zsA_i}{2} + f_{SC}(x_i)$$

$$, \; ybA_i \le y_j \le ymA_i \tag{B.8}$$

Lower surface

$$zAl_{\mathrm{i,j}} = -\sin\left(\frac{\pi}{2}\cdot\left(\frac{ymA_i - y_j}{ymA_i}\right)\right)^2 \cdot \left(zdA_i - \frac{zsA_i}{2}\right) - \frac{zsA_i}{2} + f_{SC}(x_i)$$

$$, \; 0 \le y_j \le ymA_i \tag{B.9}$$

where,

$z_{SC}(n)$ - Cambered fuselage height at n$^{\text{th}}$ station.

subscript:

i - Corresponding longitudinal sub-station

j - Corresponding y-coordinate point

Station B

***XY* Plane:** for $xB_0 \le x_i \le xB_E$

$$ybuB_i = \left(\frac{xB_E - x_i}{xB_E - xB_0}\right)\cdot yB_{bu} \tag{B.10}$$

$$ybB_i = \cos\left(\frac{\pi}{2}\cdot\left(\frac{xB_E - x_i}{xB_E - xB_0}\right)\right)\cdot(yB_{bm} - yB_b) + yB_b \tag{B.11}$$

$$ymB_i = yB_{\max} \tag{B.12}$$

***XZ* Plane:** for $xB_0 \le x_i \le xB_E$

$$zbB_i = zB_b \tag{B.13}$$

$$zcB_i = zB_c \tag{B.14}$$

$$zhB_i = \cos\left(\frac{\pi}{2}\cdot\left(\frac{xB_E - x_i}{xB_E - xB_0}\right)\right)\cdot zB_h \tag{B.15}$$

$$zeB_i = \left(\frac{xB_E - x_i}{xB_E - xB_0}\right)\cdot zB_e \tag{B.16}$$

$$zdB_i = \left(\frac{xB_E - x_i}{xB_E - xB_0}\right)\cdot(zA_d - zB_d) + zB_d \qquad \text{, if } zA_d \geq zB_d \tag{B.17}$$

$$zdB_i = \left(\frac{xB_E - x_i}{xB_E - xB_0}\right)\cdot(zB_d - zA_d) + zA_d \qquad \text{, otherwise} \tag{B.18}$$

$$zsB_i = f_{AF}(x_i, xA_E, xD_E) \tag{B.19}$$

Cambered fuselage:

$$f_{SC}(x_i) = \cos\left(\frac{\pi}{2}\cdot\left(\frac{xB_E - x_i}{xB_E - xB_0}\right)\right)\cdot(z_{SC}(2) - z_{SC}(1)) + z_{SC}(1) \tag{B.20}$$

***YZ* Plane:** for $0 \leq y_j \leq ymB_i$

Upper surface

$$zBu_{\mathrm{i,j}} = \sin\left(\frac{\pi}{2}\cdot\left(\frac{ybuB_i - y_j}{ybuB_i}\right)\right)\cdot zeB_i + h_{\mathrm{in}} + zbB_i + zcB_i + zhB_i + f_{SC}(x_i)$$

$$, 0 \leq y_j < ybuB_i \tag{B.21}$$

$$zBu_{\mathrm{i,j}} = \sin\left(\frac{\pi}{2}\cdot\left(\frac{ybB_i - y_j}{ybB_i - ybBu_i}\right)\right)\cdot(h_{\mathrm{in}} + zcB_i + zhB_i) + zbB_i + f_{SC}(x_i)$$

$$, \mathrm{y}buB_i \leq y_j < ybB_i \tag{B.22}$$

$$zBu_{\mathrm{i,j}} = \tan\left(\frac{\pi}{4}\cdot\left(\frac{ymB_i - y_j}{ymB_i - ybB_i}\right)\right)^2\cdot\left(zbB_i - \frac{zsB_i}{2}\right) + \frac{zsB_i}{2} + f_{SC}(x_i)$$

$$, \; ybB_i \leq y_j \leq ymB_i \tag{B.23}$$

Lower surface

$$zBl_{\mathrm{i,j}} = -\sin\left(\frac{\pi}{2}\cdot\left(\frac{ymB_i - y_j}{ymB_i}\right)\right)^2\cdot\left(zdB_i - \frac{zsB_i}{2}\right) - \frac{zsB_i}{2} + f_{SC}(x_i)$$

$$, \; 0 \leq y_j \leq ymB_i \tag{B.24}$$

where,

f_{AF} - Aerofoil interpolation evaluation

Station C

***XY* Plane:** for $xC_0 \le x_i \le xC_i$

$$ybC_i = \sin\left(\frac{\pi}{2}\cdot\left(\frac{xC_E - x_i}{xC_E - xC_0}\right)\right)\cdot(yB_{bm} - yC_{bn}) + yC_{bn} \tag{B.25}$$

$$ymC_i = yC_{\max} \tag{B.26}$$

***XZ* Plane:** for $xC_0 \le x_i \le xC_E$

$$zbC_i = zC_b \tag{B.27}$$

$$zuC_i = \sin\left(\frac{\pi}{2}\cdot\left(\frac{xC_E - x_i}{xC_E - xC_0}\right)\right)\cdot(zB_u - zC_u) + zC_u \tag{B.28}$$

$$zdC_i = \left(\frac{xC_E - x_i}{xC_E - xC_0}\right)\cdot(zB_d - zC_d) + zC_d \qquad \text{, if } zB_d \ge zC_d \tag{B.29}$$

$$zdC_i = \left(\frac{xC_E - x_i}{xC_E - xC_0}\right)\cdot(zC_d - zB_d) + zB_d \qquad \text{, otherwise} \tag{B.30}$$

$$wtC_i = f_{AF}(x_i, xA_E, xD_E) \tag{B.31}$$

Cambered fuselage:

$$f_{SC}(x_i) = \sin\left(\frac{\pi}{2}\cdot\left(\frac{xC_E - x_i}{xC_E - xC_0}\right)\right)\cdot(z_{SC}(3) - z_{SC}(2)) + z_{SC}(2) \tag{B.32}$$

***YZ* Plane:** for $0 \le y_j \le ymC_i$

Upper surface

$$zCu_{\mathrm{i,j}} = \sin\left(\frac{\pi}{2}\cdot\left(\frac{ybC_i - y_j}{ybC_i}\right)\right)\cdot(zuC_i - zbC_i) + zbC_i + f_{SC}(x_i) \qquad , 0 \le y_j < ybC_i \tag{B.33}$$

$$zCu_{\mathrm{i,j}} = \tan\left(\frac{\pi}{4}\cdot\left(\frac{ymC_i - y_j}{ymC_i - ybC_i}\right)\right)^2\cdot\left(zbC_i - \frac{zsC_i}{2}\right) + \frac{zsC_i}{2} + f_{SC}(x_i) \qquad , ybC_i \le y_j \le ymC_i \tag{B.34}$$

Lower surface

$$zCl_{\mathrm{i,j}} = -\sin\left(\frac{\pi}{2}\cdot\left(\frac{ymC_i - y_j}{ymC_i}\right)\right)^2 \cdot \left(zdC_i - \frac{zsC_i}{2}\right) - \frac{zsC_i}{2} + f_{SC}(x_i)$$

$$,\ 0 \le y_j \le ymC_i \qquad \text{(B.35)}$$

Station D

***XY* Plane:** for $xD_0 \le x_i \le xD_E$

$$ybuD_i = \left(\frac{xD_E - x_i}{xD_E - xD_0}\right)\cdot yD_{bu} \qquad \text{(B.36)}$$

$$ybD_i = \cos\left(\frac{\pi}{2}\cdot\left(\frac{xD_E - x_i}{xD_E - xD_0}\right)\right)\cdot(yD_{bm} - yD_b) + yD_b \qquad \text{(B.37)}$$

$$ymD_i = yD_{\max} \qquad \text{(B.38)}$$

***XZ* Plane:** for $xD_0 \le x_i \le xD_E$

$$zbD_i = \left(\frac{xD_E - x_i}{xD_E - xD_0}\right)\cdot(zC_b - zD_b) + zD_b \qquad \text{(B.39)}$$

$$zeD_i = \left(\frac{x_i - xD_0}{xD_E - xD_0}\right)\cdot zD_e \qquad \text{(B.40)}$$

$$zcD_i = \left(\frac{x_i - xD_0}{xD_E - h_{ex} - xD_0}\right)\cdot zD_c \qquad \text{(B.41)}$$

$$zhD_i = \left(\frac{xD_E - x_i}{xD_E - xD_0}\right)\cdot(zC_u - (zbD_i + h_{\mathrm{ex}} + zeD_i)) \qquad \text{(B.42)}$$

$$zdD_i = \left(\frac{xD_E - x_i}{xD_E - xD_0}\right)\cdot(zC_d - zD_d) + zD_d \qquad \text{(B.43)}$$

$$zsD_i = f_{AF}(x_i, xA_E, xD_E) \qquad \text{(B.44)}$$

Cambered fuselage:

$$f_{SC}(x_i) = \tan\left(\frac{\pi}{4}\cdot\left(\frac{xD_E - x_i}{xD_E - xD_0}\right)\right)\cdot(z_{SC}(3) - z_{SC}(4)) + z_{SC}(4) \qquad \text{(B.45)}$$

***YZ* Plane:** for $0 \le y_j \le ymD_i$

Upper surface

$$zDu_{\mathrm{i,j}} = \sin\left(\frac{\pi}{2}\cdot\left(\frac{ybuD_i - y_j}{ybuD_i}\right)\right)\cdot zeD_i + h_{\mathrm{ex}} + zbD_i + zhD_i + zscD_i + f_{SC}(x_i)$$

$$, 0 \le y_j < ybuD_i \qquad \text{(B.46)}$$

$$zDu_{\mathrm{i,j}} = \sin\left(\frac{\pi}{2}\cdot\left(\frac{ybD_i - y_j}{ybD_i - ybDu_i}\right)\right)\cdot(h_{\mathrm{ex}} + zscD_i) + zbD_i + f_{SC}(x_i)$$

$$, \mathrm{y}buD_i \le y_j < ybD_i \qquad \text{(B.47)}$$

$$zDu_{\mathrm{i,j}} = \tan\left(\frac{\pi}{4}\cdot\left(\frac{ymD_i - y_j}{ymD_i - ybD_i}\right)\right)^2\cdot\left(zbD_i - \frac{zsD_i}{2}\right) + \frac{zsD_i}{2} + f_{SC}(x_i)$$

$$, \ ybD_i \le y_j \le ymD_i \qquad \text{(B.48)}$$

Lower surface

$$zDl_{\mathrm{i,j}} = -\sin\left(\frac{\pi}{2}\cdot\left(\frac{ymD_i - y_j}{ymD_i}\right)\right)^2\cdot\left(zdD_i - \frac{zsD_i}{2}\right) - \frac{zsD_i}{2} + f_{SC}(x_i)$$

$$, \ 0 \le y_j \le ymD_i \qquad \text{(B.49)}$$

<u>Station E</u>

***XY* Plane:** for $xE_0 \le x_i \le xE_E$

$$ybE_i = \left(\frac{xE_E - x_i}{xE_E - xE_0}\right)\cdot yD_b \qquad \text{(B.50)}$$

$$ymE_i = \left(\frac{xE_E - x_i}{xE_E - xE_0}\right)\cdot yD_{\max} \qquad \text{(B.51)}$$

***XZ* Plane:** for $0 \le x_i \le xE_E$

$$zbE_i = \left(\frac{xE_E - x_i}{xE_E - xE_0}\right)\cdot zD_b \qquad \text{(B.52)}$$

$$zdE_i = \left(\frac{xE_E - x_i}{xE_E - xE_0}\right)\cdot zD_d \qquad \text{(B.53)}$$

Cambered fuselage:

$$f_{SC}(x_i) = \sin\left(\frac{\pi}{2}\cdot\left(\frac{xE_E - x_i}{xE_E - xE_0}\right)\right)\cdot(z_{SC}(4) - z_{SC}(5)) + z_{SC}(5) \qquad \text{(B.54)}$$

***YZ* Plane:** for $0 \le y_j \le ymE_i$

Upper surface

$$zEu_{\mathrm{i,j}} = zbE_i \qquad , \ 0 \le y_j < ybE_i \qquad \text{(B.55)}$$

$$zEu_{\mathrm{i,j}} = \tan\left(\frac{\pi}{4}\cdot\left(\frac{ymE_i - y_j}{ymE_i - ybE_i}\right)\right)^2 \cdot zbE_i$$

$$, \ ybE_i \le y_j \le ymE_i \qquad \text{(B.56)}$$

Lower surface

$$zEl_{\mathrm{i,j}} = -\sin\left(\frac{\pi}{2}\cdot\left(\frac{ymE_i - y_j}{ymE_i}\right)\right)^2 \cdot zdE_i$$

$$, \ 0 \le y_j \le ymE_i \qquad \text{(B.57)}$$

<u>Station S</u>

***XY* Plane:** for $xA_E \le x_i \le xB_0$

$$ybS_i = \cos\left(\frac{\pi}{2}\cdot\left(\frac{xB_E - x_i}{xB_E - xA_E}\right)\right)\cdot(yB_{bm} - yB_b) + yB_b \qquad \text{(B.58)}$$

***XZ* Plane:** for $xA_E \le x_i \le xB_0$

$$zsS_i = f_{AF}(x_i, xA_E, xD_E) \qquad \text{(B.59)}$$

Cambered fuselage:

$$f_{SC}(x_i) = z_{SC}(1) \qquad \text{(B.60)}$$

***YZ* Plane:** for $0 \le y_j \le ymS_i$

Upper surface

$$zSu_{\mathrm{i,j}} = zA_b + f_{SC}(x_i) \quad , \; 0 \le y_j < ybS_i \tag{B.61}$$

$$zSu_{\mathrm{i,j}} = \tan\left(\frac{\pi}{4} \cdot \left(\frac{ymS_i - y_j}{ymS_i - ybS_i}\right)\right)^2 \cdot \left(zA_b - \frac{zsS_i}{2}\right) + \frac{zsS_i}{2} + f_{SC}(x_i)$$

$$, \; ybS_i \le y_j \le yA_{\max} \tag{B.62}$$

Lower surface

$$zSl_{\mathrm{i,j}} = -\sin\left(\frac{\pi}{2} \cdot \left(\frac{yA_{\max} - y_j}{yA_{\max}}\right)\right)^2 \cdot \left(zA_d - \frac{zsS_i}{2}\right) - \frac{zsS_i}{2} + f_{SC}(x_i)$$

$$, \; 0 \le y_j \le yA_{\max} \tag{B.63}$$

B.2 UCAV Propulsion Ducts

Exhaust Pipe

$$xex_S = xex_0 + (xex_E - xex_0) - h_{\mathrm{ex}} \tag{B.64}$$

***XY* Plane:** for $xex_0 \le x_i \le xex_S$

$$beu_i = \left(\frac{x_i - xex_0}{xex_S - xex_0}\right) \cdot b_{\mathrm{eu}} \tag{B.65}$$

$$bel_i = \left(\frac{x_i - xex_0}{xex_S - xex_0}\right) \cdot b_{\mathrm{el}} \tag{B.66}$$

$$re_i = \left(\frac{xex_S - x_i}{xex_S - xex_0}\right) \cdot \frac{d_{\mathrm{noz}}}{2} \tag{B.67}$$

***XZ* Plane:** for $xex_0 \le x_i \le xex_S$

$$zec_i = \left(\frac{xex_S - x_i}{xex_S - xex_0}\right) \cdot \left(\frac{d_{\mathrm{noz}} - h_{\mathrm{ex}}}{2}\right) + \frac{h_{\mathrm{ex}}}{2} \tag{B.68}$$

$$zes_i = \left(\frac{x_i - xex_0}{xex_S - xex_0} \right) \cdot \frac{h_{\text{ex}}}{2} \tag{B.69}$$

Vertical deflection:

$$f_{VS}(x_i) = \sin\left(\frac{\pi}{2} \cdot \left(\frac{xex_S - x_i}{xex_S - xex_0} \right) \right)^2 \cdot \left(\frac{h_{\text{ex}}}{2} + z_{\text{eb}} + z_{\text{en}} \right) + z_{\text{en}} \tag{B.70}$$

***YZ* Plane:**

Upper section, for $0 \le y_u \le yu_{\max}$

$$zexu_{\text{i,u}} = zec_i + f_{VS}(x_i) \qquad ,0 \le y_u < beu_i \tag{B.71}$$

$$zexu_{\text{i,u}} = \frac{\sqrt{(re_i \cdot (zec_i - zes_i))^2 - ((y_u - beu_i) \cdot (zec_i - zes_i))^2}}{re_i} + zes_i + f_{VS}(x_i)$$

$$,beu_i \le y_u \le yu_{\max} \tag{B.72}$$

Lower section, for $0 \le y_l \le yl_{\max}$

$$zexl_{\text{i,l}} = -zec_i + f_{VS}(x_i) \qquad ,0 \le y_l < bel_i \tag{B.73}$$

$$zexl_{\text{i,l}} = -\frac{\sqrt{(re_i \cdot (zec_i - zes_i))^2 - ((y_l - bel_i) \cdot (zec_i - zes_i))^2}}{re_i} - zes_i + f_{VS}(x_i)$$

$$,bel_i \le y_l \le yl_{\max} \tag{B.74}$$

when, $yu_{\max} = beu_i + re_i$

$yl_{\max} = bel_i + re_i$

B.3 Tanker Propulsion Ducts

<u>Centre Intake Diffuser</u>

$$xic_S = xic_0 + (xic_E - xic_0) - d_{\text{en}} \tag{B.75}$$

***XY* Plane:** for $xic_0 \le x_i \le xic_S$

$$bic_i = \left(\frac{xic_S - x_i}{xic_S - xic_0} \right) \cdot b_{\mathrm{ic}} \tag{B.76}$$

$$ric_i = \left(\frac{x_i - xic_0}{xic_S - xic_0} \right) \cdot \frac{d_{\mathrm{en}}}{2} \tag{B.77}$$

***XZ* Plane:** for $xic_0 \le x_i \le xic_S$

$$zicc_i = \left(\frac{x_i - xic_0}{xic_S - xic_0} \right) \cdot \left(\frac{d_{\mathrm{en}} - h_{\mathrm{in}}}{2} \right) + \frac{h_{\mathrm{in}}}{2} \tag{B.78}$$

$$zics_i = \left(\frac{xic_S - x_i}{xic_S - xic_0} \right) \cdot \frac{h_{\mathrm{in}}}{2} \tag{B.79}$$

Vertical deflection:

$$f_{VS}(x_i) = \sin\left(\frac{\pi}{2} \cdot \left(\frac{xic_S - x_i}{xic_S - xic_0} \right) \right)^2 \cdot \left(\frac{h_{\mathrm{in}}}{2} + z_{\mathrm{ib}} + z_{\mathrm{en}} \right) + z_{\mathrm{en}} \tag{B.80}$$

***YZ* Plane:** for $0 \le y_i \le yc_{\max}$

Upper section

$$zicu_{\mathrm{i,j}} = zicc_i + f_{VS}(x_i) \qquad , 0 \le y_j < bic_i \tag{B.81}$$

$$zicu_{\mathrm{i,j}} = \frac{\sqrt{(ric_i \cdot (zicc_i - zics_i))^2 - ((y_j - bic_i) \cdot (zicc_i - zics_i))^2}}{ric_i} + zics_i + f_{VS}(x_i)$$

$$, bic_i \le y_j \le yc_{\max} \tag{B.82}$$

Lower section

$$zicl_{\mathrm{i,j}} = -zicc_i + f_{VS}(x_i) \qquad , 0 \le y_j < bic_i \tag{B.83}$$

$$zicl_{\mathrm{i,j}} = -\frac{\sqrt{(ric_i \cdot (zicc_i - zics_i))^2 - ((y_j - bic_i) \cdot (zicc_i - zics_i))^2}}{ric_i} - zics_i + f_{VS}(x_i)$$

$$, bic_i \le y_j \le yc_{\max} \tag{B.84}$$

when, $yc_{\max} = bic_i + ric_i$

Side Intake Diffuser

$$xis_S = xis_0 + (xis_E - xis_0) - d_{\text{en}} \tag{B.85}$$

***XY* Plane:** for $xis_0 \le x_i \le xis_S$

$$bis_i = \left(\frac{xis_S - x_i}{xis_S - xis_0} \right) \cdot b_{\text{is}} \tag{B.86}$$

$$biu_i = \left(\frac{xis_S - x_i}{xis_S - xis_0} \right) \cdot b_{\text{iu}} \tag{B.87}$$

$$bil_i = \left(\frac{xis_S - x_i}{xis_S - xis_0} \right) \cdot b_{\text{il}} \tag{B.88}$$

$$ris_i = \left(\frac{x_i - xis_0}{xis_S - xis_0} \right) \cdot \frac{d_{\text{en}}}{2} \tag{B.89}$$

Lateral deflection:

$$f_{LS}(x_i) = \cos\left(\frac{\pi}{2} \cdot \left(\frac{xis_S - x_i}{xis_S - xis_0} \right) \right)^2 \cdot \left(d_{\text{en}} + 2 \cdot w_{\text{fw}} - b_{\text{ic}} - b_{\text{is}} \right) + b_{\text{ic}} + b_{\text{is}} \tag{B.90}$$

***XZ* Plane:** for $xis_0 \le x_i \le xis_S$

$$zisc_i = \left(\frac{x_i - xis_0}{xis_S - xis_0} \right) \cdot \left(\frac{d_{\text{en}} - h_{\text{in}}}{2} \right) + \frac{h_{\text{in}}}{2} \tag{B.91}$$

$$ziss_i = \left(\frac{xis_S - x_i}{xis_S - xis_0} \right) \cdot \frac{h_{\text{in}}}{2} \tag{B.92}$$

Vertical deflection:

$$f_{VS}(x_i) = \sin\left(\frac{\pi}{2} \cdot \left(\frac{xis_S - x_i}{xis_S - xis_0} \right) \right)^2 \cdot \left(\frac{h_{\text{in}}}{2} + z_{\text{ib}} + z_{\text{en}} \right) + z_{\text{en}} \tag{B.93}$$

***YZ* Plane:**

Upper-right section, for $0 \le y_u \le yu_{\max}$

$$yiur_{\mathrm{i,u}} = y_u + f_{LS}(x_i) \tag{B.94}$$

$$ziur_{\mathrm{i,u}} = zc_i + f_{VS}(x_i) \qquad , 0 \le y_u < biu_i \tag{B.95}$$

$$ziur_{\mathrm{i,u}} = \frac{\sqrt{(ris_i \cdot (zisc_i - ziss_i))^2 - ((y_u - biu_i)\cdot(zisc_i - ziss_i))^2}}{ris_i} + ziss_i + f_{VS}(x_i)$$
$$, biu_i \le y_u \le yu_{\max} \tag{B.96}$$

Lower-right section, for $0 \le y_l \le yl_{\max}$

$$yilr_{\mathrm{i,l}} = y_l + f_{LS}(x_i) \tag{B.97}$$

$$zilr_{\mathrm{i,l}} = -zc_i + f_{VS}(x_i) \qquad , 0 \le y_l < bil_i \tag{B.98}$$

$$zilr_{\mathrm{i,l}} = -\frac{\sqrt{(ris_i \cdot (zisc_i - ziss_i))^2 - ((y_l - bil_i)\cdot(zisc_i - ziss_i))^2}}{ris_i} - ziss_i + f_{VS}(x_i)$$
$$, bil_i \le y_l \le yl_{\max} \tag{B.99}$$

Upper-left section, for $-ys_{\max} \le y_s \le 0$

$$yiul_{\mathrm{i,s}} = y_s + f_{LS}(x_i) \tag{B.100}$$

$$ziul_{\mathrm{i,s}} = zc_i + f_{VS}(x_i) \qquad , -bis_i \le y_s < 0 \tag{B.101}$$

$$ziul_{\mathrm{i,s}} = \frac{\sqrt{(ris_i \cdot (zisc_i - ziss_i))^2 - ((y_s + bis_i)\cdot(zisc_i - ziss_i))^2}}{ris_i} + ziss_i + f_{VS}(x_i)$$
$$, -ys_{\max} \le y_s \le -bis_i \tag{B.102}$$

Lower-left section, for $-ys_{\max} \le y_s \le 0$

$$yill_{\mathrm{i,s}} = y_s + f_{LS}(x_i) \tag{B.103}$$

$$zill_{\mathrm{i,s}} = -zc_i + f_{VS}(x_i) \qquad , -bis_i \le y_s < 0 \tag{B.104}$$

$$zill_{\mathrm{i,s}} = -\frac{\sqrt{(ris_i \cdot (zisc_i - ziss_i))^2 - ((y_s + bis_i)\cdot(zisc_i - ziss_i))^2}}{ris_i} - ziss_i + f_{VS}(x_i)$$
$$, -ys_{\max} \le y_s \le -bis_i \tag{B.105}$$

When, $ys_{\max} = bis_i + ris_i$

$yu_{\max} = biu_i + ris_i$

$yl_{\max} = bil_i + ris_i$

Centre Exhaust Pipe

$$xec_S = xec_0 + (xec_E - xec_0) - h_{\text{ex}} \tag{B.106}$$

***XY* Plane:** for $xec_0 \le x_i \le xec_S$

$$bec_i = \left(\frac{x_i - xec_0}{xec_S - xec_0}\right) \cdot b_{\text{ec}} \tag{B.107}$$

$$rec_i = \left(\frac{xec_S - x_i}{xec_S - xec_0}\right) \cdot \frac{d_{\text{noz}}}{2} \tag{B.108}$$

Vertical deflection:

$$f_{VS}(x_i) = \sin\left(\frac{\pi}{2} \cdot \left(\frac{xec_S - x_i}{xec_S - xec_0}\right)\right)^2 \cdot \left(\frac{h_{\text{ex}}}{2} + z_{\text{eb}} + z_{\text{en}}\right) + z_{\text{en}} \tag{B.109}$$

***XZ* Plane:** for $xec_0 \le x_i \le xec_S$

$$zecc_i = \left(\frac{xec_S - x_i}{xec_S - xec_0}\right) \cdot \left(\frac{d_{\text{noz}} - h_{\text{ex}}}{2}\right) + \frac{h_{\text{ex}}}{2} \tag{B.110}$$

$$zecs_i = \left(\frac{x_i - xec_0}{xec_S - xec_0}\right) \cdot \frac{h_{\text{ex}}}{2} \tag{B.111}$$

***YZ* Plane:** for $0 \le y_j \le yc_{\max}$

Upper section

$$zecu_{\text{i, j}} = zecc_i + f_{VS}(x_i) \qquad , 0 \le y_j < bec_i \tag{B.112}$$

$$zecu_{\text{i, j}} = -\frac{\sqrt{(rec_i \cdot (zecc_i - zecs_i))^2 - ((y_j - bec_i) \cdot (zecc_i - zecs_i))^2}}{rec_i} + zecs_i + f_{VS}(x_i)$$

$$, bec_i \le y_j \le yc_{\max} \tag{B.113}$$

Lower section

$$zecl_{\text{i, j}} = -zecc_i + f_{VS}(x_i) \qquad , 0 \le y_j < bec_i \tag{B.114}$$

$$zecl_{\mathrm{i,j}} = -\frac{\sqrt{(rec_i \cdot (zecc_i - zecs_i))^2 - ((y_j - bec_i)\cdot(zecc_i - zecs_i))^2}}{rec_i} - zecs_i + f_{VS}(x_i)$$

$$, bec_i \le y_j \le yc_{\max} \qquad \text{(B.115)}$$

when, $yc_{\max} = bec_i + rec_i$

Side Exhaust Pipe

$$xes_S = xes_0 + (xes_E - xes_0) - h_{\mathrm{ex}} \qquad \text{(B.116)}$$

***XY* Plane:** for $xes_0 \le x_i \le xes_S$

$$bes_i = \left(\frac{x_i - xes_0}{xes_S - xes_0}\right)\cdot b_{\mathrm{es}} \qquad \text{(B.117)}$$

$$beu_i = \left(\frac{x_i - xes_0}{xes_S - xes_0}\right)\cdot b_{\mathrm{eu}} \qquad \text{(B.118)}$$

$$bel_i = \left(\frac{x_i - xes_0}{xes_S - xes_0}\right)\cdot b_{\mathrm{el}} \qquad \text{(B.119)}$$

$$res_i = \left(\frac{xes_S - x_i}{xes_S - xes_0}\right)\cdot \frac{d_{\mathrm{noz}}}{2} \qquad \text{(B.120)}$$

Vertical deflection:

$$f_{VS}(x_i) = \sin\left(\frac{\pi}{2}\cdot\left(\frac{xes_S - x_i}{xes_S - xes_0}\right)\right)^2 \cdot \left(\frac{h_{\mathrm{ex}}}{2} + z_{\mathrm{eb}} + z_{\mathrm{en}}\right) + z_{\mathrm{en}} \qquad \text{(B.121)}$$

***XZ* Plane:** for $xes_0 \le x_i \le xes_S$

$$zesc_i = \left(\frac{xes_S - x_i}{xes_S - xes_0}\right)\cdot\left(\frac{d_{\mathrm{noz}} - h_{\mathrm{ex}}}{2}\right) + \frac{h_{\mathrm{ex}}}{2} \qquad \text{(B.122)}$$

$$zess_i = \left(\frac{x_i - xes_0}{xes_S - xes_0}\right)\cdot \frac{h_{\mathrm{ex}}}{2} \qquad \text{(B.123)}$$

Lateral deflection:

$$f_{LS}(x_i) = \sin\left(\frac{\pi}{2}\cdot\left(\frac{xes_S - x_i}{xes_S - xes_0}\right)\right)^2 \cdot \left(d_{\mathrm{en}} + 2\cdot w_{\mathrm{fw}} - b_{\mathrm{ec}} - b_{\mathrm{es}}\right) + b_{\mathrm{ec}} + b_{\mathrm{es}} \tag{B.124}$$

***YZ* Plane:**

Upper-right section, for $0 \le y_u \le yu_{\max}$

$$yeu_{\mathrm{i,u}} = y_u + f_{LS}(x_i) \tag{B.125}$$

$$zeu_{\mathrm{i,u}} = zesc_i + f_{VS}(x_i) \qquad ,0 \le y_u < beu_i \tag{B.126}$$

$$zeu_{\mathrm{i,u}} = \frac{\sqrt{(res_i\cdot(zesc_i - zess_i))^2 - ((y_u - beu_i)\cdot(zesc_i - zess_i))^2}}{res_i} + zess_i + f_{VS}(x_i)$$

$$,beu_i \le y_u \le yu_{\max} \tag{B.127}$$

Lower-right section, for $0 \le y_l \le yl_{\max}$

$$yel_{\mathrm{i,l}} = y_l + f_{LS}(x_i) \tag{B.128}$$

$$zel_{\mathrm{i,l}} = -zesc_i + f_{VS}(x_i) \qquad ,0 \le y_l < bel_i \tag{B.129}$$

$$zel_{\mathrm{i,l}} = -\frac{\sqrt{(res_i\cdot(zesc_i - zess_i))^2 - ((y_l - bel_i)\cdot(zesc_i - zess_i))^2}}{res_i} - zess_i + f_{VS}(x_i)$$

$$,bel_i \le y_l \le yl_{\max} \tag{B.130}$$

Upper-left section, for $-ys_{\max} \le y_s \le 0$

$$yeu_{\mathrm{i,s}} = y_s + f_{LS}(x_i) \tag{B.131}$$

$$zeu_{\mathrm{i,s}} = zesc_i + f_{VS}(x_i) \qquad ,-bes_i \le y_s < 0 \tag{B.132}$$

$$zeu_{\mathrm{i,s}} = \frac{\sqrt{(res_i\cdot(zesc_i - zess_i))^2 - ((y_s + bes_i)\cdot(zesc_i - zess_i))^2}}{res_i} + zess_i + f_{VS}(x_i)$$

$$,-ys_{\max} \le y_s \le -bes_i \tag{B.133}$$

Lower-left section, for $-ys_{\max} \le y_s \le 0$

$$yell_{\mathrm{i,s}} = y_s + f_{LS}(x_i) \tag{B.134}$$

$$zell_{\mathrm{i,s}} = -zesc_i + f_{VS}(x_i) \qquad ,-bes_i \le y_s < 0 \tag{B.135}$$

$$zell_{\mathrm{i,s}} = -\frac{\sqrt{(res_i\cdot(zesc_i - zess_i))^2 - ((y_s + bes_i)\cdot(zesc_i - zess_i))^2}}{res_i} - zess_i + f_{VS}(x_i)$$

$$,-ys_{\max} \le y_s \le -bes_i \tag{B.136}$$

when, $ys_{\max} = bes_i + res_i$

$yu_{\max} = beu_i + res_i$

$yl_{\max} = bel_i + res_i$

Appendix C – Weights and Stability

The refined weight estimation equations listed in this Appendix are provided by references [44, 47].

Nomenclature

AR	- Aspect ratio
b_W	- Wing span (ft)
d_{en}	- Engine diameter (ft)
d_F	- Fuselage structural depth (ft)
I_y	- Yawing moment of inertia (lb-ft^2)
l_{a}	- Electrical routing distance (ft)
l_{d}	- Duct length (ft)
l_{ec}	- Length from engine front to cockpit (ft)
l_{ex}	- Length of exhaust pipe (ft)
l_{mg}	- Length of main landing gear (ft)
l_{ng}	- Length of nose landing gear (ft)
l_{sh}	- Length of engine shroud (ft)
M	- Maximum cruise Mach number
M_{SL}	- Maximum sea-level Mach number
N_c	- Number of crews
N_{en}	- Number of engines
N_f	- Number of functions performed by controls
N_{ld}	- Ultimate landing load factor

N_m	- Number of mechanical functions
N_{mgs}	- Number of main gear shock struts
N_{mgw}	- Number of main wheels
N_{ngw}	- Number of nose wheels
N_s	- Number of flight control systems
N_t	- Number of fuel tanks
N_u	- Number of hydraulic utility functions
N_Z	- Ultimate load factor
R_{kva}	- System electrical rating (kv-A)
S_{cs}	- Total area of control surfaces (ft^2)
S_{csw}	- Control surface area (wing-mounted) (ft^2)
S_F	- Fuselage wetted area (ft^2)
S_{fw}	- Firewall surface area (ft^2)
S_W	- Trapezium wing area (ft^2)
sfc	- Engine specific fuel consumption
T	- Total engine thrust (lb)
T_{en}	- Thrust per engine (lb)
tc	- Maximum wing aerofoil thickness (%)
V_i	- Integral tanks volume (gal)
V_p	- Self-sealing tanks volume (gal)
V_{stall}	- Stall speed (ft/s)
V_t	- Total fuel volume (gal)
W_{APU}	- Uninstalled APU weight (lb)
W_{dg}	- Design gross weight (lb)
W_{en}	- Engine weight (lb)
W_{ld}	- Landing weight (lb)
W_{uav}	- Uninstalled avionics weight (lb)
Λ_{LE}	- Leading-edge sweep angle

Λ_{Q2}	- Mid-chord sweep angle
Λ_{Q4}	- Quarter-chord sweep angle
λ	- Taper ratio

C.1 Weight Prediction Equations - UCAV

For clean wing,

$$W_{\text{wing}} = 3.08 \cdot \left(\frac{K_{\text{vs}} \cdot N_z \cdot W_{\text{dg}}}{tc} \cdot \left\{ \left[\tan \Lambda_{LE} - \frac{2 \cdot (1-\lambda)}{AR \cdot (1+\lambda)} \right]^2 + 1 \right\} \times 10^{-6} \right)^{0.593} \times [(1+\lambda) \cdot \text{AR}]^{0.89} \cdot S_W^{\ 0.741} \tag{C.1}$$

, otherwise

$$W_{\text{wing}} = 0.0103 \cdot K_{\text{dw}} \cdot K_{\text{vs}} \cdot \left(W_{\text{dg}} \cdot N_z\right)^{0.5} \cdot S_W^{\ 0.622} \cdot AR^{0.785} \cdot tc^{-0.4} \times (1+\lambda)^{0.05} \cdot (\cos \Lambda_{Q4})^{-1} \cdot S_{\text{csw}}^{\ 0.04} \tag{C.2}$$

where, $K_{\text{vs}} = 1$; $K_{\text{dw}} = 1$

$$W_{\text{fuselage}} = 0.499 \cdot K_{\text{dwf}} \cdot W_{\text{dg}}^{\ 0.35} \cdot N_z^{\ 0.25} \cdot l_F^{\ 0.5} \cdot d_F^{\ 0.849} \cdot w_F^{\ 0.685} \tag{C.3}$$

where, $K_{\text{dwf}} = 1$

$$W_{\text{nose gear}} = (W_{\text{ld}} \cdot N_{ld})^{0.29} \cdot l_{\text{ng}}^{\ 0.5} \cdot N_{\text{ngw}}^{\ 0.525} \tag{C.4}$$

$$W_{\text{main gear}} = K_{\text{cb}} \cdot K_{\text{tpg}} \cdot (W_{\text{ld}} \cdot N_{ld})^{0.25} \cdot l_{\text{mg}}^{\ 0.973} \tag{C.5}$$

where, $K_{\text{cb}} = 1$; $K_{\text{tpg}} = 1$

$$W_{\text{intake diffuser}} = 13.29 \cdot K_{\text{vg}} \cdot l_{\text{d}}^{\ 0.643} \cdot K_{\text{d}}^{\ 0.182} \cdot N_{\text{en}}^{\ 1.498} \cdot (l_{\text{s}} / l_{\text{d}})^{-0.373} \cdot d_{\text{en}} \tag{C.6}$$

where, $K_{\text{vg}} = 1.62$; $K_{\text{d}} = 2.75$

$$W_{\text{exhaust pipe}} = 3.5 \cdot d_{\text{en}} \cdot l_{\text{ex}} \cdot N_{\text{en}} \tag{C.7}$$

$$W_{\substack{\text{engine}\\ \text{mounts}}} = 0.013 \cdot N_{\text{en}}{}^{0.795} \cdot T^{0.579} \cdot N_z \tag{C.8}$$

$$W_{\substack{\text{engine}\\ \text{section}}} = 0.01 \cdot W_{\text{en}}{}^{0.717} \cdot N_{\text{en}} \cdot N_z + 1.13 \cdot S_{\text{fw}} \tag{C.9}$$

$$W_{\substack{\text{engine}\\ \text{cooling}}} = 4.55 \cdot d_{\text{en}} \cdot l_{\text{sh}} \cdot N_{\text{en}} + 37.81 \cdot N_{\text{en}}{}^{1.023} \tag{C.10}$$

$$W_{\text{avionics}} = 2.117 \cdot W_{\text{uav}}{}^{0.933} \tag{C.11}$$

$$W_{\substack{\text{APU}\\ \text{installed}}} = 2.2 \cdot W_{\text{APU}} \tag{C.12}$$

$$W_{\text{air-condition}} = 201.6 \cdot [(W_{\text{uav}} + 200 \cdot N_c)/1000]^{0.735} \tag{C.13}$$

$$W_{\substack{\text{engine}\\ \text{controls}}} = 10.5 \cdot N_{\text{en}}{}^{1.008} \cdot l_{\text{ec}}{}^{0.222} \tag{C.14}$$

$$W_{\text{starter}} = 0.025 \cdot T_{\text{en}}{}^{0.76} \cdot N_{\text{en}}{}^{0.72} \tag{C.15}$$

$$W_{\substack{\text{fuel system}\\ \text{and tanks}}} = 7.45 \cdot V_t{}^{0.47} \cdot \left(1 + \frac{V_i}{V_t}\right)^{-0.095} \cdot \left(1 - \frac{V_p}{V_t}\right) \cdot N_t{}^{0.066} \cdot N_{\text{en}}{}^{0.052} \cdot \left(\frac{T \cdot \text{sfc}}{1000}\right)^{0.249} \tag{C.16}$$

$$W_{\substack{\text{flight}\\ \text{controls}}} = 36.28 \cdot M^{0.003} \cdot S_{\text{cs}}{}^{0.489} \cdot N_s{}^{0.484} \cdot N_c{}^{0.127} \tag{C.17}$$

$$W_{\text{hydraulics}} = 37.23 \cdot K_{\text{vsh}} \cdot N_u{}^{0.664} \tag{C.18}$$

where, $K_{\text{vsh}} = 1$

$$W_{\text{electrical}} = 172.2 \cdot K_{\text{mc}} \cdot R_{\text{kva}}{}^{0.152} \cdot N_c{}^{0.1} \cdot l_a{}^{0.1} \cdot N_{\text{en}}{}^{0.01} \tag{C.19}$$

where, $K_{\text{mc}} = 1$

$$W_{\substack{\text{refuelling}\\\text{system}}} = 13.64 \cdot (0.01 \cdot V_t)^{0.392} \tag{C.20}$$

The centres of gravity of the following components are approximately in the same longitudinal locations, thus the weights results may be grouped together.

$$W_{\text{engine}} = N_{\text{en}} \cdot W_{\text{en}} + W_{\substack{\text{engine}\\\text{mounts}}} + W_{\substack{\text{engine}\\\text{section}}} + W_{\text{starter}} \tag{C.21}$$

$$W_{\substack{\text{system}\\\text{controls}}} = W_{\text{electrical}} + W_{\substack{\text{engine}\\\text{controls}}} + W_{\text{air-condition}} \tag{C.22}$$

C.2 Weight Prediction Equations – Uninhabited Tanker

For clean wing,

$$\begin{aligned} W_{\text{wing}} &= 0.0051 \cdot \left(W_{\text{dg}} \cdot N_z\right)^{0.557} \cdot S_W{}^{0.649} \cdot AR^{0.5} \cdot tc^{-0.4} \cdot (1+\lambda)^{0.1} \\ &\quad \times (\cos\Lambda_{Q4})^{-1} \cdot S_{\text{scw}}{}^{0.1} \end{aligned} \tag{C.23}$$

, otherwise

$$W_{\text{wing}} = (4.28 \times 10^{-3}) \cdot S_W{}^{0.48} \cdot \frac{AR \cdot M_{SL}{}^{0.43}}{(100 \cdot tc)^{0.76}} \cdot \frac{(W_{\text{dg}} \cdot N_z)^{0.84} \cdot \lambda^{0.14}}{(\cos\Lambda_{Q2})^{1.54}} \tag{C.24}$$

$$W_{\text{fuselage}} = 0.328 \cdot K_{\text{door}} \cdot K_{\text{Lg}} \cdot (W_{\text{dg}} \cdot N_z)^{0.5} \cdot l_F{}^{0.25} \cdot S_F{}^{0.302} \cdot (1+K_{\text{ws}})^{0.04} \cdot (l_F / d_F)^{0.1} \tag{C.25}$$

where, ` $K_{\text{door}} = 1$; $K_{\text{Lg}} = 1$; $K_{\text{ws}} = 1$

$$W_{\text{nose gear}} = 0.032 \cdot K_{\text{np}} \cdot W_{\text{ld}}{}^{0.646} \cdot N_{ld}{}^{0.2} \cdot l_{\text{ng}}{}^{0.5} \cdot N_{\text{ngw}}{}^{0.45} \tag{C.26}$$

where, $K_{\text{np}} = 1$

$$W_{\text{main gear}} = 0.0106 \cdot K_{\text{mp}} \cdot W_{\text{ld}}{}^{0.888} \cdot N_{ld}{}^{0.25} \cdot l_{\text{mg}}{}^{0.4} \cdot N_{\text{mgw}}{}^{0.321} \cdot N_{\text{mgs}}{}^{-0.5} \cdot V_{\text{stall}}{}^{0.1} \tag{C.27}$$

where, $K_{\text{mp}} = 1$

$$W_{\substack{\text{engine}\\\text{controls}}} = 5 \cdot N_{\text{en}} + 0.8 \cdot l_{\text{ec}} \tag{C.28}$$

$$W_{\text{starter}} = 49.19 \cdot \left(\frac{N_{\text{en}} \cdot W_{\text{en}}}{1000} \right)^{0.541} \tag{C.29}$$

$$W_{\substack{\text{fuel system}\\\text{and tanks}}} = 2.405 \cdot V_t^{\,0.606} \cdot \frac{1 + V_p / V_t}{1 + V_i / V_t} \cdot N_t^{\,0.5} \tag{C.30}$$

$$W_{\substack{\text{flight}\\\text{controls}}} = 145.9 \cdot N_f^{\,0.554} \cdot (1 + N_m / N_f)^{-1} \cdot S_{\text{cs}}^{\,0.2} \cdot (I_y \times 10^{-6})^{0.07} \tag{C.31}$$

when, $$I_y = \frac{0.0775 \cdot l_F^{\,2} \cdot W_{\text{dg}}}{g} \tag{C.32}$$

$$W_{\text{hydraulics}} = 0.2673 \cdot N_f \cdot (l_F + b_W)^{0.937} \tag{C.33}$$

$$W_{\text{electrical}} = 7.291 \cdot R_{\text{kva}}^{\,0.782} \cdot l_{\text{a}}^{\,0.346} \cdot N_{\text{en}}^{\,0.1} \tag{C.34}$$

$$W_{\text{avionics}} = 1.73 \cdot W_{\text{uav}}^{\,0.983} \tag{C.35}$$

The Eq. (C.6) to Eq. (C.13) in the UCAV section are directly used for calculating the estimated weight of the associated tanker's components. Also due to their similar component configurations, the same grouped weight equations of Eq. (C.21) and Eq. (C.22) are also applied in the tanker case.

Appendix D – Performance

The engine performance analysis methods and their associated equations listed in this Appendix are adopted from reference [21].

Nomenclature

A	- Station area
A^*	- Station area corresponding to $M = 1.0$
C_p	- Specific heat at constant pressure (Btu/ lb-°R)
C_{TO}	- Power takeoff shaft power coefficient
e	- Polytropic efficiency
f	- Fuel-to-air ratio
f_0	- Overall engine fuel-to-air ratio
F	- Uninstalled thrust (lb)
fs	- Specific-fuel-consumption fudge factor
g_c	- Gravitational constant (ft /s^2)
h_0	- Static enthalpy at station 0
h_{PR}	- Fuel heating value (Btu/lb)
m	- Mass flow rate (lb /s)
M	- Mach number
P	- Pressure (psi)
P_t	- Total (or stagnation) Pressure (psi)
R	- Gas constant
sfc	- Specific fuel consumption (lb/hr/lb)
T	- Temperature (°R)
T_t	- Total (or stagnation) temperature (°R)

V	- Velocity (ft /s)
α	- Engine bypass ratio
α'	- Mixer bypass ratio
β	- Bleed air fraction
ε	- Cooling air fraction
γ	- Ratio of specific heats
η	- Component efficiency
π	- Total pressure ratio
π_r	- Isentropic freestream recovery pressure ratio
τ	- Total temperature ratio
τ_r	- Adiabatic freestream recovery temperature ratio
τ_λ	- Enthalpy ratio of burner

Subscripts

b	- Burner	n	- Exhaust nozzle
c	- Compressor	t	- Turbine
cH	- High-pressure compressor	tH	- High-pressure turbine
c'	- Fan	tL	- Low-pressure turbine
d	- Diffuser or inlet	mH	- Mechanical, high-pressure shaft
$m1$	- Coolant mixer 1	mL	- Mechanical, low-pressure spool
$m2$	- Coolant mixer 2	mP	- Mechanical, power takeoff shaft
M	- Mixer	R	- Reference on-design conditions

D.1 UCAV - Engine Performance Equations

Station	Location	Station	Location
0	Far upstream or freestream	4b	High pressure turbine exit
1	Inlet or diffuser entry		Modeled coolant mixer 2 entry
2	Inlet or diffuser exit		
	Fan entry	4c	Coolant mixer 2 exit
3'	Fan exit		Low pressure turbine entry
	High pressure compressor entry	5	Low pressure turbine exit
3	High pressure compressor exit		Core stream mixer entry
3a	Burner entry	5'	Fan bypass stream mixer entry
4	Burner exit		
	Nozzle vanes entry	6	Mixer exit
	Modeled coolant mixer 1 entry		Afterburner entry
	High pressure turbine entry for π_{tH} definition	7	Afterburner exit
			Exhaust nozzle entry
4a	Nozzle vanes exit	8	Exhaust nozzle throat
	Coolant mixer 1 exit	9	Exhaust nozzle exit
	High pressure turbine entry for τ_{tH} definition		

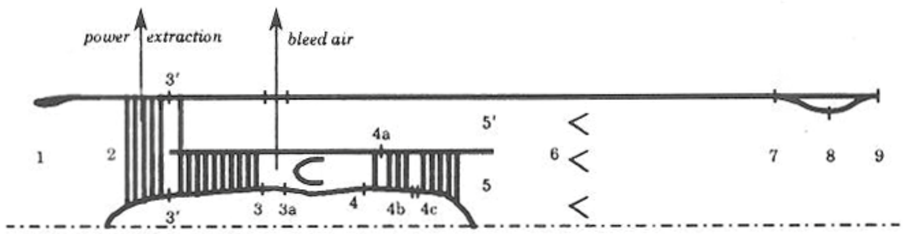

Figure D.1: Reference stations – mixed-stream turbofan engine [21]

D.1.1 On-Design Cycle Analysis

Preliminary computations

$$\varepsilon_1 = \varepsilon_2 = \frac{T_{t4} - 2400}{16000} \qquad \text{, for } T_{t4} > 2400 \qquad \text{(D.1)}$$

$$\varepsilon_1 = \varepsilon_2 = 0 \qquad \text{, otherwise} \qquad \text{(D.2)}$$

$$\tau_r = 1 + \left(\frac{\gamma_c - 1}{2}\right) \cdot M_0{}^2 \qquad \text{(D.3)} \quad ; \qquad \pi_r = \tau_r{}^{\gamma_c/(\gamma_c - 1)} \qquad \text{(D.4)}$$

$$\pi_d = \pi_{d\max} \qquad \text{, for } M_0 \le 1 \qquad \text{(D.5)}$$

$$\pi_d = \pi_{d\max} \cdot \left[1 - 0.075 \cdot (M_0 - 1)^{1.35}\right] \qquad \text{, otherwise} \qquad \text{(D.6)}$$

$$\tau_\lambda = \frac{C_{pt} \cdot T_{t4}}{C_{pc} \cdot T_0} \quad \text{(D.7)} \quad ; \quad \pi_{cH} = \frac{\pi_c}{\pi_{c'}} \quad \text{(D.8)}$$

$$R_c = 778.16 \cdot \left(\frac{\gamma_c - 1}{\gamma_c}\right) \cdot C_{pc} \quad \text{(D.9)} \quad ; \quad R_t = 778.16 \cdot \left(\frac{\gamma_t - 1}{\gamma_t}\right) \cdot C_{pt} \quad \text{(D.10)}$$

$$h_0 = 778.16 \cdot C_{pc} \cdot T_0 \quad \text{(D.11)}$$

Compressor

$$\tau_{c'} = \pi_{c'}^{(\gamma_c - 1)/(\gamma_c \cdot e_{c'})} \quad \text{(D.12)}$$

$$\eta_{c'} = \frac{\pi_{c'}^{(\gamma_c - 1)/\gamma_c} - 1}{\tau_{c'} - 1} \quad \text{(D.13)}$$

$$\tau_{cH} = \pi_{cH}^{(\gamma_c - 1)/(\gamma_c \cdot e_{cH})} \quad \text{(D.15)}$$

$$\eta_{cH} = \frac{\pi_{cH}^{(\gamma_c - 1)/\gamma_c} - 1}{\tau_{cH} - 1} \quad \text{(D.16)}$$

Burner, coolant mixers, and turbine

$$f_b = \frac{\tau_\lambda - \tau_r \cdot \tau_{c'} \cdot \tau_{cH}}{h_{PR} \cdot \eta_b / (C_{pc} \cdot T_0) - \tau_\lambda} \quad \text{(D.17)}$$

$$\tau_{m1} = \frac{(1 - \beta - \varepsilon_1 - \varepsilon_2) \cdot (1 + f_b) + \varepsilon_1 \cdot \tau_r \cdot \tau_{c'} \cdot \tau_{cH} / \tau_\lambda}{h_{PR} \cdot \eta_b / (C_{pc} \cdot T_0) - \tau_\lambda} \quad \text{(D.18)}$$

$$\tau_{tH} = 1 - \frac{\tau_r \cdot \tau_{c'} \cdot (\tau_{cH} - 1)}{\eta_{mH} \cdot \tau_\lambda \cdot \left[(1 - \beta - \varepsilon_1 - \varepsilon_2) \cdot (1 + f_b) + \varepsilon_1 \cdot \tau_r \cdot \tau_{c'} \cdot \tau_{cH} / \tau_\lambda\right]} \quad \text{(D.19)}$$

$$\pi_{tH} = \tau_{tH}^{\gamma_t / [(\gamma_t - 1) \cdot e_{tH}]} \quad \text{(D.20)}$$

$$\eta_{tH} = \frac{1 - \tau_{tH}}{1 - \pi_{tH}^{(\gamma_t - 1)/\gamma_t}} \quad \text{(D.21)}$$

$$\tau_{m2} = \frac{(1 - \beta - \varepsilon_1 - \varepsilon_2) \cdot (1 + f_b) + \varepsilon_1 + \varepsilon_2 \cdot \left(\frac{\tau_r \cdot \tau_{c'} \cdot \tau_{cH}}{\tau_\lambda \cdot \tau_{m1} \cdot \tau_{tH}}\right)}{(1 - \beta - \varepsilon_1 - \varepsilon_2) \cdot (1 + f_b) + \varepsilon_1 + \varepsilon_2} \quad \text{(D.22)}$$

$$\tau_{tL} = 1 - \frac{(1 + \alpha) \cdot \left[\tau_r \cdot (\tau_{c'} - 1) + C_{TO} / \eta_{mp}\right]}{\eta_{mL} \cdot \tau_\lambda \cdot \tau_{tH} \cdot \left[(1 - \beta - \varepsilon_1 - \varepsilon_2) \cdot (1 + f_b) + \varepsilon_1 + (\varepsilon_2 / \tau_{tH}) \cdot \tau_r \cdot \tau_{c'} \cdot \tau_{cH} / \tau_\lambda\right]} \quad \text{(D.23)}$$

$$\pi_{tL} = \tau_{tL}^{\gamma_t/[(\gamma_t-1)\cdot e_{tL}]} \tag{D.24}$$

$$\eta_{tL} = \frac{1-\tau_{tL}}{1-\pi_{tL}^{(\gamma_t-1)/\gamma_t}} \tag{D.25}$$

Engine exhaust mixer

$$\frac{P_{t5'}}{P_{t5}} = \frac{1}{\pi_{cH}\cdot\pi_b\cdot\pi_{tH}\cdot\pi_{tL}} \quad \text{(D.26)} \ ; \qquad \frac{T_{t5'}}{T_{t5}} = \frac{C_{pt}\cdot\tau_r\cdot\tau_{c'}}{C_{pc}\cdot\tau_\lambda\cdot\tau_{m1}\cdot\tau_{tH}\cdot\tau_{m2}\cdot\tau_{tL}} \quad \text{(D.27)}$$

$$\alpha' = \frac{\alpha}{(1-\beta-\varepsilon_1-\varepsilon_2)\cdot(1+f_b)+\varepsilon_1+\varepsilon_2} \tag{D.28}$$

$$R_5 = R_t \ ; \ R_{5'} = R_c \ ; \ C_{p5} = C_{pt} \ ; \ C_{p5'} = C_{pc} \ ; \ \gamma_5 = \gamma_t \ ; \ \gamma_{5'} = \gamma_c \tag{D.29}$$

$$C_{p6} = \frac{C_{p5}+\alpha'\cdot C_{p5'}}{1+\alpha'} \quad \text{(D.30)} \ ; \qquad R_6 = \frac{R_5+\alpha'\cdot R_{5'}}{1+\alpha'} \quad \text{(D.31)}$$

$$\gamma_6 = \frac{C_{p6}}{C_{p6}-R_6/778.16} \tag{D.32}$$

$$\tau_M = \frac{C_{p5}}{C_{p6}}\cdot\frac{1+\alpha'(C_{p5'}/C_{p5})\cdot(T_{t5'}/T_{t5})}{C_{p6}-R_6/778.16} \tag{D.33}$$

$$M_{5'} = \left[\frac{2}{\gamma_{5'}-1}\cdot\left\{\left[\frac{P_{t5'}}{P_{t5}}\cdot\left(1+\frac{\gamma_5-1}{2}\cdot M_5{}^2\right)^{\frac{\gamma_5}{\gamma_5-1}}\right]^{\frac{\gamma_{5'}-1}{\gamma_{5'}}}-1\right\}\right]^{0.5} \tag{D.34}$$

$$\frac{A_{5'}}{A_5} = \alpha'\cdot\left(\frac{M_5}{M_{5'}}\right)\cdot\left[\frac{T_{t5'}}{T_{t5}}\cdot\frac{\gamma_5\cdot R_{5'}\cdot\left(1+\frac{\gamma_5-1}{2}\cdot M_5{}^2\right)}{\gamma_{5'}\cdot R_5\cdot\left(1+\frac{\gamma_{5'}-1}{2}\cdot M_{5'}{}^2\right)}\right]^{0.5} \tag{D.35}$$

$$\Phi = \left[\frac{1+\alpha'}{\frac{1}{\sqrt{\phi(M_5,\gamma_5)}}+\alpha'\cdot\sqrt{\frac{R_{5'}}{\gamma_{5'}}\cdot\frac{\gamma_5}{R_5}}\cdot\sqrt{\frac{T_{t5'}/T_{t5}}{\phi(M_{5'},\gamma_c)}}}\right]^2\cdot\frac{\gamma_5\cdot R_6}{\gamma_6\cdot R_5}\cdot\tau_M \tag{D.36}$$

when, $$\phi(M,\gamma) = \frac{M^2\cdot\left(1+\frac{\gamma-1}{2}\cdot M^2\right)}{(1+\gamma\cdot M^2)^2} \tag{D.37}$$

$$M_6 = \left[\frac{2 \cdot \Phi}{(1 - 2 \cdot \gamma_6 \cdot \Phi) + \sqrt{1 - 2 \cdot (\gamma_6 + 1) \cdot \Phi}} \right]^{0.5} \tag{D.38}$$

$$\pi_M = \pi_{M\,\max} \cdot \frac{1 + \alpha'}{1 + A_{5'} / A_5} \cdot \sqrt{\tau_M} \cdot \frac{\text{MFP}\,(M_5, \gamma_5, R_5)}{\text{MFP}\,(M_6, \gamma_6, R_6)} \tag{D.39}$$

when,
$$\text{MFP}\,(M, \gamma, R) = \frac{M \cdot \sqrt{\gamma \cdot g / R}}{\left(1 + \frac{\gamma - 1}{2} \cdot M^2\right)^{\frac{\gamma + 1}{2 \cdot (\gamma - 1)}}} \tag{D.40}$$

Overall engine performance

$$f_0 = \frac{f_b \cdot (1 - \beta - \varepsilon_1 - \varepsilon_2)}{1 + \alpha} \tag{D.41}$$

$$\frac{P_{t9}}{P_9} = \left(\frac{P_0}{P_9}\right) \cdot \pi_r \cdot \pi_d \cdot \pi_{c'} \cdot \pi_{cH} \cdot \pi_b \cdot \pi_{tH} \cdot \pi_{tL} \cdot \pi_M \cdot \pi_n \tag{D.42}$$

$$M_9 = \left\{ \frac{2}{\gamma_6 - 1} \cdot \left[\left(\frac{P_{t9}}{P_9}\right)^{\frac{\gamma_6 - 1}{\gamma_6}} - 1 \right] \right\}^{0.5} \tag{D.43}$$

$$\frac{T_9}{T_0} = \frac{C_{pc}}{C_{pt}} \cdot \frac{\tau_\lambda \cdot \tau_{m1} \cdot \tau_{tH} \cdot \tau_{m2} \cdot \tau_{tL} \cdot \tau_M}{(P_{t9} / P_9)^{(\gamma_6 - 1)/\gamma_6}} \tag{D.44}$$

$$\frac{V_9}{V_0} = \left\{ \frac{\tau_\lambda \cdot \tau_{m1} \cdot \tau_{tH} \cdot \tau_{m2} \cdot \tau_{tL} \cdot \tau_M}{\tau_r - 1} \cdot \left[1 - \left(\frac{P_{t9}}{P_9}\right)^{\frac{1 - \gamma_6}{\gamma_6}} \right] \right\}^{0.5} \tag{D.45}$$

$$V_0 = M_0 \cdot \sqrt{\gamma_c \cdot R_c \cdot g_c \cdot T_0} \tag{D.46}$$

$$\begin{aligned} \frac{F}{m_0} = \frac{V_0}{g_c} \cdot \Bigg\{ & \left[\left(1 + f_0 - \frac{\beta}{1 + \alpha}\right) \cdot \frac{V_9}{V_0} - 1 \right] \\ & + \left[\left(1 + f_0 - \frac{\beta}{1 + \alpha}\right) \cdot \frac{R_6}{R_c} \cdot \frac{V_0}{V_9} \cdot \frac{T_9}{T_0} \cdot \frac{(1 - P_0 / P_9)}{\gamma_c \cdot M_0^{\,2}} \right] \Bigg\} \end{aligned} \tag{D.47}$$

$$\text{sfc} = \frac{3600 \cdot f_0}{F / m_0} \cdot fs \tag{D.48}$$

D.1.2 Off-Design Cycle Analysis

Repeat the preliminary computation part from Eq. (D.1) to Eq. (D.11) and then set the starting values of τ_{tL}, m_0 and α' as follows,

$$\tau_{tL} = \tau_{tL\,R} \;\; ; \;\; m_0 = m_{0R} \;\; ; \;\; \alpha' = \frac{\alpha_R \cdot T_0 \cdot \tau_r /(T_0 \cdot \tau_r)_R}{(1-\beta-\varepsilon_1-\varepsilon_2)\cdot(1+f_m)+\varepsilon_1+\varepsilon_2} \tag{D.49}$$

$$\pi_{tL} = \left(1 - \frac{1-\tau_{tL}}{\eta_{tL}}\right)^{\gamma_t/(\gamma_t-1)} \tag{D.50}$$

$$\alpha = \alpha_R \cdot \frac{\alpha'}{\alpha'_R} \tag{D.51}$$

Fan and high-pressure compressor

$$\tau_{c'} = 1 + A\cdot(\tau_{c'R}-1) + \left(\frac{C_{TO}}{\tau_r \cdot \eta_{mP}}\right)_R \cdot \left(A - \frac{(\tau_r \cdot m_0 \cdot T_0)_R}{\tau_r \cdot m_0 \cdot T_0}\right) \tag{D.52}$$

when, $$A = \frac{1-\tau_{tL}}{1-\tau_{tL\,R}} \cdot \frac{\tau_\lambda/\tau_r}{(\tau_\lambda/\tau_r)_R} \cdot \frac{1+\alpha_R}{1+\alpha}$$

$$\pi_{c'} = \left[1 + (\tau_{c'}-1)\cdot \eta_{c'}\right]^{\gamma_c/(\gamma_c-1)} \tag{D.53}$$

$$\tau_{cH} = \frac{1}{1-\varepsilon_1 \cdot \eta_{mH}\cdot(1-\tau_{tH\,R})} + \frac{\tau_\lambda/\tau_r}{(\tau_\lambda/\tau_r)_R}\cdot\frac{\tau_{c'R}}{\tau_{c'}}\cdot\left[\tau_{cH\,R} - \frac{1}{1-\varepsilon_1\cdot\eta_{mH}\cdot(1-\tau_{tH\,R})}\right] \tag{D.54}$$

$$\pi_{cH} = \left[1 + (\tau_{cH}-1)\cdot \eta_{cH\,R}\right]^{\gamma_c/(\gamma_c-1)} \tag{D.55}$$

Engine exhaust mixer

Set the station air properties as shown in Eq. (D.29).

$$\frac{1}{M_5}\cdot\left[\frac{2}{\gamma_5+1}\cdot\left(1+\frac{\gamma_5-1}{2}\cdot M_5^2\right)\right]^{\frac{\gamma_5+1}{2\cdot(\gamma_5-1)}} = \left(\frac{A}{A^*}\right)_{5R}\cdot\left(\frac{\pi_{tL}}{\pi_{tL\,R}}\right)\cdot\sqrt{\frac{\tau_{tL\,R}}{\tau_{tL}}} \tag{D.56}$$

Evaluate for M_5 (< 1.0) by function iteration.

$$\frac{P_{t5'}}{P_{5'}} = \frac{(\pi_{cH} \cdot \pi_{tL})_R}{\pi_{cH} \cdot \pi_{tL}} \cdot \left(\frac{P_{t5'}}{P_{t5}}\right)_R \cdot \left(1 + \frac{\gamma_5 - 1}{\gamma_5} \cdot M_5^{\ 2}\right)^{\gamma_5/(\gamma_5 - 1)} \tag{D.57}$$

If $\frac{P_{t5'}}{P_{5'}} > 1$ then continue; otherwise, decrease τ_{tL} by 0.001 and return to Eq. (D.50).

$$M_{5'} = \left\{\frac{2}{\gamma_{5'} - 1} \cdot \left[\left(\frac{P_{t5'}}{P_{5'}}\right)^{\frac{\gamma_{5'}-1}{\gamma_{5'}}} - 1\right]\right\}^{0.5} \tag{D.58}$$

If $M_{5'} < 0.95$ then continue; otherwise, increase τ_{tL} by 0.001 and return to Eq. (D.50).

Low-pressure turbine temperature ratio verification

$$\tau_{tL\,N} = \frac{\tau_r \cdot \tau_{c'}}{\tau_\lambda \cdot \tau_{m1R} \cdot \tau_{tH\,R} \cdot \tau_{m2R}} \cdot \left(\frac{\alpha'}{(A_{5'}/A_5)_R} \cdot \frac{M_5}{M_{5'}}\right)^2 \cdot \frac{\gamma_5 \cdot C_{p5}}{\gamma_{5'} \cdot C_{p5'}} \cdot \frac{\left(1 + \frac{\gamma_5 - 1}{2} \cdot M_5^{\ 2}\right)}{\left(1 + \frac{\gamma_{5'} - 1}{2} \cdot M_{5'}^{\ 2}\right)} \tag{D.59}$$

If $\left|\tau_{tL\,N} - \tau_{tL}\right| \leq 0.005$ then continue; otherwise, decrease τ_{tL} by 0.001 and return to Eq. (D.50).

Evaluate Eq. (D.27) and Eq. (D.30) to Eq. (D.39) from the engine exhaust mixer in section D.1.1.

Exhaust mixer bypass ratio verification

If $\frac{P_{t9}}{P_9} \geq \left(\frac{\gamma_6 + 1}{2}\right)^{\gamma_6/(\gamma_6 - 1)}$ then the exhaust nozzle is choked, thus

$$\alpha'_N = \left[(1 + \alpha') \cdot \frac{\sqrt{\tau_{tL} \cdot \tau_M}}{\pi_{tL} \cdot \pi_M}\right]_R \cdot \frac{\pi_{tL} \cdot \pi_M}{\sqrt{\tau_{tL} \cdot \tau_M}} \cdot \frac{\Gamma(\gamma_6)}{\Gamma(\gamma_{6R})} - 1 \tag{D.60}$$

when, $$\Gamma(\gamma) = \sqrt{\gamma} \cdot \left(\frac{2}{\gamma + 1}\right)^{\frac{\gamma+1}{2\cdot(\gamma-1)}} \tag{D.61}$$

Otherwise,

$$\alpha'_N = (1+\alpha'_R)\cdot\frac{\pi_{tL}\cdot\pi_M}{(\pi_{tL}\cdot\pi_M)_R}\cdot\sqrt{\frac{(\tau_{tL}\cdot\tau_M)_R}{\tau_{tL}\cdot\tau_M}}\cdot\frac{A_8}{A_{8R}}\cdot\frac{MFP(M_9,\gamma_6,R_6)}{MFP(M_9,\gamma_6,R_6)_R}-1 \tag{D.62}$$

If $|\alpha'-\alpha'_N|\le 0.005$ then re-calculate the α value using Eq. (D.51) and continue; otherwise, set $\alpha'=\alpha'_N$ and return to Eq. (D.50).

Mass flow rate verification

$$m_{0N} = m_{0R}\cdot\frac{1+\alpha}{1+\alpha_R}\cdot\frac{P_0\cdot\pi_r\cdot\pi_d\cdot\pi_{c'}\cdot\pi_{cH}}{(P_0\cdot\pi_r\cdot\pi_d\cdot\pi_{c'}\cdot\pi_{cH})_R}\cdot\sqrt{\frac{T_{t4R}}{T_{t4}}} \tag{D.63}$$

If $|m_{0N}-m_{0R}|\le 0.1$ then continue; otherwise, set $m_{0R}=m_{0N}$ and return to Eq. (D.50).

Burner

Determine f_b using Eq. (D.17).

$$\frac{T_{t5}}{T_{t4}} = \tau_{m1R}\cdot\tau_{tHR}\cdot\tau_{m2R}\cdot\tau_{tL} \tag{D.64}$$

Overall engine performance

This section features the same equations set as the previous on-design analysis case.

D.2 Tanker - Engine Performance Equations

Station	Location	Station	Location
0	Far upstream or freestream	4a	High pressure turbine entry for τ_{tH} definition
1	Inlet or diffuser entry	4b	High pressure turbine exit Modeled coolant mixer 2 entry
2	Inlet or diffuser exit Fan entry	4c	Coolant mixer 2 exit Low pressure turbine entry
3'	Fan exit High pressure compressor entry	5	Low pressure turbine exit Core stream mixer entry
3	High pressure compressor exit	7	Core exhaust nozzle entry
3a	Burner entry	9	Core exhaust nozzle exit
4	Burner exit Nozzle vanes entry Modeled coolant mixer 1 entry High pressure turbine entry for π_{tH} definition	7'	Bypass exhaust nozzle entry
4a	Nozzle vanes exit Coolant mixer 1 exit	9'	Bypass exhaust nozzle exit

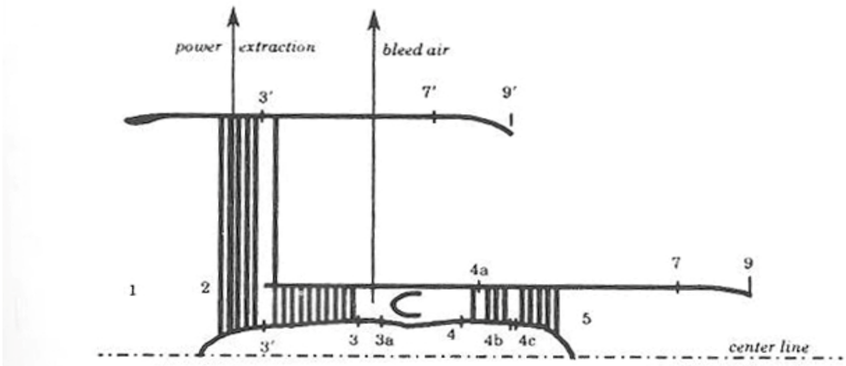

Figure D.2: Reference stations – high-bypass turbofan engine [21]

D.2.1 On-Design Cycle Analysis

Due to the similarities of tanker's and UCAV's engine station configurations, Eq. (D.1) to Eq. (D.25) from section D.1.1 can be directly applied in the initial computations of the high-bypass ratio turbofan engine.

Core-stream exhaust nozzle

$$\frac{P_{t9}}{P_0} = \pi_r \cdot \pi_d \cdot \pi_{c'} \cdot \pi_{cH} \cdot \pi_b \cdot \pi_{tH} \cdot \pi_{tL} \cdot \pi_n \tag{D.65}$$

If $\frac{P_{t9}}{P_0} > \left(\frac{\gamma_t + 1}{2}\right)^{\gamma_t/(\gamma_t - 1)}$ then

$$M_9 = 1 \;; \qquad \frac{P_{t9}}{P_9} = \left(\frac{\gamma_t + 1}{2}\right)^{\gamma_t/(\gamma_t - 1)} \;; \qquad \frac{P_0}{P_9} = \frac{P_{t9}/P_9}{P_{t9}/P_0} \tag{D.66}$$

Otherwise,

$$\frac{P_0}{P_9} = 1 \quad ; \qquad \frac{P_{t9}}{P_9} = \frac{P_{t9}}{P_0} \quad ; \qquad M_9 = \left\{ \frac{2}{\gamma_t - 1} \cdot \left[\left(\frac{P_{t9}}{P_0} \right)^{\frac{\gamma_t - 1}{\gamma_t}} - 1 \right] \right\}^{0.5} \tag{D.67}$$

Fan-stream exhaust nozzle

$$\frac{P_{t9'}}{P_0} = \pi_r \cdot \pi_d \cdot \pi_{c'} \cdot \pi_{n'} \tag{D.68}$$

If $\frac{P_{t9'}}{P_0} > \left(\frac{\gamma_c + 1}{2} \right)^{\gamma_c/(\gamma_c - 1)}$ then

$$M_{9'} = 1 \quad ; \qquad \frac{P_{t9'}}{P_{9'}} = \left(\frac{\gamma_c + 1}{2} \right)^{\gamma_c/(\gamma_c - 1)} \quad ; \qquad \frac{P_0}{P_{9'}} = \frac{P_{t9'} / P_{9'}}{P_{t9'} / P_0} \tag{D.69}$$

Otherwise,

$$\frac{P_0}{P_{9'}} = 1 \quad ; \qquad \frac{P_{t9'}}{P_{9'}} = \frac{P_{t9'}}{P_0} \quad ; \qquad M_{9'} = \left\{ \frac{2}{\gamma_c - 1} \cdot \left[\left(\frac{P_{t9'}}{P_0} \right)^{\frac{\gamma_c - 1}{\gamma_c}} - 1 \right] \right\}^{0.5} \tag{D.70}$$

Overall engine performance

f_0 can be evaluated using Eq. (D.41).

$$\frac{T_9}{T_0} = \frac{C_{pc}}{C_{pt}} \cdot \frac{\tau_\lambda \cdot \tau_{m1} \cdot \tau_{tH} \cdot \tau_{m2} \cdot \tau_{tL}}{(P_{t9} / P_9)^{(\gamma_t - 1)/\gamma_t}} \tag{D.71}$$

$$\frac{T_{9'}}{T_0} = \frac{\tau_r \cdot \tau_{c'}}{(P_{t9'} / P_{9'})^{(\gamma_c - 1)/\gamma_c}} \tag{D.72}$$

$$\frac{V_9}{V_0} = \left\{ \frac{\tau_\lambda \cdot \tau_{m1} \cdot \tau_{tH} \cdot \tau_{m2} \cdot \tau_{tL}}{\tau_r - 1} \cdot \left[1 - \left(\frac{P_{t9}}{P_9} \right)^{(1-\gamma_t)/\gamma_t} \right] \right\}^{0.5} \tag{D.73}$$

$$\frac{V_{9'}}{V_0} = \left\{ \frac{\tau_r \cdot \tau_{c'}}{\tau_r - 1} \cdot \left[1 - \left(\frac{P_{t9'}}{P_{9'}} \right)^{(1-\gamma_c)/\gamma_c} \right] \right\}^{0.5} \tag{D.74}$$

$$sft = \frac{V_0 / g_c}{1+\alpha} \cdot \left\{ \left[1 + f_0 \cdot (1+\alpha) - \beta\right] \cdot \frac{V_9}{V_0} - 1 \right.$$
$$+ \left[1 + f_0 \cdot (1+\alpha) - \beta\right] \cdot \frac{R_t}{R_c} \cdot \frac{T_9 / T_0}{V_9 / V_0} \cdot \frac{(1 - P_0 / P_9)}{\gamma_c \cdot M_0^{\ 2}} \qquad \text{(D.75)}$$
$$\left. + \alpha \cdot \left[\frac{V_{9'}}{V_0} - 1 + \frac{T_{9'} / T_0}{V_{9'} / V_0} \cdot \frac{(1 - P_0 / P_9)}{\gamma_c \cdot M_0^{\ 2}} \right] \right\}$$

sfc can be evaluated using Eq. (D.48).

D.2.2 Off-Design Cycle Analysis

Repeat the preliminary computation part from Eq. (D.1) to Eq. (D.11) and then set the starting values of τ_{tL}, $\tau_{c'}$, π_{tL} and m_0 as follows,

$$\tau_{tL} = \tau_{tL\,R} \quad ; \qquad \tau_{c'} = \tau_{c'R} \quad ; \qquad \pi_{tL} = \pi_{tL\,R} \quad ; \qquad m_0 = m_{0R} \qquad \text{(D.76)}$$

Determine τ_{cH}, π_{cH} and $\pi_{c'}$ using Eq. (D.53) to Eq. (D.55) in section D.1.2.

Repeat the core-stream and the fan-stream exhaust nozzle evaluations from Eq. (D.65) to Eq. (D.70) in section D.2.1.

$$\alpha = \alpha_R \cdot \frac{\pi_{cH\,R}}{\pi_{cH}} \cdot \sqrt{\frac{\tau_\lambda / \tau_r \cdot \tau_{c'}}{(\tau_\lambda / \tau_r \cdot \tau_{c'})_R}} \cdot \frac{MFP(M_{9'}, \gamma_c, R_c)}{MFP(M_{9'}, \gamma_c, R_c)_R} \qquad \text{(D.77)}$$

Fan total temperature ratio verification

Determine $\tau_{c'N}$ using Eq. (D.52).

If $\left|\tau_{c'N} - \tau_{c'}\right| \le 0.005$ then continue; otherwise, set $\tau_{c'} = \tau_{c'N}$ and return to τ_{cH} evaluation at the beginning.

Low-pressure turbine

$$\tau_{tL} = 1 - \eta_{tL} \cdot \left(1 - \pi_{tL}^{\ (\gamma_t - 1)/\gamma_t}\right) \qquad \text{(D.78)}$$

$$\pi_{tL} = \pi_{tLR} \cdot \sqrt{\frac{\tau_{tL}}{\tau_{tLR}} \cdot \frac{MFP(M_9, \gamma_t, R_t)_R}{MFP(M_9, \gamma_t, R_t)}} \tag{D.79}$$

Mass flow rate verification

Determine m_{0N} using Eq. (D.63).

If $|m_{0N} - m_0| \leq 0.1$ then continue; otherwise, set $m_0 = m_{0N}$ and return to τ_{cH} evaluation at the beginning.

Determine f_b using Eq. (D.17) and the overall engine performance can be evaluated directly using the same equations as the previous on-design analysis.

Appendix E – User Manual of the Design Synthesis and Optimisation Program

List of Abbreviations

Air Brake dCD0	- Drag coefficient increased due to air brakes
BA Com.Radius	- Break-away combat radius
BFL	- Balance field length
Cambered Ctrl	- Fuselage camber coordinate
Ctrl.Def.	- Control surface deflection
ECS Fraction	- Weight fraction of cockpit and pilot support systems
Ex.Area /In.Area	- Area ratio between the exhaust and the inlet
F.Factor	- Fudge factor
Fairing /F.Width	- Ratio of the fairing span to the fuselage width
Flap /Chord	- Flap-to-chord ratio
In.Area /Com.Area	- Area ratio between the inlet and the engine compressor
Inb.Span /Exp.Span	- Ratio of the inboard-wing span to the total exposed span
Inb.Ctrl Start Point	- Starting point of inboard control surface relative to the inboard-wing partition span
Inf.Pressure	- Tyre inflation pressure
Inlet Trapezium	- Trapezium angle of inlet cross-sectional area
LCN	- Load classification number
Max Base /In Base	- Ratio of maximum base width to that at the inlet plane
Outb.Ctrl End Point	- End point of outboard control surface relative to the outboard-wing partition span
PR	- Pressure ratio
Rad.Stiffness	- Radius of relative stiffness
Res.Fuel dCG	- Reserve fuel c.g. shift

RF Air Speed	- Refuelling Air speed
RF Oper.Time	- Total refuelling time
S.Duct /E. Length	- Ratio between the S-shaped part of duct component and the engine length
S.Tank /Exp.Span	- Ratio of the surge-tank span to the total exposed span
SLS Unins.Thrust	- Sea-level static uninstalled thrust
Spar /Chord	- Spar location relative to the chord
Stag. Intake	- Longitudinal stagger angle of the intake diffuser
Str.Factor	- Strut structural factor
TD	- Touchdown
TO	- Takeoff
Top Surface	- Curvature angle increasing the top-surface thickness
W.bay	- Weapon bay
Wf	- Weight fraction
X-MAC @C/4	- 25% mean aerodynamic chord location measured from the apex.
Y-Location /Outb.Span	- Spanwise HDU location relative to the outboard-wing span
Y-MAC	- Spanwise location of the mean aerodynamic chord

The `FFCombination` folder is required to be installed in the directory `C:\` and then an executable file of the program named `FFCombination.exe` can be found in the directory path `C:\FFCombination\RoutineTest\obj\Debug\`. It should be noted that in order for the entire program to run properly, the `FFCombination` folder and its associated files cannot be renamed neither changing the locations.

From the main window of the program shown in Figure E.1, tick any desired boxes in the Synthesis panel on the left to called Input/Output windows of corresponding aircraft as depicted in Figures E.2 and E.3.

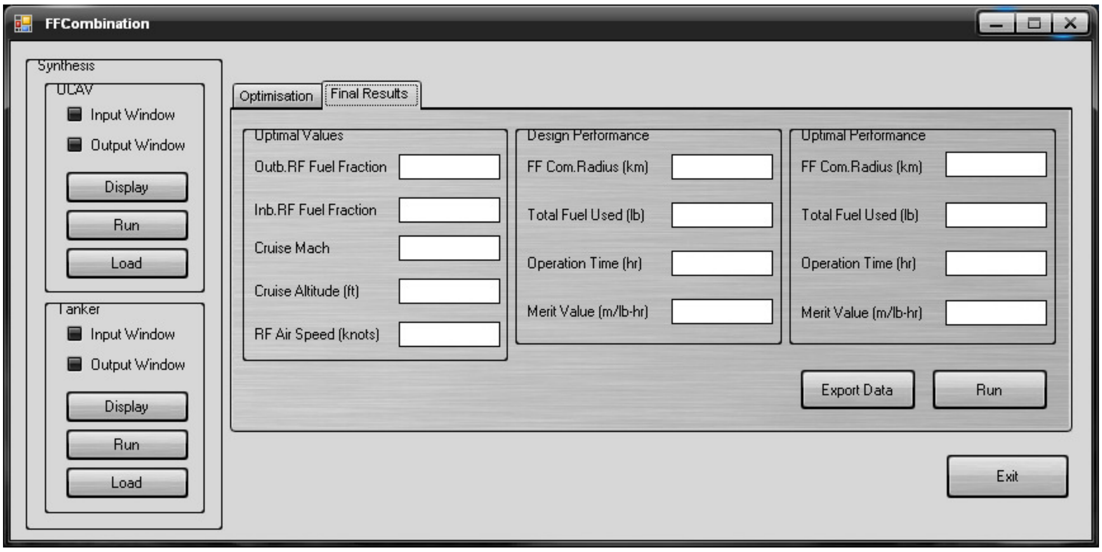

Figure E.1: Main operating window of the 'FFCombination' program

In the design synthesis inputs windows, the input values displayed on the GUI can be stored and retrieved from designated input file formats of `.uip` and `.tip` using 'Save' and 'Load' buttons below. For the first time opening the program after an installation, the input values of the aircraft should be loaded from example input files located in `C:\FFCombination\`.

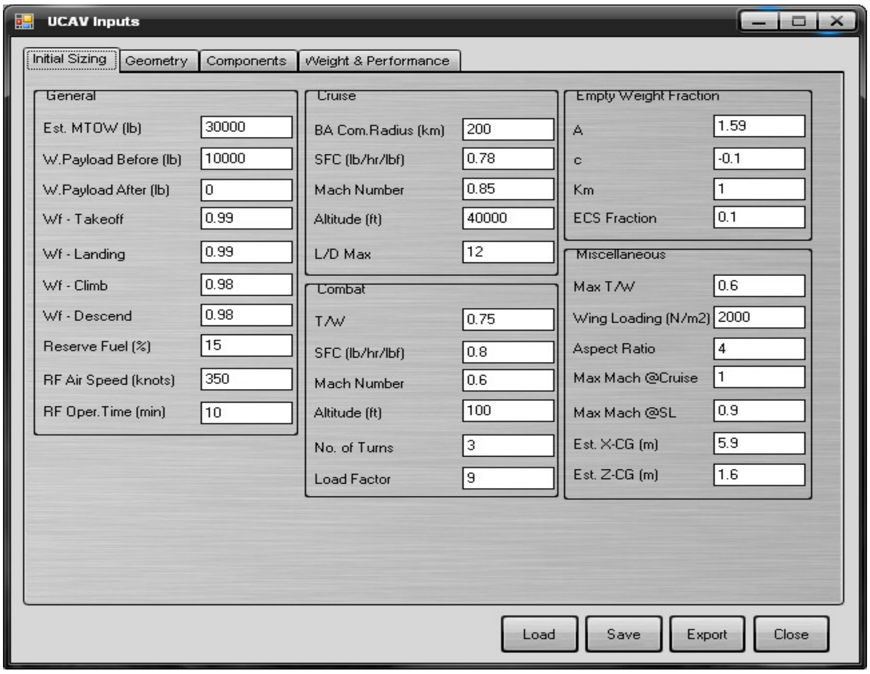

Figure E.2: UCAV Inputs window

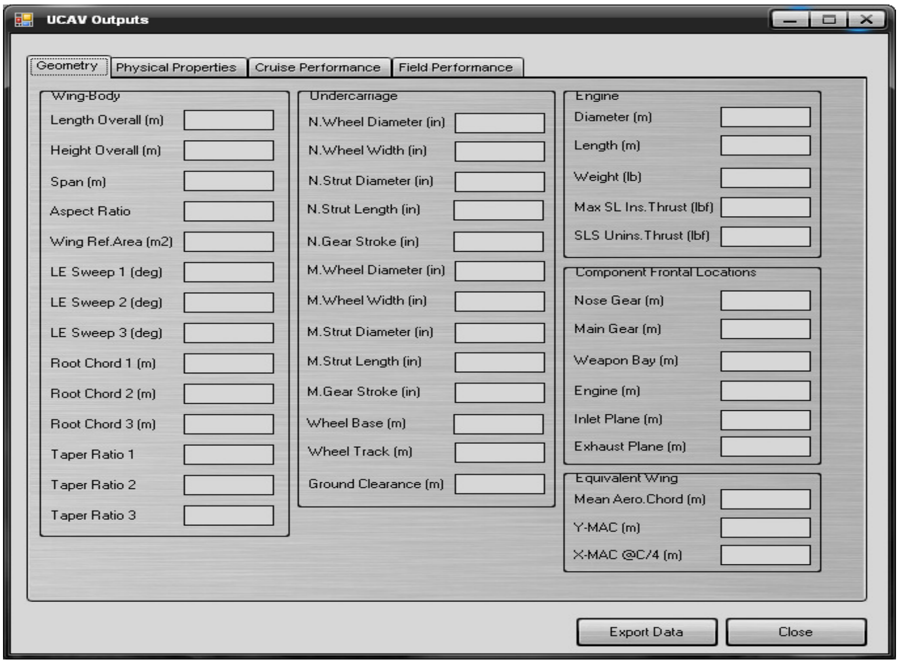

Figure E.3: UCAV Outputs window

A list of input parameters and their current assigned values may also be exported to readable text-format file using 'Export' button. For the design synthesis outputs windows, only the export option is available.

Always use 'Close' button instead of [X] to close any of the above window forms. Also press 'Exit' button to terminate the program to ensure that all input values are saved in the computer's resource.

Click 'Run' button to execute the design synthesis of corresponding aircraft and then the program will ask the user to specify the name of synthesised aircraft data file (`.ust` and `.tst`) in which will be saved after the execution is completed. This allows the user to load the same data using 'Load' button to the program for any subsequent uses.

The execution of UCAV synthesis takes approximately 2-4 minutes and 20-40 minutes for the tanker case depending on computer's speeds. It is suggested that the UCAV synthesis should be performed prior to the tanker. Alternately, the user may decide to load any `ust`-format files first and then run the tanker synthesis directly.

If the tanker design synthesis is performed before the synthesised UCAV data has been computed or loaded then the program will take current values of the UCAV and the tanker inputs to execute the design synthesises of both aircraft, however, without saving the synthesised UCAV data.

The optimisation input/output form is located on the left of the main window (see Figure E.1). The design variables values can be input in the first tab page while the displayed results and operation buttons are located on the latter page. The optimisation execution usually takes 3-7 hours to complete on Pentium 4 - 2 GHz. Thus, the same results could be achieved in much shorter time on current computers.

If the program has not been terminated after the tanker design synthesis was completed, the user can run the optimisation immediately since both UCAV and tanker synthesis data required for the operation are already stored in the program. Otherwise, the user needs to load both UCAV and tanker synthesis files before proceeding. An optimisation execution progress can be tracked in real-time from `RuntimeLog.txt` and `ResultLog.txt`. The first text file collects all optimisation search results while the latter one contains the best results so far.

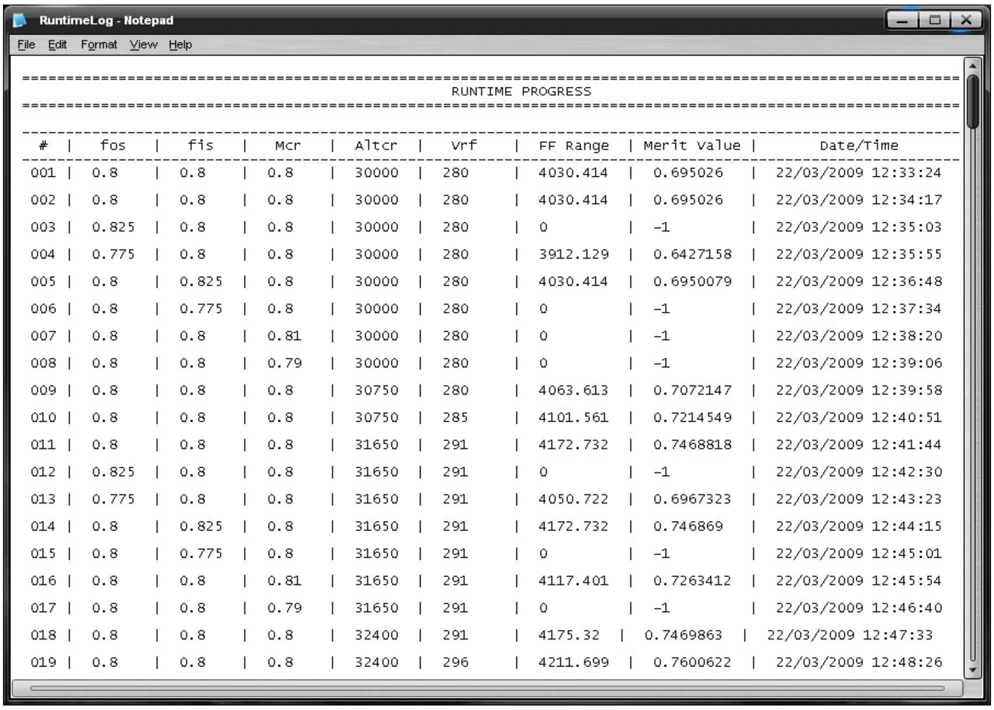

RUNTIME PROGRESS

#	fos	fis	Mcr	Altcr	Vrf	FF Range	Merit Value	Date/Time
001	0.8	0.8	0.8	30000	280	4030.414	0.695026	22/03/2009 12:33:24
002	0.8	0.8	0.8	30000	280	4030.414	0.695026	22/03/2009 12:34:17
003	0.825	0.8	0.8	30000	280	0	-1	22/03/2009 12:35:03
004	0.775	0.8	0.8	30000	280	3912.129	0.6427158	22/03/2009 12:35:55
005	0.8	0.825	0.8	30000	280	4030.414	0.6950079	22/03/2009 12:36:48
006	0.8	0.775	0.8	30000	280	0	-1	22/03/2009 12:37:34
007	0.8	0.8	0.81	30000	280	0	-1	22/03/2009 12:38:20
008	0.8	0.8	0.79	30000	280	0	-1	22/03/2009 12:39:06
009	0.8	0.8	0.8	30750	280	4063.613	0.7072147	22/03/2009 12:39:58
010	0.8	0.8	0.8	30750	285	4101.561	0.7214549	22/03/2009 12:40:51
011	0.8	0.8	0.8	31650	291	4172.732	0.7468818	22/03/2009 12:41:44
012	0.825	0.8	0.8	31650	291	0	-1	22/03/2009 12:42:30
013	0.775	0.8	0.8	31650	291	4050.722	0.6967323	22/03/2009 12:43:23
014	0.8	0.825	0.8	31650	291	4172.732	0.746869	22/03/2009 12:44:15
015	0.8	0.775	0.8	31650	291	0	-1	22/03/2009 12:45:01
016	0.8	0.8	0.81	31650	291	4117.401	0.7263412	22/03/2009 12:45:54
017	0.8	0.8	0.79	31650	291	0	-1	22/03/2009 12:46:40
018	0.8	0.8	0.8	32400	291	4175.32	0.7469863	22/03/2009 12:47:33
019	0.8	0.8	0.8	32400	296	4211.699	0.7600622	22/03/2009 12:48:26

Figure E.4: Optimisation log file presentation

Log file terminology

`Mcr`	- Cruise mach	`Altcr`	- Cruise altitude
`fos`	- Outbound offloaded fuel ratio	`Vrf`	- Refuelling airspeed
`fis`	- Inbound offloaded fuel ratio	`Altrf`	- Refuelling altitude

For the aircraft visualisation in AutoCAD 2006, all model data files will be automatically generated in `C:\FFCombination\ExportCAD\UCAV\` or `\Tanker\` after the design synthesis operation of the corresponding aircraft is completed. Use AutoLISP function in AutoCAD `[Tools > AutoLISP > Visual LISP Editor]` to open the drawing project files `[Project > Load Project]` named `UCAV.prj` or `Tanker.prj` located in the same directory path as above, and then run the project files `[Project > Load Project Source Files]` to generate the model results according to the exported data. Afterward the aircraft model will be completely drawn rapidly on the AutoCAD window.

The fuselage surface generation can be toggled to visual internal component models by disable/enable the following codes in `Fuselage.lsp` and then run the project file as normal.

```
(esurf "entt" "entt" "denta" "dentb")
(esurf "entb" "entb" "dentc" "dentd")
(esurf "entw" "entw" "dentb" "dentd")
```

The above command lines utilise the function `esurf` developed for rendering fuselage mesh surface. Any parts of AutoLISP codes can be disabled by simply inserting ‘semicolon’ in front of the desired code lines.

Appendix F – Northrop B-2 Validation

Since the uninhabited tanker developed in this PhD research programme is a novel and advanced concept both in terms of its operation and design methodology, currently there is no suitable existing aircraft to which it can be directly compared for validating purposes. Nonetheless, in an attempt to provide a validation of the uninhabited tanker's design synthesis methodology, the Northrop Grumman B-2 Spirit has been selected for comparison due to its similar overall baseline configuration and long-range capability.

Although the B-2 has been operated for more than 20 years, the majority of the information, especially regarding the performance of this aircraft, still remains highly classified. With the limited available information obtained from various sources [78, 79, 80], a comparison between the B-2 and the uninhabited tanker generated from the design synthesis methodology could be performed as shown in Table F.1 below. The three-view design drawings of both aircraft are depicted in Figure F.1. Also the input and output summaries of this uninhabited tanker are provided in Tables F.2 and F.3 respectively.

Table F.1: A comparison between Northrop B-2 and the uninhabited tanker

Specification	Northrop B-2	Uninhabited Tanker	% Difference
Length overall	21.03 m	21.28 m	+ 1.19 %
Wing span	52.43 m	52.65 m	+ 0.42 %
Total airframe area	490 m^2	509 m^2	+ 3.88 %
Takeoff weight	336500 lb	336447 lb	0.00 %
Approach speed	140 knots	156 knots	+ 11.43 %
Initial Climb	3000 fpm	3132 fpm	+ 4.40 %
Range @T-O weight	11110 km	10098 km	- 9.09 %
Runway requirement	Less than 3085 m	2659 m	N / A

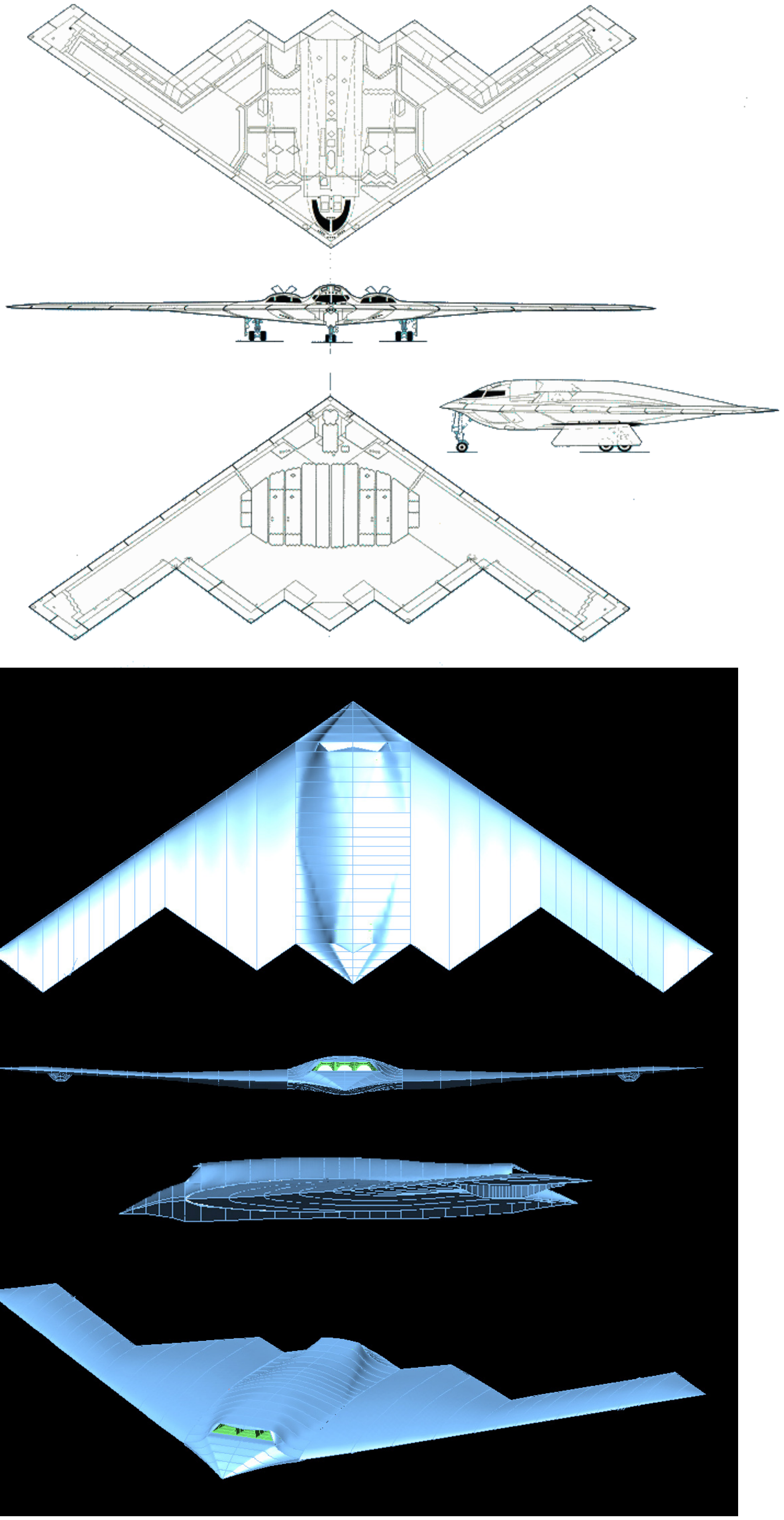

Figure F.1: Three-view drawings of the B-2 (top) [80] *and the validated tanker model (bottom)*

From Table F.1, the overall dimensions and the takeoff weight of the B-2 and the validated uninhabited tanker are approximately the same. Although no information on the B-2's field performance is available in the public domain, its runway length requirements may be still approximately investigated by considering its main operating air bases. The U.S. Air Force bases, where the B-2s have been assigned, are the Whiteman AFB and the Nellis AFB which have runway lengths of 3780 metres and 3085 metres respectively [79, 81]. This implies that the uninhabited tanker, requiring a runway length of 2659 metres, can be safely operated from the same air bases as the B-2. Hence, it may be reasonably concluded that the runway requirements of these two aircraft are generally similar.

The difference between the approach speeds of both aircraft is most likely due to differences in the assumed approach weight of the two aircraft and the type of aerofoils used. For the B-2 both of those characteristics are not released in the public domain. Furthermore, the B-2's "beaver tail" in combination with the multiple control surfaces on its wing's trailing-edge which can be optimally deflected at different angles along the span, may vary its camber characteristics to improve the generated lift, leading to a lower stall and hence lower approach speeds.

The range performance comparison is conducted at the B-2's reported cruise conditions of Mach 0.78 at 37000 feet [80]. These are not the exact optimum conditions for the tanker, which is specifically designed by the synthesis to match its operational role requirements. Aerofoil and cruise specific fuel consumption differences also play a significant role here. For trim, the tanker uses single-piece control surfaces on its inboard and outboard wing sections only, which are not segmented to produce optimal deflections throughout the wing span and they have a significantly lower total area in comparison to the B-2. Therefore, when the tanker is designed by the synthesis to match the B-2's planform geometry, as evidenced by the results, it requires relatively higher deflections to trim, with increased trim drag in cruise leading to a corresponding range reduction.

Apart from the above results comparison, this B-2 validation also demonstrated the flexibility of the modelling approach that was implemented in the developed design synthesis methodology. The mathematical modelling method provides the flexibility to generate sufficient aircraft shape variations for optimizing the design while maintaining the overall characteristics and constraints of the baseline configuration. In general the synthesis and analysis methods yield very reasonable results which are well within the expectations for such design concepts.

Table F.2: Uninhabited tanker input summary

Estimated T-O weight	336500 lb	Wing aspect ratio	4.05
Weapon payload weight	40000 lb	Thrust-to-weight ratio	2.26
Tanker fuel weight	142800 lb	Wing loading	2945 N/ m^2
Landing weight fraction	0.82	All leading-edge sweeps	35°
Reserve fuel	6 %	Cruise Mach number	0.78
Maximum load factor	2.5	Cruise altitude	37000 ft
Root incidence	1°	Inboard flap-to-chord ratio	0.35
Tip incidence	0°	Outboard flap-to-chord ratio	0.35

Table F.3: Uninhabited tanker output summary

Weights and Dimensions			
Length overall	21.28 m	Wing span	52.65 m
Height overall	4.60 m	Wheel track	10.06 m
Wing reference area	508.26 m^2	Wheel base	9.36 m
T-O weight	336447 lb	Empty weight	90375 lb
Tanker fuel weight	142800 lb	Payload fuel weight	63272 lb
Weapon weight	40000 lb	Max sea-level thrust	76037 lb
MAC	9.59 m	Spanwise MAC location	10.71 m
X-c.g. @ T-O weight	10.05 m	Z-c.g. @ T-O weight	3.06 m
Cruise performance			
Mach number	0.78	Max cruise thrust	37582 lb
Altitude	37000 ft	SFC	0.605 lb/hr/lbf
C_L Alpha	3.35 rad^{-1}	C_L Max	1.39
Stall angle	26.85°	L / D	13.93

Specific excess power	82.05 ft/s	Stall speed	168.89 knots
Static margin	1.71 %	Trim alpha	-0.80 °
Inboard control deflection	5.64°	Outboard control deflection	5.64°
Climb		**Descend**	
Mach number	0.4	Mach number	0.5
Climb rate	3132 fpm	Descend rate	2665 fpm
Climb angle	6.98°	Descend angle	-4.89°
Throttle setting	84.03 %	Throttle setting	10%
Field performance – Takeoff			
Total distance	2241 m	Takeoff speed	158.80 knots
Static margin	0.62	Takeoff alpha	10.46°
Inboard control deflection	5.13°	Outboard control deflection	5.13°
Field performance – Landing			
Total distance	1595 m	Touchdown speed	143.80 knots
Static margin	0.79	Touchdown alpha	10.42°
Inboard control deflection	5.41°	Outboard control deflection	5.41°